

AD-A249 918



NTATION PAGE

Form Approved
OMB No. 0704-0188

ated to average 1 hour per response, including the time for reviewing instructions, searching existing data sources, reviewing the collection of information, Send comments regarding this burden estimate or any other aspect of this burden to Washington Headquarters Services, Directorate for Information Operations and Reports, 1215 Jefferson Office of Management and Budget, Paperwork Reduction Project (0704-0188), Washington, DC 20503

DRT DATE

02/21/92

3. REPORT TYPE AND DATES COVERED

FINAL REPORT

4. TITLE AND SUBTITLE

Mechanical Behavior and Processing of Aluminum
Metal Matrix Composites

FUNDING NUMBERS

DAAL03-89-K-0027

6. AUTHOR(S)

E.J. Lavernia and F.A. Mohamed

7. PERFORMING ORGANIZATION NAME(S) AND ADDRESS(ES)

Dept. of Mechanical & Aerospace Engr.
University of California
Irvine, CA 92717

8. PERFORMING ORGANIZATION
REPORT NUMBER

APR 29 1992

9. SPONSORING/MONITORING AGENCY NAME(S) AND ADDRESS(ES)

U. S. Army Research Office
P. O. Box 12211
Research Triangle Park, NC 27709-2211

10. SPONSORING/MONITORING
AGENCY REPORT NUMBER

ARO 26439.48-MS

11. SUPPLEMENTARY NOTES

The view, opinions and/or findings contained in this report are those of the author(s) and should not be construed as an official Department of the Army position, policy, or decision, unless so designated by other documentation.

12a. DISTRIBUTION/AVAILABILITY STATEMENT

Approved for public release; distribution unlimited.

12b. DISTRIBUTION CODE

13. ABSTRACT (Maximum 200 words)

The objectives of the present three year research program were threefold. First the program sought to explore the potential of using spray atomization and deposition to process aluminum metal matrix composites, not only with improved mechanical properties, but also with specifications suitable for applications of interest to the Army; these applications include light weight armor vehicles, helicopter engines and other structural components. Second, the research program sought to develop an in-depth understanding of the various physical phenomena that occur during spray atomization and deposition of aluminum metal matrix composites. Third, the program sought to provide insight the fundamental mechanisms governing the elevated temperature deformation behavior, not only of metal matrix composites processed by spray atomization and deposition, but also of metal matrix composites in general. Accordingly, the present final report has been divided into six sections. The first section describes the spray atomization and deposition processing of unreinforced Al-Li base alloys with special emphasis on the role of thermomechanical processing and microstructure on mechanical properties. The second section provides insight into the factors that govern particulate injection during spray atomization and deposition of metal matrix composites. In second section, particular emphasis is placed on the resultant distribution of ceramic particulates in the metal matrix. The third section addresses heat transfer effects derived from the injection of particulates into an atomized metal stream, and the ensuing effects on the resulting grain size in metal matrix composites. The fourth section involves a detailed characterization of the metal/ceramic interfacial region, with particular emphasis on the segregation of constituent elements and wettability during processing. The fifth section involves a comprehensive study of the application of spray atomization and co-deposition to the synthesis of elevated temperature Al alloys. Accordingly, microstructural stability, phase analysis, excess solid solubility and mechanical properties are addressed. Finally, the sixth section involves a detailed investigation of the elevated temperature mechanical behavior of MMCs.

14. SUBJECT TERMS Spray Atomization and Co-Deposition; Metal Matrix Composites; Solidification Mechanisms; Non-Equilibrium Processing Discontinuous Reinforcements; Oxides; Creep Behavior; High Strength Aluminum Alloys

15. NUMBER OF PAGES

228 pages

16. PRICE CODE

17. SECURITY CLASSIFICATION
OF REPORT

UNCLASSIFIED

18. SECURITY CLASSIFICATION

UNCLASSIFIED

19. SECURITY CLASSIFICATION
OF ABSTRACT

UNCLASSIFIED

20. LIMITATION OF ABSTRACT

UL

NSN 7540-01-280-5500

92 4 27 370

**Mechanical Behavior & Processing
of Aluminum Metal Matrix Composites**

FINAL REPORT

January 1, 1989 - December 31, 1991

Submitted to:

Dr. Andrew Crowson
Dr. Edward Chen
Materials Research
United States Army Research Office
P.O. Box 12211
Research Triangle Park
North Carolina, 27709-2211

26439-MS

Grant Number: DAAL03-89-K-0027

From:

Enrique J. Lavernia
Associate Professor

Farghalli Mohamed
Professor

Materials Science and Engineering
Department of Mechanical and Aerospace Engineering
University of California, Irvine
Irvine, CA 92717

Friday, February 21, 1992

Accession For	
NTIS CRA&I	<input checked="" type="checkbox"/>
DTIC TAB	<input type="checkbox"/>
Unannounced	<input type="checkbox"/>
Justification	
By	
Distribution/	
Availability Codes	
Dist	Avail and/or Special
A-1	



APPROVED FOR PUBLIC RELEASE; DISTRIBUTION UNLIMITED¹

¹The views, opinions and/or findings contained in this report are those of the authors and should not be construed as an official Department of The Army position, policy, or decision, unless so designated by other documentation.

92-11114



TABLE OF CONTENTS

I. FOREWORD	1
1.0 Spray Atomization and Deposition Processing of Two Al-Li-X-Zr (X = Cu, Mg and Ge) Alloys	4
1.1 Introduction	5
1.2 Experimental Procedure	8
1.2.1 Spray Atomization and Deposition Experiments	9
1.2.2 Powder Sizes and Characterization	10
1.2.3 Thermomechanical Processing	11
1.2.4 Optical Microscopy	11
1.2.5 Scanning Electron Microscopy (SEM)	11
1.2.6 Transmission Electron Microscopy	12
1.2.7 Differential Scanning Calorimetry (DSC)	12
1.2.8 X-Ray Diffraction (X.R.D.)	12
1.2.9 Mechanical Testing	12
1.3 Results	13
1.3.1 Powder Sizes and Characterization	13
1.3.2 Optical Microscopy	14
1.3.3 SEM/EDAX Analysis	16
1.3.4 TEM	18
1.3.5 X-Ray Diffraction	20
1.3.6 DSC	20
1.3.7 Mechanical Behavior	21
1.3.8 Numerical Model	23
1.4 Discussion	26
1.4.1 Powder Sizes and Characterization	26
1.4.2 Grain Structure	26
1.4.3 Porosity	28
1.4.4 Cooling Rate and Solidification Front Velocity	30
1.4.5 Precipitation Behavior	31
1.4.6 Mechanical Behavior	32
1.5 Conclusions	32
2.0 The Effects of Solidification Phenomena on the Distribution of SiCp During Spray Atomization and Co-Deposition	34
2.1. Introduction	35
2.2 Experimental Procedure	36
2.2.1 Spray Atomization and Co-Deposition Processing	36
2.2.2 Optical Microscopy	42
2.2.3 Scanning Electron Microscopy (SEM)	43
2.3 Results	43
2.3.1 Fluidized Bed Experiments	43
2.3.2 Structural Characterization	45
2.3.2.1 Optical Microscopy	45
2.3.2.2 Image Analysis	50
2.3.2.3 SEM/EDAX Analysis	51
2.3.2.4 Numerical Results	53
2.4 Discussion	57
2.4.1 Microstructure	57
2.4.2 Porosity	60
2.4.3 SiCp Size and Distribution	60
2.4.4 Distribution of SiCp in the Al-Li matrix	62
2.5 Conclusions	71

3.0 The Effect of Ceramic Reinforcements During Spray Atomization and Co-Deposition of Metal Matrix Composites Part I. Heat Transfer	73
3.1. Introduction	74
3.2. Experimental Procedure	74
3.2.1. Processing	74
3.2.2. Light Microscopy	75
3.2.3. Scanning Electron Microscopy (SEM)	76
3.2.4. Transmission Electron Microscopy (TEM)	76
3.2.5. Steady State Temperature Determination	76
3.3. Results	76
3.3.1. Microstructural Characterization	76
3.4. Discussion	81
3.4.1. Solidification Effects	82
3.4.2. Heat Transfer Effects	83
3.4.2.1. Powder Size Distribution	84
3.4.2.2. Heat Transfer During Atomization	86
3.4.2.3. Heat Transfer During Deposition	93
3.4.3. Numerical Results	94
3.5. Conclusions	98
4.0 The Effect of Ceramic Reinforcements During Spray Atomization and Co-Deposition of Metal Matrix Composites Part II. Solid State Cooling Effects	99
4.1. Introduction	100
4.2. Experimental Procedure	100
4.2.1. Thermomechanical Treatment	100
4.2.2. Scanning Electron Microscopy (SEM)	101
4.3. Results	101
4.3.1. Microstructural Characterization	101
4.3.2. Grain Growth Behavior	105
4.4. Discussion	108
4.4.1. Solid State Cooling Effects	108
4.5. Conclusions	111
5.0 Wetting and Interfacial Reactions in Al-Li-SiCP MMCs Processed by Spray Atomization and Deposition	113
5.1. Introduction	114
5.2. Experimental Procedure	116
5.2.1. Materials	116
5.2.2. Spray Atomization and Co-deposition Processing	116
5.2.3. Structural Characterization	116
5.2.3.1. Optical microscopy (OM)	118
5.2.3.2. Transmission Electron Microscopy (TEM)	118
5.2.3.3. Scanning Electron Microscopy (SEM)	118
5.2.3.4. X-ray diffraction (XRD)	119
5.3. Results	119
5.3.1. Structural Characterization	119
5.3.2. Optical microscopy (OM)	119
5.3.3. Image Analysis	121
5.3.4. Transmission Electron Microscopy (TEM)	121
5.3.5. SEM/EDS	121
5.3.6. X-ray diffraction (XRD)	125
5.4. Discussion	126
5.4.1. Grain Structure	126
5.4.2. SiCp Size and Distribution	127
5.4.3. Wetting and Interfacial Reactions	128

5.4.4 Dynamic Wettability	132
5.5. Conclusions	136
6.0 Microstructure, Excess Solid Solubility and Elevated Temperature Mechanical Behavior of Spray Atomized and Co-Deposited Al-Ti- SiCp	137
6.1. Introduction	138
6.2. Experimental Procedure	139
6.2.1 Processing	139
6.2.2. Microstructure	143
6.2.3. Phase Analyses	144
6.2.4. Thermomechanical Treatment	145
6.3. Results	145
6.3.1. Processing	145
6.3.2. Microstructure	146
6.3.3. Thermomechanical Treatment	154
6.3.4. Quantitative Phase Analyses	159
6.4. Discussion	162
6.4.1. Microstructure	162
6.4.2. Secondary Phases and Thermal Stability	164
6.4.3. Excess Solid Solubility	167
6.4.4. Elevated Temperature Mechanical Behavior	171
6.5. Conclusions	173
7.0 Creep Behavior of Discontinuous SiC-Al Composites	175
7.1. Introduction	176
7.2. Analysis and Discussion	177
7.2.1 Creep Investigations on SiC-Al Composites	177
7.2.2 The Shear-lag Models	183
7.2.3 Finite Element Continuum Treatment	184
7.2.4 Deformation Models Based on Dislocation Motion	185
7.2.4.1 The stress exponent for creep	188
7.2.4.2 Activation energy for creep	198
7.3. Conclusions	202
II. NOMENCLATURE	205
III REFERENCES	210
IV. LIST OF PUBLICATIONS	223
V. LIST OF PARTICIPATING SCIENTIFIC PERSONNEL	228

I. FOREWORD

The attractive physical and mechanical properties that can be obtained with metal matrix composites (MMCs), such as high specific modulus, strength, and thermal stability have been documented extensively [1-7]. MMCs combine metallic properties (ductility and toughness) with ceramic properties (high strength and high modulus) leading to greater strength in shear and compression and higher service temperature capabilities. Interest in MMCs for aerospace, automotive and other structural applications has increased over the last five years, as a result of availability of relatively inexpensive reinforcements, and the development of various processing routes which result in reproducible microstructures and properties [8]. In aerospace applications, for example, reductions in structural weight can be effected, not only by reducing the alloy density, but also by increasing its modulus. For example, a 50 percent increase in modulus, achieved by substituting a discontinuous silicon carbide reinforced aluminum alloy for an unreinforced wrought counterpart, resulted in a 10 percent reduction in weight [9].

Reinforcement materials include carbides (e.g., SiC, B₄C), nitrides (e.g., Si₃N₄, AlN), oxides (e.g., Al₂O₃, SiO₂), as well as elemental materials (e.g., C, Si). The reinforcements may be in the form of continuous fibers, chopped fibers, whiskers, platelets, or particulates. SiC, for example, is being used in aluminum and magnesium MMCs in all of the above mentioned forms and carbon and silicon fibers are being used in aluminum-, magnesium-, and copper-matrix composites [10].

Early studies on MMCs addressed the development and behavior of continuous fiber reinforced high performance hybrid materials, based on aluminum and titanium matrices [11, 12]. Unfortunately, and despite encouraging results, extensive industrial application of these composites has been hindered by high manufacturing costs associated with the high costs of the reinforcement fibers and highly labor intensive manufacturing processes. As a result, utilization of these materials has been limited, almost exclusively, to military and other highly specialized applications.

The family of discontinuously reinforced MMCs includes those with particulate, whisker, and chopped fiber reinforcements. Recently, this class of MMCs has attracted considerable attention as a result of: (a) availability of various types of reinforcements at competitive costs, (b) the successful development of manufacturing processes to produce MMCs with reproducible structures and properties, and (c) the availability of standard or

near standard metal working methods which can be utilized to form these MMCs [13]. Moreover, the problems associated with fabrication of continuously reinforced MMCs, such as: (a) fiber damage, (b) microstructural non-uniformity, (c) fiber to fiber contact, and (d) extensive interfacial reactions can be avoided with discontinuous reinforcements [14]. In applications not requiring extreme loading or thermal conditions, such as in automotive components, discontinuously reinforced MMCs have been demonstrated to offer essentially isotropic properties with substantial improvements in strength and stiffness, relative to those available with unreinforced materials [15-19].

A variety of processing techniques have evolved over the last two decades in an effort to optimize the structure and properties of particulate reinforced MMCs. The processing methods utilized to manufacture particulate reinforced MMCs can be grouped depending on the temperature of the metallic matrix during processing. Accordingly, the processes can be classified into three categories: (a) liquid phase processes, (b) solid phase processes, and (c) two phase (solid/liquid) processes. Liquid phase processes involve the casting of a mixture of liquid- matrix and ceramic particulates. These include the DURAL process [11, 20] and melt infiltration processes [21-25]. Solid phase processes include powder metallurgy (PM) (blending and consolidation of alloy matrix powders with reinforcing particulates) techniques [11, 26]. Two phase (solid/liquid) processes include rheocasting [29, 30], and spray atomization and deposition processes [31-38]. Although liquid phase processes and solid phase processes have been carried out to various degrees of success, there is ample experimental evidence suggesting that there are some important drawbacks [22, 27, 28]. More recently, two phase techniques, in particular, spray deposition processes, have received considerable attention for the synthesis of discontinuously reinforced MMCs. This particular processing methodology involves the mixing of the reinforcements and the matrix in a regime of the phase diagram where the matrix contains both solid and liquid phases. It would appear that such an approach will inherently avoid the extreme thermal excursions, with concomitant degradation in interfacial properties and extensive macrosegregation, normally associated with casting processes. Furthermore, this approach also eliminates the need to handle fine reactive particulates, as is necessary with powder metallurgical processes.

The objectives of the present three year research program were threefold. First the program sought to explore the potential of using spray atomization and deposition to process aluminum metal matrix composites, not only with improved mechanical properties, but also with specifications suitable for applications of interest to the Army;

these applications include light weight armor vehicles, helicopter engines and other structural components. Second, the research program sought to develop an in-depth understanding of the various physical phenomena that occur during spray atomization and deposition of aluminum metal matrix composites. Third, the program sought to provide insight the fundamental mechanisms governing the elevated temperature deformation behavior, not only of metal matrix composites processed by spray atomization and deposition, but also of metal matrix composites in general. Accordingly, the present final report has been divided into six sections. The first section describes the spray atomization and deposition processing of unreinforced Al-Li base alloys with special emphasis on the role of thermomechanical processing and microstructure on mechanical properties. The second section provides insight into the factors that govern particulate injection during spray atomization and deposition of metal matrix composites. In second section, particular emphasis is placed on the resultant distribution of ceramic particulates in the metal matrix. The third section addresses heat transfer effects derived from the injection of particulates into an atomized metal stream, and the ensuing effects on the resulting grain size in metal matrix composites. The fourth section involves a detailed characterization of the metal/ceramic interfacial region, with particular emphasis on the segregation of constituent elements and wettability during processing. The fifth section involves a comprehensive study of the application of spray atomization and co-deposition to the synthesis of elevated temperature Al alloys. Accordingly, microstructural stability, phase analysis, excess solid solubility and mechanical properties are addressed. Finally, the sixth section involves a detailed investigation of the elevated temperature mechanical behavior of MMCs.

In order to present the research results in a coherent manner, each section contains its own set of figures, tables, and conclusions. The references are listed at the end of the report.

CHAPTER 1

1.0 Spray Atomization and Deposition Processing of Two Al-Li-X-Zr (X = Cu, Mg and Ge) Alloys

1.1 Introduction

The critical need for structural materials to be both cost-effective and superior in performance, coupled with an increased emphasis on efficiency and reliability, has stimulated considerable widespread interest in the development of new aluminum alloys. These alloys could potentially provide excellent combinations of reduced density, high strength, good fracture toughness, resistance to exfoliation corrosion, resistance to stress corrosion cracking, improved thermal stability and better stiffness. The family of lithium-containing aluminum alloys have, in recent years, received much attention for use in weight-critical and stiffness-critical structures for military, space and commercial applications as a result of their low density, improved specific strength, and high stiffness-to-weight ratio [39-41]. Lithium additions in aluminum result in the greatest reduction in density and increase in elastic modulus of any known alloying element. The potential to reduce the density of aluminum alloys through lithium additions is evident by comparing the atomic weight of lithium (6.94 g/mol) with that of aluminum (26.98 g/mol). In fact, each one percent increment of lithium addition to an aluminum alloy decreases the density by about three percent and increases the elastic modulus by six percent [40, 41]. The potential for substantial weight savings in aircraft structural parts, in combination with the substantial solubility of lithium in molten aluminum has resulted in the development of numerous aluminum-lithium alloys.

Unfortunately, the beneficial effects associated with lithium additions are accompanied by a reduction in monotonic ductility and fracture toughness in alloys which are solution heat treated, quenched, and aged to peak strength [40-44], making these alloys unsuitable for many structural applications. Over the past decade, considerable research efforts have been directed towards improving the poor ductility and fracture behavior of aluminum-lithium alloys. Some of the approaches taken for improving toughness in Al-Li-X alloys involve: (1) encouraging dislocation cross-slip or precipitate bypassing in the alloy by modifications of the lattice parameters to increase mismatch in the $\alpha\text{Al}/\text{Al}_3\text{Li}$ system, (2) introducing secondary precipitation systems, and (3) using a dispersion hardening system in addition to the precipitation hardening system. Other approaches taken include grain refinements via additions of Mn, Zr, Co and minimization of tramp elements (K, Na and S) through alloy control [40].

With the advent of rapid solidification technology (RST), rapid quenching was sought as the solution to improving the low fracture toughness and inferior monotonic ductility of

the lithium containing aluminum alloys. Rapid solidification technology offers several advantages over ingot metallurgy (IM) methods when used for the manufacture of lightweight aluminum-lithium alloys [45].

Although significant progress was achieved towards improving the mechanical behavior of aluminum-lithium alloys using RST, this approach introduced another problem, namely that of oxide contamination. The large surface areas generated by RST techniques, in combination with the stability of the aluminum oxide (i.e., Al_2O_3), made it impossible to completely eliminate oxides from consolidated RST materials; instead it was a matter of the amount of oxide one could tolerate. The oxide is usually present as an amorphous $\text{Al}_2\text{O}_3/\text{Al}_2\text{O}_3 \cdot 3\text{H}_2\text{O}$ film with small amounts of MgO crystallites surrounded by physically adsorbed $\text{H}_2\text{O}/\text{O}_2$. The thickness of the oxide film can vary from 5 nm up to 100 nm, depending on particulate size and processing history [46, 47]. Hence, it is usually necessary to remove adsorbed gas and hydrated water from the surface of the particulates prior to consolidation in order to achieve full density; this is usually accomplished by a degassing step. The presence of oxidation products in the form of either oxides, or physically adsorbed water, is highly detrimental to the mechanical behavior of consolidated RST materials.

The properties of high strength aluminum alloys consolidated from fine RST particulates are strongly affected by the presence of oxides on prior particle boundaries [40, 46-49]. Gysler et al [48] observed early crack nucleation at almost continuous oxide films along prior flake boundaries in consolidated Al-Li-Cu alloys. The large oxide particles were thought to dominate the crack nucleation process, and therefore the ductility of the RST materials. Kang and Grant [49], reported a sharp decrease in the fracture toughness of a consolidated RST X2020 alloy when compared to that of the equivalent IM material, and attributed this observation to a high volume fraction of oxide phases. The detrimental effects of oxides on mechanical behavior are particularly noticeable in aluminum-lithium alloys as a result of the high reactivity of lithium.

The excessive high temperature reactivity of aluminum-lithium alloys results in the formation of non-protective, porous surface films; lithium depletion; and intergranular oxidation in moist oxygen-containing environments [50-52]. It has been shown, for example, that the oxidation rate of aluminum alloys containing 3 wt.% lithium is ten times faster than that of comparable magnesium containing alloys [53]. Ashton and co-

workers [51] attributed the enhanced oxidation kinetics of aluminum-lithium alloys to the formation of a non-protective, porous AlLiO_2 film.

In an effort to control the oxide contamination problem associated with fine RST particulates and to improve the mechanical behavior of aluminum-lithium alloys, various approaches are actively being studied. These include (i) refining conventional ingot casting practices, (ii) increasing secondary alloying additions, (iii) developing alternative thermomechanical processing treatments, and (iv) developing novel RST processes. Two RST processing approaches actively being studied are mechanical alloying [54, 55] and spray atomization and deposition [37, 38, 56, 57].

Mechanical alloying improves strain localization and avoids the precipitate free zones frequently associated with aluminum-lithium alloys by introducing fine, homogeneously distributed dispersoids that interact directly with dislocations, dispersing slip and inhibiting the formation of intense slip bands. Donachie and Gilman [54] and later Gilman, Books and Bridges [55] successfully incorporated 5 volume percent of aluminum oxide and carbide dispersoids into Al - 2.5Li - 2Cu and Al - 2.5Li - 1Mg (in wt.%) powders by mechanical alloying (MA). The mechanical properties of the MA materials were reported to be superior to those of the equivalent IM material. The MA alloy, for example, showed an elongation of 7% (compared to 2% for the IM alloy) at superior strength levels. Donachie and Gilman [54] significantly improved the toughness of a MA Al-Mg-Li alloy by varying the powder processing parameters and vacuum consolidation temperatures. The K_Q value was increased from 21.8 MPa $\text{m}^{1/2}$ to 29.6 MPa $\text{m}^{1/2}$ at a yield strength of 483 MPa.

In spray atomization and deposition a stream of molten metal is disintegrated into a fine dispersion of droplets using high energy inert gases. The resultant distribution of metallic droplets is directed towards a substrate surface where it impacts and builds into a deposit of predetermined thickness. A large proportion of the latent heat of fusion is dissipated during flight, hence the distribution of droplets contain both liquid and solid phases at impact. A review on spray atomization and deposition of metals and alloys can be found elsewhere [58]. Spray atomization and deposition processes would appear to offer some of the advantages of RST while minimizing the oxidation problem, and early results are encouraging. In studies on high strength aluminum alloys containing 1.55 and 1.74 wt.% Li, improvements in room temperature tensile ductility and fatigue crack growth rates at equivalent strength levels have been reported [58]. The crack growth rates measured for

the spray deposited material were significantly retarded when compared to those for IM 2024 and PM X2020, up to a stress intensity level $\Delta K = 17 \text{ MP}\sqrt{\text{m}}^{1/2}$.

Meschter and co-workers [59-61] reported significant improvements in the notched tensile behavior of spray atomized and deposited Al - 4Li - 1Cu - 0.2Zr (in wt.%) over that shown by the same PM alloy ($\sigma_{\text{NTS}}/\sigma_{\text{YS}} = 0.64$ vs 0.18; T8 temper). Finally, the addition of 1 wt.% Li to an experimental 2024 alloy processed by spray atomization and deposition resulted in excellent combinations of strength, tensile ductility, and notched strength ($\sigma_{\text{UTS}} = 513 \text{ MPa}$; $\sigma_{\text{YS}} = 363 \text{ MPa}$; elongation = 16.4%; $\sigma_{\text{NTS}}/\sigma_{\text{YS}} = 1.44$; [58]).

The objective of the present study is to provide preliminary results on the structure and mechanical properties of two spray atomized and deposited aluminum-lithium alloys (Al - 2.5Cu - 2.1Li - 0.13Zr and Al - 4Li - 1Mg - 0.5Ge - 0.2Zr). In particular, this study seeks to enhance our understanding of the effects of heat transfer and solidification during processing on the resultant structures and properties. The selection of the Al - 4Li - 1Mg - 0.5Ge - 0.2Zr material was prompted by the attractive combinations of properties reported by Meschter and co-workers [59-61] for high lithium containing materials. The addition of Ge was based on the results of Cassada, Shiftlet, and Starke [62]. Their work indicates that Ge additions form fine, insoluble particles that may help disperse slip during plastic deformation. The Al - 2.5Cu - 2.1Li - 0.13Zr alloy was selected in order to gain some insight into the type and extent of precipitation reactions during spray atomization and deposition. This alloy composition has been extensively studied by other investigators [40].

1.2 Experimental Procedure

Reynolds Metals Company provided the aluminum-lithium master alloys as cast ingots, 100 mm x 200 mm x 600 mm. The ingots were inspected for major defects, and chemically analyzed in preparation for atomization. The chemical analysis of the remelt alloys are shown in Table 1.

Table 1. Chemical Analysis of Alloys.

<u>Alloy Designation</u>	<u>Li</u>	<u>Cu</u>	<u>Mg</u>	<u>Ge</u>	<u>Zr</u>	<u>Al</u>
A	4.00	--	1.00	0.50	0.20	bal.
B ¹	2.13	2.50	--	--	0.13	bal.

¹This alloy is produced commercially by Reynolds Co., Va.

1.2.1 Spray Atomization and Deposition Experiments

A schematic diagram of the experimental facility used in this investigation is shown in Figure 1.

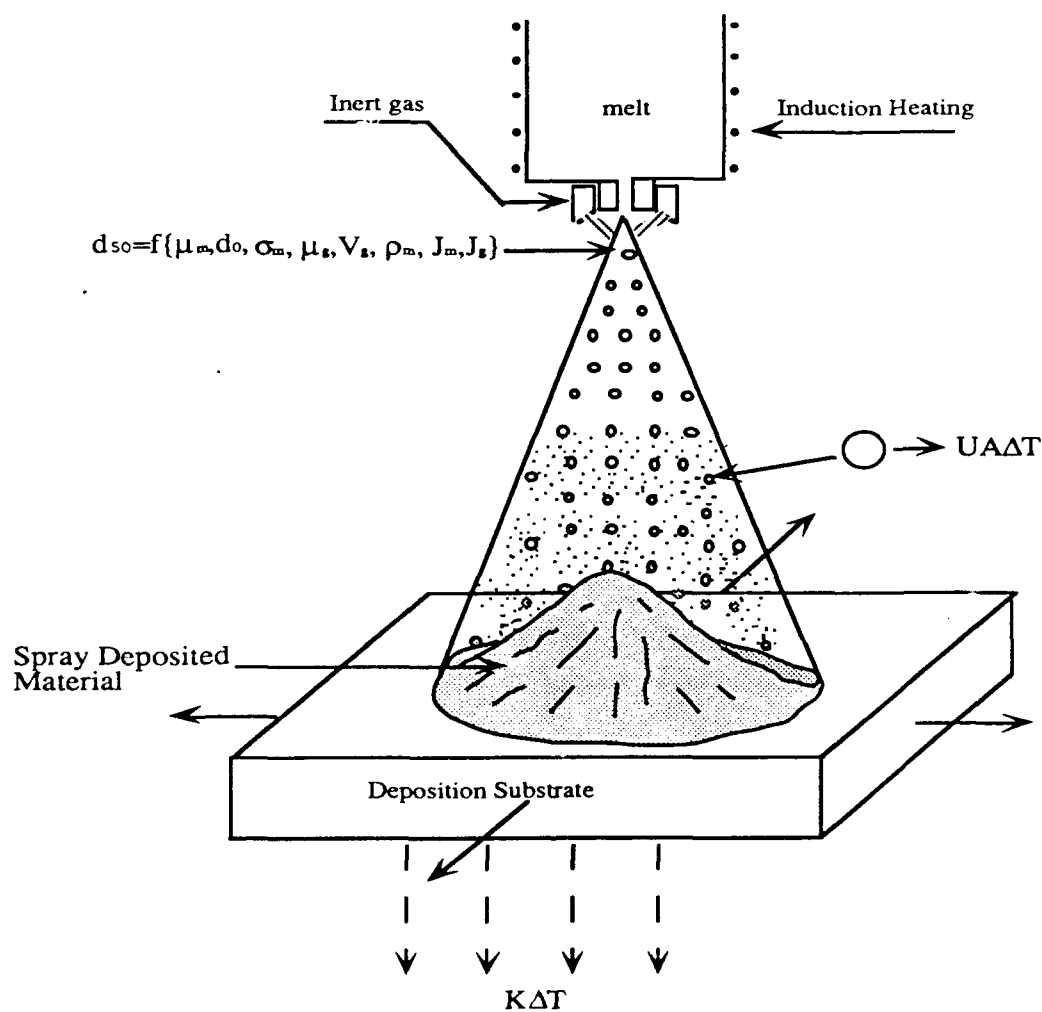


Figure 1. Schematic diagram of experimental apparatus.

The experimental set up shown schematically in Figure 1 incorporates pneumatic control of the deposition surface. This allows for simultaneous horizontal and vertical translation of the deposition surface at various translational velocities. More extensive details on the experimental apparatus and processing variables used in this study can be found elsewhere [63].

Three experiments were conducted for this study; the values of the primary experimental variables used during each experiment are listed in Table 2.

Table 2. Experimental Variables used in Study.

Variable	Experiment Number		
	1	2	3
Alloy Designation ¹	A	A	B
Charge Weight (gm)	1440	1443	1605
Atomization Time	36 s	33 s	45 s
Atomization Pressure	1.38 MPa	1.80 MPa	1.38 MPa
Atomization Gas	Nitrogen	Argon	Argon
Backfill Gas	Argon	Argon	Argon
Flight Distance	0.41 m	0.41 m	0.46 m
Pouring Temperature	848 °C	840 °C	800 °C
Metal Delivery Tube			
Diameter	3.30 mm	3.30 mm	2.79 mm
Atomization Nozzle			
Pressure condition ²	-12.4 KPa	-13.8 KPa	-11.0 KPa

¹ See Table 1.

² Negative values indicate aspiration of the metal during atomization.

1.2.2 Powder Sizes and Characterization

In order to study the size and spatial distribution of the powders during spray atomization and deposition, a fourth experiment was conducted utilizing experimental conditions identical to those used in experiment 3. In this experiment, the deposition surface was replaced by 18 oil filled test tubes designed to intercept powders during flight. In order to

obtain information from the entire spray, the test tubes were arranged radially inside of the chamber and positioned at incremental distances. The powders collected in the test tubes were subsequently analyzed, and a size distribution was established as a function of radial distance from the center. In addition, a complete size distribution analysis of overspray powders was made based on experiments 1-3. The powder size distribution analyses were accomplished utilizing sieve analysis in accordance with ASTM standard B214 and MPIF standard 5.

1.2.3 Thermomechanical Processing

The as-spray deposited material from experiment 1 was subsequently hot rolled at 375-400 °C to a 33% reduction in thickness; the rolling step was followed by hot isostatic pressing (HIP) at 350 °C and 96.53 MPa for 120 minutes. The as-spray deposited material from experiment 2 was hot isostatically pressed at 350 °C and 96.53 MPa for 120 minutes; no rolling was conducted on this material. The as-spray deposited material from experiment 3 was hot rolled at 300 °C to a 50% reduction in thickness.

1.2.4 Optical Microscopy

Optical microscopy was conducted on polished and etched samples taken at various stages throughout the thermomechanical sequence. Conventional metallography preparation techniques were used; etching was accomplished using Keller's reagent. Optical microscopy was conducted to study grain morphology, porosity, and the distribution of secondary phases.

1.2.5 Scanning Electron Microscopy (SEM)

SEM studies were conducted using a HITACHI S-500 microscope. The polished and etched samples from experiments 1-3 were examined in secondary electron mode for microstructural details such as distribution, type, and morphology of porosity, as well as the presence of secondary phases. Point analyses were carried out at selected areas on samples from experiment 3 to assess the chemical homogeneity of copper, the major alloying addition in this material.

1.2.6 Transmission Electron Microscopy

Transmission Electron Microscopy was performed on a JEOL 100 C at an operating voltage of 100 kV on samples from experiment 3. The samples were prepared both from as-spray deposited and as-spray deposited and hot rolled (300 °C) conditions. The hot rolled samples were solutionized at 550 °C for 1 hr, quenched in water, and aged at 190 °C for 18 hrs. Standard TEM samples were prepared by electrothinning in a solution of 2/3 CH₃OH and 1/3 HNO₃ cooled to -20 °C using the window technique.

1.2.7 Differential Scanning Calorimetry (DSC)

DSC analyses were conducted on the Al-Cu-Li-Zr material from experiment 3. Samples were taken from the as received ingot metallurgy material, as-spray deposited material, and a powder sample of < 45 µm size range; the latter was obtained from fine overspray powders. The analysis was performed on an omnitherm base with a DuPont cell, and carried out over a temperature range of 25 °C to 500 °C with a heating rate of 10 deg/min in a nitrogen purge. The data were plotted in terms of heat flow and temperature. The objective of the DSC analyses was to characterize the type and extent of precipitation reactions during spray atomization and deposition.

1.2.8 X-Ray Diffraction (X.R.D.)

X-ray diffraction analysis was conducted on spray deposited samples from experiment 3 to gain some insight into the precipitated phases. Thin samples were exposed to Cu K_α radiation ($\lambda=1.5418 \text{ \AA}$) using a scanning speed of 2 deg/min. A plot of intensity vs 2θ was obtained, illustrating peaks at different Bragg angles. The Bragg angles corresponding to different peaks were noted and the value of 'd' was calculated from Bragg's law ($\lambda = 2d \sin\theta$). The values of interplanar spacings obtained were then matched with the standard interplanar spacings corresponding to aluminum and other secondary phases.

1.2.9 Mechanical Testing

Tensile properties at room temperature were determined after thermomechanical processing and heat treatment. Smooth bar tensile and notch tensile properties were determined according to ASTM E8-81 and ASTM E602-81, respectively. An Instron

testing machine was used with a constant crosshead speed of 0.254 mm per minute. The notch root radius of the notch tensile samples was 0.0254 ± 0.127 mm. Samples from experiment 1 and 2 were heat treated by solutionizing the materials at 588°C for 1hr, followed by water quenching and artificial aging at 200°C for 9 hrs. The aging conditions corresponded to peak hardness; they were determined by conducting hardness tests on samples aged for various time intervals, at 200°C . Tensile and notched tensile specimens were machined from hot rolled + HIP'ed and HIP'ed materials from experiments 1 and 2, respectively.

1.3 Results

1.3.1 Powder Sizes and Characterization

The results of the powder size characterization experiments are shown in Figure 2. In this figure, the size distribution of overspray powders is compared to that obtained from the atomization experiment in the absence of a deposition substrate (experiment 4); both experiments were conducted utilizing identical processing parameters and alloy composition. Hence, comparison of both size distributions gives some insight into the actual distribution of powders that is collected on the deposition surface. In addition, the mass distribution of powders determined from experiment 4, is shown in Figure 3 as a function of radial distance.

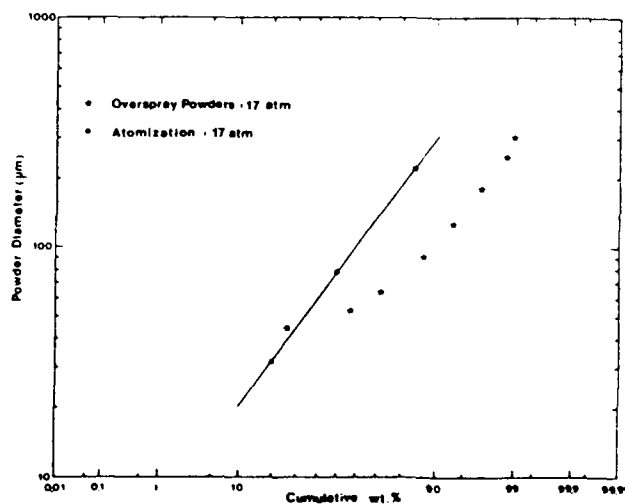


Figure 2. Powder size distribution determined from experiment 3; comparison of overspray powders with size distribution obtained from atomization.

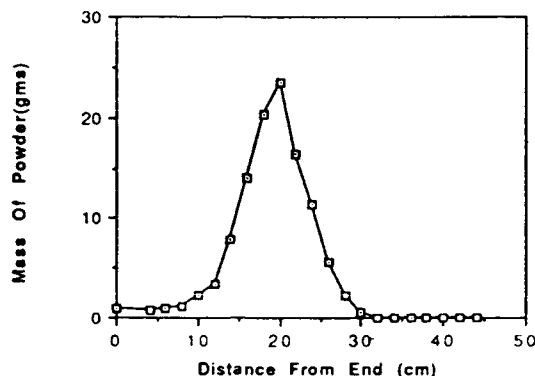


Figure 3. Mass distribution of powders as a function of radial location. The data shown in this figure were collected from oil filled test tubes placed at a flight distance of 0.41 m (experiment 4).

1.3.2 Optical Microscopy

Optical microscopy was conducted on materials obtained from experiments 1-3. The microstructure of the hot rolled and HIP'ed Al-Li-Mg-Ge-Zr alloy obtained from experiment 1 is shown in Figure 4. This micrograph was taken from a section parallel to the rolling direction; it reveals mostly equiaxed grains with relatively low aspect ratio. The absence of an elongated grain morphology can be attributed to the HIP'ing step that followed hot rolling. Figure 5 shows the as-spray deposited microstructure of the Al-Cu-Li-Zr alloy obtained from experiment 3. The microstructure of the materials obtained from all three experiments exhibited an equiaxed grain morphology, with average grain sizes of 22.9 μm , 22.0 μm and 68.0 μm for experiments 1-3, respectively. This grain morphology has also been reported by other investigators [63-66].

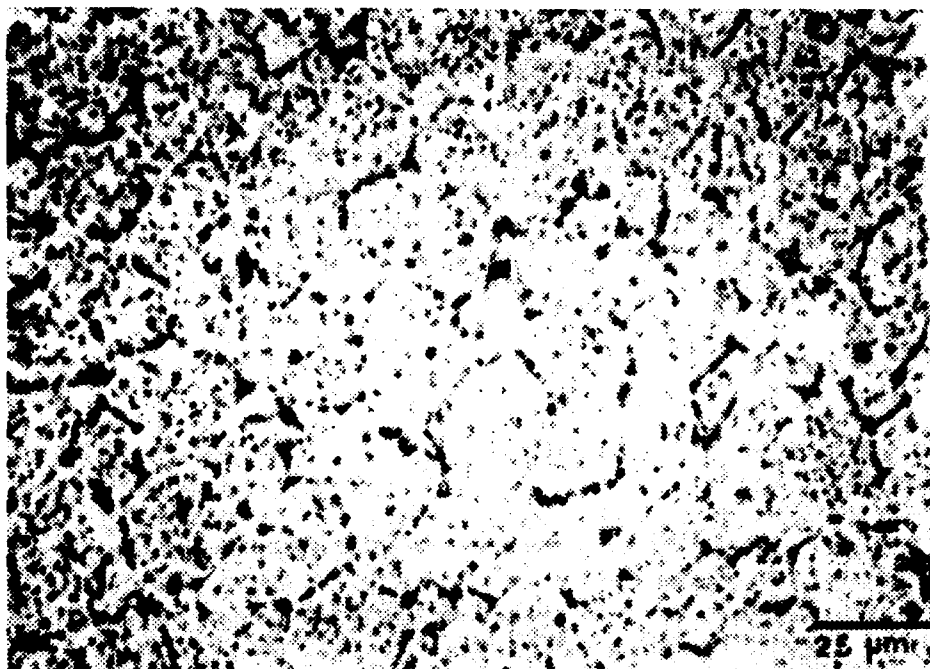


Figure 4. Optical micrograph showing the microstructure of the rolled and HIP'ed Al-Li-Mg-Ge-Zr material from experiment 1.

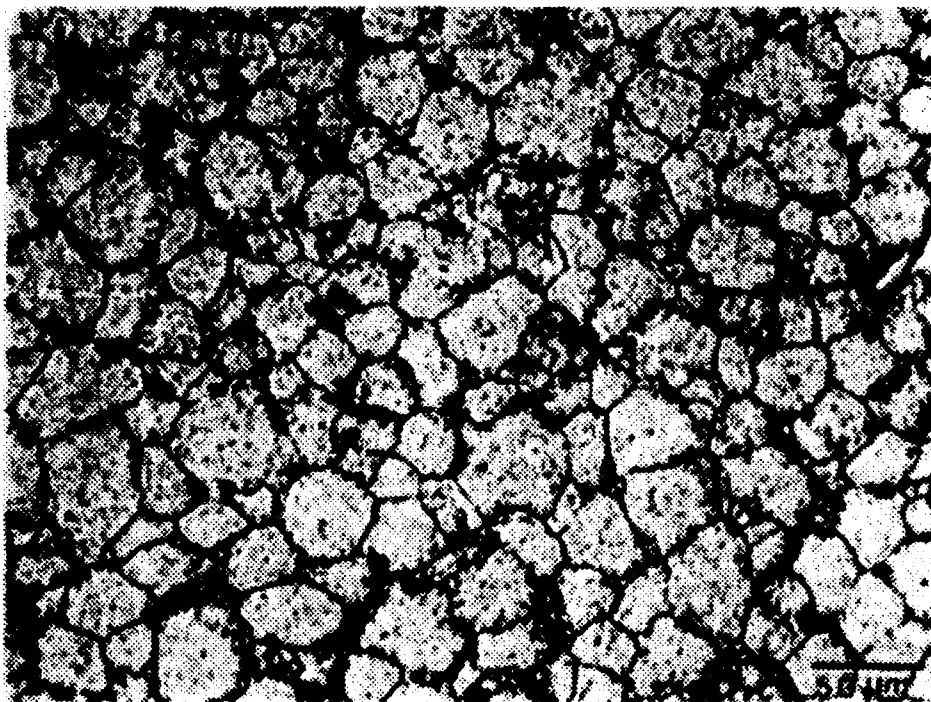


Figure 5. Optical micrograph showing the as-spray deposited Al-Cu-Li-Zr microstructure from experiment 3.

1.3.3 SEM/EDAX Analysis.

Scanning electron microscopy of samples removed from the edge portion of the as-spray deposited material from experiment 1 revealed the presence of a finite amount of non-interconnected porosity (see Figure 6). The micron sized pores were preferentially located at the grain boundaries and exhibited a near elliptical morphology. The distribution of pores in the microstructure was found to be bimodal, with a large proportion of pores in the 1-2 μm and 10 μm size ranges; the volume fraction of porosity was estimated to be approximately 8% throughout the sample. SEM studies of the spray deposited and HIP'ed material from experiment 2 revealed the presence of a low volume fraction of porosity as compared to that present in the as-spray deposited material (see Figure 7). In contrast, the microstructure of the hot rolled and HIP'ed material from experiment 1 was close to full density (see Figure 8). EDAX Cu mapping was conducted on samples of the Al-Cu-Li-Zr alloy from experiment 3 in order to determine the spatial concentration of Cu, the major alloying element. A representative Cu map revealing a homogeneous distribution of Cu throughout the matrix is shown in Figure 9; point analysis of the grain boundary region was compared to that obtained from the center of the grains, confirming these results.

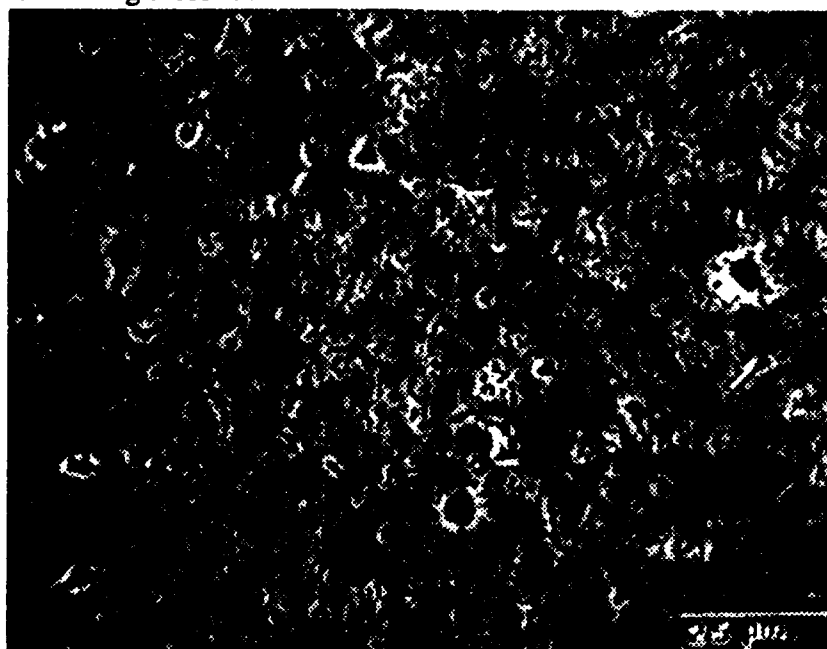


Figure 6. SEM micrograph showing size, location, and morphology of porosity in as-spray deposited Al-Li-Mg-Ge-Zr microstructure from experiment 1.

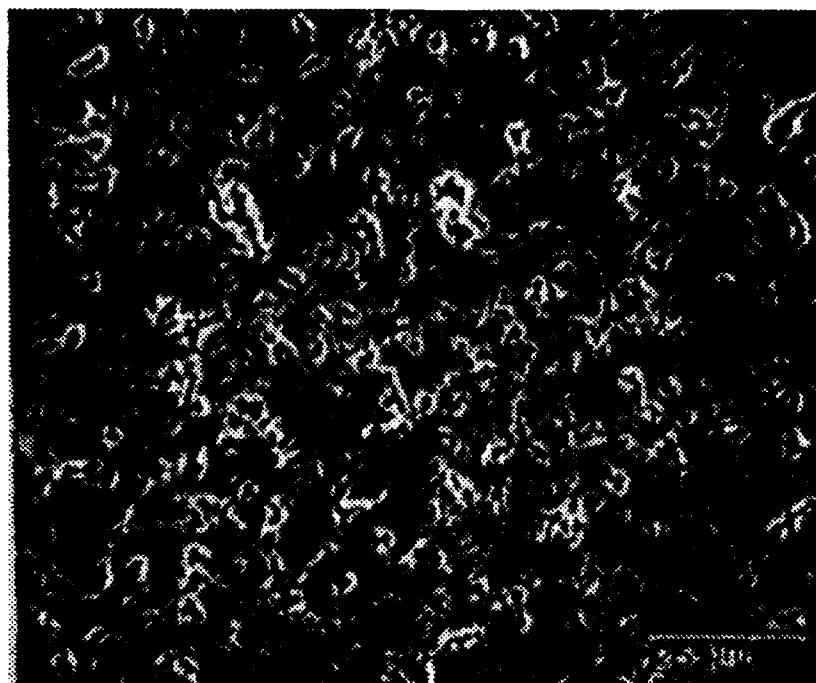


Figure 7. SEM micrograph showing size, location, and morphology of porosity in the HIP'ed Al-Li-Mg-Ge-Zr material from experiment 2.

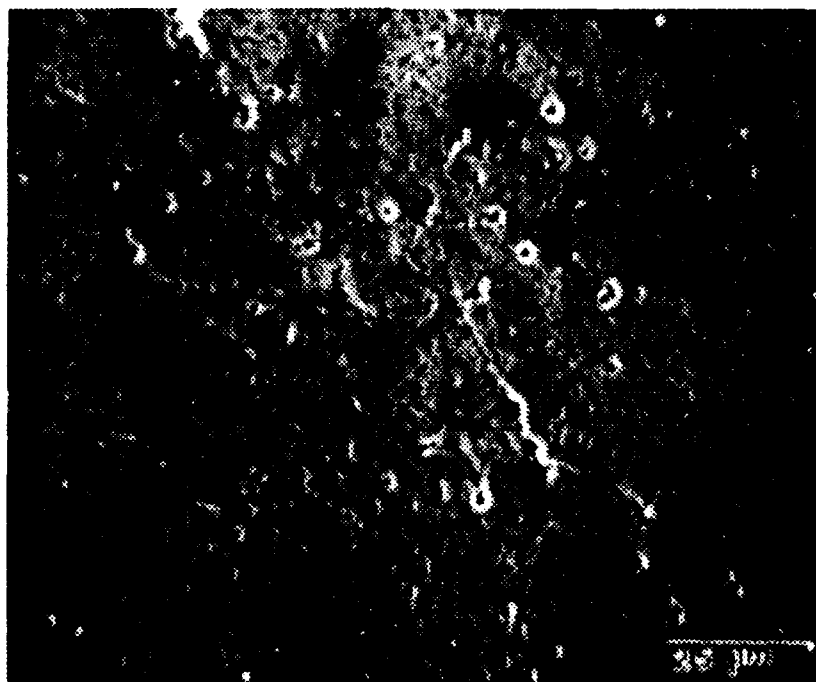


Figure 8. SEM micrograph obtained from rolled and HIP'ed Al-Li-Mg-Ge-Zr material from experiment 1; minimal porosity was evident in this material.

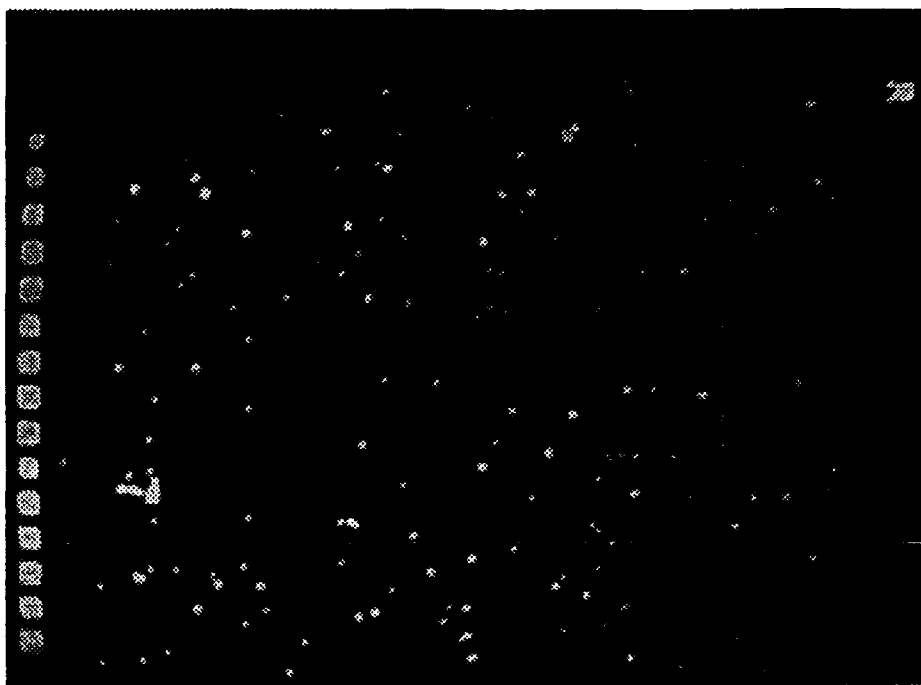


Figure 9. EDAX Cu map showing uniform Cu distribution on as-spray deposited microstructure from experiment 3.

1.3.4 TEM

Transmission electron microscopy studies were conducted on samples of the Al-Cu-Li-Zr alloy from experiment 3 in the as-spray deposited; and in the as-spray deposited, hot rolled and artificially aged conditions. A representative view of the as-spray deposited microstructure is shown in Figure 10. This figure shows the presence of fine grain boundary precipitates with needle-like morphology; spheroidal precipitates can also be observed throughout the matrix. In view of the chemical composition of the alloy, the needle-like precipitates are most likely the precursor of the T_1 (Al_2CuLi) phase; these precipitates form as thin hexagonal platelets on the $\{111\}$ matrix planes as discussed by Noble and Thompson [67]. From the work of Lavernia, Srivatsan, and Mohamed [40], the matrix precipitates are anticipated to be a combination of δ' (Al_3Li), δ ($AlLi$), β' (Al_3Zr), and the composite $Al_3(Li,Zr)$ phases.



Figure 10. TEM micrograph of the Al-Cu-Li-Zr as-spray deposited microstructure from experiment 3.



Figure 11. TEM micrograph of the spray deposited, hot rolled and heat treated Al-Cu-Li-Zr microstructure from experiment 3.

TEM analysis of the Al-Cu-Li-Zr alloy in the as-spray deposited, hot rolled and artificially aged condition revealed extensive T_1 precipitation at the grain boundaries and throughout the matrix. In addition, the presence of the δ phase was also detected; this phase can readily be discerned in Figure 11 as a coarse spherical grain boundary precipitate. The equilibrium δ phase has a cubic superlattice B_{32} structure of the NaTl type with a lattice parameter of 6.37 Å [68]. In view of the relatively large α : δ misfit, the change in lithium concentration, and a different crystal structure, heterogeneous nucleation of the δ precipitates is to be expected to occur at grain boundaries. There is, however, some disagreement as to the exact nucleation mechanism [40].

1.3.5 X-Ray Diffraction

X-ray diffraction analysis of Al-Cu-Li-Zr samples from experiment 3 in the as-spray deposited condition revealed two primary diffraction peaks with lattice spacings corresponding to those of the α Al matrix and the T_1 phase (see Table 3). The observed peaks were diffuse, confirming the presence of the T_1 phase, as discussed by Rioja and Ludwiczak [69].

Table 3. Diffraction Angle and Corresponding Interplanar Spacing
Obtained From As-Spray Deposited Samples.

2θ (degrees)	d (Å)
38.4	2.3421
44.8	2.0250
65.0	1.4366
78.4	1.2187
82.6	1.1670

1.3.6 DSC

Differential scanning calorimetry was utilized in this study to gain insight into the precipitation phenomena occurring during spray deposition. In addition, the DSC curves obtained from the as-spray deposited alloy (from experiment 3) were compared to those obtained from ingot metallurgy and powder metallurgy (< 45 μ m) materials. The

thermograms shown in Figure 12 reveal an increase in the precipitation kinetics of the as-spray deposited and powder metallurgy material as compared to those obtained from the ingot metallurgy material. The primary endotherms occur at approximately 174-262 °C and 352-374 °C for the as-spray deposited material; at approximately 166-218 °C, 220-262 °C, and 376-449 °C for the ingot metallurgy material; and at about 210-270 °C, 284-321 °C and 462 °C for the atomized powders.

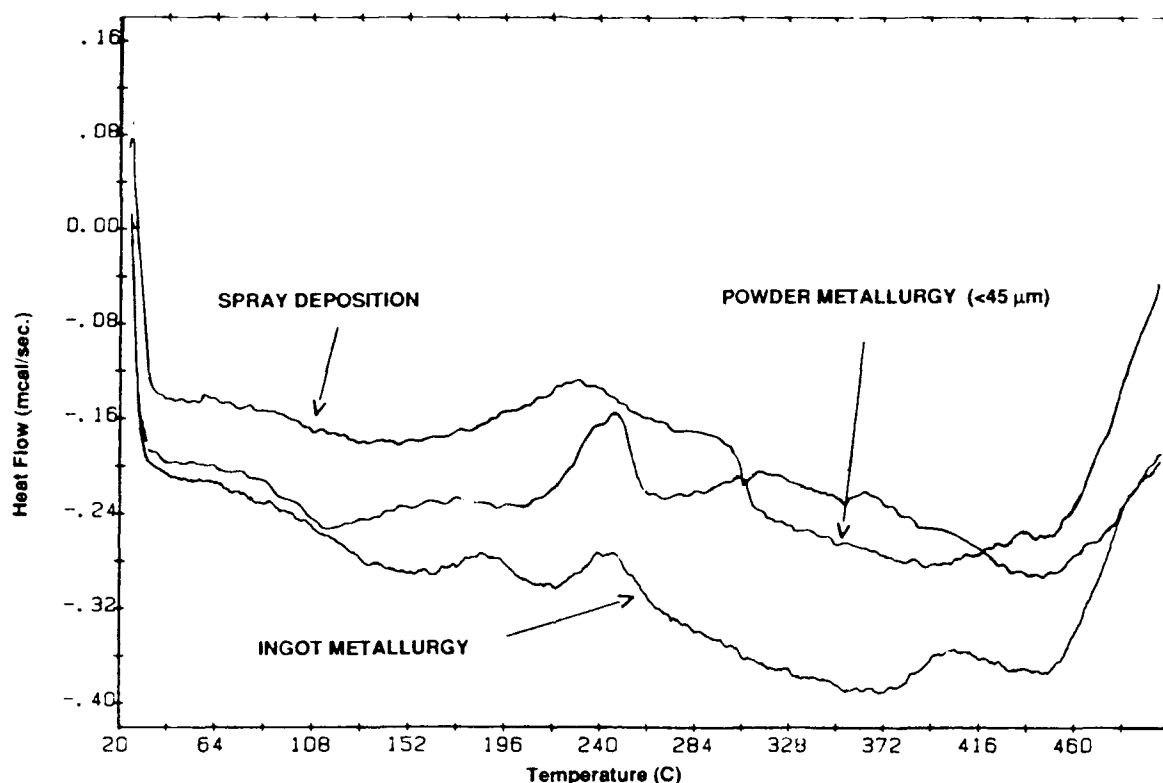


Figure 12. DSC results from ingot, powders, and as-spray deposited Al-Cu-Li-Zr alloy from experiment 3.

1.3.7 Mechanical Behavior

The results of the room temperature mechanical tests are shown in Table 4. The aging curve corresponding to peak hardness for alloy A (see Table 1) is shown in Figure 13. In order to study the fracture toughness behavior of the Al-Li-Mg-Ge-Zr alloy, notched tensile tests were conducted at room temperature. According to Grant, Kang and Wang [70] and Kang and Grant [49], notch tensile tests can be performed as a fast and

inexpensive measure of fracture toughness. Specimens fracture without macroyielding due to the constraint of the material at the notch tip. The notch tensile fracture stress is compared to the yield strength of the smooth bar tensile test as an estimate of alloy toughness. Values for the plane strain fracture toughness, K_{IC} , were calculated from the relation:

$$K_{IC}^5 = c \sigma_Y^6 - c b \sigma_Y^5 - d \sigma_Y^4 K_{IC} + e \sigma_Y^2 K_{IC}^3 \quad (1)$$

where $c = (\pi D)^{5/2} / a$; $d = 4 (\pi D)^2$; $e = 4 \pi D$;

and a is defined by:

$$\sigma_Y = a (\sigma_{nls} / \sigma_Y) + b \quad (2)$$

where a and b are the slope and y intercept, respectively, of $\sigma_Y = f(\sigma_{nls} / \sigma_Y)$. The values for a and b in Eqn. (2) can be extrapolated from the data of Kang and Grant [49] as 275.8 MPa and 696.4 MPa, respectively. Hence, from Eqs. (1) and (2), one can estimate K_Q as approximately 40 MPa $m^{1/2}$ (see Table 4).

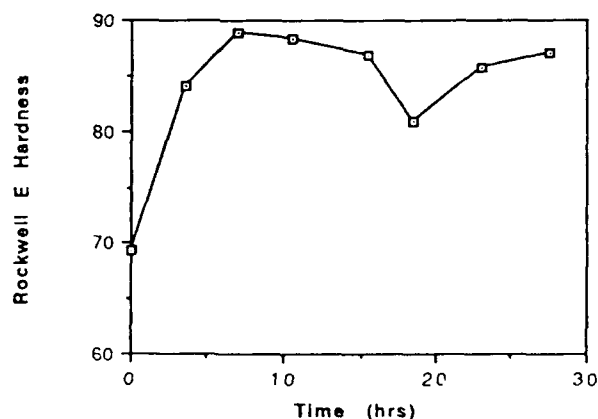


Figure 13. Artificial aging curve corresponding to peak hardness in Al-Li-Mg-Ge-Zr alloy. The material was solution heat treated at 588 °C for one hour, water quenched and aged at 200 °C.

Table 4. Room Temperature Mechanical Properties.

Alloy ¹	Condition	σ_Y (MPa)	σ_{UTS} (MPa)	El. (%)	R.A. (%)	σ_{NTS} (MPa)	σ_{NTS}/σ_Y -	$\sigma_{Y/p}$ ² (MPa cm ³ /g)	K_Q (MPa m ^{1/2})
A ³	HIP'ed + aged to peak hardness	214	351	5.3	5.0	322	1.5	90.3	40
A ³	Hot rolled + HIP'ed + aged to peak hardness	326	443	9.6	8.8	-	-	137.5	-
A ⁴	PM + forged/rolled + peak aged	430	487	6.4	-	-	-	181.4	-
X2020 ⁵ PM	T6 temper	622	649	5.0	-	-	0.8	237 ⁶	12.0
8090 ⁷	IM sheet in T6 temper	340	425	5.0	-	444 ⁸	1.3	133.9	60
2091 ⁹	IM sheet in T8 temper	310	420	14.0	-	355 ⁸	1.14	120.6	120

¹ See Table 1.² Computation was based on a density of 2.37 g/cm³.³ Values represent average of two tests.⁴ Reference [61]⁵ Reference [70]⁶ Computation was based on a density of 2.623 g/cm³.⁷ Data reported by ALCAN, Co.⁸ Unpublished data.⁹ Data reported by Cegedur Pechiney, Co.

1.3.8 Numerical Model

Recently, various investigators have modeled the various solidification and heat transfer phenomena during atomization [38, 71-73]. In the present investigation, we applied the

model developed by Lavernia and co-workers, [72] to the experimental conditions used in the present study; the results are shown in Figure 14.

The main assumptions involved in the development of the model are as follows:

(1) The atomization of the molten metal stream by the high velocity inert gas jets takes place instantaneously upon impact. At this moment, the droplet size distribution is established.

(2) The high surface tension characteristic of metallic melts causes the droplets to become spherical in shape within 10^{-5} seconds from the moment the gas impacts the metal [74].

(3) The spray of droplets travels continuously during atomization in a predictable pattern due to the combined effects of gas drag and gravity; collisions between droplets are neglected.

(4) The heat content of the droplets is dissipated by the action of a heat transfer coefficient at the droplet-gas interface.

(5) The heat transfer coefficient is calculated from established correlations for a single sphere in relative motion with respect to the surrounding fluid. Because of the very high gas velocities involved, radiation heat losses are neglected .

(6) A lumped parameter model which neglects temperature gradients across the droplet thickness is used to compute thermal histories.

(7) The formation of the solid from the melt begins once the nucleation temperature is reached. The degree of undercooling assumed in the calculations was small enough so that the nucleation temperature always remained between the solidus and liquidus temperatures of the alloys. In the undercooled droplets, recalescence was assumed to take place within a time interval at least one order of magnitude smaller than the typical time step used in the heat transfer calculations.

For the experimental conditions utilized in experiment 3, the numerical model predicts, as shown in Figure 14, that at the moment of impact the droplet distribution is comprised of

solid powders ($d_{16} = 23 \mu\text{m}$, $f_s = 1$), droplets with some proportion of liquid phase ($d_{84} = 275 \mu\text{m}$, $f_l > 90\%$), and a substantial fraction of powders in the mushy state ($d_{50} = 84 \mu\text{m}$, $f_l = 30\%$). In experiment 2, the gas atomization pressure was increased to 1.80 MPa. Numerical analysis shows that an increase in gas atomization pressure alters the thermal and solidification conditions at the moment of impact with the substrate. For the conditions utilized in experiment 2, at the moment of impact the droplet distribution is comprised of solid powders ($d_{16} = 22 \mu\text{m}$, $f_s = 1$), droplets with some proportion of liquid phase ($d_{84} = 140 \mu\text{m}$, $f_l > 80\%$), and a substantial fraction of powders in the mushy state ($d_{50} = 56 \mu\text{m}$, $f_l = 16\%$). In the following sections, the salient microstructural features observed in spray atomized and deposited aluminum-lithium materials, and the numerical results are discussed concurrently.

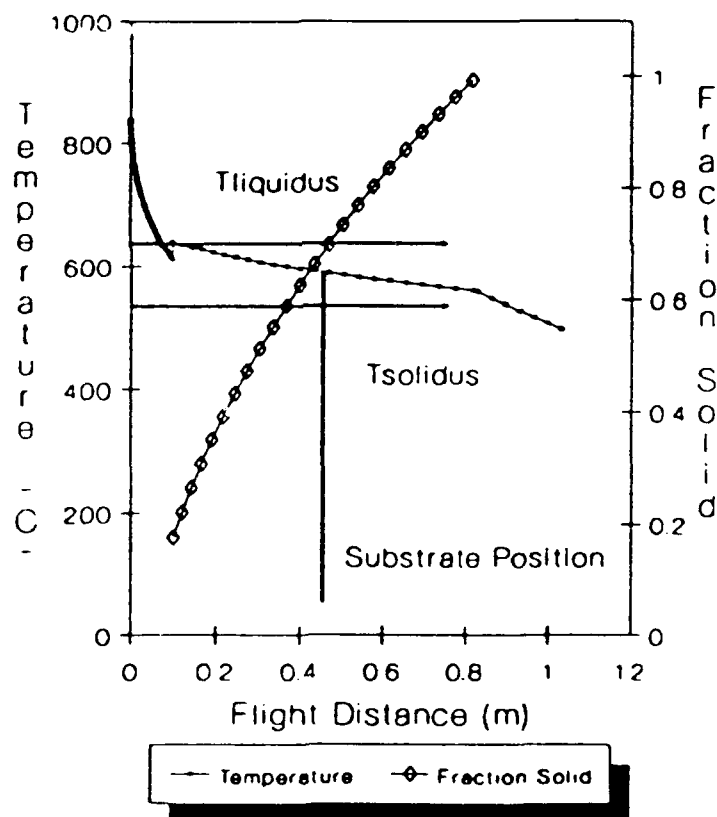


Figure 14. Computed temperature and fraction solid as a function of flight distance for the experimental conditions used in experiment 3.

1.4 Discussion

1.4.1 Powder Sizes and Characterization

The results of the powder size characterization shown in Figure 2 indicate that the overspray powder size distribution contained a higher percentage of fine powders relative to the distribution collected on the deposition surface. This observation implies that whereas the numerical model predicts an average powder size (d_{50}) of 56 and 84 μm for experiments 2 and 3, respectively, the actual average powder size collected on the substrate is likely to be coarser. In addition, the data shown in this figure indicates a strong deviation from linearity for the overspray powders. This observation is consistent with the patterning of powders during flight, commonly observed for atomization. The coarser powders, as a result of their low kinetic energy, tend to concentrate in the center region of the spray, whereas the fine powders tend to populate the periphery of the spray. This is supported by the results shown in Figure 3, which shows a higher mass concentration of powders in the center of the spray, relative to that measured for the periphery. In terms of as-spray deposited density, these results are also consistent with the higher densities typically associated with the center regions of as-spray deposited materials.

1.4.2 Grain Structure

The grain morphology of the spray deposited materials from all three experiments was equiaxed; this observation is in agreement with previous findings [38, 63-66, 75]. Lavernia [76] proposed that the formation of an equiaxed grain morphology during spray deposition is a result of three simultaneous processes: (1) dendrite arm fragmentation, (2) nucleation/grain multiplication, and (3) constrained growth.

At the moment of impact with the substrate, the solidification structure of atomized powders will consist of one or a combination of the following (a) featureless zones, (b) cellular without secondary arms, (c) dendrites, and (c) equiaxed structures, depending on the growth conditions of the solidification front (see Figure 15). Whereas powders containing cored dendrites [77] and/or equiaxed structures will readily lead to the formation of an equiaxed grain morphology during deposition, dendrite deformation and fracture can also assist equiaxed grain formation. The deformation and fracture of dendrite arms is initiated as a result of the mechanical action of the high velocity impact

of semi-solid/semi-liquid particles, and continues after impact under the action of shear forces induced by turbulent fluid convection [76]. At the moment of impact with the substrate, for example, it has been estimated by Lavernia and co-workers [72] that an 80 μm aluminum droplet will be traveling at approximately 100 m/sec.

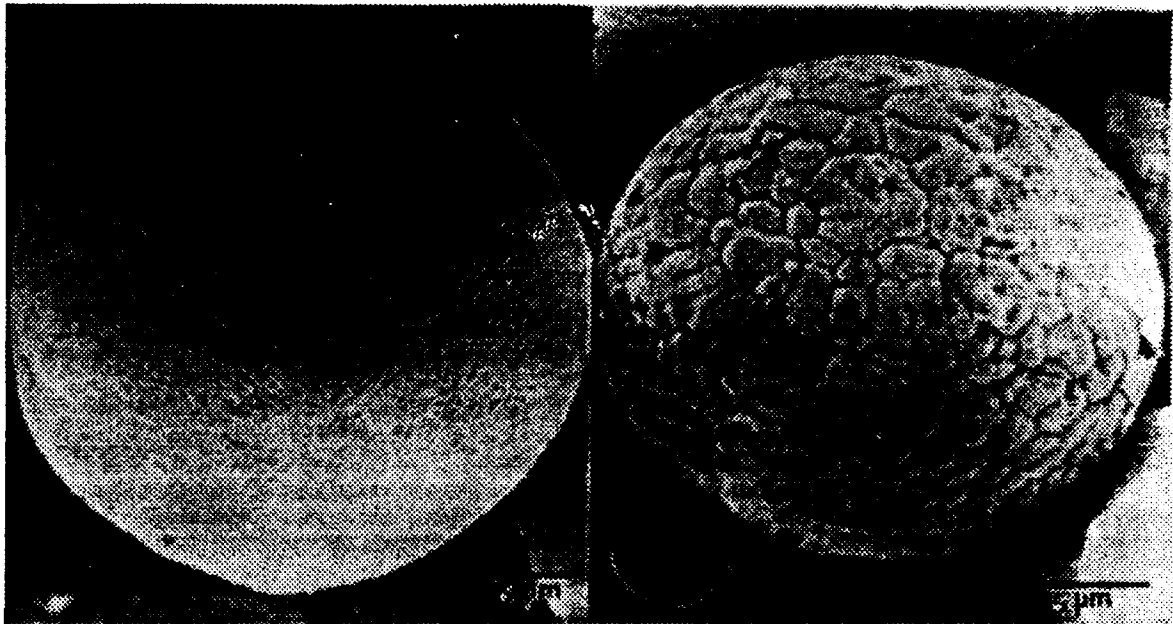


Figure 15. SEM micrograph showing solidification morphology of powders collected from test tube experiment.

More recently, a study involving Ni_3Al powders proposed that the formation of equiaxed grains from dendrites during annealing evolves from two distinct mechanisms: a) the coarsening of secondary dendrite arms, and b) the growth and coalescence of primary dendrite arms [78]. Kinetic analyses of the experimental data obtained in this study showed that the activation energy necessary for grain growth to occur was higher than the activation energy for recrystallization but lower than the activation energy for diffusion. The large amount of grain boundary area associated with the fine dendritic morphology present in the as-solidified powders was thought to provide the necessary driving force for growth to occur in the microstructure.

Regarding grain size, the predictions of the numerical model for experiment 3 are reasonable in view of the relatively coarse grains observed experimentally (68 μm). This grain size is approximately 70% coarser than those observed for experiments 1 and 2 (22 μm). The coarser grain size observed for experiment 3 is thought to have developed as a result of an excessive amount of liquid phase contained in the droplet distribution at the moment of impact with the deposition surface. Furthermore, the Ge and higher Li and Zr additions in alloy A relative to those in alloy B (see Table 1) will effectively stabilize the grain size during solid state cooling. Comparison of the grain sizes observed for experiments 1 and 2 indicates that an equally effective grain size reduction can be achieved by either increasing the gas atomization pressure, or alternatively, by using an atomization gas with higher thermal diffusivity (i.e., N_2 vs Ar).

1.4.3 Porosity

An important microstructural characteristic frequently associated with spray atomized and deposited microstructures is the presence of a finite amount of non-interconnected porosity [37, 63, 64, 66, 79]. The overall amount of porosity present in spray atomized and deposited materials depends on: (a) the thermodynamic properties of the material, (b) the thermodynamic properties of the gas, and (c) the processing parameters. Under conditions typical for aluminum alloys, for example, the amount of porosity present in spray atomized and deposited materials has been reported to be in the 1-10% range. The present results revealed that the size distribution of pores is bimodal, with a large proportion of pore sizes in the 1-2 μm and 10 μm range. It has been suggested that the origin of porosity in spray atomized and deposited materials may be attributed to one or a combination of the following mechanisms: (a) gas rejection, (b) solidification shrinkage, (c) interparticle porosity. The first mechanism, gas rejection, is anticipated as a result of the limited solid solubility of inert gases in most structural materials. As the temperature of the material decreases during solidification, any amount of gas that might have dissolved during the melting and superheating stage will be rejected into the matrix, leading to the formation of gas pores. However, results obtained using fast neutron activation analyses show that spray atomized and deposited materials exhibit extremely low levels of dissolved gases, suggesting that this mechanism is not as important as originally thought [79]. Furthermore, in view of the irregular morphology of the pores it is highly improbable that a large proportion of the porosity originates from the rejection of entrapped gases, since gas porosity generally exhibits a spheroidal morphology.

The formation of shrinkage porosity is generally associated with sluggish solidification kinetics, such as those present during ingot casting. In view of the limited amount of liquid phase present under proper spray atomization and deposition conditions, it is highly unlikely that solidification shrinkage plays an important role in the formation of the observed pore distribution. It is worth noting, however, that if the spray atomization and deposition conditions are such that there is an excessive amount of liquid phase present at the deposition surface, this mechanism may play a significant role in the formation of porosity. The presence of excess amounts of liquid phase during impact may develop as a result of: (a) coarse droplet sizes, (b) high deposition temperatures, and (c) remelting of solid phases caused by high spray enthalpies [37]. Under these conditions, the atomization gas may interact with the molten metal, leading to the formation of large amounts of porosity.

The available experimental evidence suggests that a large proportion of the porosity that is generally observed in spray atomized and deposited materials may be attributed to the third mechanism, interparticle porosity. As the droplets descend, first on the deposition surface, and eventually on each other, they overlap leaving micron-sized cavities in between. In spite of the large amount of turbulence present, the relatively rapid drop in temperature during deposition prevents any liquid phase present from filling all of the cavities, leading to the formation of irregular pores. This mechanism is consistent with the observed correlation between deposition conditions such as spray density, powder size, and fraction solidified, and the amount of porosity present throughout the deposit [56, 75, 79] (see Figure 6). For example, the higher density associated with the central region of the deposit has been attributed to the elevated mass flux of droplets in this region of the spray, relative to the periphery [80]. These droplets contain elevated fractions of liquid phase, effectively filling the interstices between droplets. In contrast, the high amount of porosity generally observed in the periphery of the spray deposited materials results from a large proportion of small, presolidified droplets. It is worth noting that under processing conditions where deposited droplets are allowed to fully solidify before the arrival of more droplets, interlayer porosity will also develop at the original droplet boundaries. In general, however, these processing conditions are avoided, since the presence of these discontinuities in the microstructure will lead to less than optimum mechanical behavior.

The presence of fine grain boundary pores observed in the present study is in agreement with the findings of other investigators [63, 79, 81]. Although the origin of this phenomenon is not completely understood, it has been suggested that during impact and solidification these fine pores effectively pin grain boundaries, preventing their migration [38, 76].

1.4.4 Cooling Rate and Solidification Front Velocity

The results of the present study suggest that the solidification front velocity present during spray atomization and deposition was sufficient to prevent segregation of the Cu in experiment 3, and extensive second phase precipitation during deposition. The results of the EDAX analysis, for example, show that there was a homogeneous distribution of Cu throughout the matrix in the spray deposited material. In addition, the TEM results reveal a relatively low volume fraction of secondary phases in the as-spray deposited condition, when compared to that of the spray deposited, hot rolled and aged conditions.

Detailed study of the solidification conditions during spray deposition is complicated by the extreme differences in thermal environment prior to, and after impact. For example, whereas an 80 μm aluminum droplet is exposed to relatively high cooling rates ($0.4 - 1 \times 10^4$ K/sec.), and consequently relatively fast solidification growth velocities (0.2-2.0 m/sec.[73]), the cooling rate after impact is relatively slow (10-20 K/sec.[75]). Recently, Ruhr and co-workers [66] determined that the amount of Mn retained in solid solution during spray deposition of an Al-6.5Mn-2.35Li-0.80Zr (wt.%) was 2.25 wt.% Mn. Furthermore, by computing the dependence of Mn excess solid solubility on cooling rate, the results of this study suggest that the "effective" cooling rate during spray atomization and deposition is approximately 1×10^3 K/sec. From the magnitude of this cooling rate, the reported presence of primary Al_6Mn needles [66] in the spray deposited microstructure, and the work of Juarez-Islas, Jones and Kurz [82], the solidification front velocity can be estimated as approximately 1-2 mm/sec. Clearly, a solidification front velocity of the magnitude present during spray deposition will not be sufficient to retain large amounts of elemental additions in solution. Therefore, some solute segregation should be expected, particularly with elemental additions which require large undercoolings for solute supersaturation (i.e., low T_0).

1.4.5 Precipitation Behavior.

The X-ray diffraction studies on the Al-Cu-Li-Zr alloy failed to reveal the presence of secondary phases; however, the diffraction peaks corresponding to the α Al matrix were diffuse. This behavior has been correlated to the presence of the T_1' phase. The presence of the T_1' phase was confirmed by DSC and TEM studies.

The DSC curve obtained from the as-spray deposited material shows that the first exotherm (precipitation) is very broad and shallow (see Figure 12), indicating simultaneous precipitation of various phases. Precipitation of the δ' and T' phases is expected in this temperature regime. In addition, the low magnitude of the heat released during this reaction is consistent with a low volume fraction of precipitates. These results indicate that the thermal conditions present during spray atomization and deposition favor simultaneous co-precipitation of various phases in the matrix.

The DSC thermograms presented in Figure 12 show that precipitation kinetics are accelerated in the powder and spray deposited materials, relative to the IM material. Katgerman and Vander Brandt [83] proposed that rapid solidification enhances precipitation kinetics; one plausible mechanism is an increase in vacancy supersaturation during rapid quenching. This observation is consistent with the results obtained in this investigation in view of the cooling rates experienced by the three different samples: 45 μm powders: 1×10^5 K/sec.; spray atomization and deposition: 1×10^3 K/sec.; and ingot metallurgy: 1×10^{-2} K/sec.

The DSC thermogram for the as-spray deposited material may be characterized in terms of the following reactions:

- o The exothermic peak corresponding to the 82-194 °C temperature regime indicates the precipitation of solute clusters, δ' and T_1' phases; solute clusters and δ' phases predominate prior to 150 °C, whereas after 150 °C, the T_1' phase is thought to dominate.
- o The endothermic peak at 230 °C corresponds to the dissolution of T_1' and δ' precipitates.
- o The exothermic peak at approximately 308 °C marks the precipitation of the δ phase and the $T_1' \rightarrow T_1$ transformation.
- o The endothermic peak at 362 °C corresponds to the dissolution of the T_1 phase.

o Finally, the exothermic peak observed at approximately 438 °C can be associated with the precipitation of high temperature intermetallic phases (T_2 (Al_6CuLi_3), and T_B ($Al_{15}Cu_8Li_2$)).

This sequence of reactions is consistent with the appearance of the T_1 phase after hot rolling and heat treatment of the spray deposited Al-Cu-Li-Zr alloy to the T3 condition (solutionized at 550 °C/1 hour, and aged at 180 °C/18 hours). TEM work is continuing with the objective of characterizing the precipitates.

1.4.6 Mechanical Behavior

The difference in the mechanical behavior of the HIP'ed material, relative to that of the hot rolled and HIP'ed material (see Table 4) can be attributed to a difference in volume fraction of porosity. Hot rolling and HIP'ing effectively closed all of the porosity resulting in an increase in σ_Y , σ_{UTS} , and elongation, relative to the HIP'ed material (see Figures 7, 8). Another difference between experiments 1 and 2 which must be taken into consideration is the type of atomization gas used in both experiments. Inspection of Table 2 shows that whereas nitrogen gas was used in experiment 1, argon was used in experiment 2. The work of Leatham and co-workers [65] indicates that the volume fraction of porosity in as-spray deposited materials is inversely proportional to the thermal diffusivity of the atomization gas, and directly proportional to gas density. This observation is consistent with the higher volume fraction of porosity present in the as-spray deposited material from experiment 2.

The improvements in elongation behavior of the spray deposited, hot rolled and HIP'ed material, relative to that of comparable IM and PM materials, can be attributed to a combination of structural refinement, minimization of oxide phases, and Ge additions. The spray atomized and deposited materials exhibited attractive combinations of strength and ductility, particularly when normalized for density. Further studies are continuing to assess the effect of hot extrusion on the resulting structure and properties.

1.5 Conclusions

- i. The preliminary results presented in this study suggest that spray atomization and deposition processing can be successfully utilized to manufacture aluminum-lithium alloys including those containing high lithium additions.

- ii. Analysis of overspray powders collected from the spray atomization and deposition experiments indicate that the distribution of powders which impacts the deposition surface is comprised of a large proportion of relatively coarse powder sizes.
- iii. The microstructure of the spray deposited Al-Cu-Li-Zr alloy consisted of relatively coarse (68 μm) equiaxed grains, a finite amount of micron-sized porosity, and a low volume fraction of secondary phases. The microstructure of the spray deposited Al-Li-Mg-Ge-Zr alloy consisted of relatively fine (22-23 μm) equiaxed grains. Comparison of the microstructure from all three experiments indicates that increasing the gas atomization pressure, or utilizing an atomization gas with a higher thermal diffusivity are equally effective in reducing grain size.
- iv. EDAX and TEM studies indicate that the magnitude of the solidification velocity present during spray atomization and deposition is sufficient to prevent excessive segregation of the alloying elements.
- v. The attractive combination of strength and ductility of the spray atomized, hot rolled and HIP'ed material was a result of microstructural refinement; minimization of oxide phases; absence of porosity; and high Li, Zr and Ge additions.

CHAPTER 2

2.0 The Effects of Solidification Phenomena on the Distribution of SiC_p During Spray Atomization and Co-Deposition

2.1. Introduction

The attractive physical and mechanical properties that can be obtained with metal matrix composites (MMCs) have been documented extensively [1, 2, 4, 7, 84, 85]. In many cases, the combination of properties that are theoretically attainable with MMCs have not been realized, partly, as a result of our lack of understanding of the microstructure/processing synergism and its ensuing effect on mechanical behavior. Despite impressive progress over the last two decades, our understanding of the fundamental kinetic mechanisms governing the behavior of the interface during processing, and subsequently, during service remains limited as a result of the complexities associated with multi-component alloy/ceramic combinations [19, 86-90].

The integrity of the metal/ceramic interface is strongly influenced by processing conditions. For example, the high temperatures commonly encountered during casting of MMCs provide the driving force necessary for interfacial diffusion to occur, often leading to the formation of complex chemical reactions. Processing is also intimately linked to mechanical behavior, since the resultant distribution of reinforcing phases is ultimately governed by the conditions present during solidification [91-98]. For example, it is now evident that in order to achieve a homogeneous distribution of ceramic particulates during solidification, it is necessary to exercise careful control of the conditions governing the behavior of the liquid/solid interface [91-96].

From the above discussion, it is apparent that in order to avoid extensive interfacial reactions, and obtain a homogeneous dispersion of reinforcements, precise control of the thermodynamic conditions during processing is critical. One approach currently being studied to achieve thermodynamic control during processing is to simultaneously atomize the matrix material, inject the reinforcing phases into the atomized spray, and deposit the multi-phase mixture onto a substrate or a shaped container [32, 37, 99-101]. This process, a modification of spray atomization and deposition, was developed in view of the attractive combinations of structure and properties reported for spray atomized and deposited materials [37, 64, 102-104]. This particular processing methodology, circumvents the disadvantages associated with ingot metallurgy processes [15, 28] and powder metallurgy processes [27, 105]. In analogous studies, other investigators have reported successful incorporation of SiC_p into an aluminum matrix using the Osprey process [106, 107] and a modified gas metal arc welding torch [34].

The objective of the present study was to provide insight into the effects of matrix solidification on the microstructural evolution during spray atomization and co-deposition, with particular emphasis on the kinetic mechanisms governing the entrapment and distribution of ceramic particulates. An Al-Li-SiC_p MMC was selected for the present study on the basis of the results of Delannay, Froyen and Deruyttere [108], and Wolf, Levitt and Brown [109]. Their work indicates that lithium effectively enhances the wettability of ceramics by molten metals by segregating to the interfacial region and weakening any oxide layers present; these results are supported by the work of Webster [110]. Moreover, the addition of Li to Al significantly decreases the density and simultaneously increases the elastic modulus (i.e., higher E/ρ) [40].

2.2 Experimental Procedure

Reynolds Metals Company provided the Al-Li master alloy as cast ingots, 100 mm x 200 mm x 600 mm. The ingots were inspected for major defects, and chemically analyzed in preparation for atomization. Chemical analysis of the remelt alloy revealed a matrix composition of Al-2.1 Li (in wt. %).

The SiC_p were obtained from the Superior Graphite Company. The size distribution of the SiC_p (β phase) was Gaussian and exhibited an average of 3 μm (d_{50}). In addition, 90% of the distribution of the SiC_p sizes was less than 5 μm (d_{90}) with 10% of the distribution falling under 1 μm . Overall, most of the SiC_p sizes (99%) were under 15 μm . The bulk and particulate density was 0.78 and 3.1 g/cm³, respectively; the surface area was 8.3 m²/g. In order to ensure moisture desorption from the surface of the particulates, these were vacuum degassed at 800 °C for 30 minutes prior to the experiments.

2.2.1 Spray Atomization and Co-Deposition Processing

During spray atomization and co-deposition, the matrix material is disintegrated into a fine dispersion of droplets using high velocity inert gas jets, followed by deposition onto a substrate where the droplets impact and accumulate into a preform of predetermined thickness (see Figure 16). As the distribution of atomized metallic droplets travel towards the deposition surface, one or more jets of ceramic particulates are co-injected into the atomized spray at a previously determined flight distance. The potential of using this technique to incorporate multiple ceramic particulates into a metallic matrix is shown schematically in Figure 17a, where white and black spheres, representing two types of

ceramic phases, are being simultaneously co-injected into the atomized metallic spray. The precise co-injection position is determined on the basis of numerical analysis of the fraction solid and the temperature of the atomized matrix droplets, as a function of flight distance; a more thorough discussion of the numerical results is presented in a subsequent section. The objective of this technique is to achieve interfacial control by injection of the reinforcing particulates at a spatial location where the atomized matrix spray contains a limited amount of volume fraction liquid. In this manner, contact time, thermal exposure of the reinforcing particulates to the partially solidified matrix, and interfacial reactions may be minimized. In order to avoid extensive oxidation of the Al-Li matrix during processing, the experiments were conducted inside of an environmental chamber. The latter was evacuated down to a pressure of 150 microns of Hg, and backfilled with inert gas prior to melting and atomization. For metal/ceramic combinations exhibiting no reactivity, the reinforcing phases can also be introduced in the liquid alloy matrix prior to spray atomization and deposition.

Regarding the differences between Osprey [64, 102, 103, 106, 107] and spray atomization and co-deposition processing, a few comments are in order. First, during spray atomization and co-deposition processing the environmental chamber is evacuated to a relatively high mechanical vacuum prior to atomization, resulting in an inert atmosphere suitable for atomizing reactive alloys, such as those based on magnesium [100]. In comparison, during Osprey processing the environment is maintained inert by flushing the atomizing chamber with inert gas. Second, the atomization devices used to disintegrate the metallic matrix during Osprey and spray atomization and co-deposition processing differ in design, resulting in differences in the powder size distribution. Finally, injection of the ceramic particulates is normally accomplished close to the atomization region during Osprey processing, whereas during spray atomization and co-deposition processing, injection of the ceramic particulates can be made at any point during the flight distance; the injection details are discussed subsequently. The interested reader is encouraged to refer to the available scientific literature [32, 64, 99-104, 106, 107].

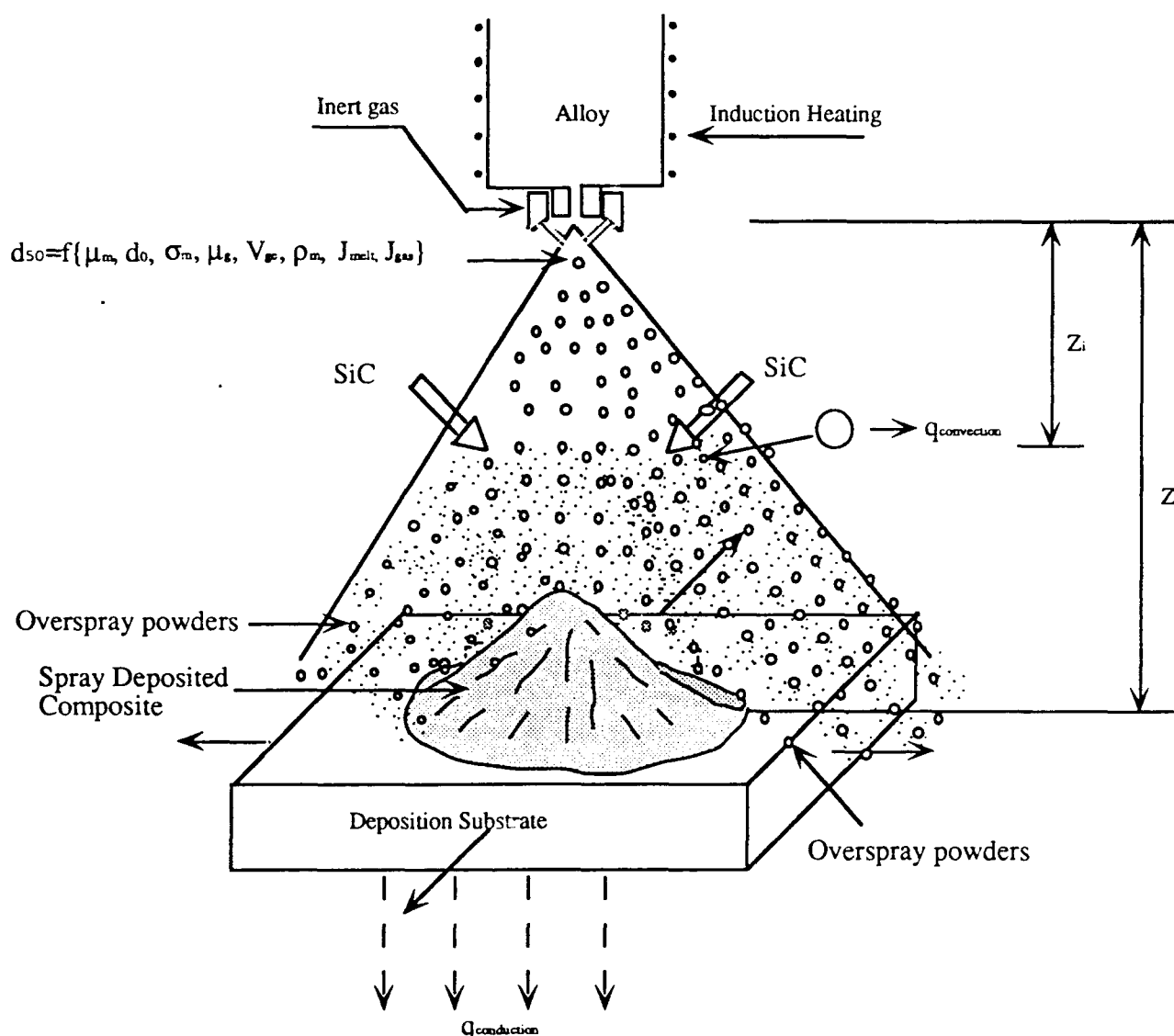


Figure 16. Schematic diagram of experimental apparatus.

In the present study, injection of the strengthening particulates was accomplished utilizing a fluidized bed principle, which involves using an inert gas to entrain the ceramic particulates (see Figure 17b). As shown in Figure 17b, when the gas flow through a static bed of SiC_p is increased, the bed begins to expand eventually reaching a condition known as *minimum fluidization*. *Minimum fluidization* represents the fluid flow conditions when the drag force exerted by the carrier gas on the particulates in the static bed becomes equal to the gravitational force holding the particulates inside the container.

At this point the particulates are free to move relative to each other within the container.
Further increase in

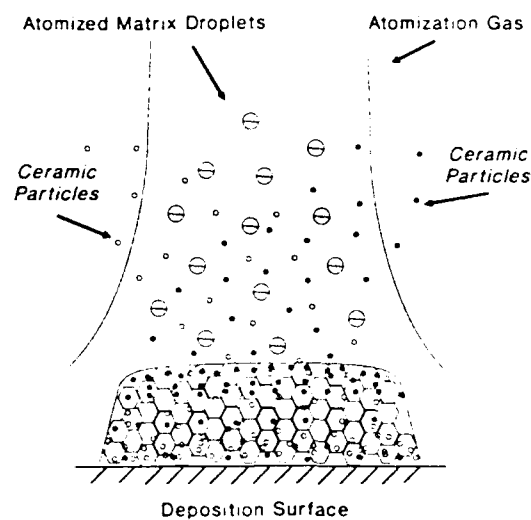


Figure 17. Schematic diagram showing: a) spray atomization and co-deposition processing, and

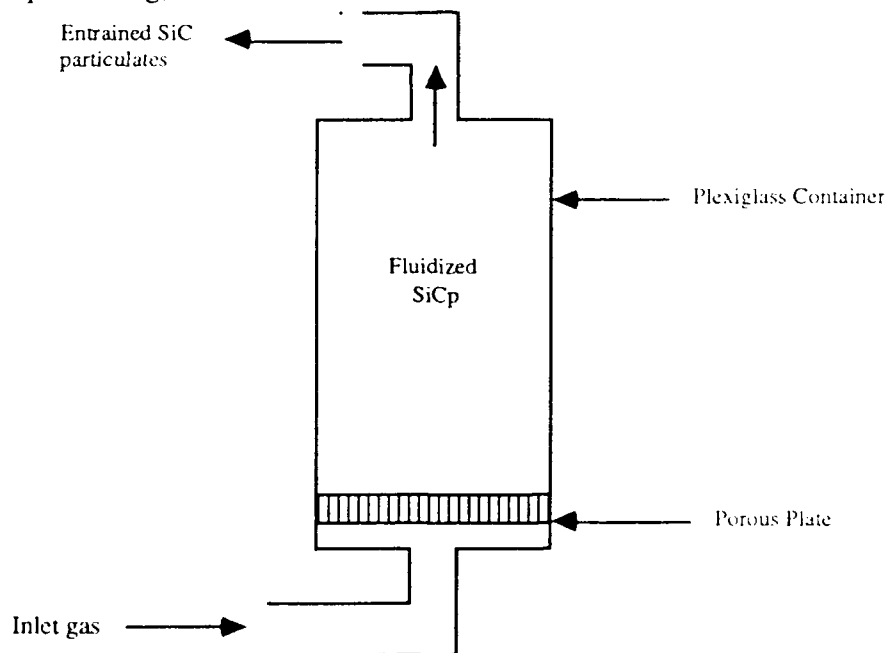


Figure 17. (cont'd), b) fluidized bed.

the gas pressure beyond that needed for *minimum fluidization* leads to an increase in the value of the void fraction. The void fraction asymptotically approaches unity with continued fluidization. The following equations were used in the present study to calculate void fraction (w), conditions for minimum fluidization, terminal velocity, and mass flow rate of the gas and particulates [111]:

$$w = 1 - (\text{bulk density} / \text{particulate density}) \quad (3)$$

$$\text{Re}_{\text{Dmf}}' = \{(33.7)^2 + 0.0408 \text{ Ga}\}^{1/2} - 33.7 \quad (4)$$

$$\text{Ga} = D_p^3 (\rho_s - \rho_c) \rho_c g / \eta^2 \quad (5)$$

$$V_t = D_p^2 (\rho_s - \rho_c) g / 18 \eta \quad (6)$$

$$1/(f)^{1/2} = 4.0 \log (\text{Re}_{\text{Dmf}}' (f)^{1/2}) - 0.40 \quad (7)$$

$$W = \pi D(f)^2 \rho_c v / 4 \quad (8)$$

$$W_{\text{SiC}} = K W \quad (9)$$

where Re_{Dmf}' is the Reynold's number for minimum fluidization; Ga is Galileo's number; D_p is the nominal size of the SiC_p ; ρ_c and ρ_s are the densities of the carrier fluid and the solid particulates, respectively; g is the acceleration due to gravity; η is the viscosity of the carrier fluid; V_t is the terminal velocity of the particulates (i.e, the velocity of the fluidizing gas when $w = 1$); f and $D(f)$ are the friction factor and diameter of the fluidization chamber, respectively; W is the mass flow rate; v is the average operating gas velocity inside the fluidization chamber, and K is a constant whose value depends on the dimensions of the fluidized bed and the type of fluidization gas. It is worth noting that in order for the particulates to be entrained by the fluidizing gas, the average operating gas velocity inside the fluidization chamber, v , must exceeds the terminal velocity, V_t .

Two distinct fluidized beds were utilized in the present study. Although the geometry of the fluidized bed was identical in both cases, the volume was increased from $4.73 \times 10^{-4} \text{ m}^3$ in the first one to $1.74 \times 10^{-3} \text{ m}^3$ in the second one, in order to accommodate higher

mass flow rates of strengthening particulates; this is discussed further in the results section. Correspondingly, the values of K were determined as 1.2 and 0.58 for N_2 and Ar respectively for fluidized bed #1, and 1.2 for both N_2 and Ar for fluidized bed #2. These values of K were determined experimentally on the basis of fluid flow experiments conducted utilizing both fluidized beds. The experimental parameters used in the present investigation are listed in Table 5. It is not presently understood why the value of K varied with gas type for fluidized bed #1, whereas it remained independent of gas type for fluidized bed #2, however, some differences in behavior were evident. For example, during the course of the fluid experiments it was noted that the tendency for gas bubbling (i.e., flow condition where the fluidizing gas bypasses the particulates with minimal or no entrainment) increased as the volume of the fluidized bed was increased, and became more prominent when N_2 gas was used. In contrast, this behavior was not observed when Ar gas was used as the fluidizing gas. Further work is continuing in this area.

Table 5. Input Parameters used in Fluidized Bed Calculations.

Parameter	Value	Units
Bulk Density	780	kg/m ³
Particulate Density	3100	kg/m ³
Volume of fluidized bed # 1	4.73×10^{-4}	m ³
Volume of fluidized bed # 2	1.74×10^{-3}	m ³
Particulate Size	5×10^{-6}	m
Density of Argon	1.68	kg/m ³
Viscosity of Argon	2.2×10^{-5}	kg/m s
Density of Nitrogen	1.187	kg/m ³
Viscosity of Nitrogen	1.54×10^{-5}	kg/m s
Height of Fluidized Bed # 1	0.18	m
Height of Fluidized Bed # 2	0.18	m

Five spray atomization and co-deposition experiments were conducted for the present study; the primary experimental variables used during each experiment are listed in Table 6. In addition, a sixth experiment (experiment no. 10) was conducted for the binary Al-Li

matrix material, using experimental conditions identical to those listed for experiment 7, except for the atomization pressure which was increased to 1.38 MPa.

Table 6. Experimental Variables Used in Study.

Variables	Experiment Number				
	5	6	7	8	9
Matrix Alloy	Al-Li	Al-Li	Al-Li	Al-Li	Al-Li
Fluidized Bed Type	1	1	1	2	2
Atomization Pressure (MPa)	1.20	1.20	1.20	1.20	1.20
Atomization Gas	Argon	Argon	Argon	Nitrogen	Nitrogen
Fluidized Bed Gas	Argon	Argon	Argon	Argon	Nitrogen
Injection Angle ¹ (°)	30	20	90	30	30
Injection Distance (m)	0.21	0.13	0.15	0.14	0.14
Fluidizing Pressure (MPa)	0.69	0.69	0.69	0.69	0.69
Flight Distance (m)	0.41	0.41	0.41	0.41	0.41
Pouring Temperature (°C)	840	840	840	840	840
Metal Delivery Tube					
Diameter (mm)	3.30	3.27	3.33	3.05	3.00
Atomization Nozzle					
Pressure Condition ² (kPa)	~0	6.0	~0	~0	~0

¹ The injection angle refers to the relative angle between the spray of SiCp and the concentric vertical axis of the atomized matrix.

² Positive and zero values represent pressurization and metal free-fall, respectively.

2.2.2 Optical Microscopy

Optical microscopy was conducted on polished and etched as-deposited samples using conventional and Differential Interference Contrast (DIC) techniques; the use of DIC microscopy facilitated identification of the SiCp in the matrix. The size, volume fraction, and distribution of the SiCp was quantitatively characterized using a Buehler Omnimet II Image Analyzer.

2.2.3 Scanning Electron Microscopy (SEM)

SEM studies were conducted using a HITACHI S-500 microscope. The samples were sectioned to a thickness of 0.5 μm and mirror polished using conventional techniques. The polished samples were then examined in secondary electron mode for microstructural details; point analysis was carried out at selected regions of the sample surface to detect the presence of silicon.

2.3 Results

2.3.1 Fluidized Bed Experiments

The operating conditions used for the fluidized beds in the present study are shown in Table 7, and were calculated from Eqns. (3-9), in combination with the input parameters shown in Table 5. A comparison of the measured and computed SiC_p mass flow rates, for various experimental conditions, is shown in Figure 18 and Table 8. In Table 8, the theoretical values of the SiC_p mass flow rates were used to calculate an upper bound of the volume fraction of reinforcing particulates, for two carrier gases and three pressures; these results are shown graphically in Figure 18. It is worth noting that a SiC_p size of 5 μm (d_{90}) was used in these calculations, instead of the average SiC_p size of 3 μm (d_{50}), on the basis of information obtained from Reference 111 which recommended using the largest significant particle size when applying Eqns. (3-9) to predict fluidization behavior.

Table 7. Typical Operating Conditions of Fluidized Bed.

Operating Variables	<u>Type of Gas</u>	
	Argon	Nitrogen
w (-)	0.75	0.75
ΔP^1 (Kg m/sec ²)	7647.72	7648.87
Re_{Dmf} (-)	1.31×10^{-5}	1.15×10^{-5}
Ga (-)	0.0217	0.0190
V_t (m/sec)	0.00248	0.00274

¹Pressure drop across fluidized bed.

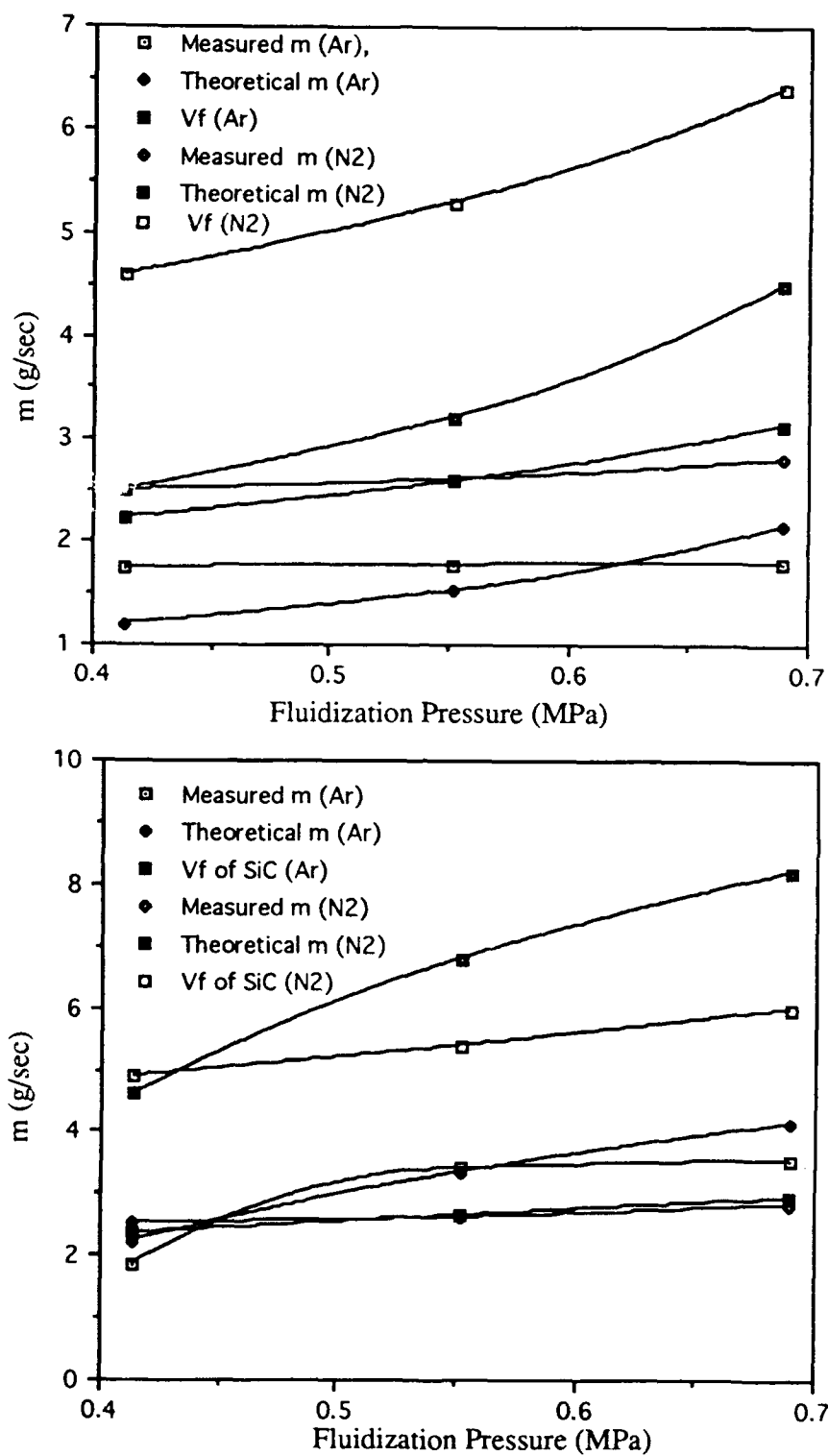


Figure 18. Computed and measured mass flow rates of SiC_p as a function of gas type and fluidization pressure for : a) fluidized bed #1, and, b) fluidized bed #2.

2.3.2 Structural Characterization

The overall dimensions of the preforms from all five experiments were approximately 360 mm in length, and 180 mm in width. The thickness of the preforms decreased from 50-75 mm in the central portion to approximately 5 mm in the thickness dimension. All of the microstructural characterization studies conducted for the present investigation were performed on material removed from the central portion of the preforms.

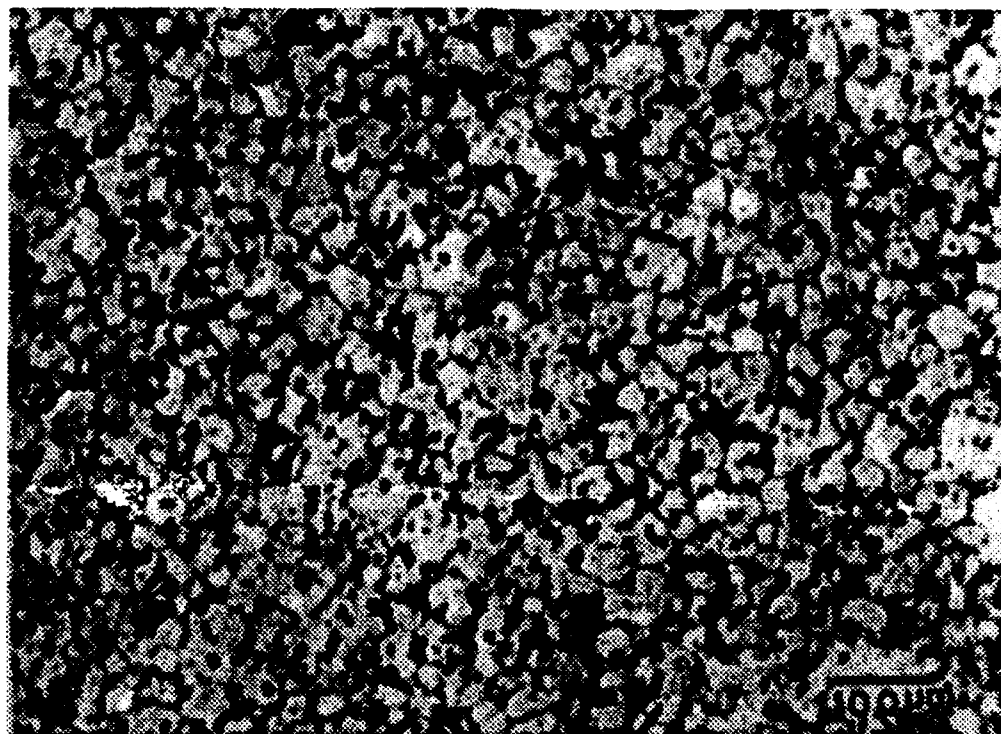
2.3.2.1 Optical Microscopy

Optical microscopy was conducted on coupons of the spray atomized and co-deposited Al-Li-SiC_p materials; one example taken from experiment 6 is shown in Figure 19. This figure reveals the presence of an equiaxed grain morphology, with an average grain size of 68 μm . This grain morphology, which is characteristic of spray atomized and deposited materials, has also been reported by other investigators [32, 37, 64, 102-104]. The average grain sizes for experiments 5-9 were determined as 71 μm , 68 μm , 66 μm , 50 μm and 44 μm , respectively. Optical microscopy of the binary Al-Li matrix material (i.e., unreinforced) showed that the microstructure of the as-spray atomized and deposited binary Al-Li alloy consisted of equiaxed grains, 207 μm in diameter; the as cast grain size was 1270 μm . Shown in Figure 20 are three representative optical (DIC) micrographs taken from various regions of the spray atomized and deposited Al-Li-SiC_p materials. Two high magnification micrographs showing the location of the SiC_p in the Al-Li matrix are presented in Figure 21.

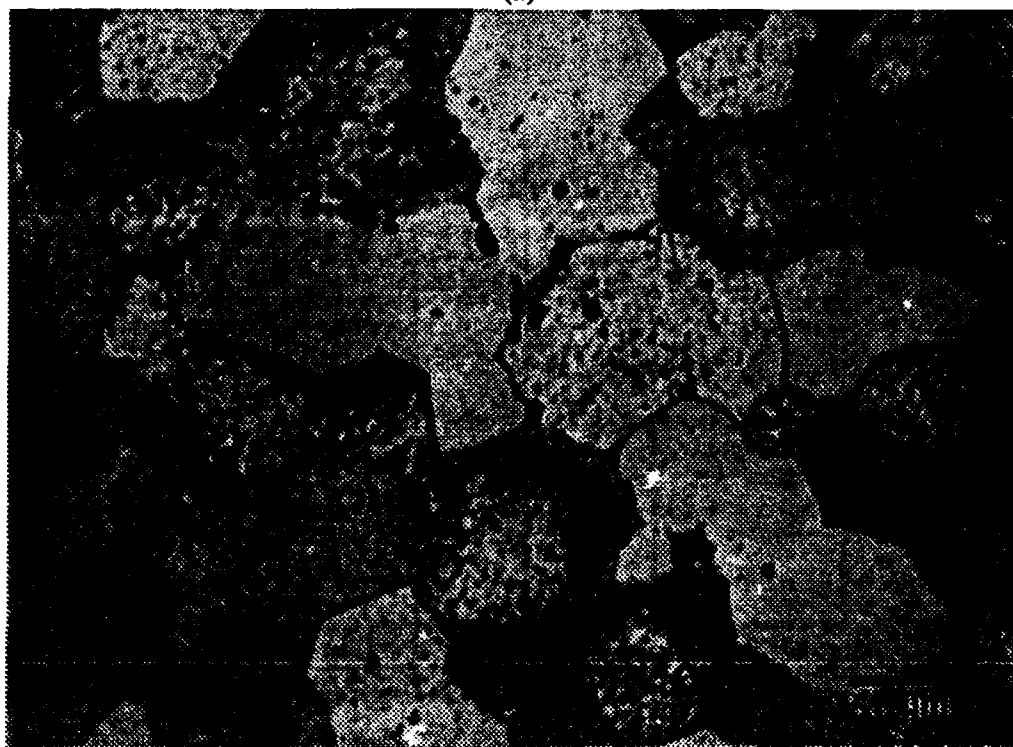
Table 8. Computed and Measured Mass Flow Rates of SiC_p.

Gas Type	Fluidization Pressure (MPa)	Fluidized Bed # 1			Fluidized Bed # 2		
		Measured m (g/sec)	Theoretical m (g/sec)	Vf* of SiC _p (%)	Measured m (g/sec)	Theoretical m (g/sec)	Vf* of SiC _p (%)
Argon	0.41	1.75	1.20	2.5	1.87	2.22	4.6
	0.55	1.78	1.52	3.2	3.42	3.34	6.8
	0.69	1.80	2.15	4.5	3.55	4.13	8.2
Nitrogen	0.41	2.50	2.23	4.6	2.52	2.36	4.9
	0.55	2.60	2.58	5.3	2.62	2.65	5.4
	0.69	2.80	3.12	6.4	2.83	2.93	6.0

* The volume fraction of the SiC_p was computed from the theoretical SiC_p mass flow rate, for a metal flow rate of 40 g/second.



(a)



(b)

Figure 19. Optical micrograph showing equiaxed microstructure of the as-spray deposited: (a) Al-Li-SiC_p material, and b) Al-Li material.

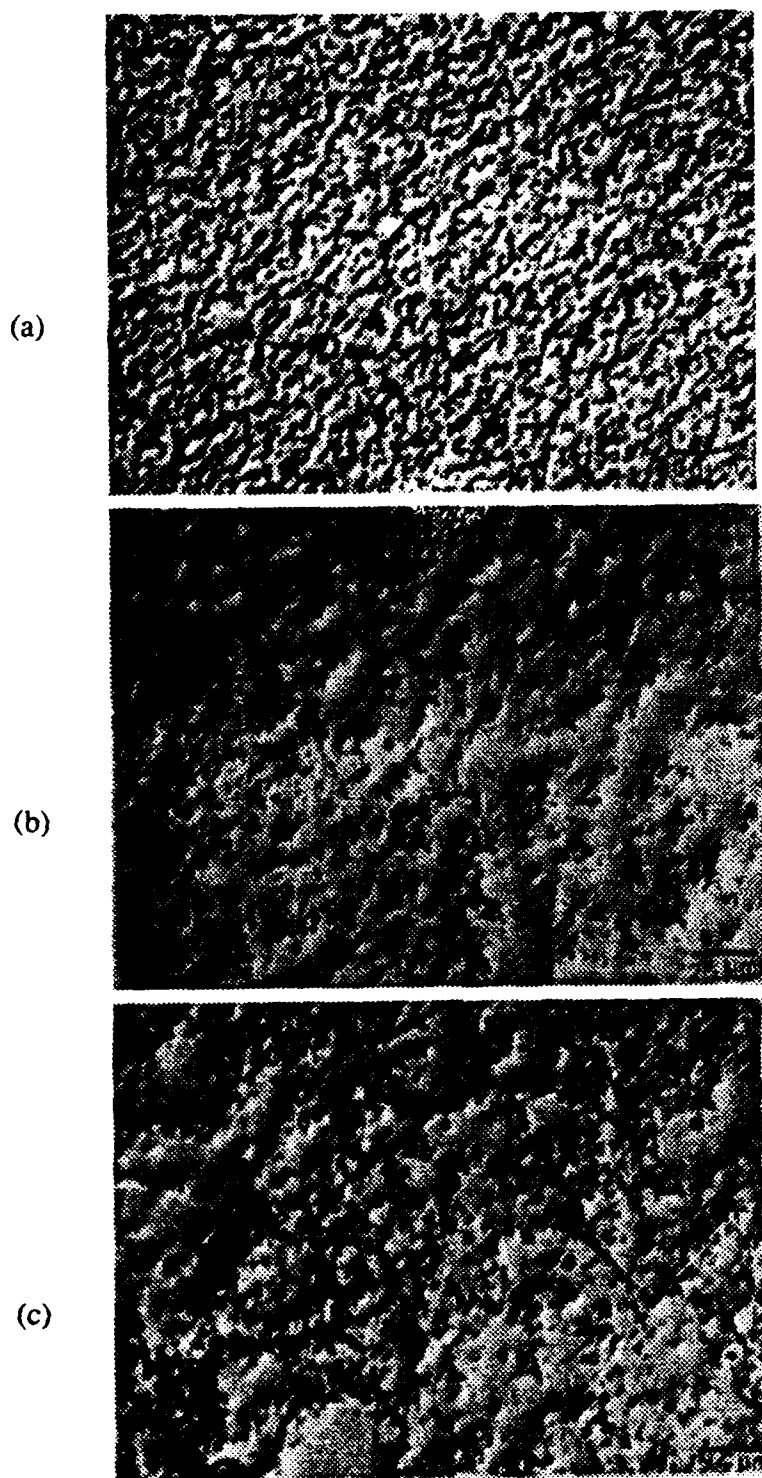
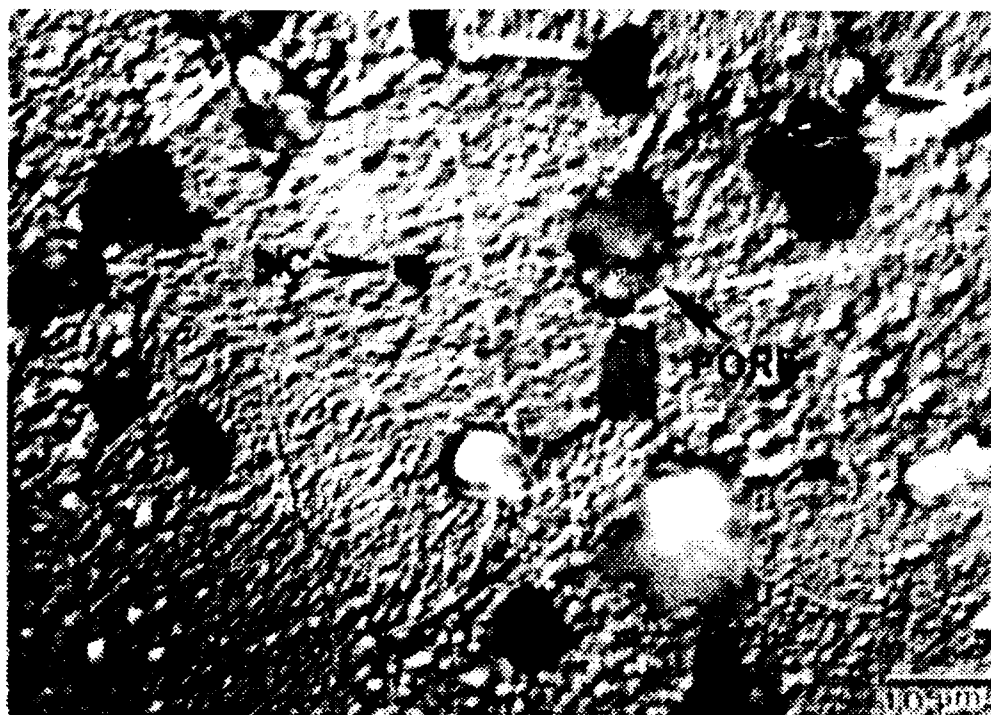
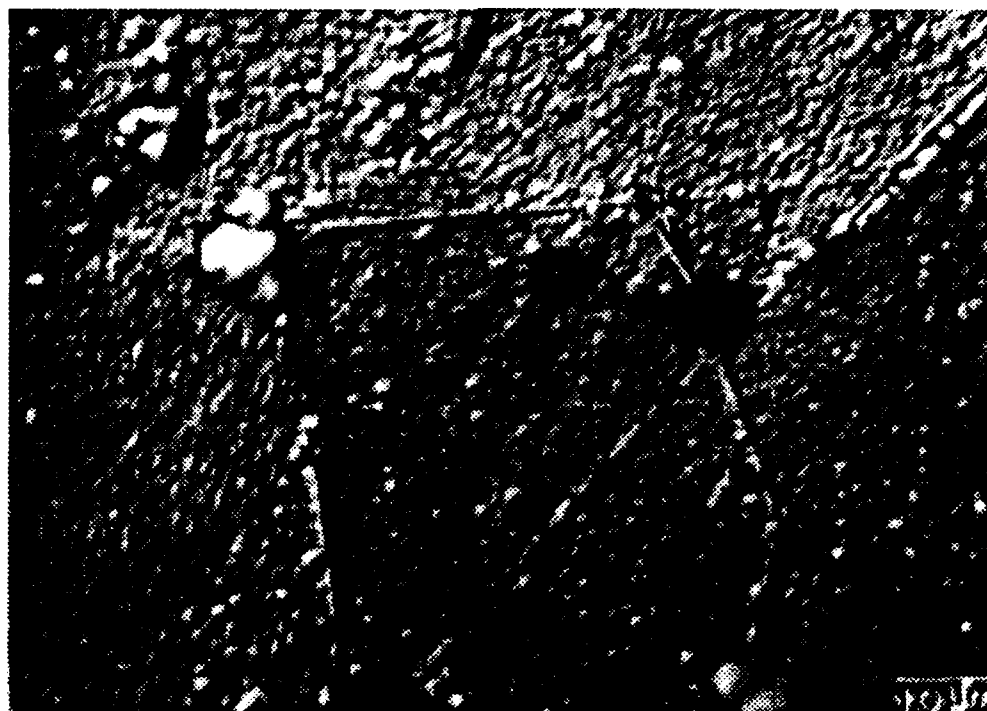


Figure 20. Optical DIC micrograph showing : a) distribution of SiC_p in the Al-Li matrix, b) presence of clustered SiC_p particulates, and c) SiC_p decorating splat boundaries.



(a)



(b)

Figure 21. DIC micrograph showing: a) engulfed SiC_p in the Al-Li matrix, and b) presence of a SiC_p at a grain boundary triple point.

2.3.2.2 Image Analysis

Image analysis was conducted on a number of samples taken from experiments 5-9 in order to characterize the size, distribution, and location of SiC_p in the Al-Li matrix. The size and distribution of the SiC_p obtained from image analyses were then used to compute the SiC_p interparticle spacing according to the formula discussed by Nardone and Prewo [7]:

$$\lambda = (\ell t / V_f)^{1/2} \quad (10)$$

where λ is the interparticle spacing; and t , ℓ and V_f are the thickness, length, and volume fraction of the SiC_p, respectively. The results of the image analysis and the computed interparticle spacings, λ , are shown in Table 9. The frequency histograms corresponding to the size distribution of the SiC_p from experiment 5, are shown in Figure 22.

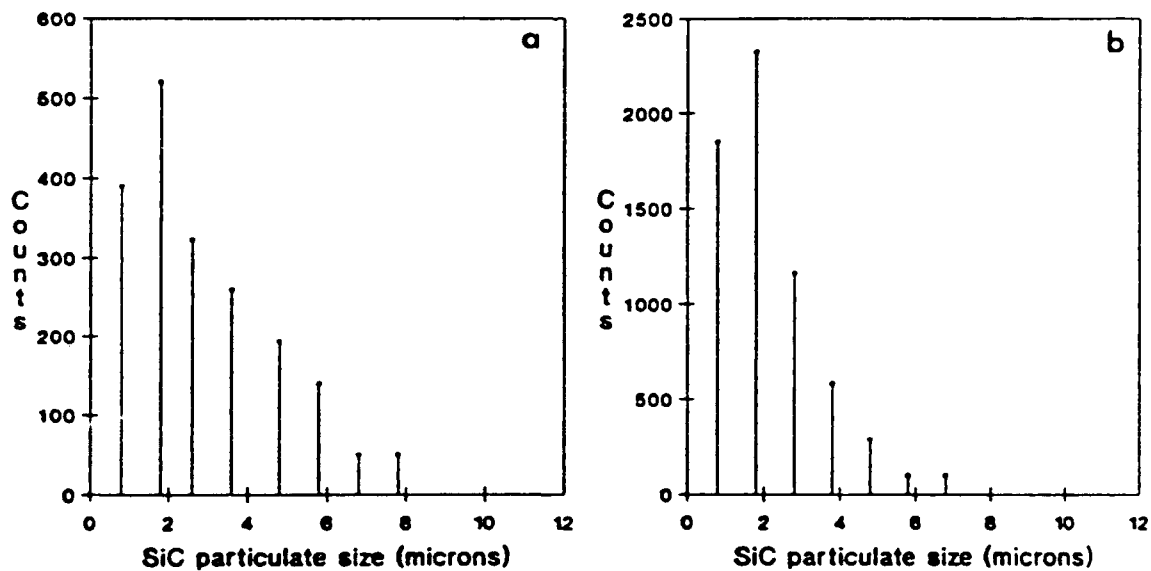


Figure 22. Frequency histogram showing SiC_p size distribution for: a) top and b) bottom regions of experiment 5.

Table 9. Results of Image Analysis of the Al-Li-SiC_p MMCs.

¹ Sample #	² Equivalent Diameter(μm)				Volume Fraction (%)				Inter-particle Spacing (λ , μm)
	Min.	Max.	Mean	σ	Min.	Max.	Mean	σ	
#5 A	0.57	9.00	2.70	2.01	1.92	8.33	3.49	1.82	14.48
#5 B	0.57	10.00	2.71	2.10	2.89	6.15	4.56	1.13	12.69
#5 C	0.57	12.00	2.10	1.76	4.40	13.44	7.89	1.91	7.48
#6 A		-----NOT DETERMINED-----				-	9.60	-	⁴ 8.71
#6 C		-----NOT DETERMINED-----				-	³ 11.65	-	⁴ 7.91
#7 A	0.57	11.00	2.76	2.13	4.69	7.19	6.12	0.85	11.14
#7 B	0.57	10.00	2.86	2.12	4.38	6.10	5.13	0.50	12.62
#7 C	0.57	9.00	3.34	2.16	1.34	3.16	2.49	0.54	21.16
#8 A	0.25	13.56	1.65	2.92	18.39	24.72	20.75	2.25	18.14
#8 B	0.25	9.33	1.54	2.34	3.17	7.36	5.41	1.56	25.71
#9 A	0.25	10.68	1.61	2.79	2.60	7.63	3.70	1.54	19.99
#9 B	0.25	16.95	2.27	4.24	2.77	8.95	6.00	2.29	11.89
#9 C	0.25	18.92	2.58	4.83	0.76	15.00	5.29	5.23	10.78

¹ A, B, C designations refer to top, center and bottom regions, respectively, of the spray atomized and deposited Al-Li-SiC_p.

² The equivalent diameter is a measure of the size of the SiC_p.

³ These values of the volume fraction were determined using quantitative metallography.

⁴ These values were computed from Eqn. 10 for a SiC_p size of 2.7 μm .

2.3.2.3 SEM/EDAX Analysis

Scanning electron microscopy of samples removed from the central portion of the spray atomized and deposited material revealed a fairly uniform distribution of SiC_p throughout the matrix (see Figure 23). In addition, SEM analyses revealed the presence of a finite amount of non-interconnected porosity (see Figure 24). The micron sized pores were

preferentially located at the grain boundaries, and exhibited an irregular, faceted morphology. The distribution of pores in the microstructure was observed to be bimodal, with a large proportion of pores in the 1-2 μm and 10 μm size ranges; the volume fraction of porosity was estimated to be approximately 4-5%. The presence of SiC_p in the Al-Li matrix was confirmed using EDAX analysis.

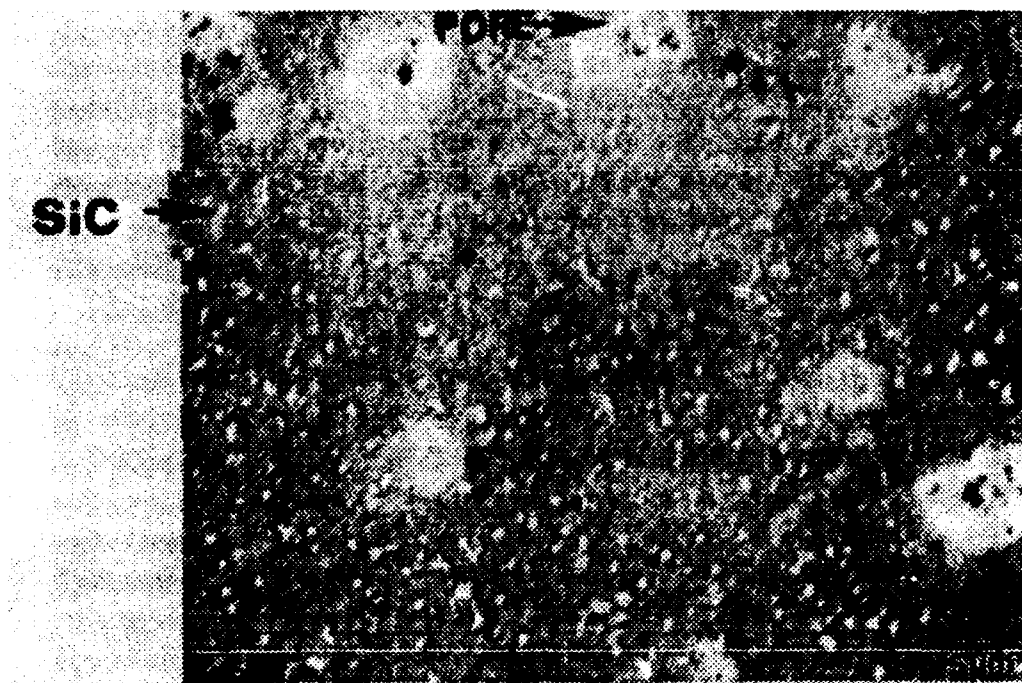


Figure 23. SEM photograph showing SiC_p size distribution in the Al-Li matrix.

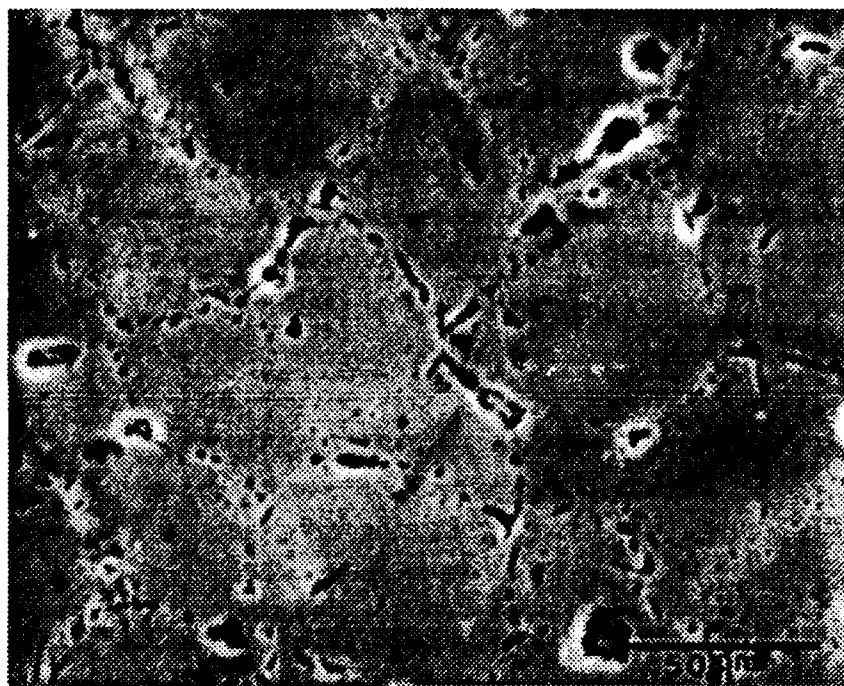


Figure 24. SEM micrograph showing location and morphology of porosity in the Al-Li matrix.

2.3.2.4 Numerical Results

In an effort to provide insight into the various solidification and heat transfer phenomena that are active during spray atomization and deposition, several investigators have developed mathematical models to predict the effects of processing variables on the distribution of droplet sizes, droplet velocities, positions, temperatures, cooling rates and dendrite arm spacings (DAS) [38, 71-73, 102]. Although most of these models either incorporate a number of limiting assumptions, such as small Biot numbers, small undercoolings, etc., or are based on simplistic thermal energy arguments, i.e., enthalpy formulations, they provide some interesting insight into fundamental solidification phenomena during atomization. The ultimate objective of these models is to predict the thermal and solidification behavior of rapidly moving droplets as a function of flight distance. This information can then be utilized to understand the evolution of the microstructure, and consequently to optimize the processing parameters during spray atomization and deposition. In the present study, we used a mathematical model based

on an enthalpy formulation developed elsewhere [38, 72] in order to gain some insight into the solidification and heat transfer behavior of the atomized droplets during atomization, and its subsequent effect on microstructure. The main assumptions involved in the formulation of the model were discussed in section 1.3.8 and are briefly described below.

The disintegration of a molten metal by high energy gas jets (atomization) is complex and only aspects of it have been addressed from a theoretical view point [112]. The work of Lubanska [113] has shown that the disintegration of liquids by high velocity jets obeys a simple correlation. A slightly modified form of the original correlation was incorporated into the model of interest and shown to represent the results of molten metal atomization experiments reasonably well [38, 72, 114]. According to the modified Lubanska's correlation, the mass mean droplet diameter (i.e., the opening of a screening mesh which lets through 50 percent of the mass of the powder resulting from an atomization experiment), d_{50} is given by:

$$d_{50} = K_d [(\mu_m d_o \sigma_m / \mu_g V_{ge}^2 \rho_m)(1 + J_{melt}/J_{gas})]^{1/2} \quad [11]$$

where K_d is an empirically determined constant with a value between 40 and 400 (a value of 162 was selected for the conditions used in the present study, since this was shown to yield a good correlation between theory and experiment [38]; μ_m , σ_m , ρ_m , and J_{melt} are the viscosity, surface tension, density and mass flow rate of the melt, respectively; μ_g , V_{ge} , and J_{gas} are the viscosity, nozzle exit velocity and mass flow rate of the atomizing gas, respectively; and d_o is the diameter of the metal delivery nozzle. Expressions for the flow rates were obtained as functions of the process parameters from Bernoulli's equation in the case of the metal [111] and from theory of compressible flow [115] in the case of the gas. Once the mass mean droplet diameter, d_{50} , was computed from Eqn. (11), other useful characteristic particle sizes such as d_{16} and d_{84} may be readily calculated from d_{50} and experimental information about the standard deviation of the (log-normal) size distribution function for atomized powders [37, 38, 113]. Since d_{16} and d_{84} represent the opening of a screening mesh which lets through 16 and 84 percent of the mass of the powder, respectively, one may use d_{50} , d_{16} and d_{84} to exemplify the complete size distribution of atomized powders.

Once the distribution of droplets sizes (i.e., d_{50} , d_{16} and d_{84}) were computed from Eqn. (11), in combination with experimentally determined values of the standard deviation [37,

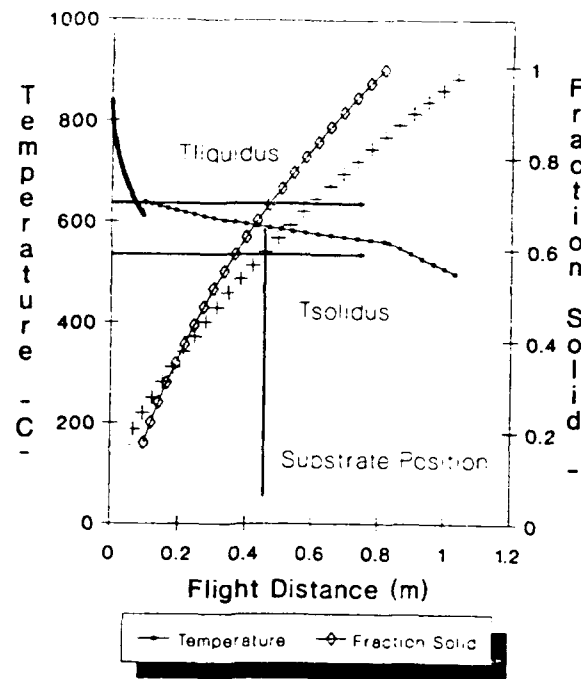
38], the velocity fields of the droplets and gas were calculated from momentum considerations. The final step involved the computation of the droplet temperature and fraction solidified, as a function of flight distance from the atomization point. In the model this was achieved by establishing an energy balance during cooling and solidification, that takes into account, among other variables, the velocity and temperature of the atomization gas. A widely accepted simplifying assumption incorporated into the model involved neglecting the spatial variation in temperature inside the droplet (lumped-parameter representation [116]). This has been shown to be a reasonable assumption for small droplets ($< 1000 \mu\text{m}$) in which the resistance to heat transfer at the outer droplet surface predominates over the internal resistance to heat conduction [38, 73]. Other details and assumptions associated with this particular model are published elsewhere, and hence will not be reproduced here [38, 72].

The aforementioned enthalpy model was applied to the conditions used in the present study (see Table 10) to compute the variations in temperature and fraction solid of the distribution of droplet sizes (i.e., d_{16} , d_{50} and d_{84}) with flight distance for the conditions used in the Al-Li and Al-Li-SiC_p experiments (see Table 6). The numerical results show that for the Al-Li experiment, the distribution of droplets was comprised of solid powders ($d_{16} = 23 \mu\text{m}$, $f_s = 1$), droplets with some proportion of solid phase ($d_{84} = 275 \mu\text{m}$, $f_l > 0.90$), and a substantial fraction of droplets in the mushy state ($d_{50} = 84 \mu\text{m}$, $f_l = 0.30$), during impact with the deposition substrate. For the Al-Li-SiC_p experiments, the distribution of droplets consisted of solid powders ($d_{16} = 30 \mu\text{m}$, $f_s = 1$), droplets with some proportion of liquid phase ($d_{84} = 290 \mu\text{m}$, $f_l > 0.90$), and a substantial fraction of droplets in the mushy state ($d_{50} = 92 \mu\text{m}$, $f_l = 0.42$). Figure 25 shows the thermal and solidification behavior of the mean powder size (d_{50}) for the conditions used in the Al-Li experiment. The fraction solid as a function of flight distance is also shown in the same graph, for the conditions used in the Al-Li-SiC_p experiments. It is important to note, however, that the enthalpy model used in the present study was developed for monolithic materials, and therefore did not incorporate the effects of the SiC_p on the cooling and solidification behavior of the atomized droplets. Hence, the differences in the computed solidification behavior between the reinforced and unreinforced experiments solely reflect the effects of changes in the processing parameters. The possible effects that the SiC_p might have on the thermal and solidification behavior of the atomized Al-Li droplets are discussed in a subsequent section.

Table 10. Input Parameters Used in Numerical Model.

Variable	Description	Value
C_{pg}	Specific heat of argon	518.8 J/kgK
C_{pm}	Specific heat of Al	0.86 KJ/kgK
H_f	Heat of fusion of Al	398 KJ/kg
k_m	Al thermal conductivity	209 W/mK
T_L	Liquidus temperature	640 °C
T_S	Solidus temperature	600 °C
ρ_m	Al density	2.7 g/cm ³
γ	Ratio of C_p/C_v for gas	1.65
T_N	Nucleation temperature	610 °C
σ_m	Melt surface tension	0.840 kg/s ²
ρ_g	Gas density	1.654 kg/m ³
μ_g	Gas viscosity	1.7X10 ⁻⁵ kg/ms
μ_m	Melt viscosity	0.001 kg/ms
P_g	Atomization gas pressure	1.20 MPa ¹

¹The gas atomization pressure used for the Al Li binary materials was 1.38 MPa.



+ = fraction solid of Al-Li-SiC

Figure 25. Computed temperature and fraction solid as a function of flight distance for the conditions used in Al-Li experiment. Also shown is the fraction solid as a function of flight distance for conditions used in the Al-Li-SiC_p experiment.

2.4 Discussion

2.4.1 Microstructure

The grain morphology of the spray deposited materials was equiaxed; this observation is in agreement with previous findings [32, 37, 64, 99-104]. A more thorough discussion of these mechanisms can be found elsewhere [37].

The relatively coarse grained microstructure obtained in the present study for both reinforced and unreinforced materials (44-71 μm for Al-Li-SiC_p; 207 μm for Al-Li) is consistent with the large amount of volume fraction liquid present during impact, as anticipated from the numerical results (see Figure 25). This range of grain sizes is approximately 75% coarser than those reported by other investigators for spray atomized and deposited aluminum alloys [37, 38]. Gutierrez and co-workers [38], for example, reported grain sizes ranging from 12-25 μm for a spray atomized and deposited 7075

aluminum alloy. The coarse grain size found in the present investigation is thought to have developed first, as a result of an excessive amount of liquid phase contained in the droplet distribution at the moment of impact with the deposition surface, and second, due to the lack of secondary precipitates to prevent grain coarsening during solid state cooling. The results of Gutierrez and co-workers [38] show that at the moment of impact with the substrate, the average droplet contained only 10-15 volume fraction liquid; this is substantially lower than that achieved in the present investigation for both types of materials (Al-Li-SiC_p, $V_{fl} = 0.42$; Al-Li, $V_{fl} = 0.30$).

Regarding the difference in microstructure between the reinforced and unreinforced materials, the present results show a substantial decrease in the grain size of the Al-Li-SiC_p material, relative to that obtained in the Al-Li alloy. This observation, however, is inconsistent with the numerical results which suggest that the experimental conditions used during the Al-Li experiment resulted in a finer droplet diameter ($d_{50} = 84 \mu\text{m}$) and a greater extent of presolidification ($f_s = 0.70$) during impact with the deposition substrate, relative to the conditions of the average droplet during the Al-Li-SiC_p experiments ($d_{50} = 92 \mu\text{m}$, $f_s = 0.58$). The numerical results may be readily understood by considering the important effects of gas atomization pressure on the behavior of the atomized droplets. The gas atomization pressure used during the Al-Li experiment (1.38 MPa) was higher than that used during the Al-Li-SiC_p experiment (1.20 MPa), effectively promoting both a finer droplet diameter, as well as a more efficient convective heat flux from the surface of the atomized droplets during solidification [38, 63, 72, 114]. It is worth noting that when the experiments were conducted utilizing identical processing parameters, for both reinforced and unreinforced materials, the microstructure of the former exhibited a high degree of porosity, rendering quantitative microstructural analysis extremely difficult. In view of this apparent discrepancy between the computed and experimental results, the fine grained microstructure of the Al-Li-SiC_p material may be attributed to the presence of SiC_p; this is discussed in more detail below.

The suggestion that the co-injection of ceramic particulates during spray atomization and deposition results in a marked reduction in the grain size of the MMC material, relative to that of the monolithic alloy, is supported by the findings of other investigators. This phenomenon has also been noted by White and co-workers [117] and Kojima and co-workers [118], who report a decrease in grain size of up to 30% for an Al-Li-Cu-Mg-Zr alloy spray atomized and co-deposited with SiC_p and B₄C particulates, relative to that noted for the monolithic materials. In view of the complex thermal, fluid, and

solidification phenomena involved during spray atomization and co-deposition it is highly improbable that the observed reduction in grain size can be attributed to a single mechanism. Most likely, the observed changes in microstructure can be attributed to the combined effects of several, non-linear mechanisms. One approach proposed by Gupta and co-workers [101] in order to provide insight into the effects of the ceramic particulates on the microstructural evolution during spray atomization and deposition, is to decouple the thermal, momentum and solidification phenomena into three distinct mechanisms: solidification effects, thermal effects, and solid state cooling effects. Regarding thermal effects, Gupta and co-workers [101] formulated a heat transfer model to quantify the changes in thermal energy of an atomized droplet distribution derived from the presence of a distribution of randomly mixed ceramic particulates. The degree of complexity associated with high spray densities necessitated the incorporation of a number of simplifying assumptions into the thermal and momentum equations. In particular, the treatment of an atomized spray as a collection of individual droplets, with no interactions among each other, is perhaps the most limiting. Nevertheless, from a conservation of thermal energy standpoint, the results provide insight into the effects of ceramic phases on the evolution of microstructure during impact with a deposition surface. In this study, the percentage heat dissipated during flight as a result of the presence of SiC_p , $Q_{(\text{SiC}, \text{flight})}$, was calculated from:

$$Q_{(\text{SiC}, \text{flight})} = \frac{Q_{\text{Total}}(\text{SiC}, \text{flight})}{H_{\text{spray}}} \times 100 \quad [12]$$

where $Q_{\text{Total}}(\text{SiC}, \text{flight})$ represents the total amount of thermal energy transferred during flight and H_{spray} represents the total enthalpy content of the atomized spray. The results of this study show that the co-injection of a distribution of SiC_p into an Al spray will decrease the average enthalpy at impact by 10%, relative to that for the unreinforced spray, and that 8% of the thermal energy will be transferred to the SiC_p after deposition. In spite of the fact that these results are consistent with the reduction in grain size observed in the present study, there are other mechanisms that are likely to influence the final microstructure. For example, the effects of the ceramic particulates on the solidification mechanisms operating during atomization and on the migration of grain boundaries during solid state cooling, have not been not addressed; further work is continuing in this area.

2.4.2 Porosity

Porosity is an important microstructural characteristic frequently associated with spray atomized and deposited microstructures [32, 37, 63, 64, 66, 79, 99-104]. The various mechanisms governing the formation of porosity in the spray deposited materials has been discussed in section 1.4.3. Under conditions typical for aluminum alloys the amount of porosity present in spray atomized and deposited materials has been reported to be in the 1-10% range. This is consistent with the results of the present study which showed the porosity levels in the 5-6% range. Furthermore, the present results also revealed that the size distribution of pores is bimodal, with a large proportion of pore sizes in the 1-2 μm and 10 μm range. Finally, although an investigation of the role of the SiC_p on the evolution of porosity during spray atomization and deposition was outside the scope of the present study, it is likely that the presence of the particulates will affect the porosity present.

2.4.3 SiC_p Size and Distribution

In order to verify the theoretically determined mass flow rates of the SiC_p shown in Table 8, and determine the values of K and v in Eqns. (3-9), a number of fluid flow experiments were conducted independently. The results of these experiments indicate that the SiC_p mass flow rate depends on the gas type and fluidization gas pressure (see Table 8 and Figure 18). The discrepancy between the computed and measured mass flow rates of SiC_p may be attributed to difficulties encountered in estimating some of the parameters utilized in Eqns. (3-9). For example, determination of the average velocity of the fluidizing gas, v , requires a knowledge of the fluid flow conditions in the fluidized bed. Since these conditions were not accurately known, this velocity was determined from the experimentally measured volumetric gas flow rate through the fluidized bed. It is anticipated that the actual average velocity of the fluidizing gas will be lower than the computed value, on the basis of the geometry of the fluidizing chamber and the bubbling tendency of the gas noted for some fluidization conditions.

If the theoretical and measured values of the SiC_p mass flow rates, and the mass flow rate of the Al-Li matrix are taken into consideration, it is possible to estimate an upper bound for the volume fraction of the SiC_p . Such calculations yield a volume fraction of SiC_p in the 2.5% - 8.2% range for the first and second fluidized beds, depending on the fluidization gas pressure and gas type. The results shown in Table 8 and Figure 18

suggest various trends. First, increasing the volume of the fluidized bed from $4.73 \times 10^{-4} \text{ m}^3$ to $1.74 \times 10^{-3} \text{ m}^3$ results in a marginal increase in the mass flow rate of the SiC_p . Although this observation is consistent with the results anticipated from Eqn. (8), which show that the mass flow rate of the particulates, W_{SiC} , depends on the diameter of the fluidizing chamber, D , one must consider other effects, such as the decrease in v brought about by a larger fluidizing chamber diameter. Second, increasing the fluidization pressure also results in an increase in the mass flow rate of the SiC_p . This is to be expected, since increasing the fluidization pressure increases the average operating velocity, v , as a result of an increase in the volumetric gas flow rate of the gas. It is worth noting, however, that the rate of increase in mass flow rate with pressure, asymptotically reaches a maximum value at a pressure of approximately 0.69 MPa. This is thought to be a result of the increased back pressure inside the fluidizing chamber at the higher pressures. Regarding the effects of gas density on mass flow rates, examination of Eqn. (8) suggests that a higher gas density will result in an increase in the mass flow rate of the particulates. The results shown in Table 8, however, indicate that whereas the maximum SiC_p mass flow rate was achieved with N_2 for fluidized bed #1, Ar resulted in the maximum SiC_p flow rate for fluidized bed #2. This behavior although not precisely understood, is thought to be associated with the interaction of Ar and N_2 with the fluidizing chamber. For example, during the flow experiments it was noted that the tendency for bubbling in fluidized bed #2 was higher for N_2 than for Ar, limiting the ability of N_2 to entrain the SiC_p . Overall, the results shown in Table 8 suggest an order of magnitude correlation between the computed and experimentally observed volume fraction of SiC_p in the Al-Li matrix (See Table 9).

Regarding the variations in volume fraction of SiC_p for a single experiment, the results shown in Table 9 do not reveal a clear correlation between spray deposited thickness, the amount of SiC_p , and the experimental conditions (see Table 6). Although a systematic investigation of the effects of the injection angle on the distribution of SiC_p was outside of the scope of the present study, the variations in volume fraction with spray deposited thickness are most likely affected by changes in the fluidization conditions (i.e., pressure drop) and mass flow rate of the metal during the experiments, in addition to the injection angle. Furthermore, since the volume fraction of SiC_p was determined using image analysis, the results should be treated as an order of magnitude approximation of the actual SiC_p volume fraction. The results do suggest, however, that it is possible to alter the resulting variations in volume fraction of SiC_p through changes in processing parameters, such as, for example, the injection angle. The higher volume fraction of SiC_p

observed for experiment 6 was attributed to the pressurization condition at the metal delivery tube (see Table 6). This behavior, which is caused by the relative position of the metal delivery tube to the gas jets, has been studied extensively [119]. The pressurization condition present at the metal delivery tube reduced the metal flow rate of the matrix, effectively decreasing the Al-Li/SiC_p mass flow ratio, resulting in a higher SiC_p concentration.

Comparison of the theoretically determined SiC_p volume fractions shown in Table 8, to the results of the image analysis shown in Table 9, suggest good agreement between theory and experiment. The experimentally determined volume fractions of the SiC_p, averaged over the thickness of each experiment, were 5.3, 10.6, 4.6, 13.1, and 5.0 for experiments 5-9, respectively. In comparison, the theoretically determined volume fractions were 4.5 for experiments 5-7; 8.2 and 6.0 for experiments 8 and 9, respectively (see Table 8). The discrepancy between the computed and experimentally determined values observed for experiment 6 can be attributed to the pressurization condition during atomization, as previously discussed. The difference between the computed and experimentally determined values for experiment 8, however, remains unclear, since no pressurization was present during this experiment. It is worth noting that the presence of porosity in the microstructure of the spray atomized and deposited materials made it difficult in some cases, to distinguish between micron sized pores, and SiC_p.

2.4.4 Distribution of SiC_p in the Al-Li matrix

The resultant distribution of reinforcing phases during processing of metal matrix composites is of interest, since the mechanical behavior of these materials will depend on the size, distribution and orientation of these phases in the matrix. In turn, it is the interaction of these reinforcing phases -commonly ceramics - with solidification mechanisms that governs the resultant distribution. A review of the available scientific literature shows that over the last three decades various investigators have addressed the fundamental problem posed by the interaction of a particulate with a moving fluid front [91-98]. In particular, the results of these studies have enhanced our understanding of the kinetic and thermodynamic factors that govern the entrapment or rejection of particulates by a moving liquid front. According to the results available from these studies, a particulate will be engulfed or rejected by a moving solidification front on the basis of one of the following criteria:

- (a) thermodynamic criterion,
- (b) critical velocity criterion,
- (c) thermal conductivity criterion, or
- (d) thermal diffusivity criterion.

A discussion of these criteria follows.

The thermodynamic criterion is based on the principle that engulfment or rejection of particulates by a moving solidification front will depend on the net change in the free energy of the system. The change in free energy of the system can be defined as:

$$\Delta F_{\text{net}} = \sigma_{\text{PS}} - \sigma_{\text{PL}} \quad (13)$$

where σ_{PS} is defined as the surface energy between the particulate and the solid, and σ_{PL} is defined as the surface energy between the particulate and the liquid. Hence, if $\Delta F_{\text{net}} < 0$, engulfment of the particulates by the moving solidification front can be anticipated; if $\Delta F_{\text{net}} > 0$ rejection of the particulate will occur [98].

The critical interface velocity criterion has been documented extensively [91-93, 97]. This criterion is based on the principle that the engulfment or rejection of particulates during solidification will depend on the velocity of the solidification front. The critical velocity (V_{cr}) of the solidification front for the engulfment or rejection of the particulates can be defined as:

$$V_{\text{cr}} = \frac{\Delta\sigma_0 d_0}{6(n-1)\eta r} \left(2 - \frac{K_{\text{P}}}{K_{\text{L}}} \right) \quad (14)$$

where d_0 is the interatomic distance, η is the viscosity of the melt, r is the radius of the particulate, K_{P} is thermal conductivity of the particulate material, K_{L} is the thermal conductivity of the melt, n is a constant having integral values from 2-7 [97]. $\Delta\sigma_0$ is the difference in surface tension, as computed from:

$$\Delta\sigma_0 = \sigma_{\text{PS}} - (\sigma_{\text{PL}} + \sigma_{\text{SL}}) \quad (15)$$

where σ_{PS} is the surface energy between particulate and solid, σ_{PL} is the surface energy between the particulate and liquid and σ_{SL} is the surface energy between solid and liquid. Hence, if the velocity of the solidification front is greater than V_{cr} , particulate engulfment is anticipated; conversely, if the velocity of the solidification front is less than V_{cr} , rejection of the particulate will occur [97].

The thermal conductivity criterion can be used to predict engulfment or rejection of particulates by an advancing solid/liquid interface solely on the basis of the ratio of thermal conductivities of the particulates and the melt. This criterion anticipates particulate engulfment if $K_P/K_L > 1$ and rejection if $K_P/K_L < 1$, where K_P and K_L represents thermal conductivities of particulate and melt, respectively. This criterion has been extensively studied by Zubko and co-workers [94].

The thermal diffusivity criterion is based on the principle that engulfment or rejection of the particulate is a function of the ratio of the thermal diffusivities of particulate and melt. The ratio of thermal diffusivities (R) can be expressed as follows:

$$R = \left(\frac{\lambda_P C_P \rho_P}{\lambda_L C_L \rho_L} \right)^{1/2} \quad [16]$$

where λ_P , C_P and ρ_P represent the thermal conductivity, specific heat and density of the particulate, respectively; and λ_L , C_L and ρ_L represent the thermal conductivity, specific heat and density of liquid, respectively. Hence, if this ratio is greater than one, the particulate will be captured; if this ratio is less than one the particulate will be rejected [96, 98].

It is evident from the above description of the four criteria, that these were originally developed for steady state conditions, such as those present during equilibrium solidification (e.g., planar solid / liquid interfaces, spherical particles, and constant thermal properties). In contrast, the conditions present during spray atomization and deposition are far from being at equilibrium, and as previously discussed, involve both solid and liquid phases. However, in order to provide some insight into the kinetic mechanisms governing the distribution of SiC_p during spray atomization and co-deposition, Eqns. (13-16) were used to predict engulfment or rejection of the particulates

by the solidification front. The properties of the Al-Li matrix and the SiC_p used for the computation are shown in Table 11.

The results of these calculations are shown in Table 12 for each of the four criteria. Clearly, whereas none of the four approaches predict particulate engulfment during solidification, the results of image analyses and optical microscopy studies indicate otherwise. For example, the results shown in Table 9 indicate that the interparticle spacing for the SiC_p is in 7-21.2 μm range, whereas the grain size is in the 66-72 μm range for all five experiments. These results, which are supported by optical (see Figure 20) and scanning electron microscopy (see Figures 21 and 23), suggest that SiC_p can be found both intra- and intergranularly. The presence of SiC_p in the center region of the grains suggests particulate engulfment during solidification, since particulate rejection by the solidification front would result in pushing of the particulates towards the interdendritic regions. It is unlikely that the presence of SiC_p in the center region of the grains may be attributed to grain growth following solidification, since preliminary results from grain growth studies suggest that the SiC_p tend to immobilize the grain boundaries during grain growth [120].

Table 11. Input Parameters Used to Calculate the Results shown in Table VIII.

Viscosity of Al	$2 \times 10^{-3} \text{Pa.s}^*$
σ_{PS}	10.547 N/m^*
σ_{PL}	2.26 N/m^*
σ_{SL}	0.016 N/m
d_0	$3 \times 10^{-8} \text{ cm}$
ρ_{Al}	$2.7 \times 10^3 \text{ kg/m}^3$
ρ_{SiC}	$3.1 \times 10^3 \text{ kg/m}^3$
K_{SiC}	15.57 W/mK
K_{Al}	109.5 W/mK
$C_p(\text{SiC})$	0.963 kJ/kg
$C_p(\text{Al})$	1.086 kJ/kg

*as reported by Stefanescu et al⁹⁷.

The failure of the above criteria to account for the experimental results is not surprising in view of the extreme non - equilibrium conditions present during spray atomization and deposition. Therefore, since the microstructural characteristics of spray deposited materials cannot be rationalized in terms of the aforementioned criteria, an alternate mechanism for particulate entrapment must be explored.

Table 12. Results and Predictions of Various Criteria for Particulate Engulfment/Rejection.

Criterion	Result	Prediction
Thermodynamic approach	$\Delta F = 8.287 \text{ N/m}$	Engulfment not possible
Critical velocity approach	$V_{cr} = 2.31 \text{ cm/s}$	Engulfment not possible since $V_{deposition} \approx 2 \text{ mm/s}^{37}$.
Thermal conductivity approach	$K_p/K_1 = 0.1421$	Engulfment not possible
Thermal diffusivity approach	$R = 0.38$	Engulfment not possible

During spray atomization and co-deposition, the thermal and solidification conditions of the droplet distribution at the moment of impact with the deposition surface will depend on: (a) the thermodynamic properties of the matrix material, such as: (i) liquidus temperature, (ii) solidus temperature, (iii) melting temperature, (iv) density, (v) thermal conductivity, (vi) surface tension, (vii) heat capacity, and (viii) heat of fusion; (b) the thermodynamic properties of the atomization gas such as: (i) density, (ii) heat capacity, (iii) viscosity, and (iv) thermal conductivity; (c) the characteristics of the reinforcement phase(s), such as: (i) size distribution, (ii) mass flow rate, and (iii) temperature; and (d) the processing parameters, such as: (i) atomization gas pressure, (ii) nozzle/substrate

flight distance, (iii) metal/gas flow ratio, and (iv) reinforcement injection. Under conditions typical for aluminum alloys, and as previously discussed, the droplet distribution at impact is comprised of solid powders, droplets with some proportion of solid phase, and a substantial fraction of powders in the mushy state. As a result, during impact with the deposition surface, the SiC_p will be surrounded by either: (a) dendrite fragments, (b) fully solidified fine droplets, or (c) liquid phase. This event is shown schematically in Figure 26. Whereas the presence of either dendrite fragments and/or fully solidified droplets will not permit migration of the SiC_p - in this case the particulates will be found decorating the splat boundaries - the interaction of the particulates with the liquid phase and the ensuing solidification events must be considered. In the presence of a liquid phase, the SiC_p may be

- (a) engulfed by the moving solidification front,
- (b) pushed to interdendritic regions,
- (c) agglomerated and engulfed, or
- (d) agglomerated and pushed towards interdendritic region

Comparison of the initial SiC_p size distribution ($d_{50} = 3\mu\text{m}$) to that determined from the image analysis ($1.5\text{-}3.3\mu\text{m}$; see Table 9) indicates that the SiC_p did not agglomerate during deposition. Only for sample 7C, from the bottom region of the spray atomized and deposited material, was there some agglomeration present ($3.34\mu\text{m}$); this is discussed subsequently. Whereas one would not anticipate entrapment of the SiC_p by the solidification front on the basis of the low solidification front velocities after impact [36, 37, 75] and on the basis of the large difference in thermal properties between the particulates and the liquid/solid front, entrapment during deposition will be facilitated as a result of the kinetic energy present during deposition, which will lead to a mechanically driven entrapment. This mechanism is illustrated schematically in Figure 27.

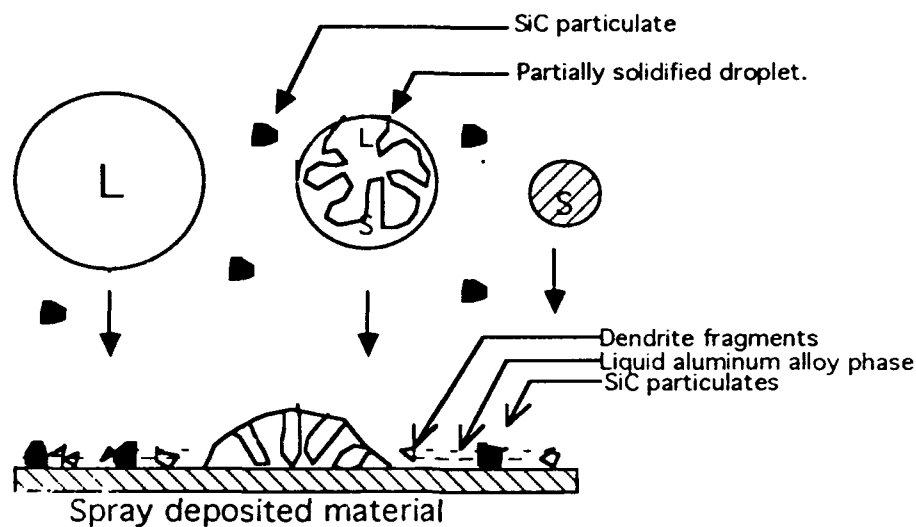


Figure 26. Schematic diagram showing the events during impact of droplets and SiC_p at the deposition surface.

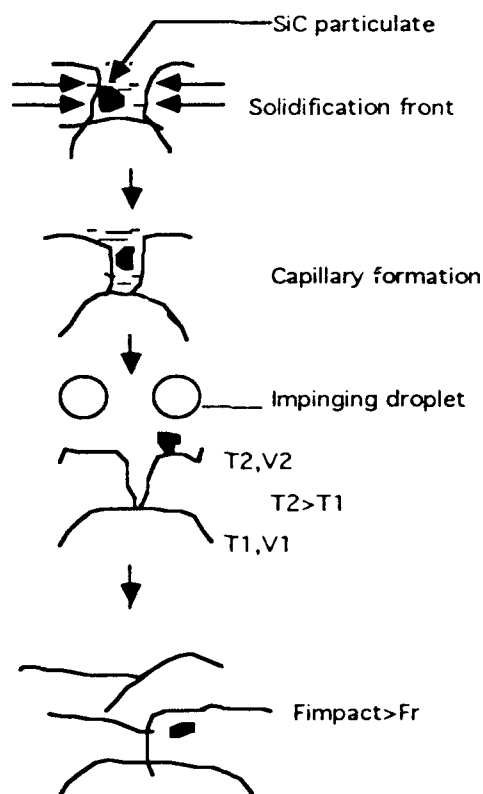


Figure 27. Schematic diagram showing mechanically driven entrapment during spray atomization and deposition; T₁, T₂, V₁ and V₂ refer to the temperature and velocity before and after deposition, respectively.

In mechanically driven entrapment, a SiC_p is approached by multiple solidification fronts, as shown schematically in Figure 27. As the solidification fronts converge, a capillary region will form around the particulates. At this point, the particulates will not only experience the repulsive forces from the solidification fronts, but also capillary forces and fluid convective forces resulting from droplet impact and fracture. The combined effect of all three types of forces will be to push the particulate(s) out of the capillary region. As the SiC_p is displaced, subsequent impact by a droplet becomes highly probable as a result of the high spray density present during spray atomization and deposition [37, 80]. Since the impinging droplets arrive at the deposition surface with velocities ranging from 100-400 m / s - depending on size - the high kinetic energy associated with the impact will lead to a mechanically stimulated engulfment of the ceramic particulates. This mechanism, however, assumes that the SiC_p can move freely under the action of the aforementioned forces, and hence possess a relatively smooth surface and a low aspect ratio. Whereas the particular SiC_p size distribution used in this study exhibited a relatively irregular, equiaxed morphology (i.e., low aspect ratio), SEM studies revealed that the surfaces of these particulates were highly irregular.

A straight forward mathematical treatment may be utilized to assess whether mechanically driven entrapment of the SiC_p during spray atomization and co-deposition processing is possible. By computing the magnitude of the repulsive forces acting on a particulate as a result of the solidification front, and comparing these with the impact forces exerted by the droplets, it will be possible to determine whether engulfment is possible or not. Thus, if $F_{\text{impact}}/F_r > 1$ the particulate will be engulfed; otherwise it will be rejected. The repulsive force experienced by a particulate as a result of a solid/liquid front can be computed from [97]:

$$F_r = -\pi r \Delta \sigma_o / (n - 1) \quad [17]$$

where r , is the radius of the particulate, $\Delta \sigma_o$ represent the difference in surface tension as defined in Eqn. (15), and n is a constant defined in Eqn. (14). The impact force due to the impinging droplets can be calculated from:

$$F_{\text{impact}} = V(d_i) \rho(d_i) a(d_i) \quad [18]$$

where $V(d_i)$, $\rho(d_i)$ and $a(d_i)$ represent the volume, density and acceleration of a droplet of size d_i , respectively. The value of the repulsive forces computed according to Eqn. (17) and the impact forces computed according to Eqn. (18) are shown in Table 13.

Based on the ratio of impact to repulsive forces, it can be predicted whether the SiC_p will be engulfed or not. It can be seen from the results shown in Table 13, that the impact forces resulting from d_{16} droplets are not sufficient to overcome the repulsive forces for a large proportion of the SiC_p sizes used in this study. However, the impact forces exerted by d_{50} and d_{84} droplets can lead to engulfment of 1 μm , 3 μm and 5 μm particulates. Since the d_{50} and d_{84} droplets comprise a large proportion of the entire distribution, it may be concluded that a large proportion of the SiC_p should be engulfed.

Table 13. Computed Repulsive and Impact Forces for Spray Atomization and Deposition.

Repulsive Force (N)	Impact Force (N)	Prediction
	$F(d_{16}) = 2.51 \times 10^{-6}$	Engulfment not possible for 1, 3 or 5 μm particulate size.
$F_r(1\mu\text{m}) = 4.33 \times 10^{-6}$		
$F_r(3\mu\text{m}) = 1.30 \times 10^{-5}$	$F(d_{50}) = 3.00 \times 10^{-5}$	Engulfment possible for 1,3 and 5 μm particulate size.
$F_r(5\mu\text{m}) = 2.16 \times 10^{-5}$		
	$F(d_{84}) = 3.14 \times 10^{-4}$	Engulfment possible for 1,3 and 5 μm particulate size.

* where d_{16} (30 μm), d_{50} (92 μm) and d_{84} (290 μm) characterize the droplet size distribution³⁷.

Whereas the optical and SEM microscopy studies, as well as the interparticle spacings computed from Eqn. (10) confirm that particulate entrapment will occur during spray atomization and deposition (see Figure 21a), the presence of SiC_p at the grain boundaries was also noted (see Figure 21b). Figure 20c shows the SiC_p decorating prior droplet boundaries; this micrograph was taken from the bottom region of the deposit, close to the water cooled surface. Local clustering of SiC_p during deposition (see Figure 20b) can be related to the thermal history of the droplets. The thermal history of the material throughout deposition is dictated, in part, by the rate of transfer of thermal energy from

the atomized spray into the deposited material. In turn, the rate of transfer of thermal energy from the spray into the deposit is directly related to the average enthalpy content of the spray at the moment of impact. For example, under conditions of high spray enthalpies, it has been suggested that remelting of solid phases may occur locally [37, 38]. In this case the SiC_p , rather than being allowed to move freely under the action of repulsive, convective and capillary forces, will remain in contact with the molten matrix. This will lead to the formation of high temperature regions, resulting in low solidification front velocities, with concomitant segregation of the particulates to the grain boundary regions.

The presence of SiC_p at prior-droplet boundaries, as observed for the region of the spray deposited material deposit closest to the water cooled surface, can be rationalized in terms of the fast quench rates experienced by this region. Sample 7C, for example, shows a SiC_p interparticle spacing (λ) of 21 μm , which is relatively close to the diameter of the d_{16} droplets (30 μm). This observation is also consistent with the mechanically driven entrapment mechanism proposed here, which predicts that engulfment of 1, 3, or 5 μm particulates will not occur for d_{16} droplets (see Table 13).

2.5 Conclusions

1. The results obtained from the present study suggest that it is possible to spray atomize a metallic matrix and simultaneously co-deposit a distribution of ceramic particulates. Furthermore, it was observed that the resultant distribution of SiC_p was affected by the fluidization parameters and the atomization conditions.
2. The SiC_p were found to promote substantial grain refinement of the spray atomized and deposited materials. This observation was discussed in terms of the processing variables and the computed solidification behavior.
3. Quantitative analysis of the size and distribution of the SiC_p in the Al-Li microstructure indicated minimal agglomeration. Retention of a suitable particulate dispersion throughout the matrix was facilitated by the presence of primary dendrite debris resulting from droplet impact. Some agglomeration was noted in regions of the spray atomized and deposited material containing excess amounts of liquid phase.

4. In the present study, an alternate criterion based on mechanically driven engulfment was proposed to explain the observed entrapment of SiC_p by an Al-Li matrix. The validity of this criterion was established for Al-Li- SiC_p metal matrix composites using optical microscopy, SEM, and image analysis.

CHAPTER 3

3.0 The Effect of Ceramic Reinforcements During Spray Atomization and Co-Deposition of Metal Matrix Composites: Part I. Heat Transfer

3.1. Introduction

The experimental and theoretical studies described in the previous two chapters demonstrate that spray atomization and co-deposition may be successfully utilized to synthesize MMCs. It is also evident, however, that the conditions during processing critically affect the resultant distribution of reinforcing phases. Despite encouraging preliminary results [31, 33-35, 117, 118, 121, 122, 123], our understanding of the thermal and momentum mechanisms which govern the interaction between the ceramic and metallic phases, remains very limited. In particular, the effects associated with the energetic co-injection of a distribution of ceramic particulates into a partially solidified metallic spray, and its ensuing effects on the heat transfer during atomization and subsequently during deposition are not well understood.

The objective of the present investigation was to provide insight into the thermal effects of ceramic particulates on the evolution of microstructure during spray atomization and co-deposition of metal matrix composites. The numerical results will be correlated with the grain sizes of the unreinforced and reinforced spray deposited materials.

3.2. Experimental Procedure

The experimental studies were conducted using an aluminum matrix reinforced with silicon carbide particulates (SiC_p). Two aluminum alloys were selected for the present study: Al-2.1Li (wt. %) and Al-(5.0-7.0)Cu-(0.1-0.3)Mg-(0.0-0.8)Mn-(0.0-0.1)Ti-(0.0-0.25)V-(0.0-0.25)Zr-(0.0-0.5)Fe-(0.0-0.5)Si-(0.0-0.12)Zn (wt. %) (2519 designation). The Reynolds Metals Company (Richmond, Virginia, U.S.A) provided the Al-Li matrix alloy as cast ingots, whereas the 2519 alloy was provided by the Army Materials Technology Laboratory (Watertown, Massachusetts, U.S.A.). The two matrix alloys will be referred to hereafter as Al-Li and Al-Cu, respectively.

The details regarding the type, size and distribution of SiC_p were described in section 2.2.

3.2.1. Processing

The experimental details regarding spray atomization and co-deposition processing were described in section 2.2. Five experiments (experiments 5, 10-13) were conducted for the

present study; the primary experimental variables used during each experiment are listed in Table 14.

Table 14. Experimental Variables.

Variables	Experiment Number				
	10	5	11	12	13
Matrix Alloy	Al- 2.1 Li	Al-2.1 Li	Al-5.0 Cu	Al-5.0 Cu	Al-5.0 Cu
Reinforcement	--	SiC _p	--	SiC _p	SiC _p
Atomization Pressure	1.36 MPa	1.2 MPa	1.2 MPa	1.2 MPa	1.2 MPa
Atomization Gas	Argon	Argon	Nitrogen	Nitrogen	Nitrogen
Fluidized Bed Gas	--	Argon	--	Nitrogen	Nitrogen
Injection Angle ^(a)	--	30°	--	30°	30°
Injection Distance	--	0.21 m	--	0.21 m	0.21 m
Fluidizing Pressure	--	0.69 MPa	--	0.17 MPa	0.17 MPa
Flight Distance	0.41	0.41 m	0.41 m	0.41 m	0.41 m
Pouring Temperature	840°C	840°C	800 °C	800 °C	800 °C
Metal Flow Rate(J_{melt}) (kg/sec)	0.027	0.032	0.038	0.038	0.038
Gas Flow Rate(J_{gas}) (kg/sec)	0.015	0.013	0.010	0.010	0.010
Exit gas velocity (V_{ge}) (m/s)	341	296	327	327	327

(a) The injection angle refers to the relative angle between the spray of SiC_p and the concentric vertical axis of the atomized matrix.

3.2.2. Light Microscopy

Light microscopy was conducted on polished and etched as-spray deposited samples taken from experiments 5, 10-13, using conventional optical microscopy and Differential Interference Contrast (DIC) microscopy; the use of DIC microscopy facilitated identification of the SiC_p in the matrix. Keller's reagent (0.5 HF-1.5 HCl-2.5 HNO₃-95.5 H₂O) was used in the present study to reveal the grain boundaries for microstructural analysis. The volume fraction of the SiC_p were quantitatively characterized using a Buehler Omnimet II Image Analyzer. The grain size was measured using the linear intercept method, as described in ASTM E 112-84.

3.2.3. Scanning Electron Microscopy (SEM)

SEM studies were conducted using a HITACHI S-500 microscope. The overspray powders collected after spray deposition were spread on an aluminum stub and gold coated. The overspray powder samples were then examined in secondary electron mode for microstructural details and for determining the number of SiC_p on the surface of the powders of different sizes.

3.2.4. Transmission Electron Microscopy (TEM)

Transmission electron microscopy (TEM) studies were conducted using JEOL 100C microscope at an operating voltage of 100 kV on SiC_p. The TEM studies were carried out in order to provide insight into the morphological characteristics of the SiC_p.

3.2.5. Steady State Temperature Determination

In order to determine the average temperature of the spray during impact and validate the numerical results, a thermocouple (Chromel - Alumel, Type K) was placed on the surface of the deposition substrate during experiments 11 and 13. The variation of temperature with time was then recorded using a Tracor Westronics Model 4030 strip chart recorder.

3.3. Results

3.3.1. Microstructural Characterization

The overall dimensions of the spray atomized and deposited preforms from the five experiments were approximately 360 mm in length, and 180 mm in width. The thickness of the preforms decreased from 50-75 mm in the center portion to approximately 5 mm at the periphery. All of the structural characterization studies conducted for the present study were performed on material removed from the central 80-90 % portion of the preforms (minimum thickness = 10 mm); the remaining 10-20 % of the preforms was considered too porous for detailed analysis.

Metallographic analysis was conducted on coupons of the spray deposited Al-Li, Al-Cu, Al-Li-SiC_p and Al-Cu-SiC_p materials; one example taken from experiment 5 is shown in Figure 28. The microscopy studies revealed the presence of equiaxed grains. This grain

morphology has also been reported by other investigators [36-38, 58, 63, 64, 71, 102, 103]. The results of the grain size measurements for experiments 5, 10-13 are shown in Table 15.

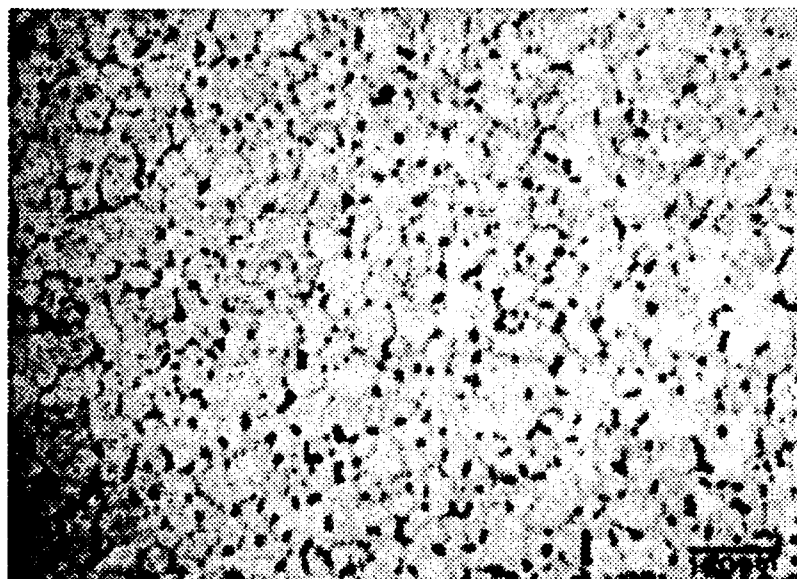


Figure 28. Optical micrograph showing equiaxed grain morphology of the spray deposited Al-Li-SiC_p sample taken from experiment 5.

Table 15. Results of Metallographic Analysis.

Experiment #	Droplet size ^(a) , d_{50} (μm)	Grain size (μm)	V_f of SiC _p ^(b) (%)
5	92	68 ± 2.2	5.3 ± 0.8
10	84	75 ± 3.2	--
11	57	36 ± 3.2	--
12	57	28 ± 1.2	8.4 ± 0.5
13	57	22 ± 2.2	16.5 ± 1.2

(a) These values of the droplet sizes were determined using the previously established numerical model (38).

(b) These values of the volume fraction were determined using quantitative metallography.

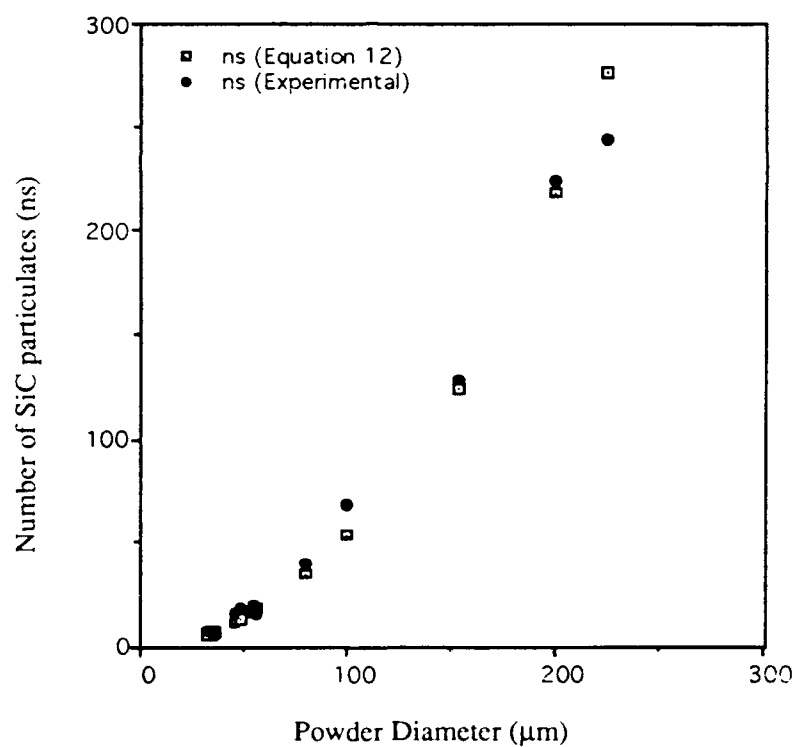
Regarding grain size, the present results show that the co-injection of ceramic particulates during spray atomization and co-deposition promotes grain refinement. This observation is consistent with the results of other investigators [31, 99, 117, 118, 122, 123]. It is worth noting, however, that the reduction in grain size observed in the present study for the SiC_p containing material for experiments 5 and 10 was approximately 9.3%, whereas it was approximately 22.2% for experiments 11 and 12 when compared to that of monolithic material. The relatively small difference in grain size between the reinforced and unreinforced materials observed in the present study between experiments 5 and 10 can be attributed to the higher gas atomization pressure and lower metal flow rate used in experiment 10, (1.36 MPa and 0.027 kg/sec) relative to that of experiment 5, (1.2 MPa, and 0.034 kg/sec) (see Table 14). As will be discussed in the results section, an increase in gas atomization pressure coupled with a decrease in the metal flow rate will effectively decrease the droplet size formed during atomization. The higher quench rate associated with a smaller droplet diameter will promote extensive solidification prior to impact with the deposition surface, with concomitant refinement in the spray deposited microstructure [31]. Hence, the use of a lower gas atomization pressure, and a larger metal flow ratio helped offset the quenching effect brought about by the presence of SiC_p.

Scanning electron microscopy of overspray powder samples revealed the presence of SiC_p on the surface of the powder samples (see Figure 29a). In order to determine the concentration of SiC_p present on the surface of the atomized powders, a large number of overspray powder samples were collected and studied in the SEM. The results are shown in Figure 29b where the experimental measurements are compared to those deduced from theoretical considerations (discussed further in the discussion section). The results shown in this figure suggest that there is strong correlation between the number of SiC_p present on the surface, and the powder diameter.

Transmission electron microscopy conducted on the SiC_p revealed the existence of a serrated surface morphology. The average depth of these serrations was found out to be approximately 0.05 μm . Figure 30 shows the typical morphological features of the SiC_p.



(a)



(b)

Figure 29. a) SEM micrograph showing the presence of SiC_p on the surface of overspray powders, and b) graphical representation of the number of SiC_p for various droplets sizes.



Figure 30. TEM micrograph showing the serrated surface morphology of SiC_p.

The temperature - time curves obtained from experiments 11 and 13 are shown in Figure 31. The results show that during deposition the steady state temperatures for unreinforced 2519 alloy (experiment 11) and reinforced 2519 alloy (experiment 13) were 733 K and 568 K, respectively.

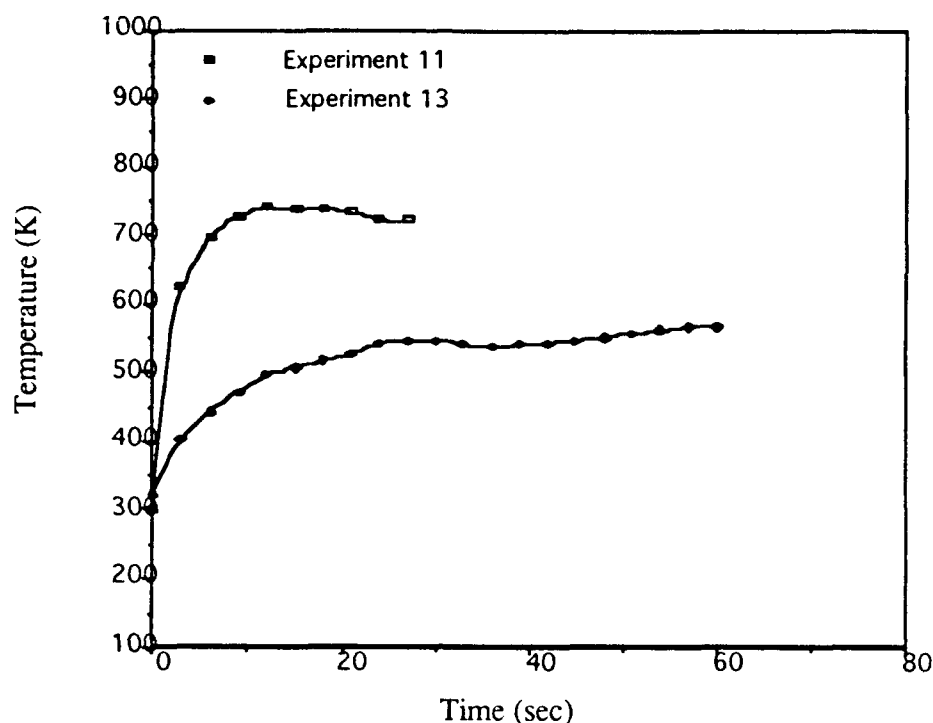


Figure 31. Graphical representation of temperature-time curves for unreinforced and reinforced 2519 alloy during spray atomization and co-deposition.

3.4. Discussion

The results of the present study show that the co-injection of ceramic particulates during spray atomization and co-deposition promotes a reduction in grain size. This phenomenon has also been noted by White et al. [117] and Kojima et al. [118], who report a decrease in grain size of up to 30% for an Al-Li-Cu-Mg-Zr alloy spray atomized and co-deposited with SiC_p and B₄C particulates, relative to that noted for the monolithic materials.

In view of the complex thermal, fluid and solidification phenomena involved during spray atomization and co-deposition, it is highly improbable that the observed reduction in grain size can be attributed to a single mechanism. Most likely, this phenomenon is a result of several non-linear effects brought about by the additional kinetic energy introduced into the metallic spray during co-injection of ceramic particulates. One approach that may be utilized to provide insight into the effects of the ceramic particulates on the microstructural evolution during spray atomization is to de-couple the thermal, fluid and solidification phenomena by considering three distinct mechanisms:

solidification effects, thermal effects and solid state cooling effects. The solidification and thermal effects will be discussed in more detail below while the solid state cooling effects will be discussed in Part II of this paper.

3.4.1. Solidification Effects

In order to provide insight into the effects of ceramic particulates on the solidification behavior of atomized droplets, it is necessary to consider first the thermal history of the droplets during co-injection. To that effect, several investigators [38, 71, 102] have studied the solidification and heat transfer phenomena during atomization, using numerical simulations. In these studies, the effects of processing variables on the droplet size distribution, droplet velocity, droplet positions, droplet temperatures, and dendrite arm spacings (DAS) were investigated. Although most of these models either incorporate a number of limiting assumptions, such as small Biot numbers, small undercoolings, etc., or are based on simplistic thermal energy arguments, i.e., enthalpy formulations, they can be used to provide some insight into fundamental solidification phenomena during atomization. On the basis of these investigations, and for processing parameters similar to those used in this study (see Table 14), one can deduce that the average aluminum droplet contains approximately 50% liquid at the time of co-injection of the ceramic particulates. It is anticipated that the transfer of kinetic energy during impact of SiC_p with an undercooled droplet during atomization may result in partial or full penetration of the SiC_p. Such an event may catalyze heterogeneous nucleation of the solid phase at the site of SiC_p. Recent experimental results[124] show such an effect for Al-Si alloys co-injected with SiC_p (see Figure 32). In addition, other investigators in related studies [125, 126] have proposed that there is a population of catalysts, which results from surface oxidation processes during atomization, that promote heterogeneous surface nucleation of the solid phase. In other studies, Gupta et al. [127] used X-ray diffractometry to show that a spray atomized and deposited Al-4.0 wt.% Ti material retained 0.88 wt.% Ti in solid solution, whereas the corresponding as-spray atomized and deposited Al-2.3 wt.% Ti-SiC_p material retained up to 1.13 wt.% Ti in solid solution. Although a systematic analysis of this phenomena was beyond the scope of this work, it was suggested that the increased excess solid solubility in the SiC_p containing material could be related to an acceleration in solidification kinetics during ceramic-droplet impact.

Therefore, it is likely that the presence of a distribution of SiC_p , and the ensuing catalytic effect on solidification mechanisms, will increase the volume fraction solidified during impact. This will effectively contribute towards the formation of a fine grained microstructure, by decreasing the overall enthalpy content of the atomized spray prior to impact with the deposition substrate. The catalytic effect of SiC_p on solidification kinetics is the subject of further study.

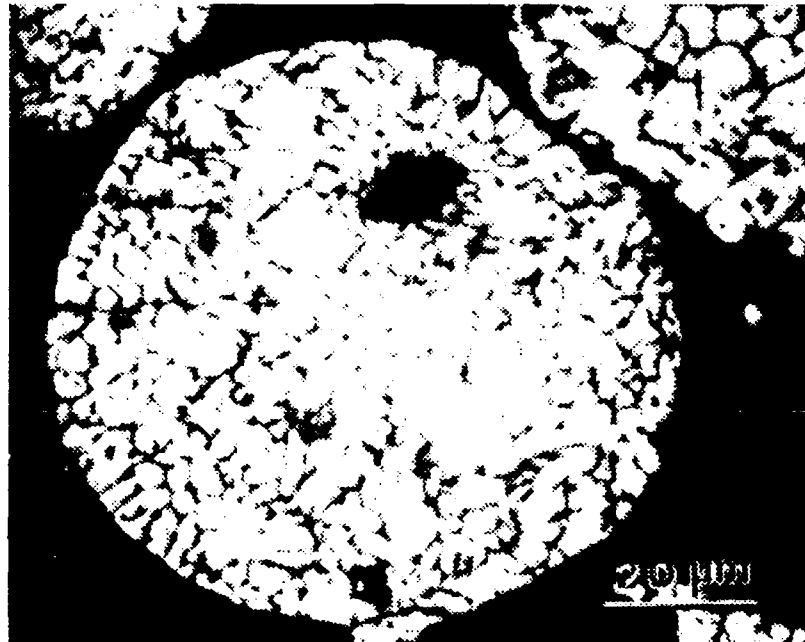


Figure 32. Optical micrograph showing a SiC_p initiating solidification event in a droplet of 6061 Al alloy [124].

3.4.2. Heat Transfer Effects

An important mechanism that is likely to affect the evolution of microstructure during spray atomization and co-deposition is the transfer of thermal energy from the atomized droplets to the ceramic particulates. In view of the fact that during ceramic injection, the droplet size distribution will be comprised of solid, semi/solid and liquid droplets, it is likely that the thermal effects will be closely linked to the solidification mechanisms discussed in the previous section. Nevertheless, the overall decrease in the enthalpy content of the spray brought about by the presence of ceramic particulates will affect the resulting microstructure.

In order to provide insight into the transfer of thermal energy during spray atomization and co-deposition, and its subsequent effect on microstructure, a heat transfer model was formulated for the present study. The degree of complexity associated with high spray densities necessitated the incorporation of a number of simplifying assumptions into the thermal and momentum equations. In particular, the treatment of an atomized spray as a collection of individual droplets, with no interactions among each other, is perhaps the most limiting. Nevertheless, from a conservation of thermal energy standpoint, the present results will provide insight into the effects of ceramic phases on the evolution of microstructure during impact with a deposition surface. The formulation of the model is divided into three interrelated sections: a) powder size distribution, b) heat transfer during atomization, and c) heat transfer during deposition. In the following sections, the governing equations are established, followed by a discussion of the results obtained with the experimental parameters used in the present study

3.4.2.1. Powder Size Distribution (see section 2.3.3 also). The disintegration of a molten metal by high energy inert gas jets (atomization) is complex, and only a few aspects of it has been addressed from a theoretical viewpoint [112]. The work of Lubanska [113] demonstrated that the disintegration of liquid by high velocity gas jets obeys a simple correlation. A slightly modified form of the original correlation was incorporated into the present model, and has been shown by other investigators [38, 72] to represent the results of molten metal atomization experiments reasonably well. According to the modified Lubanska's correlation, the mass mean droplet diameter (i.e., the opening of a screening mesh which lets through 50 percent of the mass of the powder result from an atomization experiment), d_{50} , is given by

$$d_{50} = k_d \left[\frac{\eta_m d_o \sigma_m}{\eta_g V_{ge}^2 \rho_m} \left(1 + \frac{J_{melt}}{J_{gas}} \right) \right]^{1/2} \quad (11)$$

where k_d is an empirically determined constant with a value between 40 and 400 (a value of 162 for Ar [38] and 51.7 for nitrogen was selected for the conditions used in the present study since this has been shown to yield a good correlation between theory and experiment). A detailed description of the symbols used in Eqn. (11) may be found in the Nomenclature section at the end of the paper. Expressions for the flow rates (J_{gas}) can be obtained as functions of the process parameters from Bernoulli's equation in the case of the metal [111] and from the theory of compressible flow [115] in the case of the gas. In

the present work, J_{melt} was determined experimentally by measuring the time required to empty the melting crucible. Other useful characteristic powder sizes, such as d_{16} and d_{84} , are readily calculated from d_{50} and information about the standard deviation, σ_g , of the (log-normal) size distribution function for the atomized powders, which is defined by

$$\sigma_g = d_{84}/d_{50} \quad (19)$$

where 84 and 50 in d_{84} and d_{50} represent 84% and 50% of the size distribution under this powder size.

The mass mean droplet diameter of the powder size distribution (d_{50}) was computed from Eqn. (11), using the processing parameters and physical constants corresponding to each experiment (see Tables 14 and 16). The results show that Eqn. (11) predicts a d_{50} value of 84 μm for experiment 10. In addition, the results obtained from Eqn. (19) in combination with experimentally determined values of the standard deviation [58, 63], showed that 16 cumulative weight percent of the distribution was under 23 μm , and 84 cumulative weight percent of the distribution was less than 390 μm .

Since the atomized spray will contain a distribution of droplets in the 23-390 μm size range, one can anticipate a mixture of solid, liquid, and mushy droplets during injection, and subsequently, during deposition. Therefore, the thermal analysis that follows will be accomplished by considering the d_{84} , d_{50} and d_{16} droplet sizes as representative of the entire Gaussian distribution of droplet sizes.

Table 16. Input Parameters Used in Numerical Model.

Variable	Description	Value	Units
C_{pg}	Specific heat of argon	518.8	J/kgK
C_{SiC}	Specific heat of SiC_p	0.963	KJ/kgK
H_f	Heat of fusion of Al	398	KJ/kg
k_m	Al thermal conductivity	209	W/mK
k_{SiC}	SiC thermal conductivity	12	W/mK
h	Heat transfer coefficient	1.676	KJ/m ² ° C sec
T_L	Liquidus temperature	654	° C
T_S	Solidus temperature	640	° C
ρ_m	Al density	2700	kg/m ³
ρ_{SiC}	SiC Density	3100	kg/m ³
γ	Ratio of C_p/C_v for gas	1.65	---
T_N	Nucleation temperature	645	° C
σ_m	Melt surface tension	0.840	kg/s ²
ρ_g	Gas density	1.8	kg/m ³
μ_g	Gas viscosity	1.7×10^{-5}	kg/m sec
μ_m	Melt viscosity	0.001	kg/m sec
d_{SiC}	Particulate Size	3×10^{-6}	m
D_{LM}	self diffusion coefficient	1.21×10^{-12}	m ² /sec
K_m	kinetic growth coefficient	0.02	m/sec K
δ	length of an interface step	4.05×10^{-10}	m
ΔT^*	undercooling	9	K

3.4.2.2. Heat Transfer During Atomization. Once the powder size distribution has been determined, it is possible to compute the droplet temperature and fraction solid as a function of flight distance. This was accomplished in the present study using a numerical model based on an enthalpy formulation, developed elsewhere [38, 72]. The main assumptions involved in the model were described in section 1.3.8.

This enthalpy model was applied to the conditions used in the present study (see Tables 14 and 16) to compute the temperature and fraction solid of the powder size distribution as a function of flight distance for both the Al-Li and Al-Li- SiC_p experiments. The enthalpy model (using lumped parameter formulation) of the droplet cooling and

solidification process can be described as follows. For the first stage (cooling of liquid droplet), the energy balance equation is:

$$\rho_m V_d dH(d_i)/dt = -A_d h (T_2 - T_0) - dQ/dt \quad (20a)$$

It can be shown that radiative losses (dQ/dt) are relatively small and can be neglected, particularly in the case of the lower melting point materials [38, 72, 128, 129]. The heat transfer coefficient, h , can be estimated from the standard Ranz-Marshall correlation [130]. Once the droplet enthalpy has been calculated from Eqn. (20a), the droplet temperature is calculated from:

$$T = (H(d_i) - H_f) / C_p + T_L \quad (20b)$$

The appearance of the first nucleus of solid inside the droplet marks the beginning of the second stage of the droplet quenching process. In order to simplify the analysis, the model makes the assumption that a single nucleus forms in the center of the droplet and grows radially thereafter. In order to incorporate undercooling effects into the calculations, it was necessary to introduce two additional parameters from crystal growth kinetics [131] in the model which are difficult to measure and must be estimated; these are the nucleation temperature and the kinetic growth coefficient. In the model, the variation in fraction solid, f_s , with temperature was calculated from the kinetic relationship between growth rate, R , and undercooling, ΔT^* , originally proposed by Coriell and Turnbull [132]:

$$R = K_m \Delta T^* \quad (20c)$$

where K_m is a kinetic growth coefficient, given by:

$$K_m = \beta (D_{LM}/\delta) (H_f/R T_L^2) \quad (20d)$$

where β is a factor introduced by Cahn et al.[133] whose value varies from 1-100. Eqn. (20c), also known as the "linear growth rate law", represents a special case of the kinetic relationship originally developed by Coriell and Turnbull [132] in which the steady state continuous growth of a planar front is an exponential function of the undercooling. The validity of Eqn. (20c) is limited to cases involving small to moderate undercoolings.

Depending on the value of the kinetic growth coefficient, K_m , the droplet temperature may or may not reach the liquidus temperature at the end of recalescence [38, 72].

The volume fraction solidified, f_s , is readily calculated, once the nucleus radius has been determined and the instantaneous enthalpy and temperature of the droplet are calculated, from:

$$dT/dt = (H_f / C_p) df_s/dt - A_d h (T_2 - T_0) / \rho_m V_d C_p \quad (20e)$$

Finally, in the third (solidification after the end of recalescence) and fourth stages (solid state cooling) the droplet temperature and volume fraction are computed from the total enthalpy content at a particular temperature. A more thorough discussion on the thermal and solidification behavior during the last two stages can be found elsewhere [38, 72, 129, 134].

The computed temperature and solid fraction of the droplet size distribution, at the SiC_p injection distance and at the deposition surface, are shown in Figure 33 and 34, respectively for experiment 5. The results shown in these figures were computed for droplet sizes corresponding to the 30-390 μm range. The results shown in Figure 33 and 34 indicate an increase in temperature and a decrease in fraction solid, with powder diameter, both at the SiC_p injection distance as well as at the deposition distance. It is important to note, however, that the results shown in these figures do not incorporate the effects associated with SiC_p injection.

Once the droplet temperature is known, the thermal energy content of the atomized spray can be computed. The specific heat of the matrix material (aluminum alloy), C_p (kJ/kg), can be calculated from [135]

$$\begin{aligned} C_p &= 0.7661 + 0.46145 \times 10^{-3} T & T \leq 933.2 \text{ K} \\ C_p &= 1.086 & T \geq 933.2 \text{ K} \end{aligned} \quad (21)$$

It must be noted that equations shown above for the calculation of specific heat are primarily meant for pure Al. These equations are used in the present study since similar information for the Al-Li or Al-Cu alloys used in the present study was not available in

the literature. In addition, the effect of segregation during solidification and its influence on the computations of specific heat are ignored in the present calculations.

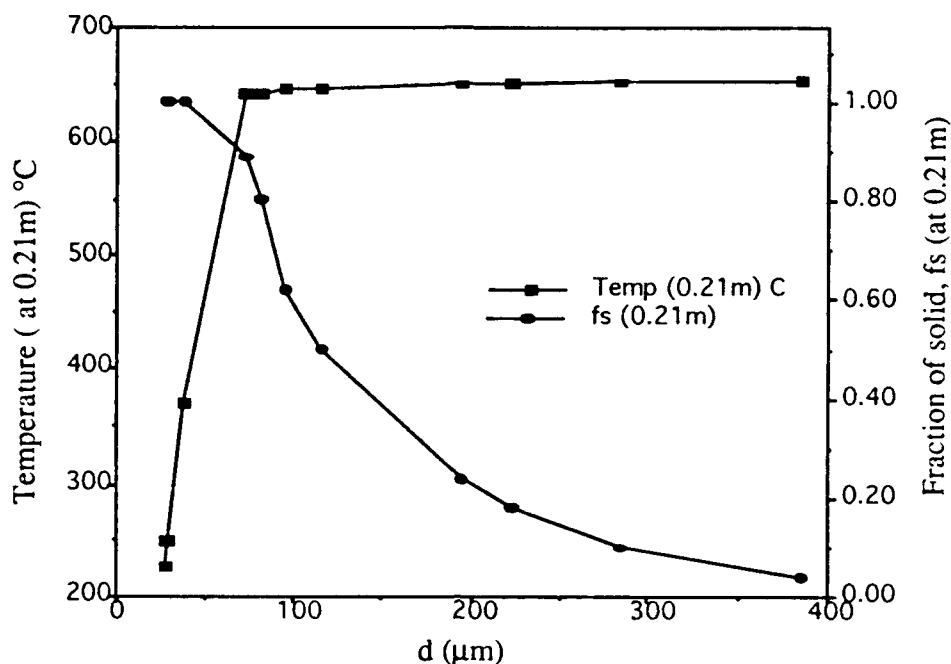


Figure 33. Graphical representation of the thermal and solidification history of the droplet size distribution at the SiC_p injection distance.

It then follows that the total thermal energy per unit mass of a single droplet, $H_{\text{droplet/kg}}$, can be obtained from

$$H_{\text{droplet/kg}} = f_s C_p \Delta T + f_l \Delta H_f + f_l C_p \Delta T \quad (22)$$

Since $f_s + f_l = 1$, Eqn. (5) can be expressed as

$$H_{\text{droplet/kg}} = \int_{T_l}^T C_p dT + f_l \Delta H_f \quad (23)$$

Hence, from Eqn. (23), the heat content of the droplet of mass, $m(d_i)$ can be computed from

$$H(d_i) = H_{\text{droplet}} = m(d_i) \left(\int_{T_1}^T C_p dT + f_l \Delta H_f \right) \quad (24)$$

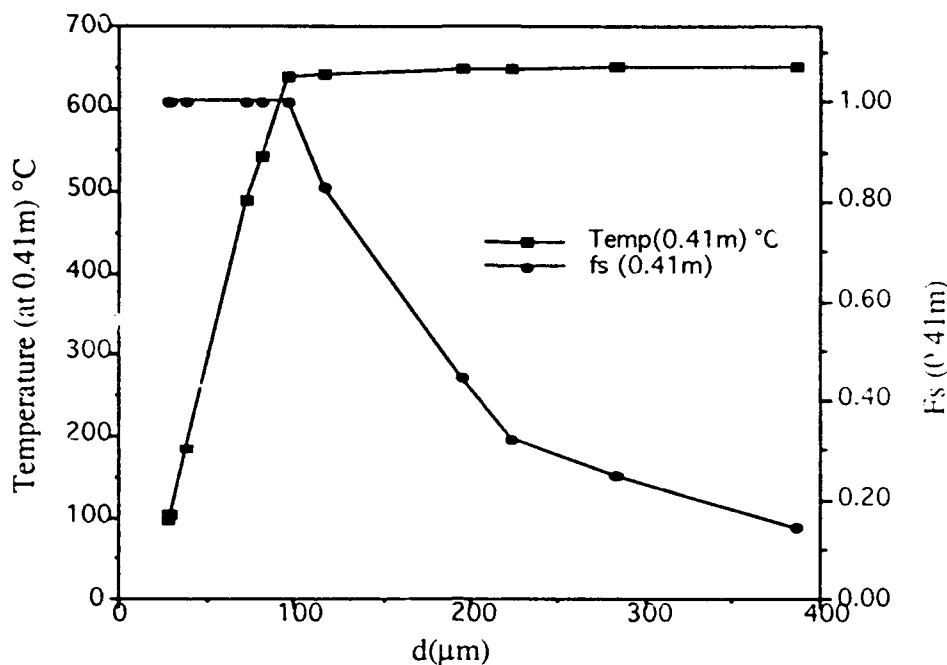


Figure 34. Graphical representation of the thermal and solidification history of the droplet size distribution at the deposition surface.

The total enthalpy of the atomized spray at any spatial location, can be computed from information on the droplet size distribution as

$$H_{\text{spray}} = \sum n(d_i) H(d_i) \quad (25)$$

In Eqn. (25) the number of droplets of diameter d_i , $n(d_i)$ can be calculated from

$$n(d_i) = \frac{m_{\text{metal}} \cdot f(d_i)}{m_{\text{droplet},i}} \quad (26)$$

Therefore, the total number of droplets for a given distribution, N , can be calculated as

$$N = \sum n(d_i) \quad (27)$$

Similarly, the number of SiC_p can be calculated from

$$n_{(\text{SiC})} = \frac{\text{wt \% SiC} \cdot m_{\text{deposit}}}{100 \times m_{\text{SiC}}} \quad (28)$$

The number of SiC_p in intimate contact with a matrix droplet, n_s , can be computed from

$$n_s = \frac{0.5 A_f A_d}{A_s} \quad (29)$$

The results obtained using Eqn. (29) were found to be in excellent agreement with those determined experimentally, as shown in Figure 29b.

Once the number of SiC_p in contact with one matrix droplet has been determined, and assuming Newtonian conditions (i.e., the temperature gradient within the droplet is negligible [38, 72]), the overall rate of conductive heat transfer, \dot{q}_r , can be computed from

$$\dot{q}_r = U A (T_2 - T_1) \quad (30a)$$

The value of overall heat transfer coefficient, U , used in Eqn. (30a) can be obtained from

$$U = 1 / (L_d / K_a + L_{\text{SiC}} / K_{\text{SiC}}) \quad (30b)$$

Eqn. (30b) takes into consideration the serrated surface associated with SiC_p (see Figure 30). The voids/facets present will lead to the formation of cavities when the SiC_p attaches itself to the droplet. The cavities thus formed at the interface will contain the atomizing gas or the carrier gas. The presence of the atomizing gas/carrier gas at the interface between the droplet and the particulate will affect the heat transfer from the droplet to the SiC_p . It is hence expected that the physical properties of the atomizing gas/carrier gas will have an influence on heat transfer between droplet and SiC_p .

In order to determine the magnitude of the overall heat transfer of thermal energy, one must consider in detail the effects of the SiC_p on the surface of the droplets. The SiC_p will have two opposite effects on the transfer of thermal energy from the matrix droplets. On the one hand, since the ceramic particulates are injected at room temperature, a

portion of the thermal energy losses can be accounted for by considering conductive heat transfer from the droplet to the particulates. On the other hand, however, the presence of ceramic particulates on the surface of the atomized droplets will inhibit convective heat transfer from the droplets to the atomization gas. Therefore, it is necessary to compensate for the rate of conductive heat transfer \dot{q}_r , computed from Eqn. (30). This can be achieved by subtracting the value of the effective convective heat transfer due to the presence of SiC_p, \dot{q}_e , from the rate of conductive heat transfer, \dot{q}_r . The effective convective heat transfer due to the presence of SiC_p, \dot{q}_e , can be computed from

$$\dot{q}_e = h A (T_2 - T_1) \quad (31)$$

In Eqn. (14) the heating of the particulate was neglected due to the cooling effect associated as a result of high velocity of atomizing gas (see Table 14).

In turn, one can take the value of \dot{q}_r and \dot{q}_e and multiply it by the time of flight t , as determined from

$$s = u(d_i) \cdot t + \frac{1}{2} g \cdot t(d_i)^2 \quad (32)$$

and compute the total thermal energy transferred from the atomized droplets to the ceramic particulates, during flight.

The velocity of the droplet at any flight distance can be calculated from momentum considerations as discussed by Gutierrez et al [38].

$$\rho_d V_d \frac{dv_d}{dt} = V_d (\rho_d - \rho_g)g + (A_d/8) C_{drag} \rho_g (v_g - v_d) |(v_g - v_d)| \quad (33a)$$

where

$$C_{drag} = 0.28 + 6/N_{Re}^{0.5} + 21/N_{Re} \quad (33b)$$

The two terms on the right hand side of Eqn. (33a) represent, respectively, the gravitational force acting on the droplet and the accelerating force exerted on the droplet by the atomizing gas. The equation used to determine C_{drag} was obtained from correlations available elsewhere [136].

Therefore the total amount of thermal energy lost by the atomized droplets to the SiC_p, $Q(d_i)(SiC, flight)$, is given by

$$Q(d_i)_{(SiC, flight)} = \dot{q}_r t_{(di)} n_s - \dot{q}_e t_{(di)} n_s \quad (34a)$$

$$Q(d_i)_{(SiC, flight)} = (\dot{q}_r - \dot{q}_e) t_{(di)} n_s \quad (34b)$$

It must be noted that the average velocity of the SiC_p was experimentally determined (on the basis of the flow rate) to be ~ 63 m/sec using the present co-injection conditions. The kinetic energy (K.E. = 0.5 x m_{SiC} x v_{SiC}²) imparted by a single SiC_p (d₅₀ = 3 μm) to a droplet of size 84 μm (T = 916 K) at the injection point was computed to be 8.70 x 10⁻¹¹ J. The magnitude of the total kinetic energy (n_s = 42; K.E. = 3.65 x 10⁻⁹ J) will give rise to a temperature differential (ΔT) of ~3.66 x 10⁻³ K. In view of such a small temperature increase the heat-up of the droplets due to the absorption of kinetic energy from the particulates may be safely ignored in the present study.

The total amount of thermal energy transferred during flight, Q_{Total}, can be calculated as

$$Q_{Total} = \sum Q(d_i)_{(SiC, flight)} n(d_i) \quad (35)$$

It must be noted that Eqns. (21-35) were used in the present study to isolate the effect associated with SiC_p in transferring the thermal energy from the droplets. The convective heat losses from the droplets were calculated using a model described elsewhere and briefly summarized in Eqns. (20a-20e) [38, 128-134]. The results shown in Figures 33 and 34 incorporates the convective heat loss to the atomizing gas.

3.4.2.3. Heat Transfer During Deposition. In the previous section, a methodology has been described which can be used to compute the thermal energy dissipated by the SiC_p, prior to impact with the deposition surface. In this section, we intend to describe the second part of the mathematical model, namely the thermal behavior after deposition and impact. The total thermal energy content of the spray at the moment of impact with the deposition surface can be computed taking into account Eqn. (25). It is worth noting, however, that the temperature and fraction solid of the powder size distribution at the deposition point will be substantially different as compared to the conditions present during injection of the SiC_p.

The amount of thermal energy required to bring the SiC_p to the deposit temperature can be calculated from

$$Q_{\text{SiC}} = \frac{\text{wt. \% SiC}}{100} \cdot m_{\text{deposit}} C_{\text{SiC}} [T_d - T_1] \quad (36)$$

It then follows that the percentage of thermal energy dissipated by the SiC_p , using the aforementioned assumptions, can be calculated as

$$\% Q_{\text{Deposition}} = \frac{Q_{\text{SiC}}}{H_{\text{spray, deposition}}} \times 100 \quad (37)$$

It must be noted that while calculating the deposit temperature, the enthalpy of the spray in presence of SiC_p , $H_{\text{spray, SiC}}$, was used at the deposition distance, which incorporates the heat loss from the droplet as a result of convection (atomizing gas) and due to the presence of SiC_p .

3.4.3. Numerical Results

A mathematical representation has been developed in the present study to quantify the changes in thermal energy of an atomized droplet distribution derived from the presence of a distribution of randomly mixed ceramic particulates. The first part of the model computes the thermal energy of the atomized droplet during flight, whereas the second part addresses the transfer of thermal energy after impact and deposition.

In computing the number of SiC_p in intimate contact with a matrix droplet (Eqn. (29)), it was assumed that only half of the surface area of the droplet is covered by SiC_p . The computed number of particulates per droplet, n_s , was found to be in good agreement with experimental results obtained from scanning electron microscopy observations of the overspray powders (see Figure 29). It is further assumed in Eqn. (29) that complete penetration of the ceramic particulates into the metallic matrix does not occur readily, and therefore some proportion of the area of the particulate will be exposed to the atmosphere. This appears to be reasonable on the basis of a simple comparison of the impact force of the ceramic particulates per unit distance ($6.50 \times 10^{-4} \text{ N/m}$) to the surface tension of the droplets (0.914 N/m). The overall heat transfer coefficient used in Eqn. (30a) was estimated as $6.70 \times 10^5 \text{ J/sec m}^2 \text{ K}$ considering the thermal conductivity of the particulate / particulate-metal interface as a series resistance [137].

There are some comments in order regarding the calculation of thermal energy transfer during deposition, as discussed in Section 4.2.3. In computing the transfer of thermal energy required to bring the SiC_p to the deposit temperature, radiative energy losses to the environment, and conductive heat transfer into the water cooled substrate were ignored. This assumption is supported by the experimental [106] and computational [38, 71, 72] results of other investigators, which show that the cooling rates during the solidification of the deposit were on the order of 1-10 °C/second, and therefore, the rate at which thermal energy is lost to the environment will be relatively slow as compared to the rate at which thermal equilibrium is achieved within the deposit. Moreover, the radiative energy losses to the environment and conductive heat transfer to the water cooled substrate will be common to both unreinforced and reinforced materials.

Regarding the transfer of thermal energy to the SiC_p, the results given in Table 17 and Figures 35-36 show that co-injection of 10 volume fraction of SiC_p decreases the total enthalpy during flight (i.e., prior to impact with the deposition surface) by 10%. Furthermore, the results also show that 10% of the thermal energy available after impact will be consumed during the process of equilibrating the temperature of the SiC_p with that of the spray deposited material. Regarding the effect of volume fraction of reinforcement on the transfer of thermal energy, the results shown in Figures 36-37 suggest an almost linear trend. In related studies^[38] it has been shown that the grain size of the spray deposited material decreases with increasing volume fraction of reinforcement (see Tables 15 and 18). These results, in combination with the present experimental findings summarized in Table 15, suggest that the presence of a distribution of ceramic particulates during spray atomization and co-deposition leads to a reduction in grain size. Furthermore, the results of the numerical model described in this paper suggest that this decrease in grain size may be partially attributable to the transfer of thermal energy from the atomized droplets to the co-injected ceramic particulates.

Experimental support to this suggestion is provided by the temperature profiles obtained during experiments 11 and 13 (conducted utilizing identical processing parameters) as shown in Figure 31 . These results show that the average temperature during deposition of the SiC_p containing material was substantially lower than that recorded during deposition of the unreinforced material.

Table 17. Results of Heat Transfer Computations for Reinforced and Unreinforced Al-Li Material.

	Flight distance		
	0.21 m ⁽¹⁾	0.41 m ⁽²⁾	After deposition
Spray Enthalpy (kJ/kg) (Al-Li material)	1230	1094	—
Spray Enthalpy (kJ/kg) (Al-Li-SiC _p material)	1230	968	871
Percent heat transferred due to the presence of SiC _p		10 %	10 %
(1) SiC _p injection distance			
(2) Deposition distance			

Table 18. Volume Fraction of Reinforcement and Corresponding Grain Sizes for Spray Atomized and Co-deposited 6061 Al Alloy [124].

Matrix material	SiC _p size (μm)	Volume fraction (V _f , %)	Grain size (μm)
6061	----	----	33.6 ± 9.9
6061	3.0	2.6 ± 0.3	25.5 ± 6.0
6061	3.0	5.2 ± 0.2	22.5 ± 6.6
6061	3.0	11.5 ± 1.7	20.5 ± 5.5

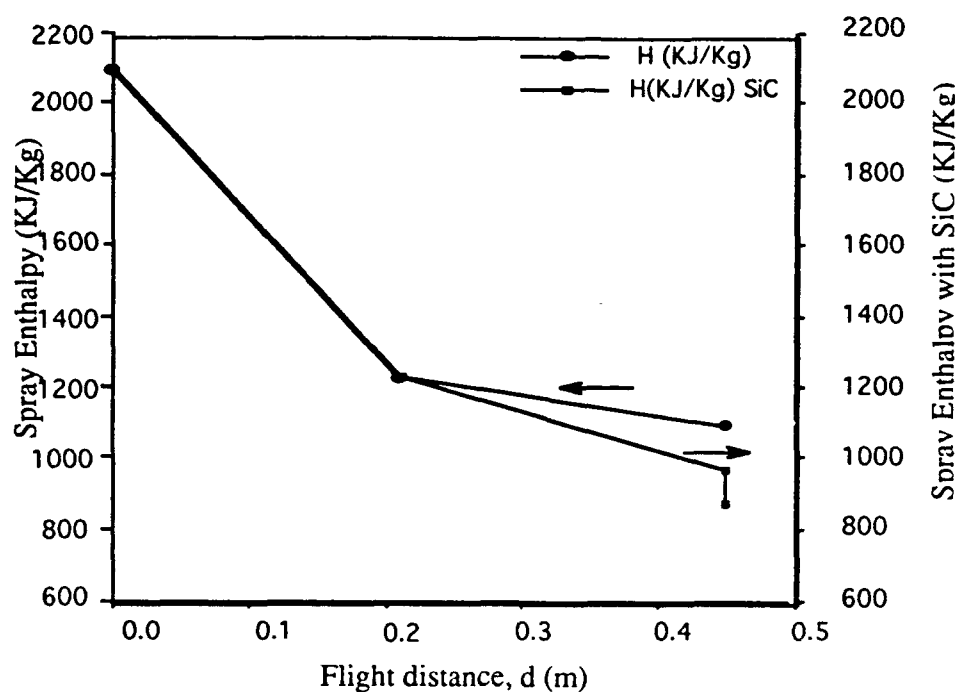


Figure 35. Graphical representation of the effect of SiC_p on the heat transfer during spray atomization and co-deposition of Al-Li- SiC_p metal matrix composites.

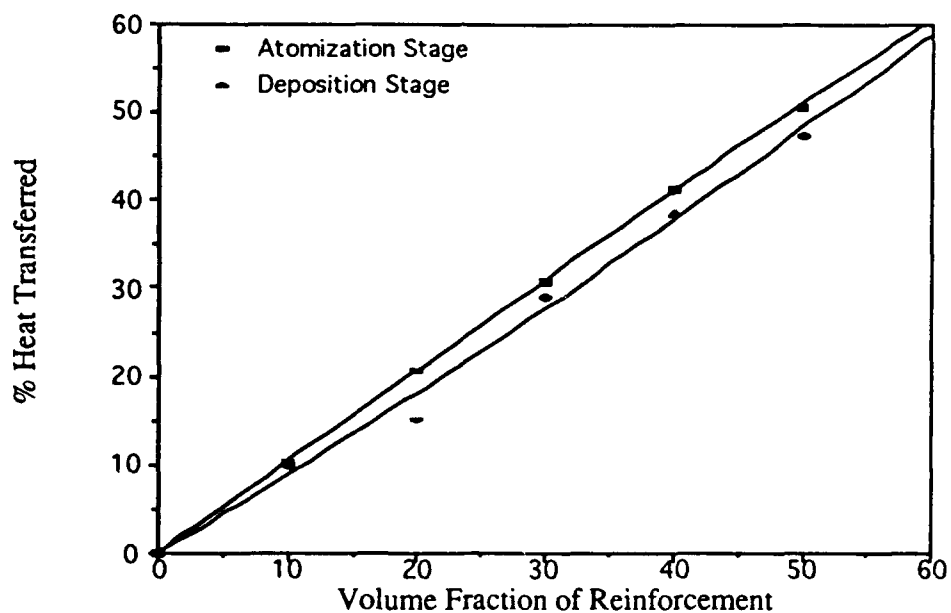


Figure 36. Graphical representation of the effect of volume fraction of SiC_p on the heat transferred during atomization stage and deposition stage of Al based metal matrix composites.

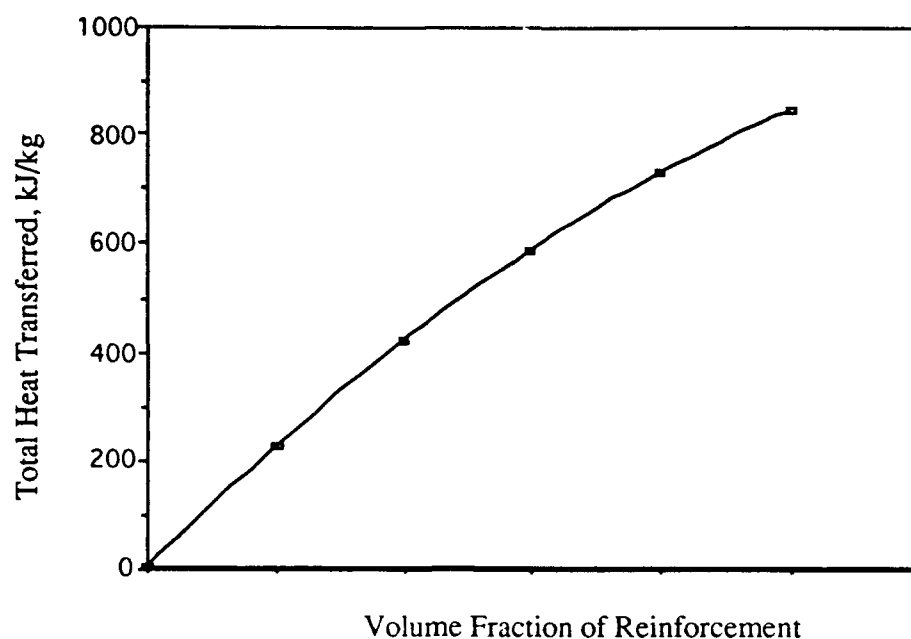


Figure 37. Graphical representation of the effect of volume fraction of reinforcement on the total heat transferred during spray atomization and co-deposition of Al based metal matrix composites.

3.5. Conclusions

The primary conclusions that may be drawn from this work are as follows:

1. The observed decrease in grain size which results from the co-injection of ceramics during spray atomization and deposition is influenced by the transfer of thermal energy from the atomized droplets to the co-injected ceramic particulates.
2. Numerical analysis of the transfer of thermal energy shows that co-injection of a distribution of SiC_p decreases the average enthalpy during flight (i.e., prior to impact with the deposition surface) by 10%. Furthermore, the results also shows that 10% of the thermal energy available after impact will be consumed during the process of equilibrating the temperature of the SiC_p with that of the spray deposited material.
3. Finally, further work is required in order to determine the effects of the ceramic particulates on the solidification mechanisms during atomization.

CHAPTER 4

4.0 The Effect of Ceramic Reinforcements During Spray Atomization and Co-Deposition of Metal Matrix Composites: Part II. Solid State Cooling Effects

4.1. Introduction

In Chapter 3 [138], it was demonstrated that the co-injection of ceramic particulates during spray atomization and co-deposition promotes a reduction in grain size. In order to provide insight into the effects of the ceramic particulates on microstructural evolution, a model was formulated [138] to account for the transfer of thermal energy from the atomized matrix to the ceramic particulates during two stages: a) atomization and b) deposition. The numerical results obtained using SiC_p in an aluminum matrix show that 10% of the enthalpy of the atomized spray is transferred to ceramic particulates during atomization, whereas 10% of the thermal energy available after deposition will be consumed in the process of equilibrating the temperature of the particulates to that of the matrix. In addition, solidification effects were also considered [124], although a thorough study of this phenomenon was outside of the scope of the work.

In the present study, the effects of SiC_p on the microstructure during solid state cooling (e.g., after the matrix/particulate mixture has arrived on the substrate) were investigated with particular emphasis on the rate of grain growth. To identify the role of SiC_p during grain boundary migration, the reinforced and unreinforced materials were exposed to various isothermal heat treatments.

4.2. Experimental Procedure

The details of the processing and the microstructural analysis were described in Chapter 3 [138]; other relevant details are given below.

4.2.1. Thermomechanical Treatment

Following spray atomization and co-deposition, thermal treatment was conducted on as-spray deposited, and spray deposited and hot extruded samples of reinforced and unreinforced Al-Li materials. The extrusion step was accomplished using an 82.7 MPa press at a temperature of 400 °C and with an area reduction of 16:1. The extrusion step was used in the present study in order to close the micrometer size porosity normally associated with spray atomized and deposited materials [31-35, 117, 118, 123]. Following spray atomization and co-deposition, samples from experiments 5 and 10 were isochronally annealed at 400 °C and 600 °C for time intervals up to 100 minutes in order to study the effects of temperature and time, on grain growth. In order to restore the grain

size obtained after extrusion to that obtained immediately after spray deposition, as-spray deposited and hot extruded samples from experiments 5 and 10 were given a normalizing treatment, which consisted of thermal annealing at 400 °C for 40 and 30 minutes, respectively before being annealed further at 400 °C and 600 °C. Finally, as-spray deposited samples from experiment 11 were annealed at 400 °C for 100 minutes in order to study the segregation of constituent elements and the presence of precipitated phases in regions adjacent to porosity.

4.2.2. Scanning Electron Microscopy (SEM)

SEM studies were conducted using a HITACHI S-500 microscope. The samples were sectioned to a thickness of 0.5 cm and mirror polished using conventional techniques. The polished samples were then examined in secondary electron mode for microstructural details; point analysis was carried out at selected regions of the sample surface to detect the presence of constituent elements.

4.3. Results

4.3.1. Microstructural Characterization

In order to characterize the size, distribution, and location of SiC_p in the Al-Li matrix, image analysis was conducted on a number of samples taken from experiment 5. The size and distribution of the SiC_p obtained from image analysis were then used to compute the SiC_p interparticulate spacing according to the formula discussed by Nardone and Prewé [7]

$$\lambda = (\ell t / V_f)^{1/2} \quad (10)$$

where λ is the interparticulate spacing; and t , ℓ and V_f are the thickness, length, and volume fraction of the SiC_p, respectively (see section 2.3.2.2 also). For the present case, the dimensions of SiC_p is characterized by the equivalent diameter, d . The value of λ , was calculated by assuming $\ell=t=d$ [139]; this assumption is reasonable in view of the equiaxed geometry of the particulates. The results of the image analysis and the computed interparticulate spacings, λ , for experiment 5 are shown in Table 19.

Scanning electron microscopy of samples removed from the central portion of the spray deposited material from experiment 11 revealed the presence of a finite amount of unconnected porosity (see Figure 38). The micron sized pores were preferentially located

Table 19. Results of Image Analysis of Al-Li-SiC_p Composite.

Sample # ^(a)	Equivalent Diameter(μm) ^(b)				Volume Fraction ^(c) (%)				Interparticulate Spacing ^(d) (λ , μm)
	Min.	Max.	Mean	σ	Min.	Max.	Mean	σ	
#5 A	0.57	09.00	2.70	2.01	1.92	08.33	3.49	1.82	14.48
#5 B	0.57	10.00	2.71	2.10	2.89	06.15	4.56	1.13	12.69
#5 C	0.57	12.00	2.10	1.76	4.40	13.44	7.89	1.91	07.48

(a) A, B, C designations refer to top, center and bottom regions, respectively, of the spray deposited Al-Li-SiC_p.

(b) The equivalent diameter is a measure of the size of the SiC_p.

(c) These values of the volume fraction were determined using quantitative metallography.

(d) These values were computed from Eqn. (10).

at the grain boundaries, and exhibited an irregular, faceted morphology. The distribution of pores in the as spray deposited microstructure was found to be bimodal, with a large proportion of pores in the 1-2 μm and 6 μm size ranges. In addition, the results of the scanning electron microscopy also reveals the evidence of precipitation at the free surface of the porosity (see Figure 39) in the as spray deposited sample taken from experiment 11. The results of elemental point analyses conducted on the porosity and at 2 and 10 μm from the porosity after thermal exposure of the samples at 400 °C for 100 minutes, are shown in Figure 40.

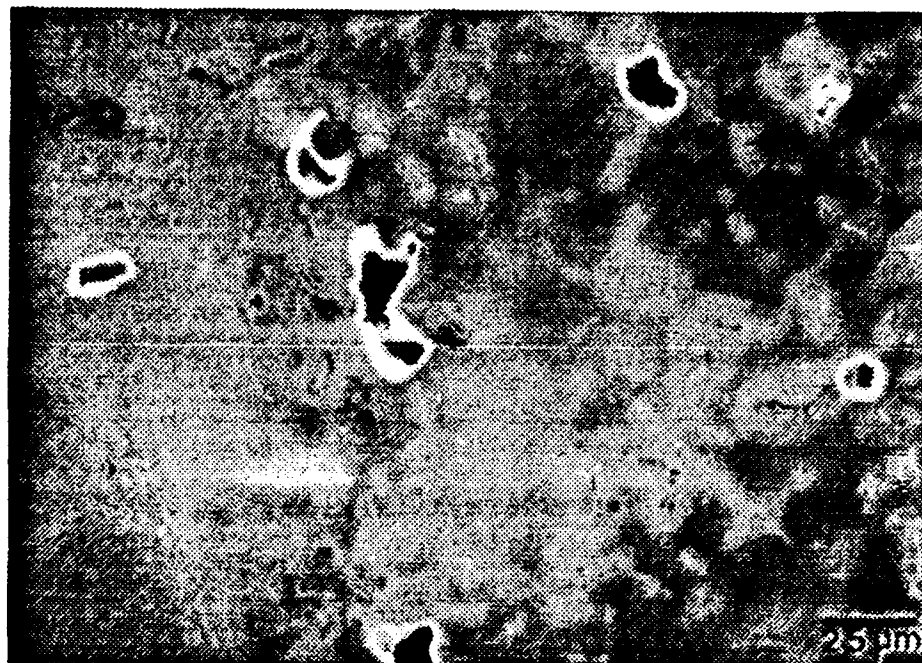


Figure 38. SEM micrograph showing the presence of unconnected porosity in the as-spray deposited sample taken from experiment 11.



Figure 39. SEM micrograph showing the evidence of precipitation at the free surface of the porosity in the as-spray deposited sample taken from experiment 11.

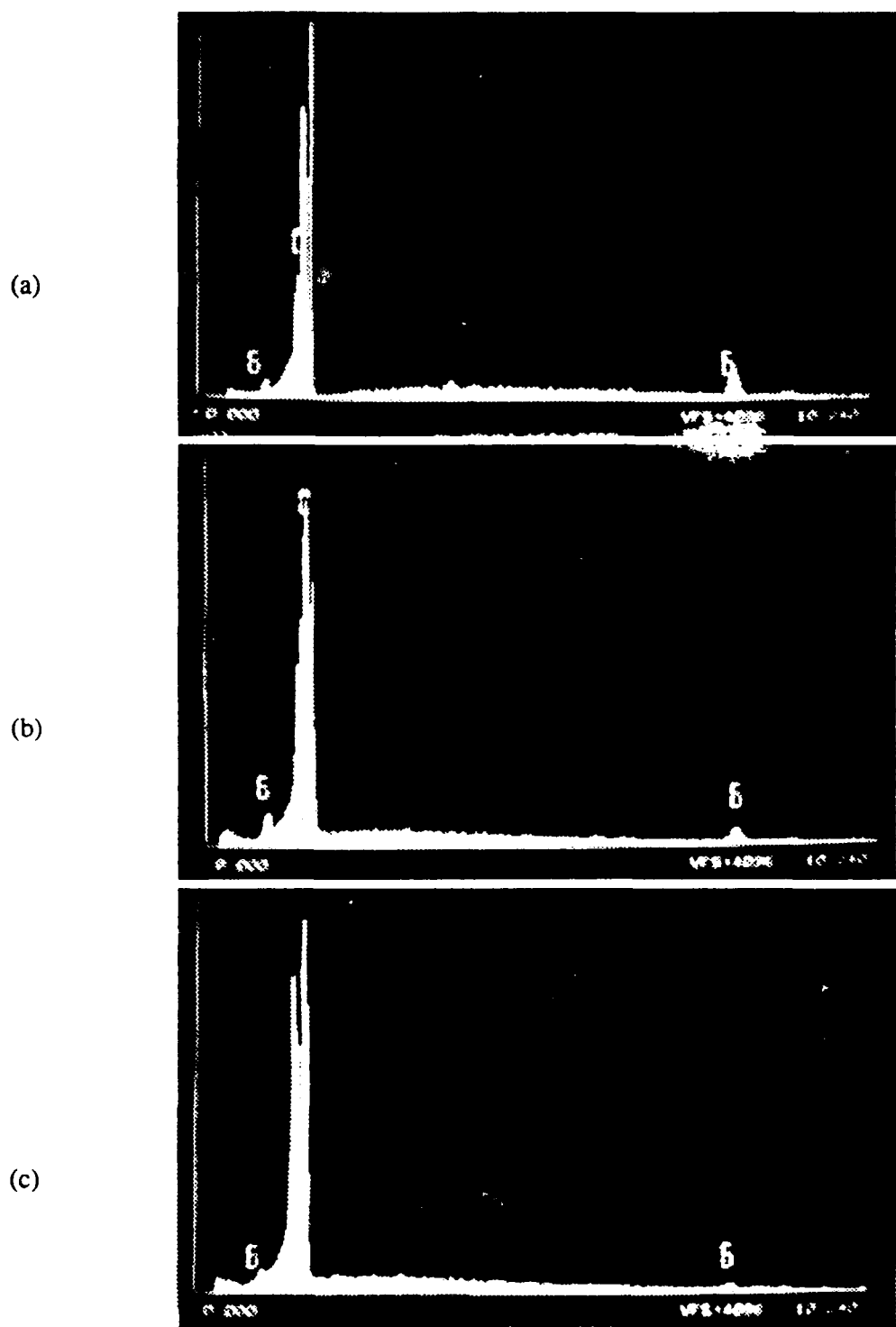


Figure 40. Results of the EDAX point analyses conducted at various locations in the spray deposited Al-Cu material: a) inside a pore, b) 2 μm from a pore and c) 6 μm from the pore.

Metallographic analysis was conducted on coupons of the spray deposited Al-Li, Al-Cu, Al-Li-SiC_p and Al-Cu-SiC_p materials. The microscopy studies revealed the presence of equiaxed grains. This grain morphology has also been reported by other investigators [36, 37, 58, 63, 64, 102, 103, 140]. A more thorough discussion regarding the equiaxed grain formation was described in section 1.4.2.

4.3.2. Grain Growth Behavior

In order to provide insight into the effects of the SiC_p on the microstructure during solid state cooling, grain growth studies were conducted on the samples taken from experiments 5 and 10. The grain sizes were determined using the linear intercept method after isochronal anneals at 400°C and 600°C (see Table 20 and Figure 41). The results of grain size measurements shown in Figure 41 indicate a logarithmic trend of grain

Table 20. Results of the Grain Size Measurements for Different Intervals of Time and Temperature for As Spray Atomized and Deposited Samples of Al-Li and Al-Li-SiC_p Materials.

Material	Al-Li/400°C	Al-Li-SiC _p /400°C	Al-Li/600°C	Al-Li-SiC _p /600°C
Time (min)	Grain size (μm)	Grain size (μm)	Grain size (μm)	Grain size (μm)
0 ^a	75.0 ± 3.2	68.0 ± 2.2	75.0 ± 3.2	68.0 ± 2.2
1	76.0 ± 4.1	70.0 ± 2.1	140.0 ± 8.5	81.0 ± 4.5
10	79.0 ± 4.8	75.0 ± 2.4	152.0 ± 9.5	88.0 ± 4.7
50	145.0 ± 8.2	92.0 ± 2.4	230.0 ± 8.9	101.0 ± 2.8
100	175.0 ± 9.8	95.0 ± 1.4	261.0 ± 5.2	110.0 ± 8.2

^a time 0 refers to as-spray deposited grain size.

growth with time for both the Al-Li and Al-Li-SiC_p materials. Not unexpectedly, it can be seen that the rate of grain growth of the Al-Li-SiC_p material at 400°C and 600°C is lower than that of the Al-Li material. The microstructure of both the as-spray deposited binary Al-Li alloy and the SiC_p reinforced Al-Li alloy consisted of equiaxed grains, before and after the isochronal heat treatments (see Figures 42-43).

The results of grain growth studies conducted on as-spray deposited and hot extruded samples of the Al-Li and Al-Li-SiC_p materials are summarized in Table 21. The results presented in this table show that at 400 °C the rate of grain growth of the Al-Li-SiC_p material was higher than that observed for the Al-Li material, while this trend was reversed at 600 °C. It is worthwhile noting that the as-spray deposited and hot extruded samples were given a normalizing treatment, following the hot extrusion, in order to restore the initial grain size (see Table 21) to that obtained after spray deposition (see Table 21), and thereby provide a valid comparison; this normalizing treatment was described in the experimental section. In order to gain some insight into the effects of porosity on grain growth, the results in Tables 20 and 21 show that the presence of porosity retards grain growth in the SiC_p containing material whereas the presence of porosity either increases (400 °C) or has no significant effect (600 °C) on grain growth on unreinforced Al-Li samples exposed for more than fifty minutes. Not unexpectedly, however, a monotonic increase in grain size with temperature was noted for all samples, regardless of the presence of porosity (see Tables 20 and 21).

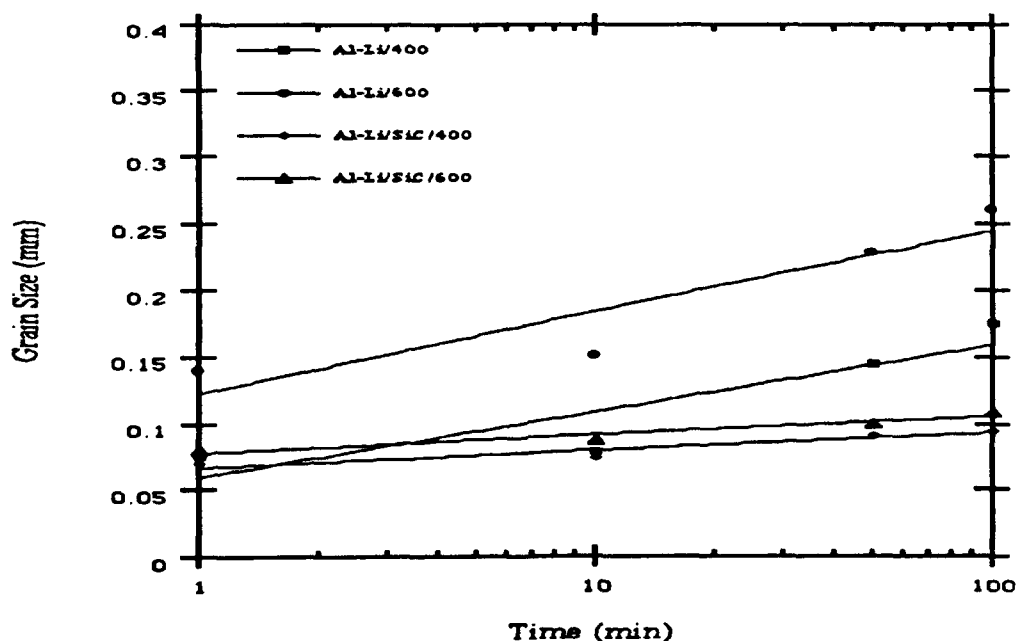


Figure 41. Graphical representation of the logarithmic grain growth relationship observed in as-spray deposited Al-Li and Al-Li-SiC_p metal matrix composites.



Figure 42. Optical micrograph showing equiaxed grain morphology of a spray deposited Al-Li sample taken from experiment 10, heat treated at 400°C for 100 min.

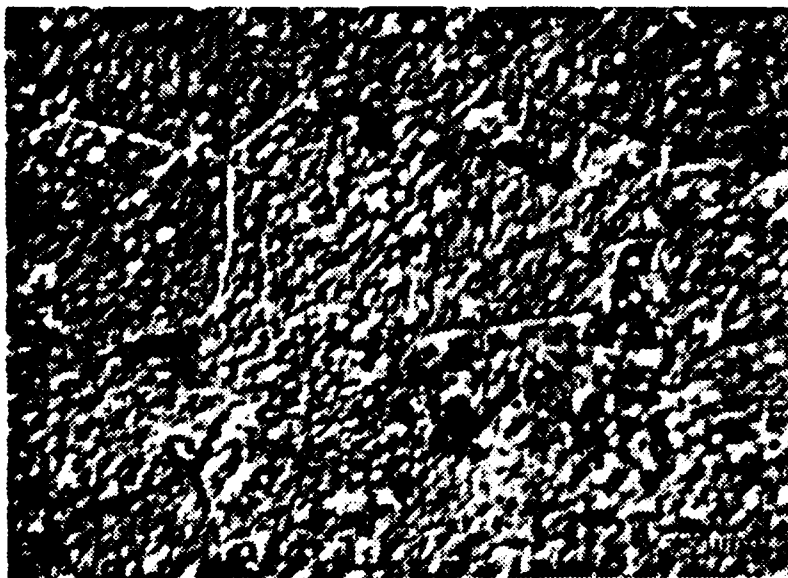


Figure 43. Optical micrograph showing equiaxed grain morphology of the spray deposited Al-Li-SiC_p sample taken from experiment 5, heat treated at 600°C for 100 min.

Table 21. Results of the Grain Size Measurements for Different Intervals of Time and Temperature for Extruded Samples of Al-Li and Al-Li-SiC_p Materials.

Material	Al-Li/400°C	Al-Li-SiC _p /400°C	Al-Li/600°C	Al-Li-SiC _p /600°C
Time (min)	Grain size (μm)	Grain size (μm)	Grain size (μm)	Grain size (μm)
0 ^a	76.0 ± 4.9	65.0 ± 2.7	76.0 ± 4.1	65.0 ± 2.7
1	80.0 ± 7.6	81.0 ± 3.2	165.0 ± 7.1	100.0 ± 5.8
10	87.0 ± 4.6	95.0 ± 6.6	207.0 ± 17.1	128.0 ± 13.4
50	99.0 ± 9.1	108.0 ± 12.4	211.0 ± 11.0	138.0 ± 10.0
100	104.0 ± 13.2	121.0 ± 3.6	251.0 ± 26.8	142.0 ± 27.3

^a time 0 refers to as-spray deposited grain size achieved after normalizing heat treatment given to the spray deposited and extruded samples.

4.4. Discussion

4.4.1. Solid State Cooling Effects

Once the distribution of solid, liquid, and mushy droplets impact the deposition substrate, the newly formed grains will continue to grow during solid state cooling. In order to gain some insight into the growth of grains in the reinforced and unreinforced materials, kinetic analysis of the data given in Table 20 was used in the present study to calculate the grain growth exponent. The grain growth exponent, n , represents the slope of the line when the grain size (in mm) is plotted against time (in min) on a log - log scale [140-142]. The empirical relationship correlating grain size, annealing time and grain growth exponent may be represented as:

$$D = C \cdot t^n \quad (38)$$

where D is the average grain diameter; t is the annealing time; and C and n are constants. The numerical values of C and n depend on alloy composition and on annealing temperature. The values of n have been reported to range from 0.05 to 0.50; a discussion on the significance of the grain growth exponent, n , can be found elsewhere [143, 144]. The main assumptions involved in the development of Eqn. (38) are as follows: a) the

grains have an equiaxed morphology, b) there is no prior deformation, and c) the grain growth is normal [140-142]. Regarding the grain morphology, the presence of equiaxed grains has been established in a previous section. In addition, the presence of recrystallized grain morphology after hot extrusion and thermal treatment precludes any significant effects of deformation on grain growth. Finally, the linear relationship observed between grain growth and annealing time, as seen in Figure 41, provides experimental basis to the assumption of normal growth. The results of grain growth studies conducted on the as-spray deposited and extruded materials showed that this material began to exhibit abnormal grain growth behavior after extended annealing times. This is evident from the large standard deviations obtained from the grain size measurements (see Table 21). Therefore, no attempt was made to calculate the grain growth exponent for the extruded materials.

A few comments are in order regarding the values of grain growth exponent (n) obtained in the present study. It can be seen from Table 22 that the value of the grain growth exponent (n) for a constant temperature is lower for the Al-Li-SiC_p material (0.065-0.070) relative to that of the Al-Li material (0.139-0.187). Furthermore, the results also show that the value of n decreases with an increase in temperature for Al-Li and Al-Li-SiC_p materials. On the basis of the results of other investigators [143, 144] one would anticipate an increase in the value of n with temperature. While this anomalous behavior of the Al-Li and Al-Li-SiC_p materials is not clearly understood, it is thought to be related to the segregation of alloying elements to free surfaces, and to the nucleation of precipitated phases (see Figures 39 and 40). For example, the results of SEM/EDAX studies shown in Figure 40 clearly suggest segregation of elemental copper to the matrix regions adjacent to the porosity. A similar analysis could not be conducted for lithium as a result of the limitations associated with the SEM/EDAX technique to detect the elements with atomic number below 5. However, it is anticipated that the effect will be more pronounced for lithium as a result of its high diffusivity in the aluminum matrix. Regarding the effects of second phase precipitation on grain growth, one needs to consider the composition of the binary alloy. On the basis of the binary Al-Li phase diagram and the Li composition used in the present study, precipitation of the ordered Ll₂ δ' (Al₃Li) phase can be anticipated at 400 °C [40]. In addition, annealing (500-600 °C) of Al-Li alloys has been reported to result in the formation of δ (AlLi) phase at grain boundaries [40].

Table 22. Results of the Grain Growth Kinetic Studies.

Material	n	C
Al-Li /400 °C	0.187	0.067
Al-Li /600 °C	0.139	0.129
Al-Li-SiC _p /400 °C	0.070	0.068
Al-Li-SiC _p /600 °C	0.065	0.079

A qualitative explanation for the observation that as a result of isochronal anneals, the grain sizes for Al-Li-SiC_p samples are smaller than those for Al-Li may be offered as follows. The presence of SiC_p at the grain boundaries decreases the overall free energy of the system by decreasing the available grain boundary area. Therefore, the thermodynamic driving force for the grain boundary migration in the Al-Li-SiC_p is decreased, relative to that present in the Al-Li matrix. The results from optical and SEM studies conducted on the as-spray deposited materials, show that the SiC_p are located both transgranularly and intragranularly within the Al-Li matrix; this is consistent with previous findings (see also Table 19) [31]. In addition to decreasing the effective grain boundary area, the presence of SiC_p at the grain boundaries may result in a drag force on the boundary, effectively slowing grain boundary migration. Inspection of Figure 41 and Table 20 shows that the grain size of the Al-Li alloy exposed at 400 °C for 100 minutes was 175 μm, whereas the grain size of the Al-Li-SiC_p at the same temperature and time was only 95 μm. The same trend was observed at 600 °C for all exposure times (see Table 20). It is anticipated that at low temperatures the dragging effect associated with the presence of SiC_p at the grain boundaries may be enhanced by the presence of a dislocation network in the vicinity of the interface formed between the SiC_p and the Al-Li matrix. The presence of a dislocation network at SiC_p/Al interfaces has been confirmed by numerous investigators [16, 64], and has been proposed to develop as a result of the large difference in coefficient of thermal expansion between SiC and Al. Furthermore, the presence of a dislocation network at the SiC_p/Al interface will enhance solute segregation, which in turn will reduce the mobility of the grain boundaries. The

preferential segregation of constituent elements at reinforcement/matrix interfaces has been documented by various investigators [123, 145]. It must be noted that the presence of SiC_p in the matrix introduces strain energy due to the difference in coefficient of thermal expansion between SiC_p and the matrix. The strain energy thus introduced in the lattice may have an influence in retarding grain growth as suggested in related studies [146] and is the subject of continuing research work.

Regarding the effect of porosity on grain growth, the results shown in Tables 20 and 21 suggest that the magnitude of grain size of the as-spray deposited Al-Li- SiC_p material is 21-23 % lower than that of the as-spray deposited and extruded Al-Li- SiC_p material. The presence of a fine distribution of pores at the grain boundaries will have a similar effect to that of SiC_p effectively slowing down grain boundary migration [146]. The results for the Al-Li material are unexpected, however, in that the data shown in Table 21 suggest that the presence of porosity increases the rate of grain growth, after a short transient. The experimental results from Tables 20 and 21 show that the grain size of the Al-Li material with porosity at 400 °C/100 min is 46 % higher than the corresponding grain size of the extruded material under identical conditions. This unusual behavior, analogous to the decrease in the value of the grain growth exponent with temperature noted previously, is thought to be related to elemental segregation and to the nucleation of secondary phases, and is the subject of continuing studies.

4.5. Conclusions

The primary conclusions that may be drawn from this work are as follows:

1. The observed decrease in grain size which results from the co-injection of ceramics during spray atomization and deposition is influenced by a decrease in grain boundary migration during solid state cooling.
2. The sharp decrease in the rate of grain growth, observed in the present study for the SiC_p containing material, suggests that the SiC_p effectively slow grain boundary migration. This observation is supported by kinetic analyses of the grain growth data, which showed that the values of the grain growth exponent in the 400-600 °C temperature range were 0.065-0.070 and 0.139-0.187 for the Al-Li- SiC_p and Al-Li materials, respectively.

3. Finally, further work is required in order to identify the role of porosity in affecting the grain growth behavior of monolithic Al-Li alloy.

CHAPTER 5

5.9 Wetting and Interfacial Reactions in Al-Li-SiC_p MMCs Processed by Spray Atomization and Deposition

5.1. Introduction

Systematic studies of metal/ceramic interfaces were initiated in the early 1960's [148]. It is now widely accepted that in order to maximize interfacial bond strength in MMCs, it is necessary to promote wetting, control surface interactions, and minimize oxide formation. Wetting is effected between a metal and a liquid when the strength of the interfacial bond exceeds the surface tension of the liquid. Wetting is difficult to achieve in molten metals due to their relatively high surface tension values (60- 2400 mJm⁻²). There are, however, various techniques which can be utilized to improve the wetting characteristics of MMCs. These techniques are based on the principle that the contact angle formed in a molten metal/ceramic system can be decreased through: (a) increasing the surface energy of the solid, (b) decreasing the solid/liquid interfacial energy, and (c) decreasing the surface tension of the liquid metal. In practice, the bond formed between the matrix and reinforcement can be enhanced by [98]: (a) applying metallic coatings such as Ni and Cu to the ceramic particulates [149, 150], (b) alloying the metallic matrix with reactive materials such as Li, Mg, Ca, Ti, Zr, and P, to reduce the surface tension of the melt and/or the solid/liquid interfacial energy, and to induce chemical reactions at the interface [87, 109, 151, 152], and (c) heat treating the ceramic particulates in order to promote desorption of adsorbed gases from the ceramic surfaces [153]. The principles underlying these practices are discussed subsequently.

Wetting can be promoted in certain metal/ceramic systems through additions of elements which have a high affinity for oxygen, such as elements in groups I and II of the periodic table, e.g., Li and Mg in aluminum alloys [109, 151]. These elements segregate to the interfacial region and weaken any oxide layers present [154]. For the case of Mg additions to aluminum, for example, additional improvements in wetting behavior result from a decrease in surface tension, as a result of the low surface tension of Mg (0.599 N/m) relative to that of aluminum (0.760 N/m). The addition of 3 wt.% Mg to Al reduces the surface tension from 0.760 to 0.620 N/m [87]. Furthermore, the addition of reactive elements to the melt can also enhance wetting by promoting interfacial reactions. For example, chemical reactions have been observed to occur readily between Al₂O₃ and divalent transition metal oxides to form aluminates spinels such as MgO·Al₂O₃ [152]. Such mineral spinels or oxides promote interfacial bonding, since they form strong bonds between both metals and ceramics.

From the above discussion, it is apparent that some interfacial activity will be beneficial to the wetting behavior of MMCs. In the presence of high processing temperatures, however, extensive interfacial reactions with concomitant degradation in the metal/ceramic bond will have an adverse effect on mechanical behavior. Hence, the formation of extensive interfacial reactions must be avoided and the thermodynamic activity of certain elements during processing must be controlled. In the Al/SiC system, for example, intermediate phases such as Al_4C_3 and Al_4SiC_4 may form during thermal exposure either as a continuous layer or isolated precipitates [155]. At temperatures above the melting point of Al, SiC reacts with molten Al according to the following reactions:



In the case of reaction 1, further growth of the reaction products occurs by solid state diffusion through the formed Al_4C_3 layer. In the case of reaction 2, however, the reaction continues by the dissolution of the SiC into the molten Al matrix. It is important to note, however, that the presence of the Al_4SiC_4 phase has not been confirmed experimentally. Although the bond formed between the SiC and Al_4C_3 is generally strong, the topology of the resulting Al_4C_3 -SiC interface can be highly irregular when the original interface is irregular, or if there is dissolution/growth reaction between SiC and liquid Al. The irregular topology of the interface may promote stress localization during deformation. This is best exemplified in the C(graphite)/Al system, where the presence of cracks, cavities and voids, formed at the C/ Al_4C_3 interface introduces additional mechanisms of crack nucleation and propagation, relative to those active in the unreinforced metal [156]. In addition to extensive interfacial reactions, high processing temperatures will promote oxide formation and segregation of the constituent elements [156-158]. Segregation of elements such as Cu and Mg from grain interiors will promote localized corrosion, and limit precipitation-hardening mechanisms.

The various processing techniques developed in past few decades to fabricate MMCs have been discussed by various investigators [20-24, 26, 29, 30-35, 121, 149]. A review of the available literature on particulate reinforced MMCs may be found elsewhere [19].

Although the results of recent studies [31-35] suggest that spray atomization and deposition processes can be successfully utilized to incorporate ceramic reinforcements into a metallic matrix with minimal reactivity, there exists no information on the mechanisms affecting the wetting behavior of the reinforcements during processing. Therefore the objective of the present study was to provide insight into the wetting and interfacial behavior of Al-Li-SiC_p MMCs processed by spray atomization and co-deposition, a spray atomization and deposition technique, with particular emphasis on wetting characteristics and interfacial reactions.

4.2. Experimental Procedure

5.2.1. Materials

Reynolds Metals Company provided the aluminum-lithium master alloy as cast ingots, 100 mm x 200 mm x 600 mm. The ingots were inspected for major defects, and chemically analyzed in preparation for atomization. The chemical analysis of the remelted alloy was Al-2.1wt% Li. The selection of an Al-Li binary alloy (solid solution) as a matrix material was prompted by the results of Wolf et al. [109] and Delannay et al. [87]. Their work indicates that lithium enhances the wettability of ceramic particulates by molten metals by segregating to the interfacial region and weakening any oxide layers present. In addition, lithium effectively reduces the density and increases the modulus of the MMCs [40].

The details regarding the type, size and distribution of SiC_p has been addressed in section 2.2.

5.2.2. Spray Atomization and Co-deposition Processing

The details of the spray atomization and co-deposition processing has been described in section 2.2.1. Five experiments were conducted for this study. The primary experimental variables used during each experiment are listed in Table 6 (see section 2.2 also).

5.2.3. Structural Characterization

In order to study the resulting microstructure and phases, metallographic samples were prepared from various locations in the as-spray deposited Al-Li-SiC_p MMCs. The

microstructural studies were conducted: (a) on the as spray deposited material, and (b) on the as-spray deposited material after two isochronal anneals at preselected temperatures. The details of the thermal exposure are given in Table 23. In addition, some of the as-spray deposited materials were machined into a square prism, of cross-section $1.0 \times 1.0 \text{ cm}^2$, and fractured at room temperature. The resulting fracture surfaces were then analyzed.

Table 23. Specimen Thermal History.

Designation	Conditions
Ht1	as-spray deposited condition
Ht2	as-spray deposited + heat treated at 600°C for 2 hours
Ht3	as-spray deposited + furnace re-melting under a flow of argon atmosphere at 870°C for 1 hour.

The heat treatment temperature of 600°C shown in Table 23 was selected on the basis of the Al/SiC phase diagram (see Figure 44). As shown in this figure, the Al_4C_3 phase is thermodynamically stable at this temperature.

The microstructural characterization was accomplished using optical microscopy, transmission electron microscopy (TEM), scanning electron microscopy (SEM) with energy dispersive x-ray spectroscopy (EDS), and x-ray diffractometry (XRD).

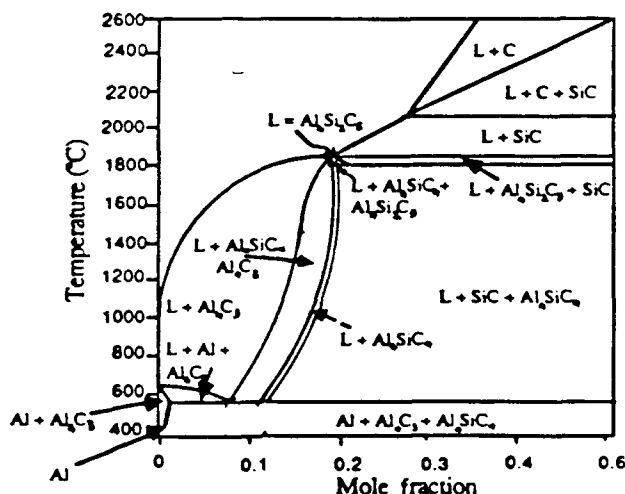


Figure 44. Phase diagram of Al-SiC system [155].

5.2.3.1. Optical microscopy (OM)

Optical microscopy was conducted on polished and etched, as-spray deposited samples using conventional and Differential Interference Contrast (DIC) techniques. The size, volume fraction and distribution of the SiC_p was characterized from the optical micrographs using a Buehler Omnimet II Image Analyzer.

5.2.3.2. Transmission Electron Microscopy (TEM)

Transmission electron microscopy was performed on a JEOL 100 C at an operating voltage of 100kV. The TEM specimens were prepared by sectioning and mechanical polishing into thin foils of about 0.1-0.5mm in thickness. The foils were then chemically polished to perforation, using the window technique in a 1:2 solution of HNO_3 and methanol at approximately $-20^\circ C$ and a voltage of approximately 10V.

5.2.3.3. Scanning Electron Microscopy (SEM)

SEM studies were conducted using a HITACHI S-500 microscope. The samples were cut to a thickness of 0.5 cm and mirror polished using conventional techniques. The polished samples were then examined in secondary electron mode for microstructural details; point analyses were carried out at selected regions of the sample surface to detect the presence of reaction products. SEM/EDS analyses were also conducted on as-deposited and fractured Al-Li- SiC_p specimens in order to avoid surface contamination during

metallographic preparation. The exposed SiC_p on the fracture surface were then analyzed by varying the accelerating electron voltage (10, 15, 20, and 25keV) and measuring the intensity of the Al and Si x-ray peaks at different depths throughout the thickness of the particulates.

5.2.3.4. X-ray diffraction (XRD)

X-ray diffraction analysis was conducted on spray deposited samples in the Ht1 and Ht3 conditions (see Table 23). Thin samples were exposed to $\text{Cu K}\alpha$ radiation ($\lambda = 1.5418\text{\AA}$) using a scanning speed of 2 deg/min. A plot of intensity versus 2θ was obtained, illustrating peaks at different Bragg angles. The Bragg angles corresponding to different peaks were noted and the values of interplanar spacings, 'd', was calculated from Bragg's law ($\lambda = 2d\sin\theta$). The values of 'd' obtained were then matched with standard values for aluminum and other phases.

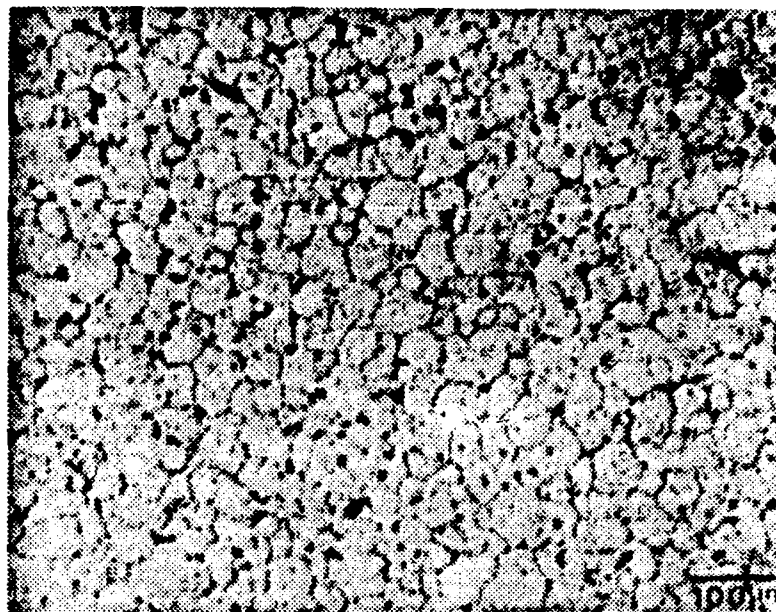
5.3. Results

5.3.1. Structural Characterization

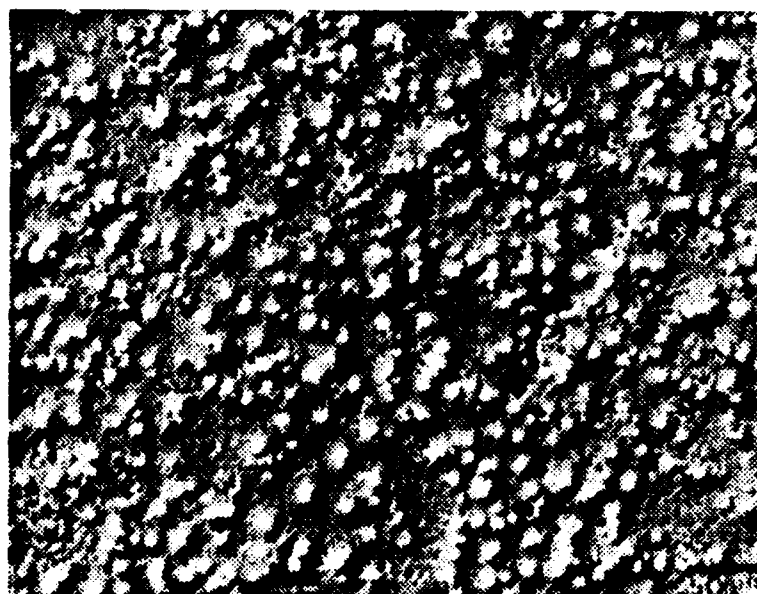
The as-spray deposited materials exhibited a discoidal geometry, 50 mm in height by 150 mm in diameter. The height of the deposits decreased from a maximum of 50 mm at the center, to a minimum of 5 mm towards the periphery. The density of the as-spray deposited materials ranged from 2.4 g/cm^3 to 2.6 g/cm^3 . These density values correspond to approximately 88 - 97% of the theoretical density, as computed for an Al-Li-5 vol.% SiC_p material.

5.3.2. Optical microscopy (OM)

Optical microscopy was conducted on coupons of the spray deposited Al-Li/ SiC_p material; one example is shown in Figure 45a. This figure reveals the presence of an equiaxed grain morphology with an average grain size of $65 \mu\text{m}$. This grain morphology has also been reported by other investigators [63, 64, 66]. The average grain size for experiments 5 to 9 was in the range of $66\text{--}71 \mu\text{m}$; the as cast Al-Li grain size was $207 \mu\text{m}$. Optical micrographs of the deposits were taken using Differential Interference Contrast (DIC); one example is shown in Figure 45b. The use of DIC technique facilitated the identification of the distribution of the SiC_p in the matrix.



(a)



(b)

Figure. 45 . Optical micrograph showing: (a) the grain structure of the as-spray deposited material and (b) SiC_p distribution in the matrix.

5.3.3. Image Analysis

The results of image analysis were described in section 2.3.2.2 (see Table 9 also).

5.3.4. Transmission Electron Microscopy (TEM)

Transmission electron microscopy studies were conducted on samples of the as-spray deposited materials in the Ht1, Ht2 and Ht3 conditions (see Table 23). A representative view of the as-spray deposited Al-Li-SiC_p microstructure is shown in Figure 46. This figure shows the presence of a highly irregular Al-SiC interfacial region. In some regions of the TEM samples, the particulates could be seen suspended by thin ligaments of the matrix across narrow interfaces. In addition, a high dislocation density in the matrix region surrounding the particulates was also noted (See Figure 46).



Figure 46. Representative TEM micrograph of the Al-Li-SiC_p in the Ht2 condition.

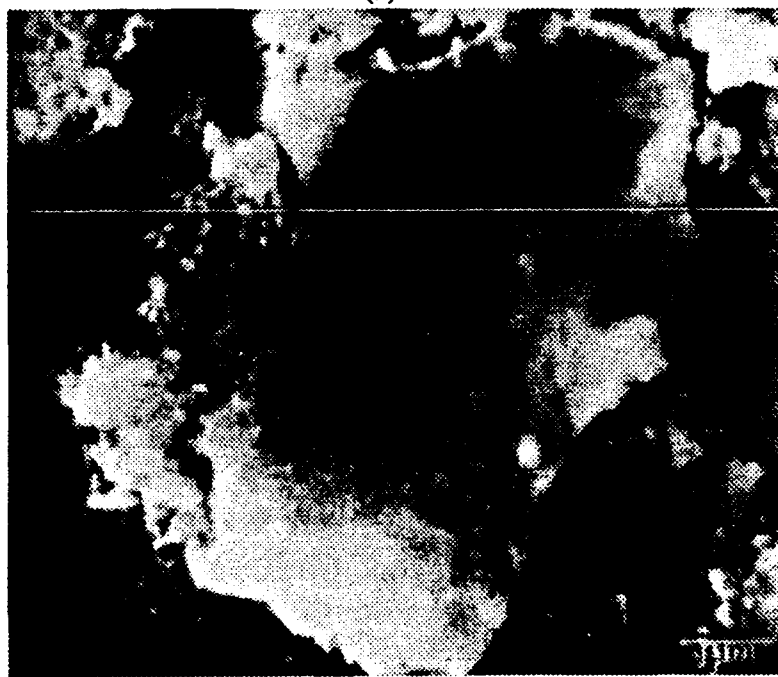
5.3.5. SEM/EDS

Scanning electron microscopy of samples removed from the as-spray deposited Al-Li-SiC_p materials revealed the presence of a finite amount of non-interconnected porosity. The micron size pores were randomly located throughout the microstructure, and

exhibited a near elliptical morphology. The distribution of pores was found to be bimodal, with a large proportion in the 1- 2 μm and 10-20 μm size ranges; the volume fraction of porosity was estimated to be approximately 3-12 % throughout the material.



(a)



(b)

Figure 47. Representative SEM micrograph showing: (a) the fractured surface of the as-deposited Al-Li-SiC_p, and (b) the presence of reaction products in the remelted Al-Li-SiC_p material (Ht3 condition).

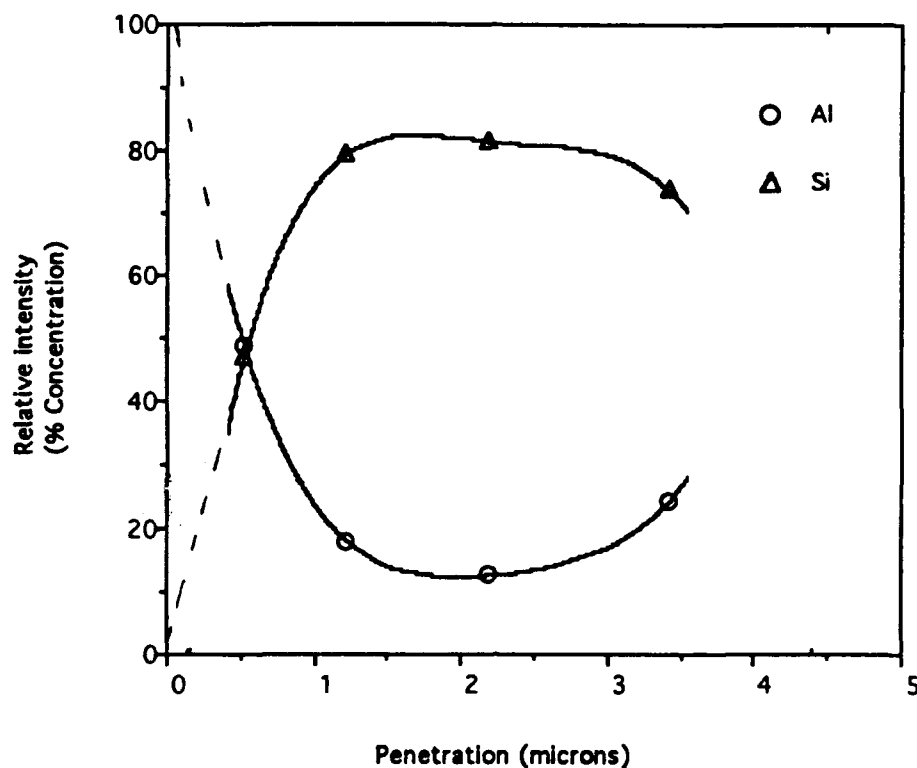


Figure 48. Concentration of Al and Si as a function of penetration in the SiC_p for the as-spray deposited material.

Representative SEM micrographs of the deposited Al-Li- SiC_p MMCs are shown in Figure 47 for the Ht1 and Ht3 conditions. Figure 47a illustrates the morphology of the fractured surface corresponding to a sample in the Ht1 condition. The surfaces of the particulates shown in Figure 47a exhibit an irregular, faceted morphology. Detailed examination of the fracture surface revealed that particulate fracture, rather than pullout, during deformation, suggesting a strong interfacial bond. Figure 47b shows the extensive interfacial reaction which occurs between the SiC_p and the Al-Li matrix during remelting of the Al-Li matrix (Ht3 condition).

The results of EDS analyses conducted on the as-spray deposited material (Ht1 condition) are shown in Figure 48. The results shown in this figure correspond to the location shown in Figure 47a. The relative concentration of the constituent elements were calculated from the intensity of the x-ray beam, and are plotted in Figure 48 as a function of depth of penetration into the SiC_p . The depth of penetration, R , of an electron beam into a SiC_p was computed from [159]:

$$R = (4120/\rho_a)E^n \quad (41)$$

where $n = 1.265 - 0.0954 \ln E$, E = primary electron energy (in MeV), and ρ_a = density of absorbing media (in g/cm³). The results obtained using Eqn. (41) show that the accelerating voltages used in the present study, namely 10, 15, 20, and 25 keV, correspond to penetration depths of 0.519, 1.218, 2.189, and 3.413 μm , respectively.

Finally, the relative concentrations of the constituent elements corresponding to the location shown in Figure 47b, (Ht3 condition), are shown in Figure 49. The results shown in Figure 49 show that the Al/SiC interface contains O, C, Si and Al. In this figure, the location designated as Matrix 1 refers to a region approximately 2 μm from the interface, whereas location designated as Matrix 2 was approximately 10 μm away from the interface.

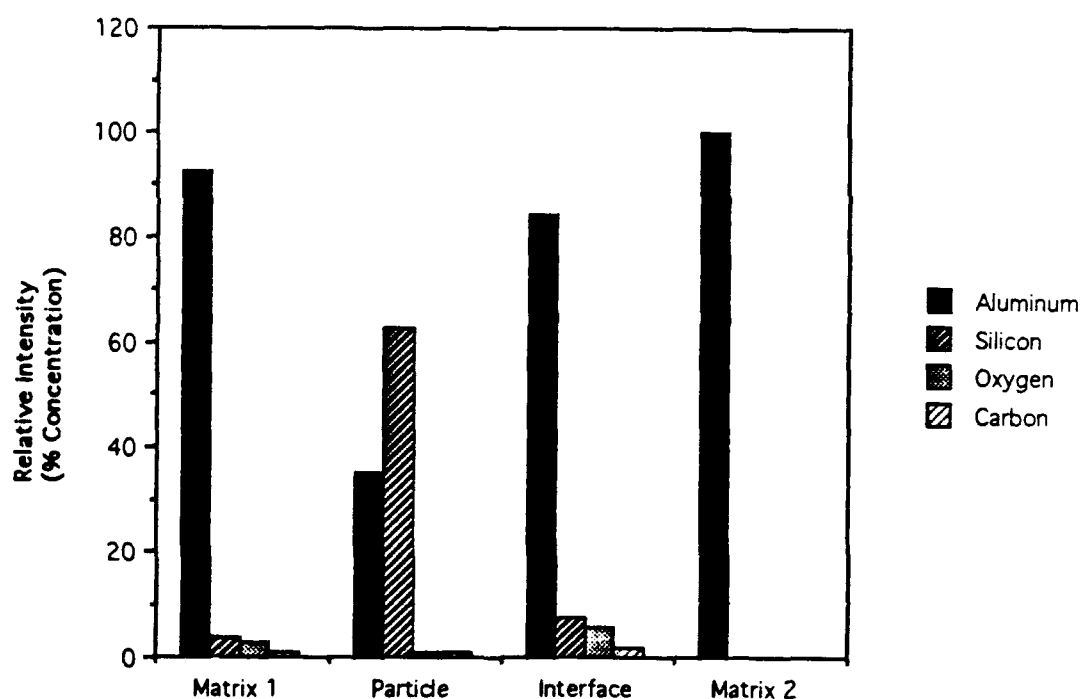


Figure 49. Histogram of the Al-Li-SiC_p material in the Ht3 condition showing the relative intensities of SEM/EDS signals for Al, Si, O, and C. The Matrix 1 and Matrix 2 designations refer to EDS analyses conducted on the matrix at distances of 2 and 10 μm , from the interface, respectively.

5.3.6. X-ray diffraction (XRD)

The x-ray diffraction spectra corresponding to samples in the Ht1 and Ht3 conditions were analyzed. The lattice spacings (d) corresponding to the observed Bragg angles are shown in Table 24. Also included in this table are the standard lattice spacings corresponding to pure Al, SiC, Al_4C_3 , AlSiC, Al_2O_3 and Al_2Mg_3 . The XRD spectrum corresponding to the as-spray deposited Al-Li-SiC_p material (Ht1) indicates the presence of pure aluminum. The XRD spectrum corresponding to the re-melted Al-Li-SiC_p material (Ht3), however, exhibits additional peaks. Inspection of Table 24 suggests that these additional peaks correspond to Al_2O_3 . The absence of x-ray peaks corresponding to SiC, Al_4C_3 and AlSiC phases was thought to result from the relatively low volume fraction of SiC_p present in the samples utilized for the XRD study (see Table 9).

Table 24. Results of X-ray Diffractometry Studies.

<u>Ht1 sample</u>									
Angle		36.4	39.0	45.3	54.6	60.6	65.8	78.8	82.9
Calculated d values		-	2.36	2.00	-	-	1.42	1.21	1.16
Band size(%)		-	60	100	-	-	15	21	10
<u>Ht3 sample</u>									
Angle		36.4	39.0	45.3	54.6	60.6	65.8	78.8	82.9
Calculated d values		2.47	2.36	2.00	1.68	1.53	1.42	1.21	1.16
Band size(%)		10	100	59	5	5	36	35	13
<u>Standard d values</u>									
Al		2.338	2.025	1.432	1.221	1.169			
Al ₂ O ₃		2.379	1.601	1.510					
Al ₂ Mg ₃		2.48	1.60	1.52					
Al-Li		2.26	1.92	1.58					

5.4. Discussion

5.4.1. Grain Structure

The experimental results show that the grain morphology of the as-spray deposited material is equiaxed; this observation is in agreement with previous findings [38, 63, 64, 66]. The mechanism proposed for equiaxed grain formation has been described in section 1.4.2.

Comparison of the grain size of the spray deposited Al-Li binary alloy to that of the Al-Li-SiC_p material indicates that the presence of the SiC_p effectively reduces the grain size by approximately 10 %. The finer grain morphology of the Al-Li-SiC_p is thought to result from a combined effect of three distinct mechanisms: enhanced heat transfer, increased solidification prior to impact, and grain boundary pinning effects. During flight, the SiC_p spray from the fluidized bed effectively enhances the convective heat transfer from the matrix droplets as a result of its lower temperature (the particulates are injected into the matrix spray at room temperature) and high relative velocity. The high relative velocity between the atomized droplets and the SiC_p carrier gas is a direct result of the injection angle (see Table 6). Further work is in progress in this area in order to develop an understanding of the effects of the reinforcements on the resulting microstructure during spray deposition.

Regarding the presence of pores in the as-spray deposited material, the observed irregular morphology of the pores suggests that porosity develops from interstices formed as droplets impact on one another. This is consistent with the findings of other investigators [63, 64, 66]. A discussion on the origin of porosity in spray deposited materials can be found elsewhere [32, 37].

The high dislocation density observed in the Al-Li matrix adjacent to the SiC_p is in agreement with previous findings [16, 64]. The high dislocation density observed in MMCs is thought to result from the large difference in coefficient of thermal expansion (CTE) of Al and SiC (10:1) which causes thermal mismatch strains, ϵ , between reinforcement and matrix during solid state cooling. These strains are relaxed by the formation of a dislocation network, which in turn, will alter the response of the MMC to thermomechanical processing, relative to that of unreinforced alloys [15, 16, 155].

5.4.2. SiC_p Size and Distribution

The results shown in Table 9 indicate that there were variations in the volume fraction of SiC_p with spray deposited thickness. Regarding the variations in volume fraction of SiC_p for a single experiment, the results shown in Table 25 do not reveal a clear correlation between spray deposited thickness, the amount of SiC_p, and the experimental conditions (see Table 6). Although a systematic investigation of the effects of the injection angle on the distribution of SiC_p in the matrix was outside of the scope of the present study, the variations in volume fraction with spray deposited thickness are most likely affected by changes in the fluidization conditions (i.e., pressure drop) and mass flow rate of the metal during the experiments, in addition to the injection angle. Furthermore, since the volume fraction of SiC_p was determined using image analysis, the results should be treated as an order of magnitude approximation of the actual SiC_p volume fraction. The results do suggest, however, that it should be possible to alter the resulting variations in volume fraction of SiC_p through changes synthesis parameters. The higher volume fraction of SiC_p observed for experiment 6 was thought to result from a pressurization condition at the metal delivery tube (see Table 6). This behavior, which is caused by the relative position of the metal delivery tube to the gas jets, has been studied extensively [119]. In the present study, the pressurization effect reduced the metal flow rate of the matrix, effectively decreasing the Al-Li/SiC_p mass flow ratio, hence resulting in higher SiC particulate concentration.

Regarding the size distribution of the SiC_p, the results from Table 9 ($d_{50} = 2.7\mu\text{m}$) are consistent with the initial SiC_p size ($d_{50} = 3.0\mu\text{m}$). The slight reduction in particulate size can be attributed to the difficulties associated with fluidizing the coarse SiC_p. The results also indicate that the processing methodology does not favor clustering of the SiC_p.

In terms of the location of the SiC_p in the matrix, comparison of the computed interparticle spacings from Table 9 to the resulting grain sizes, indicates that the particulates were randomly distributed in the matrix (i.e. not preferentially located at the grain boundaries). This was also confirmed through SEM analyses. After impact with the substrate, retention of a suitable particulate dispersion throughout the matrix is facilitated by the presence of primary dendrite debris resulting from droplet impact. The mechanisms affecting the distribution of SiC_p during spray deposition processing were discussed in section 2.4.

Table 25. Numerical model results of the thermal history of the droplets of varying sizes.

Diameter of droplet (μm)	Temperature ($^{\circ}\text{C}$) (at 0.21 m)	f_s (%)	Temperature ($^{\circ}\text{C}$) (at 0.35 m)	f_s (%)	Thickness of oxide film (\AA)	Oxide film (0.21m)*	Oxide film (0.35m)*
25	182	100	100	100	2.34	Al_2O_3 3H ₂ O/ $\text{Al}_2\text{O}_3\text{H}_2\text{O}/\text{Li}_2\text{O}$	Al_2O_3 3H ₂ O/ $\text{Al}_2\text{O}_3\text{H}_2\text{O}/\text{Li}_2\text{O}$
62	605	95	472	100	5.85	γ Al_2O_3 / γ LiAlO_2	Al_2O_3 H ₂ O/ γ Al_2O_3
156	650	33	647	48	14	γ Al_2O_3 / γ LiAlO_2	γ Al_2O_3 / γ LiAlO_2

* The type of oxides shown for the indicated temperatures and droplet sizes are for equilibrium conditions, and were determined from the work of [169, 170] on the basis of the average temperature of the droplet.

5.4.3. Wetting and Interfacial Reactions

In order to discuss the wetting behavior during spray atomization and co-deposition, it is necessary to review our current understanding of the factors which govern the behavior of liquid/solid interfaces under equilibrium conditions.

A concept commonly used to measure the adhesive strength between a solid and liquid interface is the work of adhesion W_{ad} , defined by the Young-Dupre' equation as:

$$W_{ad} = \gamma_{lg} (1 + \cos \theta) \quad (42)$$

W_{ad} has been defined [87, 154] as the work required to separate a unit area of the solid-liquid interface; γ_{lg} is the liquid/gas interfacial energy. Wetting of a solid surface by a liquid is achieved when $\cos \theta > 0$, that is when $\gamma_{sg} > \gamma_{sl}$; where γ_{sg} and γ_{sl} are the solid/gas and solid/liquid interfacial energies respectively. Moreover, it can be shown [87] that wetting will occur when the driving force for wetting D_f exceeds the liquid interfacial energy, i.e.,:

$$D_f \geq \gamma_{lg} \quad (43)$$

The driving force for wetting, D_f , is governed by two factors: the surface tension of the liquid, and the strength of the liquid/solid interaction at the interface [87]. In turn, these two factors are affected by variables such as interfacial reactions, surface characteristics, heat of formation, valence electron concentration, temperature and time [160]. For molten metals, it is difficult to satisfy Eqn. (43), because metals typically exhibit rather high surface tension values (64-2400 mJm⁻²). Hence, the wettability of oxides by molten metals is generally poor. Recent results suggest that the wettability of molten metals against ZrO₂ [87] and Al₂O₃ [161] is approximately proportional to the free energy of oxide formation of the metal. In the presence of oxygen, however, metals with a high free energy of oxide formation form stable oxides which act as effective diffusion barriers that decrease the level of interaction at the interface. Furthermore, the absorption of oxygen from the atmosphere can also be detrimental to the wetting behavior by decreasing γ_{sg} . As a result, wetting is not observed in molten metal/ceramic systems until a certain threshold temperature is achieved which allows penetration of the molten metal through the oxide layer. For example, Laurent et al. [162] and Warren et al. [163] attributed the transition from non-wetting to wetting behavior in Al/SiC system to the disappearance of the oxide layer from the molten Al droplet. Furthermore, Warren et al. [163] also singled out the destabilization of oxide layer (by the presence of reactive elements) and the improvement of interfacial reaction kinetics with temperature as the main factors contributing to wettability.

Even in systems that exhibit a strong driving force promoting chemical reactions, the presence of oxides can prove detrimental to the wetting behavior. In SiC/Al, for example, the high value of the work of adhesion ($W_{ad} = 1000 - 1200 \text{ mJm}^{-2}$) [87], indicates that there is a strong tendency for chemical interaction at the interface. However, wetting in this system is hindered not only by the formation of Al₂O₃ on the molten metal, but also by the formation of SiO₂ on the surface of the SiC_p. In the presence of SiO₂ and Al₂O₃, the contact angle formed between Al at its melting point and SiC can be extrapolated [163] to be approximately 155° which corresponds to non-wetting behavior. Under these conditions, the value of work of adhesion calculated using the method discussed by Delannay et al. [87] is 98.37 mJ/m². The latter also suggests non-wetting between the Al and SiC since the work of adhesion, W_{ad} , must be greater than the liquid-gas interfacial energy, γ_{lg} (1050 mJm⁻²) for wetting to occur.

The wetting characteristics and the extent of interfacial activity during spray atomization and co-deposition are affected by the thermal conditions of the matrix during reinforcement injection and subsequently, during deposition. During spray atomization and co-deposition, the thermal and solidification conditions of the droplet distribution will depend on: (a) the thermodynamic properties of the matrix material, such as: (i) liquidus temperature, (ii) solidus temperature, (iii) melting temperature, (iv) density, (v) thermal conductivity, (vi) surface tension, (vii) heat capacity, and (viii) heat of fusion; (b) the thermodynamic properties of the atomization gas, such as: (i) density, (ii) heat capacity, (iii) viscosity, and (iv) thermal conductivity; (c) the characteristics of the reinforcement phase(s), such as: (i) size distribution, (ii) mass flow rate; and (d) the processing parameters, such as: (i) atomization gas pressure, (ii) nozzle/substrate flight distance, (iii) metal/gas flow ratio, and (iv) reinforcement injection. For processing conditions typical for aluminum alloys, the droplet distribution during reinforcement injection and subsequently during impact has been reported to consist of solid powders ($d_{16} = 20\text{--}45\text{ }\mu\text{m}$, $f_s \sim 1$), droplets with mostly liquid phase ($d_{84} = 150\text{--}250\text{ }\mu\text{m}$, $f_s \sim 0$), and a substantial fraction of powders in the mushy state ($d_{50} = 50\text{--}90\text{ }\mu\text{m}$, $f_s \sim 0.5$) (The subscripts 84, 50, and 16 in d_{84} , d_{50} , and d_{16} represent 84%, 50%, and 16% of the size distribution under this particle size)[37, 72]. As a result, during impact with the deposition surface, the SiC_p will be surrounded by either: (a) dendrite fragments, (b) completely solidified fine droplets, or (c) liquid phase. This event is shown schematically in Figure 26.

The presence of either dendrite fragments and/or fully solidified droplets will promote mechanical entrapment of the SiC_p during deposition. The highly irregular surface morphology of the SiC_p , which was evident from SEM observations (see Figure 47), will facilitate mechanical entrapment of the particulates during deposition. In related studies, Mehrabian et al. [95] showed that during stir casting of an Al-Si-Fe alloy containing SiC_p or Al_2O_3 particulates, the presence of primary dendrite debris prevents settling, flotation, or agglomeration of the ceramic particulates. The presence of either dendrite fragments and/or pre-solidified droplets during deposition will have a similar effect to that present during stir-casting. Furthermore, the presence of small crevices in the surface of the SiC_p increases the effective surface area available for interfacial activity, and enhances the mechanical bond formed between the particulate and matrix. In the presence of pre-solidified droplets, however, the inter-particle spacing will be limited by the droplet size. This is supported by the results shown in Table 9, for samples 3C and 4B. The inter-

particle spacings computed for these two samples, 21.2 and 25.7 μm , respectively, approach the value of the d_{16} droplet diameter, where $d_{16} = 30 \mu\text{m}$. A more thorough discussion on particulate entrapment during spray atomization and co-deposition processing can be found elsewhere [31, 32].

Regarding the interaction of the SiC_p with the molten Al-Li matrix during spray atomization and co-deposition processing, the preliminary results found in this investigation indicate that the temperature during deposition was sufficient to promote the formation of a stable bond, but remained sufficiently low to avoid extensive interfacial activity. The presence of a strong Al-Li/ SiC_p bond is supported by the SEM results which showed fracture rather than pullout of SiC_p during deformation. Furthermore, the results shown in Figure 48 suggest that the temperature during deposition promoted some diffusion of Al into the SiC_p . Regarding the diffusion of Al into the SiC_p , the present results are apparently unexpected since previous studies have shown that the calculated mean diffusion rate of Al in SiC at 500 °C will be less than 0.1 nm/yr [164]. It is worthwhile noting, however, that the present results are consistent with the findings of other investigators who have also reported diffusion of matrix elements into the reinforcing phases. Nourbakhsh et al. [165], for example, observed extensive diffusion of Ti into Al_2O_3 reinforcing fibers. In that study, approximately 1 wt pct Ti was added to a Ni_3Al (Ni-Al-Cr-Zr-B) matrix in order to enhance wetting of the reinforcing fibers. In related studies, J.M. Yang et al [166] also reported diffusion of Ni into SiC fibers in a nickel aluminide (Ni_3Al) matrix. In view of these results, and the fact that the atomic radius of Al is small, relative to that of Ti, the diffusion of Al into the SiC observed in the present study is not unexpected. Furthermore, the presence of a dislocation network at the SiC_p/Al interface (see Figure 46) will most likely enhance the diffusion of Al into the SiC_p .

The presence of small amounts of C detected near the interface of the as-spray deposited material after heating to 600°C for two hours (Ht2 condition) suggests the diffusion of free carbon (~0.60 wt. %) from the SiC_p thus resulting in an increase in the activity of carbon as also discussed in the related studies by Kannikeswaran and Lin [167]. Although interfacial reaction layers were not observed in the Ht1 specimens, the interfacial reaction layers were appreciably large, with thicknesses on the order of 5 μm , in the Ht3 specimen. This is consistent with the EDS results from Figure 49, which indicate the presence of high levels of C and O near the interface, relative to the matrix. Furthermore, this is in agreement with earlier observations [155] which suggest that fast

reactions occur between SiC and molten aluminum to form carbide phases such as Al_4C_3 and Al_4SiC_4 [15, 16, 154, 155]. In the related studies, Iseki et al. [168] reported the presence of a thin reaction layer about 10 μm in thickness for the sintered SiC and aluminum block heat treated at 1100 °C in a vacuum of 10^{-2} Pa.

5.4.4 Dynamic Wettability

The results discussed in the previous section suggest, first, that a strong interfacial bond was established between the Al matrix and the SiC_p and second, that prolonged thermal exposure of the as-spray deposited material resulted in the formation of a reaction layer consisting primarily of carbon containing phases, such as Al_4C_3 . The presence of a strong interfacial bond and the ensuing interfacial reactions during thermal treatment are indicative of wetting of the SiC_p by the Al-Li matrix. In view of the fact that the interaction of the Al-Li matrix with the SiC_p during spray atomization and co-deposition will take place under extremely non-equilibrium conditions, it is unlikely that Eqns. (42) and (43) may be used to predict wetting behavior, since these equations were developed for highly equilibrium conditions. One approach that may be utilized to provide insight into the wetting behavior during spray atomization and co-deposition processing is to consider the solidification conditions of the matrix droplets during co-injection, and subsequently, during deposition.

In order to determine the effect of the thermal conditions of the matrix droplets on the wetting behavior of the SiC_p , an enthalpy model developed elsewhere [31, 32] was used in the present study to calculate the temperature and fraction solid of the droplets, as a function of the flight distance. The numerical results are summarized in Table 25 for three droplet sizes: 25 μm , 62 μm and 156 μm . These three droplet sizes represent d_{16} , d_{50} and d_{84} of the droplet size distribution used in the present study, and hence can be used to gain some insight into the behavior of the entire population of droplet sizes. In addition, the results shown in Table 25 were computed for two flight distances: (a) the reinforcement injection point, and (b) the deposition point.

The range of temperatures and fraction solids shown in Table 25 do not suggest wetting of the SiC_p by the Al-Li matrix, since a large proportion of the droplet sizes will have developed substantial solidification structures prior to being exposed to the SiC_p . Therefore, an alternate wetting mechanism is proposed in the present study in order to account for the observed experimental results.

During spray atomization and co-deposition processing, as already mentioned, the SiC_p are injected at a previously selected spatial point in the atomized melt stream. At the reinforcement injection point, as shown in Table 25, the SiC_p will encounter fully solid, fully liquid, or partially solidified Al-Li droplets. The interaction of atomized droplets with SiC_p during flight and after deposition is shown schematically in Figure 50. SEM analysis of the presolidified, overspray powders provided experimental support to the results shown in Table 25. Figure 51, for example, shows the presence of SiC_p on the surface of presolidified Al-Li powders, approximately $25\text{ }\mu\text{m}$ in diameter. This droplet size corresponds to the d_{16} droplet diameter. Also evident from this figure is the dendritic structure formed during solidification of the powders.

In order to discuss the interaction of the SiC_p with the partially solidified or fully liquid droplets, it is necessary to consider the surface condition of the atomized droplets.

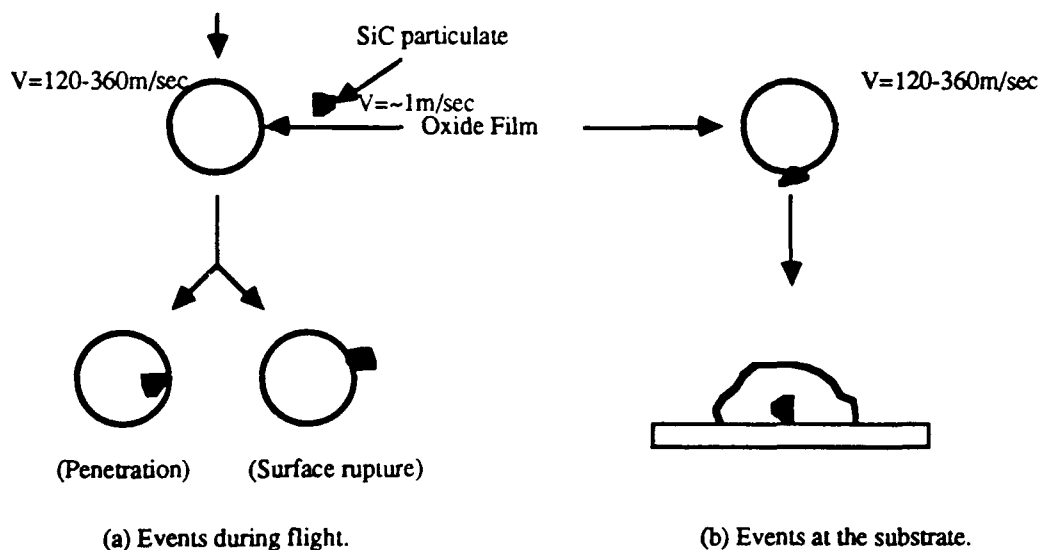


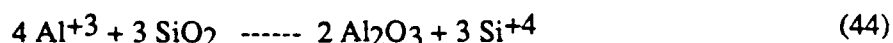
Figure 50. Types of interaction of the SiC_p with atomized droplets during flight and after deposition.



Figure 51. Presence of SiC_p on the surface of presolidified Al-Li overspray powders.

The large surface area of the fine Al droplets, in combination with the high thermodynamic stability of lithium and aluminum based oxides [169] will result in the formation of surface oxides immediately following atomization even under highly inert conditions, such as the one used in the present study. The extent of oxidation, and other reactions on the surface of the atomized droplets will depend primarily on the temperature and chemical composition of the droplets and their surrounding environment [169, 170]. On the basis of the work by Couper et al. [169], and taking into account the temperature of the droplets, it is possible to predict the types of oxides that will be present on the surface of the atomized droplets. The results are shown in Table 25, for the three droplet sizes representing the entire distribution, and two flight distances representing the SiC_p injection flight distance (0.21m) and deposition distance (0.35 m), respectively. The results shown in Table 25 suggest that even after assuming that all the oxygen (71 ppm [171]) present in the droplets appears in the form of a surface oxide, the thickness of oxide will not exceed 14 \AA . For the case of partially solidified, or fully liquid droplets (corresponding to $62 \text{ }\mu\text{m}$ and $156 \text{ }\mu\text{m}$ in Table 25), exposure of the SiC_p to unoxidized, molten Al-Li is highly probable, either during flight or after deposition. The brittle character of the aluminum oxide ($\gamma \text{ Al}_2\text{O}_3$) [169] formed on the surface of the droplets enhances the probability of rupture during impact of the SiC_p with the atomized droplets.

It is anticipated that the type of oxide present on droplets 25 μm in diameter will consist of primarily brittle and crystalline oxides ($\gamma\text{Al}_2\text{O}_3/\gamma\text{LiAlO}_2$) [169, 170], since the time associated with the droplet flight is only a fraction of second. This minimizes the possibility of absorbing moisture on the oxide layer and forming stable oxides ($\text{Al}_2\text{O}_3 \cdot x\text{H}_2\text{O}/\text{Li}_2\text{O}$) as shown in Table 25, for equilibrium conditions. Furthermore, the large velocity difference between the SiC_p ($\sim 1\text{m/sec}$) and the atomized droplets (120-360 m/sec) and the impact energy during deposition are also likely to promote rupture of any surface oxide films formed on the surfaces of the matrix droplets. Once the surface of the SiC_p has been exposed to unoxidized, molten aluminum, the relatively high thermodynamic stability of the Al ($\Delta G^\circ \sim -220\text{ kCal}$ at 660°C) and Li ($\Delta G^\circ \sim -230\text{ kCal}$ at 660°C) oxides [172] will result in the reduction of any SiO_2 present on the surface of the SiC_p into Al_2O_3 , or Li_2O . The formation of Al_2O_3 and/or Li_2O at the Al/ SiC_p interface may result from the following reactions:



In view of the above discussion, one may anticipate that the Al/ SiC_p bond will consist of a series of layers involving Al, Si, Al_2O_3 , Li_2O and SiC. The aforementioned sequence of reactions is supported by the results of EDS analyses (see Figure 49), which revealed a high concentration of Si at approximately 2 μm from the interface while Si was not detected at a matrix location, 10 μm from the interface. In related studies, Kannikeswaran and Lin [167] showed through x-ray mapping the presence of a 2 μm Si rich interaction zone, slightly darker in appearance, near the surface of SiC_p .

The absence of interfacial reaction products in the as-sprayed deposited material, such as Al_4C_3 , can be attributed to the fast rate of heat extraction during atomization, and the absence of extensive liquid phase after impact with the deposition substrate (see Table 25). The formation of a strong interfacial bond can thus be attributed to : (a) the formation of a chemical bond between Si, O and Al atoms at the surface of SiC_p , and (b) the ability of aluminum to form a strong bond with its oxide (Al_2O_3) at the Al/SiC interface [109]. Both of these factors effectively increase the work of adhesion, W_{ad} , and therefore contribute to the wetting behavior observed in the present study.

The proposed mechanism accounts for the observed wetting of SiC_p by an Al-Li matrix during spray atomization and co-deposition processing, by taking into consideration the

processing history. This type of wettability, where the dynamic forces associated with the processing history play an important role in determining the extent of wetting and interfacial activity, and affect the resulting bond strength, is designated as dynamic wettability.

5.5. Conclusions

- i) The preliminary results presented in this study suggest that the interfacial activity during spray atomization and co-deposition processing promoted the formation of a stable Al-Li/SiC_p bond. This was confirmed by the fracture, rather than pullout, of the SiC_p during deformation.
- ii) The results of EDS analyses conducted on fractured SiC_p indicate that thermal conditions associated with spray atomization and co-deposition processing promotes diffusion of Al into SiC_p.
- iii) The absence of interfacial reaction products in the as-spray deposited material, as confirmed by TEM and SEM/EDS analyses, suggests that the temperature of the interface during deposition remained relatively low.
- iv) The concept of dynamic wettability is introduced to explain the wetting behavior in Al-Li/SiC_p observed in the present study.

CHAPTER 6

6.0 Microstructure, Excess Solid Solubility and Elevated Temperature Mechanical Behavior of Spray Atomized and Co-Deposited Al-Ti-SiC_p

6.1. Introduction

Dispersion strengthened, elevated temperature aluminum alloys derive their strength and thermal stability from the presence of a dispersion of nanometer-size particles which effectively impede dislocation motion during deformation. The strengthening characteristics of these particulates at elevated temperatures are dependent on their ability to resist coarsening, and therefore low diffusivities and limited or no equilibrium solid solubility are desirable [173]. Two approaches can be utilized to synthesize aluminum alloys containing a dispersion of thermally stable, nanometer-size phases. The first approach involves energetically blending a mixture of fine aluminum alloy powders with a ceramic phase, typically oxides, carbides or nitrides, to produce a matrix containing a distribution of well dispersed, incoherent fine particles. Since these ceramic particles typically have no solubility in the aluminum matrix, they provide effective high temperature strengthening. The origin of this approach may be traced to work on *sintered aluminum powders* (SAP) during the late 1940's and early 1950's that eventually became the predecessor of various mechanically alloyed aluminum products investigated ever since [174, 175]. The second approach involves precipitating a fine dispersion of transition metal aluminide phases from the matrix through solid state reactions. Since the addition of transition elements to α Al under the near-equilibrium conditions present during ingot solidification commonly results in the formation of coarse, embrittling second phases as a result of their limited liquid and solid solubilities, these are usually added under rapid solidification (RS) conditions. The highly non-equilibrium conditions present during RS lead to the formation of extended solid solutions and metastable phases; the former can subsequently be decomposed into a fine dispersion of thermally stable precipitates [176]. The addition of transition elements to aluminum alloys, in combination with RS processing, has been successfully utilized to produce manifold aluminum alloys containing complex second phase dispersoids based on additions of Fe, Ce, V, Si, Cr, Mo, Ti and Zr [177-184].

Among the family of transition metal, high temperature alloys, Al-Ti alloys are actively being studied as a result of their attractive combination of elevated temperature properties [182-184]. These materials derive their excellent strength, ductility, and creep resistance from their refined microstructure and dispersion of Al_3Ti particles, in combination with the low solid solubility (0.8 at.%) and low volume diffusivity (3.86×10^{-15} at.% cm^2/sec . at 427 °C) of Ti in Al [185]. In order to curtail the formation of coarse primary Al_3Ti , rapid solidification must be employed to extend the solid state solubility of titanium in

aluminum. For example, it has been reported that 1.4 weight percent titanium (the equivalent of 3.5 volume percent Al_3Ti at equilibrium) can be trapped in solid solution during gas atomization [186].

Al-Ti alloys are being studied as potential candidate matrix materials in metal matrix composites (MMCs) [99, 187] in an effort to further increase the alloys' modulus and strength. The extreme reactivity akin to high additions of Ti, and the difficulties associated with the processing of MMCs have prompted the development of alternate synthesis approaches. One such approach, spray atomization and deposition, is actively being studied as a result of its ability to rapidly quench, reinforce and consolidate in a single step, thus avoiding the difficulties associated with the handling of fine, reactive particulates [31, 99, 122, 123, 187]. This particular processing methodology involves the mixing of ceramic particulates and metallic matrix in a regime of the phase diagram where the matrix contains both solid and liquid phases. Ostensibly, such an approach will inherently avoid the extreme thermal excursions, with concomitant degradation in interfacial properties and extensive macrosegregation, normally associated with casting processes [15, 28]. Furthermore, this approach also eliminates the need to handle fine reactive particulates, as is often necessary with powder metallurgical processes [27, 105]. In analogous studies, other investigators have reported successful incorporation of SiC_p into an aluminum matrix using the Osprey process [106, 107, 117, 118] and a modified gas metal arc welding torch [34].

The objective of the present work was to provide insight into the effects of spray atomization and co-deposition processing on the resultant microstructure and elevated temperature properties of Al-Ti- SiC_p MMCs. In particular, this study sought to establish the effects of processing on the extended solid solubility of Ti in α Al.

6.2. Experimental Procedure

6.2.1 Processing

The matrix compositions of the Al-Ti matrix used in the present study were obtained by mixing an Al-6wt.%Ti master alloy provided by KBAloys Inc. (Robards, KY) with commercial purity Al (99.99%) provided by the Aluminum Company of America (Pittsburgh, PA). These two master alloys were mixed in order to obtain four target alloy compositions as shown in Table 26. In order to ensure dissolution of the primary Al_3Ti

intermetallic phase and to promote sufficient mixing during melting, the alloys were slowly heated (under a nitrogen atmosphere) in a zirconia crucible to the desired superheat temperatures as shown in Table 26. The melt was subsequently maintained at the superheat temperature for approximately 10-20 minutes prior to atomization. The chemical compositions of the materials were verified following the spray atomization and deposition experiments. The details regarding the type, size and distribution of SiC_p has been addressed in section 2.2.

Table 26. Experimental Parameters.

Variable	Experiment #				Units
	1	2	3	4	
Matrix alloy	Al-0.87Ti	Al-4.0Ti	Al-2.3Ti	Al-2.1Ti	wt. %
Reinforcement	---	--	SiC _p	SiC _p	--
Atomization pressure	1.72	2.73	1.38	1.21	MPa
Atomization gas	N ₂	N ₂	N ₂	N ₂	--
Superheat Temp.	1276	1573	1373	1573	K
Fluidized bed gas	---	--	N ₂	N ₂	--
Fluidization pressure	---	--	0.69	0.17	MPa
Metal flow rate	0.043	0.035	0.029	0.031	kg/s
Gas flow rate	0.015	0.024	0.011	0.010	kg/s

The details of the spray atomization and co-deposition processing has been described in section 2.2.1. Five experiments were conducted for this study. The primary experimental variables used during each experiment are listed in Table 26 (see section 2.2 also).

In this study, the SiC_p were introduced into the atomized Al droplets during atomization utilizing two different injectors (see Figure 52). The first injector, based on a fluidized bed principle, was used in order to obtain relatively low SiC_p volume fractions [122] (see Figure 52a). The second injector (see Figure 52b), designed utilizing a coaxial tube that entrained SiC_p as the gas flowed from the inlet to the outlet orifices, was used in order to obtain SiC_p flow rates which were higher than those achievable with the first injector.

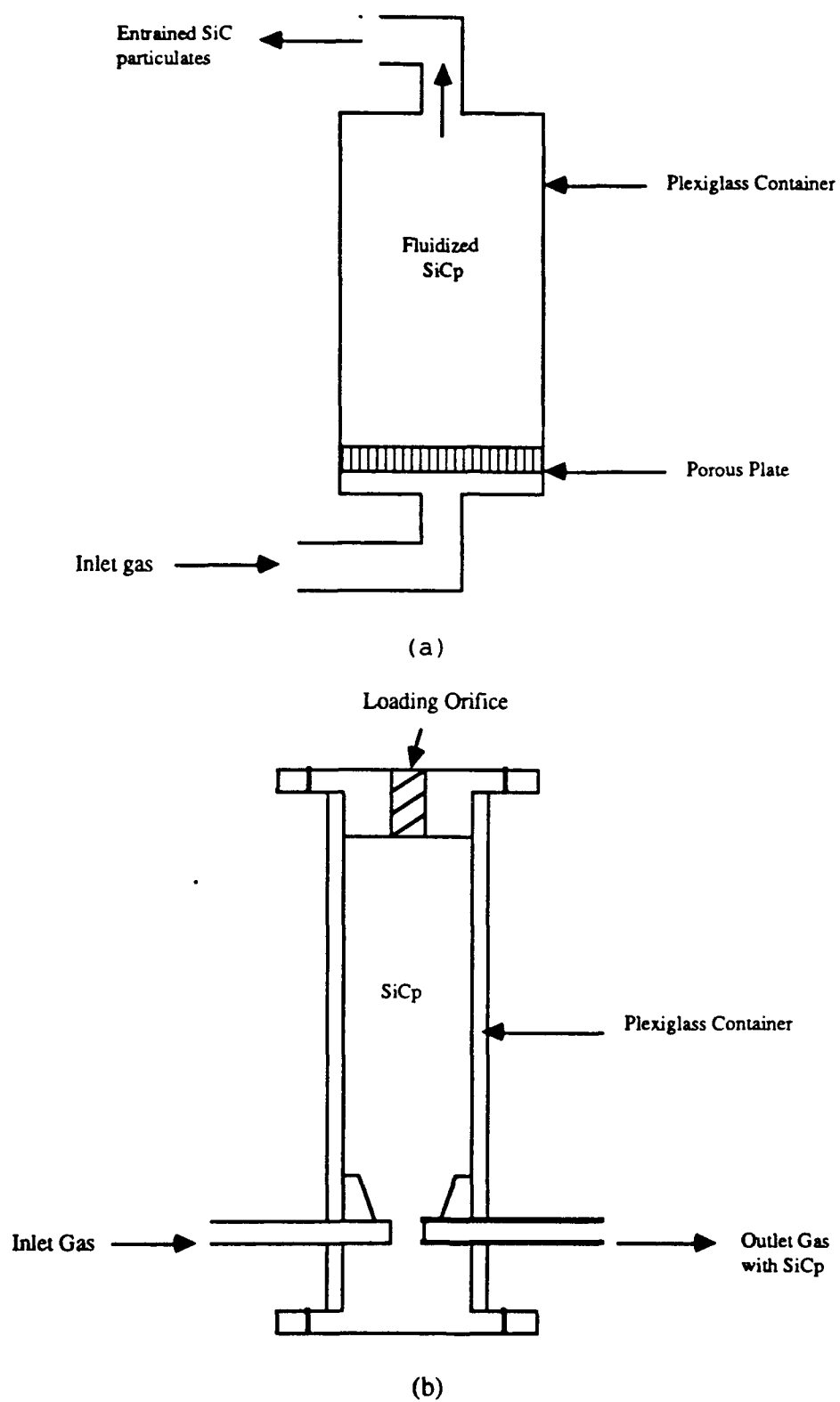


Figure 52. Schematic diagram showing: a) fluidized bed, and b) coaxial tube injector.

The description of fluidized bed used in the present study has been previously addressed in section 2.2.1. The physical characteristics and typical operating conditions for the fluidized bed used in the present study are shown in Table 27 and 28, respectively. The behavior of the coaxial injector is the subject of further study.

Four spray atomization and co-deposition experiments were conducted for the present study; the primary experimental variables used during each experiment are listed in Table 26.

Table 27. Input Parameters for Fluidized Bed.

Parameter	Value	Units
Bulk Density	780	kg/m ³
Particulate Density	3.1×10^3	kg/m ³
Particulate Size	5×10^{-6}	m
Volume of fluidized bed	1.74×10^{-3}	m ³
Density of Nitrogen	1.187	kg/m ³
Viscosity of Nitrogen	1.54×10^{-5}	kg/m s
Height of Fluidized Bed	0.18	m
⁽¹⁾ K	1.20	--

⁽¹⁾ The value of the K was determined experimentally from the mass flow rates of SiC_p[122].

Table 28. Typical Operating Conditions of Fluidized Bed.

w	0.75
⁽¹⁾ ΔP	7648.87 Kg m/sec ²
Re _{Dmf}	1.15×10^{-5}
Ga	0.0190
V _t	0.00274 m/sec
W _{SiC}	0.00293 kg/sec.
⁽²⁾ v _f of SiC	0.088

⁽¹⁾ Pressure drop across fluidized bed.

⁽²⁾ The volume fraction of the SiC_p was computed from the theoretical SiC_p mass flow rate, for a metal flow rate of 0.029 kg/second.

6.2.2. Microstructure

Microstructural characterization studies were conducted on both the unreinforced and reinforced materials in order to determine the density, grain size, volume fraction of SiC_p and the presence of secondary phases in the spray atomized and deposited samples. All of the microstructural characterization studies conducted for the present study were performed on material removed from the central 80-90 % portion of the preforms; the remaining 10-20 % of the preforms was considered too porous for detailed analysis.

Optical microscopy was conducted on polished and etched, as-received and as-deposited samples using conventional and Differential Interference Contrast (DIC) techniques; the use of DIC microscopy facilitated identification of the SiC_p in the matrix. The samples were sectioned to a thickness of 0.5 cm, polished using conventional techniques, and etched with Keller's reagent (0.5 HF-1.5 HCl-2.5 HNO₃-95.5 H₂O). The grain size was measured using the linear intercept method, as described in ASTM E 112-84.

Density measurements were conducted on polished, as-spray deposited and thermomechanically treated samples utilizing Archimedes' principle. The weight of each sample was determined using a Mettler H78AR Analytical Balance with an accuracy of ± 0.0005 g.; Ethylene glycol was used as a fluid.

The volume fraction of SiC_p was determined using a chemical dissolution method. This method involved measuring the mass of composite samples, dissolving the samples in dilute hydrochloric acid (38.0% max.), followed by filtering to separate the SiC_p. The particulates were then subsequently dried and the weight fraction was determined. The weight fraction was then converted into volume fraction, $V_f(\text{SiC})$, using the following equation:

$$V_f(\text{SiC}) = \frac{\text{wt\% SiC}/\rho_{\text{SiC}}}{\text{wt\% SiC}/\rho_{\text{SiC}} + \text{wt\% Matrix}/\rho_{\text{matrix}}} \quad (46)$$

where, ρ_{SiC} and ρ_{matrix} represent the densities of SiC_p and matrix, respectively.

Scanning electron microscopy (SEM) studies were conducted on as-spray deposited, and as-spray deposited and thermomechanically treated samples using a HITACHI S-500

(UCI) and JEOL JSM T-200 (MEXICO) microscopes. Image analysis was conducted using an ImageSet image analysis system developed by Dapple Systems Incorporated. This procedure involved computerized analysis of SEM micrographs in order to determine the effects of thermal exposure on the size and distribution of Al_3Ti precipitates in the Al matrix. In addition, SEM studies were conducted on fractured samples in order to provide insight into the effects of Al_3Ti on the fracture morphology.

Transmission electron microscopy (TEM) studies were conducted using JEOL 100C (UCI) and JEOL STEM CX-100 (MEXICO) microscopes at an operating voltage of up to 300 kV on as spray deposited samples. The TEM studies were carried out in order to identify SiC_p and Al_3Ti precipitates, to investigate the effects of thermal exposure on the Al-Ti/ SiC_p interface, and to provide insight into the coarsening behavior of the Al_3Ti particulates. The TEM samples were prepared using the window technique in a solution of 1:3:: HNO_3 : CH_3OH at 12 V and 1.5 ma; the solution was maintained at a temperature of -10°C . In addition, samples were prepared using Struers twin jet polisher using a solution of 5% perchloric acid in ethanol, 0°C , 0.12A and $\sim 25\text{V}$.

6.2.3. Phase Analyses

X-ray profiles of the spray atomized and deposited reinforced and unreinforced materials were generated on a Rigaku $\theta/2\theta$ powder diffractometer, using a Cu tube operating at 45 KV and 15 ma. Several of the samples were also studied using a Siemens D-500 diffractometer (MEXICO) operating under similar conditions in order to confirm the results. The lattice parameter of the Al-Ti solid solution was extrapolated from the Nelson-Riley (N-R) function, assuming that the absorption factors of the α Al matrix and the Al_3Ti phases were identical [187]. The advantage of using the N-R function lies in its ability to incorporate both low and high incidence angles. Once the lattice parameter of Al-Ti solid solution was determined, the amount of Ti in solid solution was estimated from the data of Tonejc and Bonafacic [188]. Finally, the relative intensity of the Al_3Ti peaks was obtained by dividing the height of the $(113)_\gamma$ peak by the height of the $(111)_\alpha$ Al peak.

The amount of Ti present in α Al as a solid solution was also determined from microanalysis using a STEM CX-100 equipped with EDAX (MEXICO). The objective of these studies was to confirm the precise location of Ti in the matrix and provide a comparison with the X-ray results.

6.2.4. Thermomechanical Treatment

Following spray atomization and co-deposition, the materials were subsequently hot extruded at 275 °C, using an area reduction ratio of 16:1. The hot extrusion step was used in the present study in order to eliminate the micron-sized porosity normally associated with spray atomized and deposited materials [37]. The Al-6Ti ingot metallurgy (IM) material was also hot extruded under identical conditions in order to provide a valid comparison with the spray deposited and hot extruded materials.

In order to investigate the effects of thermal exposure on the microstructure and phases of the as-spray deposited and as-spray deposited and hot extruded materials, samples were exposed to temperatures in the 200-500 °C range, for times of up to 240 hours. In order to avoid surface oxidation, the as-spray deposited and hot extruded samples were encapsulated under an inert atmosphere and annealed at 250 °, 350 ° and 450 °C for 99 hours. Vicker's microhardness (MHV) and Rockwell B hardness measurements were made on spray-deposited and spray-deposited and hot extruded samples prior to and subsequent to thermal annealing. The microhardness measurements were determined on a Surface Physical Tester model M8 apparatus, using a 10 g load. The extruded Al-6wt.%Ti master alloy was also studied for comparison purposes. All of the hardness measurements were conducted at room temperature.

The smooth bar tensile properties were determined according to ASTM E8-81, using 0.64 cm diameter specimens, in an Instron testing machine at a constant crosshead speed of 0.254 mm per second. The specimens were allowed to equilibrate at temperature for 1 hour, and subsequently tested under a tensile load; the room temperature properties were also studied. All of the mechanical testing studies were carried out in an electrical resistance furnace under an inert atmosphere (Argon) with a temperature accuracy of ± 4 °C.

6.3. Results

6.3.1. Processing

The operating conditions for the fluidized bed used in the present study are shown in Table 28, and were calculated from Eqns. (3-9), in combination with the input parameters

shown in Table 27. Regarding the behavior of the fluidized bed, a few comments are in order. On the basis of Eqns. (3-9), one would anticipate that increasing the fluidization pressure would lead to an increase in the mass flow rate of the SiC_p , with a concomitant increase in volume fraction. It was noted, however, that the rate of increase in mass flow rate with pressure asymptotically reached a maximum value at a pressure of approximately 0.69 MPa, which corresponds to the fluidization pressure used in experiment 16 (see Table 26). This behavior is thought to be a result of the increased back pressure inside the fluidizing chamber at higher fluidization pressures [122]. If the theoretical value of the SiC_p mass flow rates and the mass flow rate of the metallic matrix are taken into consideration, it is possible to estimate an upper bound for the volume fraction of the SiC_p . These results yield an estimate of the SiC_p volume fraction as 8.8% for the conditions used in experiment 16. The results of acid analysis, however, reveal that the volume fraction of the SiC_p was 2 %. The discrepancy between the calculated and measured volume fractions of SiC_p may be attributed to difficulties encountered in estimating some of the parameters utilized in Eqns. (3-9). For example, determination of the average velocity of the fluidizing gas, v , requires a knowledge of the fluid flow conditions in the fluidized bed. Since these conditions were not accurately known, this velocity was determined from the experimentally measured volumetric gas flow rate through the fluidized bed. On the basis of the geometry of the fluidizing chamber and the bubbling tendency of the gas noted for some fluidization conditions, it is anticipated that the actual average velocity of the fluidizing gas will be lower than the computed value. The co-injection of SiC_p using a coaxial tube injector (see experiment 17), appeared to be more effective than the fluidized bed in achieving higher volume fractions; this injector is the subject of continuing research.

6.3.2. Microstructure

Optical microscopy was conducted on coupons of the as-received, unreinforced and reinforced Al-Ti materials; one example taken from experiment 14 is shown in Figure 53. This figure reveals the presence of an equiaxed grain morphology, with an average grain size of approximately 16 μm . Table 29 shows the grain size determined for each of the four experiments and for the as-received ingot metallurgy processed material before and after extrusion. The microstructure of the as-spray atomized and deposited material from experiment 16 is shown in Figure 54. The SiC_p are readily discernible in this figure as light second phases in the dark Al-Ti matrix. The microstructure of the as-spray

deposited unreinforced material from experiment 15 is shown in Figure 55. The presence of the Al_3Ti phase is readily discernible in this figure as elongated plate-like precipitates.

Table 29 Results of Density, Volume Fraction and Grain Size Measurements.

(1) Experiment Number	(2) $\rho_{\text{spd}}/\rho_{\text{th}}$	(3) Volume fraction (%)	(4) Interparticle spacing (λ , μm)	Average Grain Size (μm)
1	0.98	--	--	16.2
2	0.99	--	--	43.6
3	0.94	2	21.21	21.7
4	0.97	12	8.66	53.1
Al-6 wt. % Ti	--	--	--	(5) 138.0
Al-6 wt. % Ti	--	--	--	(6) 20.6

(1) See Table I.

(2) ρ_{spd} and ρ_{th} represent the density of spray deposited and spray deposited and extruded samples

(3) Determined from Eqn. (46)

(4) These values were computed from Eqn. (10) for a SiC_p size of $3.0 \mu\text{m}$.

(5) This value correspond to the as-received ingot metallurgy processed material.

(6) This value correspond to the as-received ingot metallurgy processed material after extrusion.

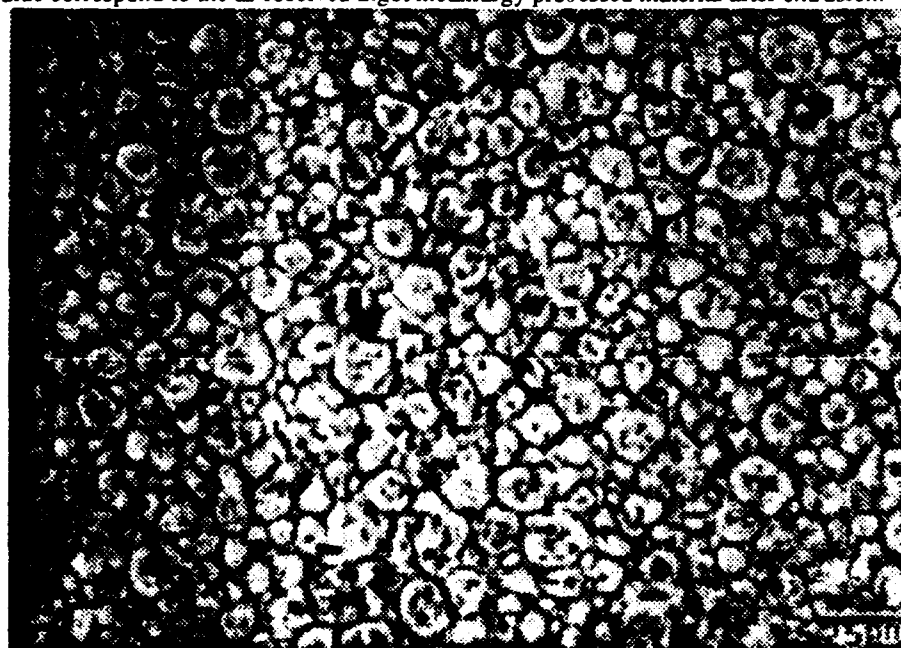


Figure 53. Optical micrograph from experiment 14 showing equiaxed microstructure of the Al-Ti material.

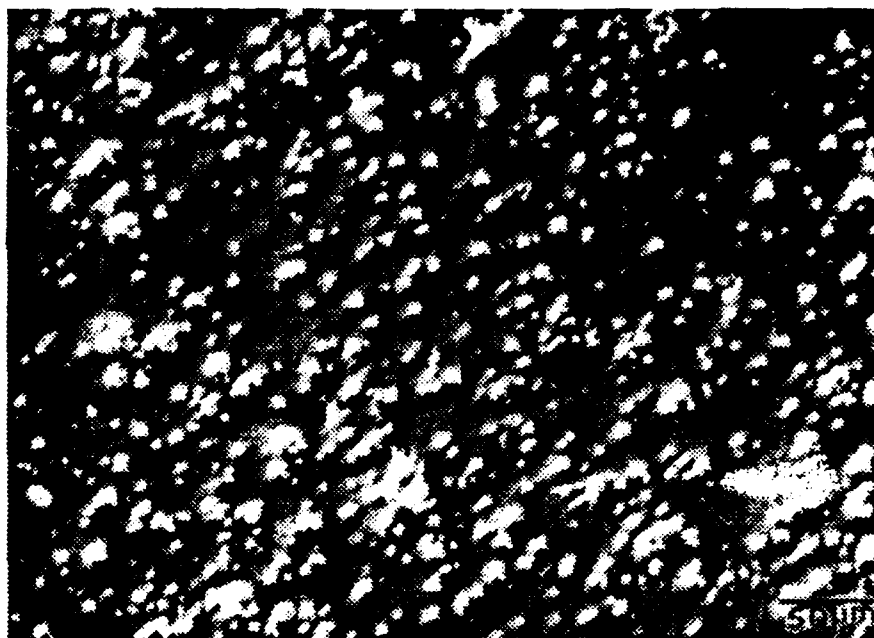


Figure 54. Optical micrograph showing the microstructure of the as-spray atomized and deposited material from experiment 16.

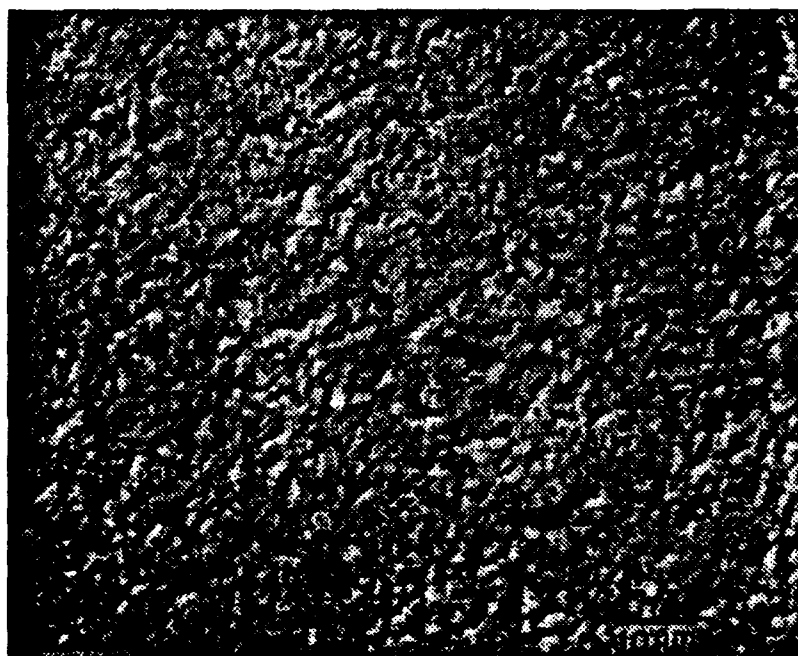


Figure 55. Optical micrograph of the as-spray atomized and deposited material from experiment 15.

The results of the density and acid test measurements are summarized in Table 29. The volume fraction of SiC_p present in the as-spray deposited material was estimated to be approximately 2 and 12 vol.% for experiments 16 and 17, respectively. The interparticulate spacings were calculated according to the formula used by Nardone and Prewo [7]

$$\lambda = (lt / Vf)^{1/2} \quad (10)$$

where λ is the interparticulate spacing; and t , l and f are the thickness, length, and volume fraction of the SiC_p , respectively (see section 2.3.2.2 also). The results of the computed interparticulate spacings, λ , are also shown in Table 29.

Scanning electron microscopy of samples removed from experiment 14 failed to reveal the presence of Al_3Ti precipitates. SEM analysis of materials from experiments 15, 16, and 17, however, did reveal the presence of secondary phases. One example, taken from the central portion of experiment 16, is shown in Figure 56. In this figure, the SiC_p exhibit an irregular morphology, whereas the Al_3Ti phase appears as elongated needles. Figures 57a and b, SEM micrographs taken from the central bottom region of experiment 16, show spherical Al powders decorated with irregular SiC_p particles. Careful observation of the Al powders reveals an internal cellular microstructure with cell boundaries decorated with irregular SiC_p . Inside the grain boundaries flower-like second phase (showed by an arrow) particles were observed, presumably of the type Al_3Ti . The presence of SiC_p and Al_3Ti phase in the Al-Ti matrix was confirmed using EDAX analyses.

In addition to SiC_p and Al_3Ti , SEM analyses revealed the presence of a finite amount of non-interconnected porosity (see Figure 57). The micron sized pores were preferentially located at grain boundaries and exhibited an irregular, faceted morphology. The distribution of pores in the microstructure was found to be bimodal, with a large proportion of pores in the 1-2 μm and 10 μm size ranges; the volume fraction of porosity was estimated to be approximately 1-6%, in agreement with the density results shown in Table 29.

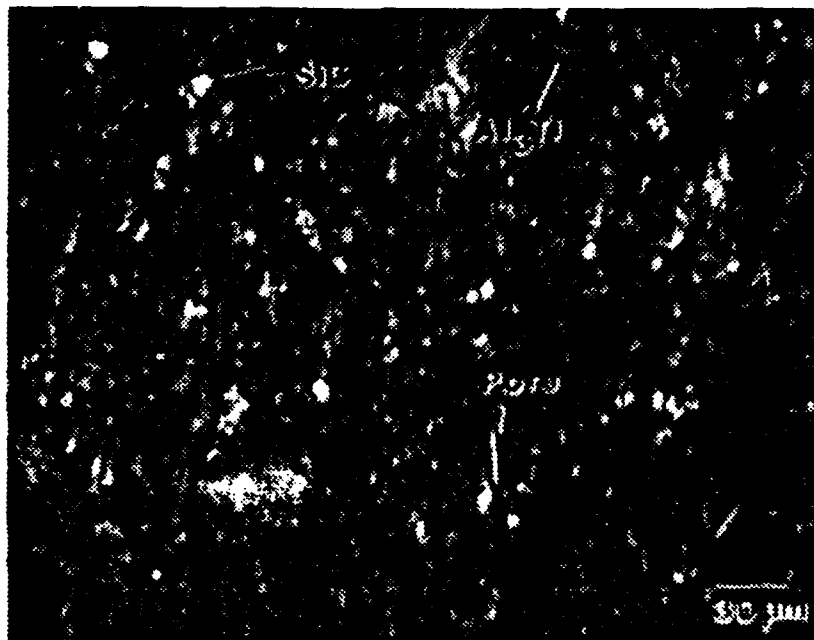
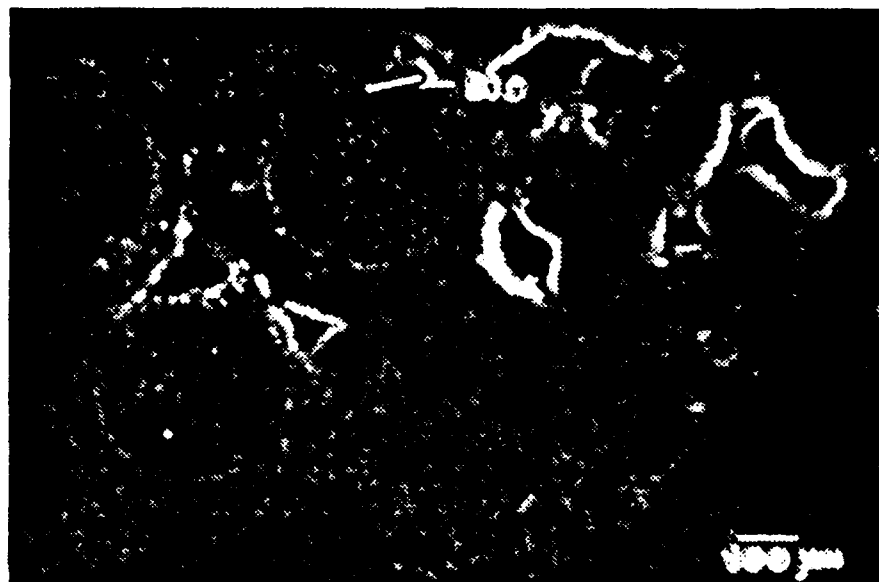
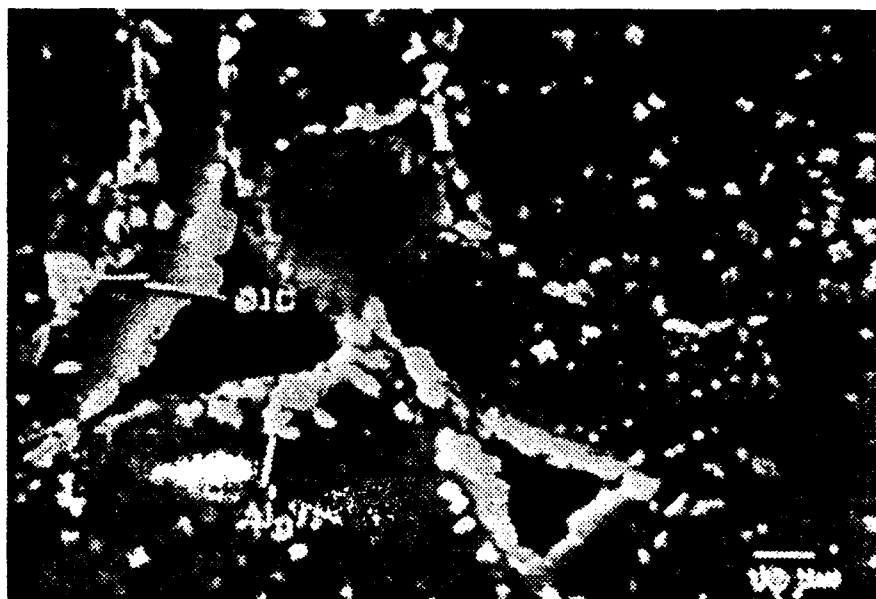


Figure 56. SEM micrograph taken from experiment 16 showing the presence of the SiC_p and Al_3Ti phases.



(a)

Figure 57. SEM micrograph taken from experiment 16 and showing: a) the presence of the SiC_p at the boundary of spherical particles and



(b)

Figure 57 (cont'd), b) flower-like Al_3Ti phases.

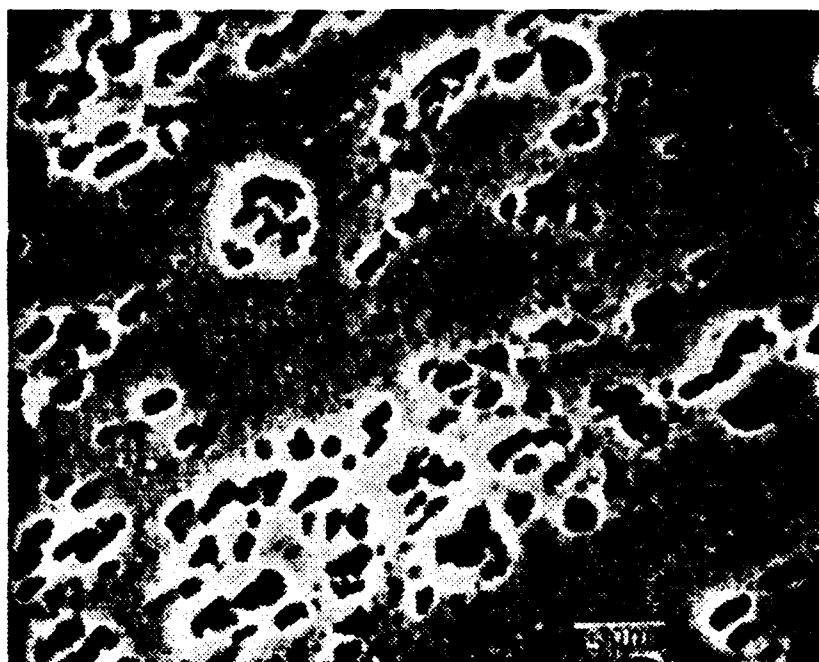


Figure 58. SEM micrograph of the spray deposited and hot extruded material, following a thermal anneal for 20 hours at 500 °C, showing the presence of Al-Ti phases. The specimen was etched using Kellers reagent.

The morphology of Al_3Ti phase, following hot extrusion and thermal annealing (20 hours at 500°C) from the sample taken from experiment 15, is shown in Figure 58. The plate-like Al_3Ti precipitates coarsened substantially, and their principal axis became aligned parallel to the extrusion direction (see Figure 58).

Transmission electron microscopy studies were conducted on samples in the as spray deposited and annealed conditions. Figure 59 offers a representative view of the as-spray deposited Al-Ti- SiC_p microstructure from experiment 16; the presence of a SiC_p (Figure 59a) is identified by means of its diffraction pattern. This spherical SiC_p was linked by dislocations. Also observable in the matrix, nanometric spherical second phase particles were looped by dislocations and formed subcells (see Figure 59b). Analysis of the diffraction patterns identified these nanometric second phases as SiC_p . It is possible that the presence of Al_3Ti in the microstructure may have affected the values of SiC_p volume fraction shown in Table 29. The results of a study by Chanda and co-workers [99] on

alloys of similar composition, however, show relatively good agreement with the present volume fraction results. In this study, they used image analysis, instead of acid dissolution, to determine the volume fraction of SiC_p present in the microstructure. The high dislocation density observed in the Al-Ti matrix adjacent to the SiC_p (see Figure 59) concurs with previous findings [16, 64]. The high dislocation density observed in MMCs is thought to result from the large difference in coefficient of thermal expansion (CTE) of Al and SiC_p (10:1) which causes thermal mismatch strains, ϵ , between reinforcement and matrix during solid state cooling. These strains are relaxed by the formation of a dislocation network, which in turn, alters the response of the MMC to thermomechanical processing, relative to that of unreinforced alloys [15, 16, 155].

In addition to SiC_p , TEM studies of the as-spray deposited material from experiments 15, 16, and 17 revealed the presence of plate-like second phase particles. These plate like particles were identified as the tetragonal Al_3Ti by means of its diffraction pattern.

The results of TEM studies, conducted on the as-sprayed samples taken from experiment 16 at the Al-Ti/ SiC_p interfacial region, failed to reveal the presence of any interfacial reaction products (see Figure 59), consistent with the results of SEM and X-ray analysis.

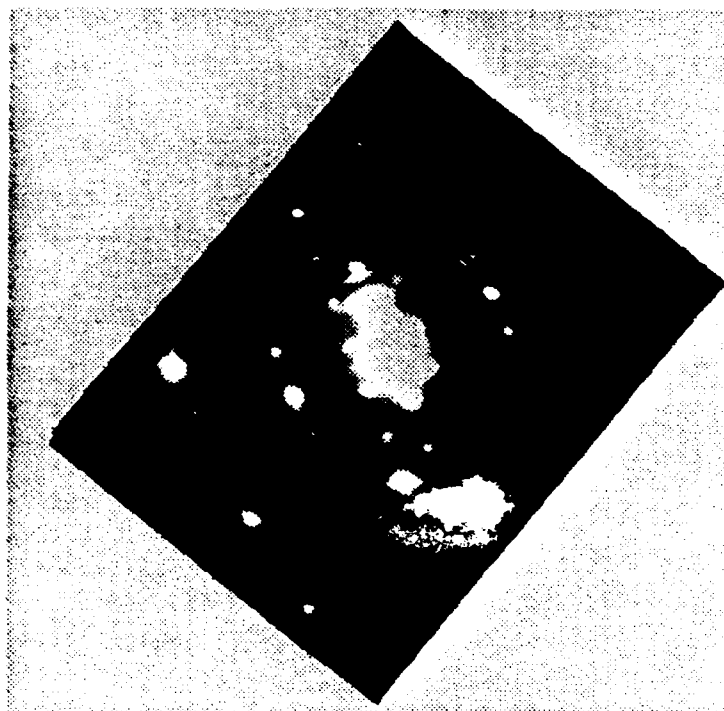


Figure 59. Transmission electron micrograph of the Al-Ti-SiC_p alloy from experiment 16 showing: a) a SiC_p (on the right hand side) which was identified by its diffraction pattern as cubic-SiC_p, and b) the presence of nanometric SiC_p which are linked by dislocations forming a subcell arrangement.

6.3.3. Thermomechanical Treatment

A comparison of the results of Rockwell hardness measurements conducted on coupons taken from the IM material with those of the material from experiment 16 in Figure 60a indicates the following. The IM results show a considerable loss in hardness at temperatures as low as 300 °C (see Figure 60a) whereas the material from experiment 16 remained thermally stable up to temperatures as high as 500 °C (see Figure 60a and 60b). The Rockwell hardness results for the material from experiment 16 were repeated using a microhardness tester in order to determine if the presence of SiC_p in the Al-Ti matrix affected the results obtained with a R_B hardness indenter. The microhardness results coincided with those obtained using the Rockwell indenter and furthermore, revealed an increase in hardness in the 300-400 °C range (see Figure 60b). The hardness results shown in Figures 60a and 60b were carried out at room temperature on specimens that were thermally annealed for 99 hrs at the designated temperature.

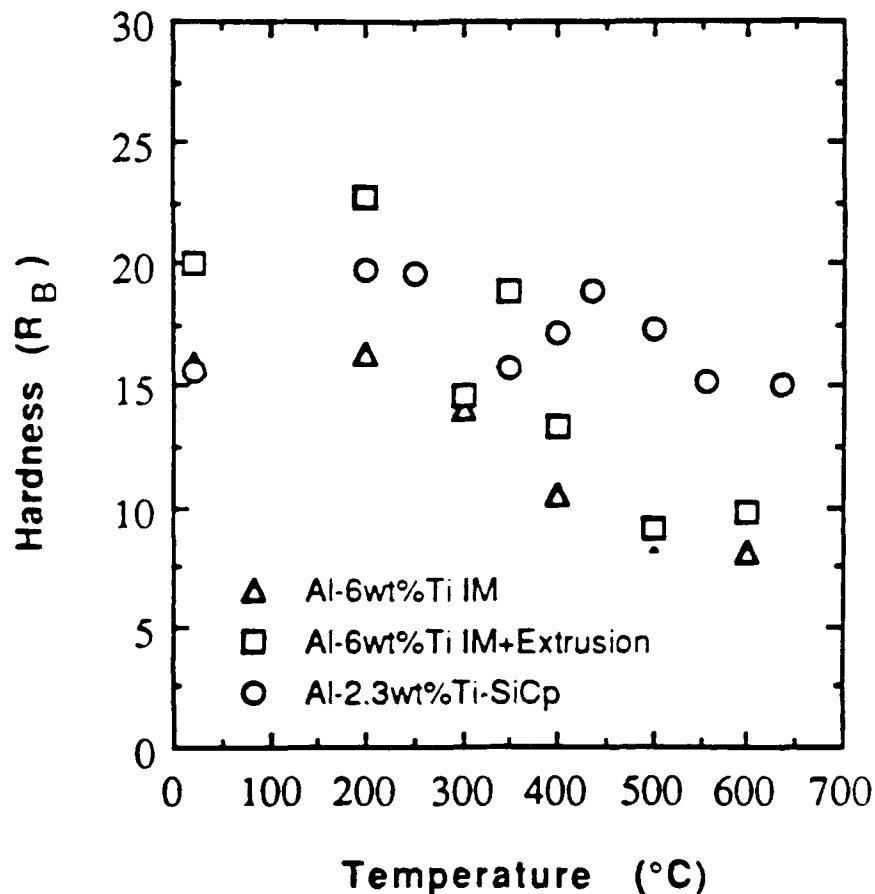


Figure 60. Hardness results showing the variations in: (a) Rockwell (R_B), and

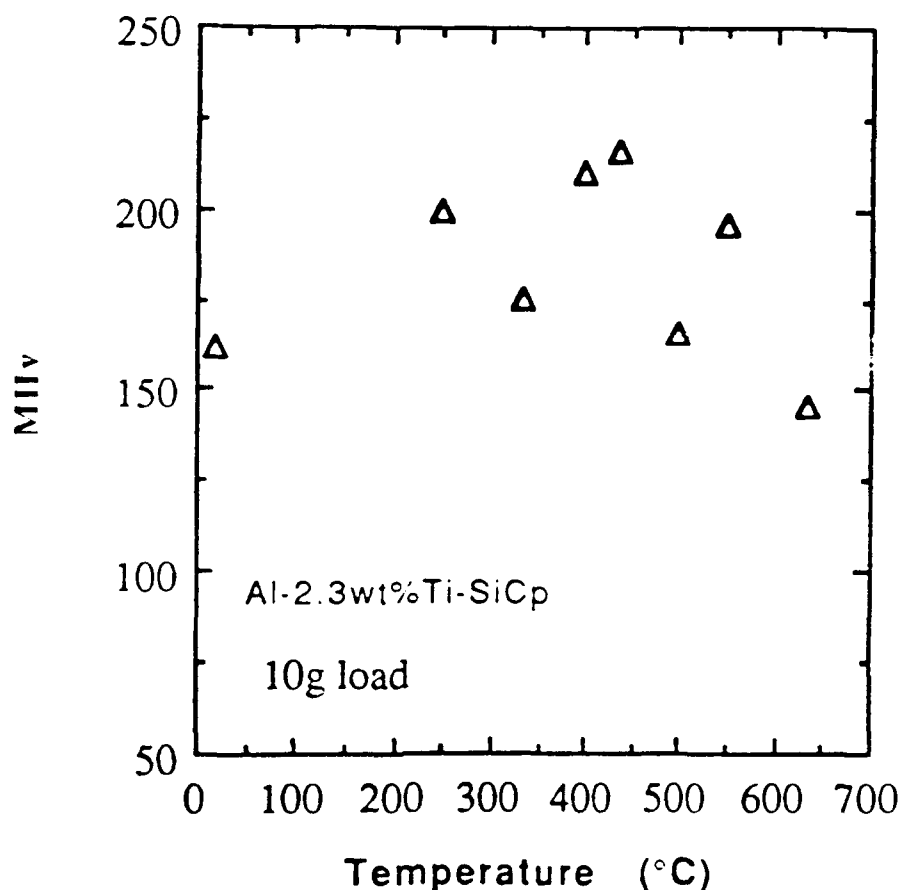


Figure 60. (cont'd) (b) microhardness (MHV) as a function of annealing temperature for the as spray atomized and deposited Al-Ti-SiC_p material from experiment 16.

The results of the elevated temperature testing of the spray atomized, deposited and hot extruded Al-Ti alloys (SD) are summarized in Table 30 and Figure 61, and compared to those of equivalent materials prepared by powder metallurgy (PM) and mechanical alloying (MA). The results shown in this table for the Al-4Ti and Al-2.3Ti-SiC_p materials were obtained after a 99 hour anneal, followed by mechanical testing at the designated temperature. The results shown in Table 30 and Figure 61 show that the elevated temperature properties of the spray deposited materials compare favorably to those of the powder metallurgical materials, are superior to those of the ingot materials, but are inferior to those of the mechanically alloyed material.

Table 30 Elevated Temperature Mechanical Properties of Al-Ti-SiC_p Materials.

Material	Processing	Temperature °C	σ_{UTS} (MPa)	σ_{YS} (MPa)	Elong. (%)
Al-2.3Ti-SiC _p (Experiment # 16)	(1)SD	25	200	198	7
		250	130	116	11
		350	51	48	18
		450	24	22	32
Al-4.0Ti (Experiment # 15)	(2)SD	25	250	235	7
		250	127	106	24
		350	57	51	23
		450	20	18	40
Al-4.0Ti	(3)PM	25	180	145	23
		200	100	95	22
		300	65	59	30
		400	42	35	30
Al-4.0Ti	(4)MA	25	--(5)	320	--(5)
		160	--	280	--
		240	--	190	--
		290	--	170	--
		350	--	150	--

(1) Spray atomized, deposited and hot extruded materials thermally annealed for 100 hrs at the designated temperature. The SiC_p size used here was 3 μ m; the volume fraction was 2%.

(2) Spray atomized, deposited and hot extruded unreinforced materials thermally annealed for 100 hrs at the designated temperature.

(3) Material prepared by powder metallurgy thermally annealed for 10 minutes at the designated temperature [184].

(4) Material prepared by mechanical alloying [184].

(5) No values were reported.

Figure 62 shows the fracture surface of a tensile sample of the as spray deposited and extruded material from experiment 16 and the fracture surface of the spray deposited, extruded and annealed material. The presence of dimples on the fracture surface indicates a ductile mode of fracture; careful examination revealed the presence of SiC_p inside some of the dimples. The apparent discrepancy between the dimple spacing and the SiC_p interparticulate spacing (see Table 29) suggests that the Al_3Ti phase may have also played a role in the plastic deformation of the matrix.

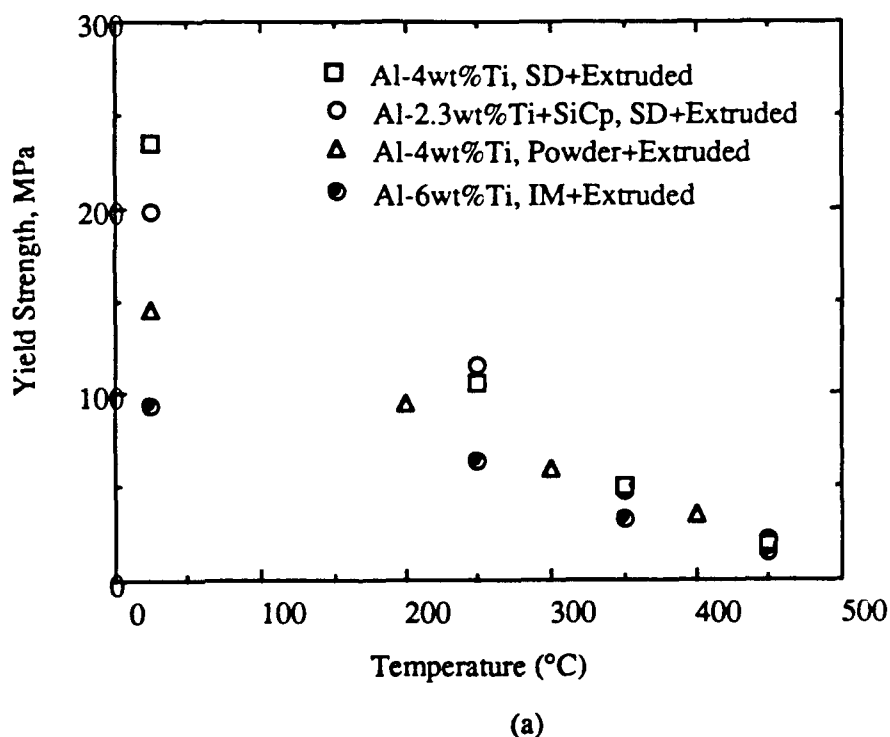


Figure 61. Comparison of the elevated temperature mechanical behavior of the spray atomized Al-Ti alloys to those of similar materials processed by powder metallurgy, and ingot metallurgy; (a) yield strength, and

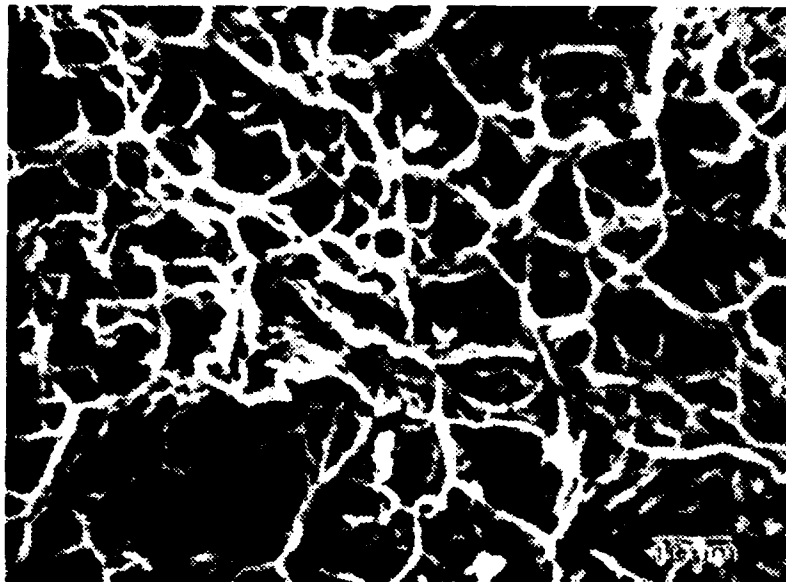
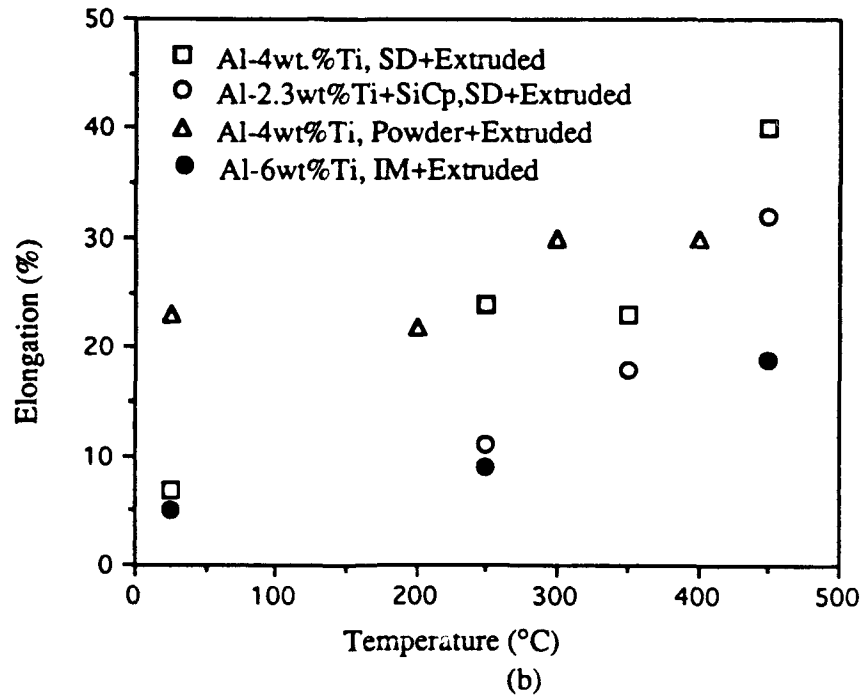
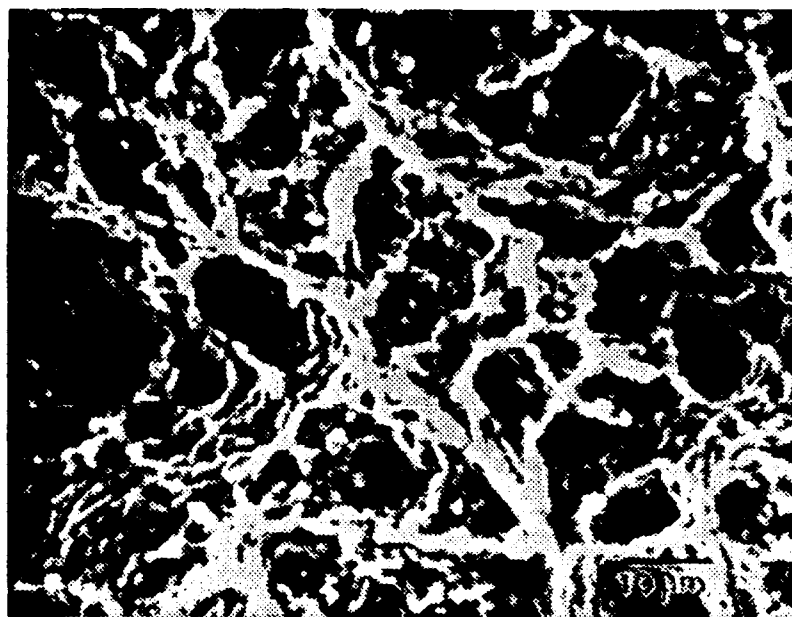


Figure 62. SEM micrograph showing the ductile mode of fracture as observed in: a) the spray deposited and extruded material and



(b)

Figure 62.(cont'd). b) spray deposited, extruded and annealed (350 °C for 100 hrs) material from experiment 16.

6.3.4. Quantitative Phase Analyses

Quantitative determination of the amount of Ti present in solid solution in the α Al matrix was accomplished on the basis of X-ray diffraction and STEM studies. Figure 63 shows one example, taken from as-spray deposited material from experiment 16. Peaks from the X-ray diffractogram were identified by means of the interplanar spacing, d_{hkl} and I/I_0 data reported in the literature [Search Manual for Selected Powder Diffraction Data for Metals and Alloys, JCPDS]. As can be observed in Figure 63, the diffractogram exhibits the peaks of Al, Al_3Ti and SiC_p . Following the work of Tonejc and Bonefacic [188], the X-ray results were analyzed using the Nelson-Riley (N-R) function, to determine the amount of Ti present in solid solution. These results, together with those determined using STEM microanalysis, are summarized in Table 31. The results from the annealing studies are shown in Figure 64 as the relative intensity of the Al_3Ti peaks, obtained by dividing the height of the $(113)_\gamma$ peak by the height of the $(111)_\alpha$ Al peak [184]. The results show an increase in the relative intensity of the Al_3Ti peak in 300-400 °C temperature range, a finding consistent with the microhardness results. The results shown in Figure 64 provide experimental support to the X-ray diffraction and STEM studies, which indicated the presence of a supersaturated solid solution of Ti in α Al.

Figure 63. X-ray diffractogram from material corresponding to experiment 16 showing the peaks corresponding to Al matrix, SiC_p and Al_3Ti phase.

Microanalyses were carried out on the plate-like second phase particles, and showed a composition of 63.6 wt% Al and 36.4 wt% Ti which according to its Al/Ti atomic ratio gives stoichiometry close to Al_3Ti . Microanalysis carried out on the spherical particles linked by dislocations (see Figure 59) showed a composition of 69.8 wt.% Si and 31.213 wt.% C, which gives a stoichiometry close to SiC_p .

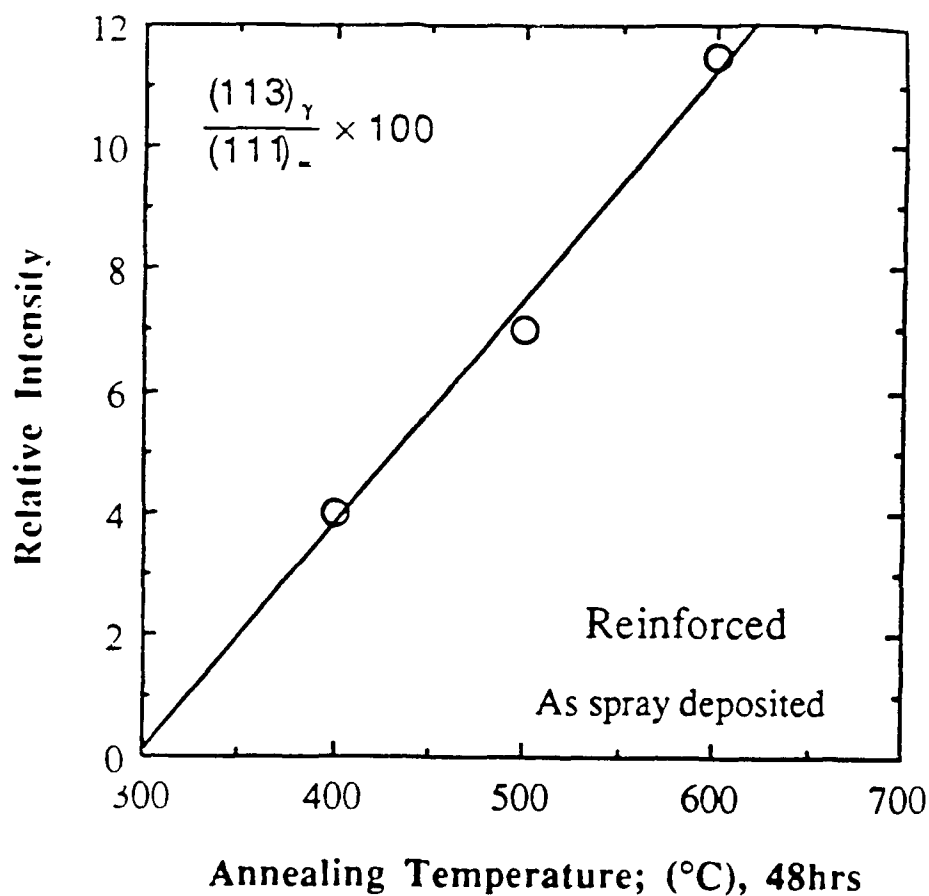


Figure 64. Schematic diagram showing the effect of annealing temperature on the relative intensity of the Al_3Ti peak on the as-spray deposited material taken from experiment 16.

Table 31. Results of the X-ray and Microanalytical Studies.

⁽¹⁾ Experiment #	⁽²⁾ a (Å°)	Wt. % Ti in solid solution	
		⁽³⁾ X-ray results	Microanalysis results
1	4.0444	0.87	Not Determined
2	4.0443	0.88	1.14 ± 0.10
3	4.0428	1.13	0.87 ± 0.05
4	4.0469	0.46	0.80 ± 0.06

⁽¹⁾ see Table 26.

⁽²⁾ the accuracy in lattice parameter is of the order of ±0.0001 Å°.

⁽³⁾ the value of wt.% Ti in solution for a given lattice parameter value is taken from Reference (188).

6.4. Discussion

6.4.1. Microstructure

Three salient features are associated with the microstructure of the spray atomized and co-deposited Al-Ti-SiC_p MMCs: the grain structure, the presence of micrometer sized pores, and the amount and distribution of reinforcing particulates. The grain morphology of the spray atomized and co-deposited MMCs was equiaxed (see Figure 53), in agreement with the results of other investigators [31, 64, 99, 100, 103, 104, 106, 107, 118, 122, 123, 138, 187, 189]. A more thorough discussion of these mechanisms can be found elsewhere [37]. The results from Table 29 show that the experimentally observed grain sizes for the unreinforced and reinforced spray deposited materials ranged from 16.2 to 53.1 μm . The relatively coarse grained microstructure noted for experiments 15 and 17 (43.6 and 53.1 μm , respectively), are consistent with the high melt superheat temperatures used during atomization for these two alloys in order to completely dissolve the Al₃Ti phase necessary as a result of elevated Ti content of the alloys. The smaller grain size obtained in experiment 15 (43.6 μm), relative to that obtained in experiment 17 (53.1 μm), is consistent with the higher atomization pressure used in experiment 15 (2.73 MPa), relative to that used in experiment 17 (1.21 MPa). A more thorough discussion of the effects of the atomization variables on the resulting microstructure obtained during spray atomization and deposition may be found elsewhere [31, 37, 104].

A second important microstructural characteristic frequently associated with spray atomized and deposited microstructures is the presence of a finite amount of non-interconnected porosity [31, 37, 64, 56, 75, 99, 103, 104, 107, 117, 118, 122, 123, 187]. The porosity levels present in the spray deposited materials used in the present study were in the 1-6% range, as inferred from the results of density measurements which showed densities in excess of 94% (see Table 29). Although the origin of porosity in spray atomized and deposited materials is poorly understood, the available experimental evidence suggests that a large proportion of the porosity is generally observed in spray atomized and deposited materials may be attributed to the interparticulate porosity. As the droplets descend, first on the deposition surface, and eventually on each other, they overlap leaving micron-sized cavities in between. In spite of the large amount of turbulence, the relatively rapid drop in temperature during deposition prevents any liquid phase present from filling all of the cavities present, leading to the formation of irregular pores. This mechanism is consistent with the observed correlation between deposition

conditions such as spray density, powder size, and fraction solidified, and the amount of porosity present throughout the deposit [56, 75, 79, 138]. For example, the higher density associated with the central region of the deposit has been attributed to the elevated mass flux of droplets in this region of the spray, relative to the periphery [190]. These droplets contain elevated fractions of liquid phase, effectively filling the interstices between droplets. In contrast, the high amount of porosity observed in the periphery of the deposit results from a large proportion of small, presolidified droplets. Under deposition conditions where the droplets are allowed to fully solidify before the arrival of more droplets, interlayer porosity will also develop in the regions separating the different droplets. In general, however, this is not a desirable condition since the presence of these discontinuities in the microstructure will lead to less than optimum mechanical behavior. Finally, although an investigation of the role of the SiC_p on the evolution of porosity during spray atomization and deposition was outside the scope of the present study, it is highly probable that the presence of the particulates will affect the porosity present [122]. Other mechanisms proposed to govern the formation of porosity in the spray deposited materials has been discussed in section 1.4.3.

The resultant amount and distribution of reinforcing particulates is significant because the mechanical behavior of the MMCs will depend on the amount and distribution of these particulates in the matrix. The volume fraction of SiC_p present in spray atomized and co-deposited materials has been correlated with a number of processing parameters and physical properties, such as: injection angle, injection pressure, SiC_p /metal mass flow ratio, and surface tension of the atomized droplets [31, 122, 124, 191]. The SiC_p are incorporated into the Al matrix by two possible mechanisms: a) the SiC_p penetrate the atomized droplets during co-injection and remain entrapped in the matrix during subsequent impact with the deposition surface [124] or b) the SiC_p remain on the surface of the atomized droplets and are entrapped by the matrix after impact with the deposition surface. Gupta and co-workers [31, 122] propose that the extent of particulate entrapment after impact will depend on the magnitude of the impact and repulsive forces present at the metal/ceramic interface. If entrapment fails to take place either during co-injection, or subsequently, during deposition, the microstructure of the spray atomized and co-deposited materials will be characterized by a high concentration of ceramic particulates at the prior droplet boundaries. Such a situation has been reported by Ibrahim and co-workers [192] for a spray atomized and deposited 6061 Al/ SiC_p MMC.

One way to provide insight into the extent of SiC_p entrapment taking place during the present experiments is to compare the calculated droplet sizes to the measured SiC_p interparticulate spacings (see Tables 29 and 33). The results show that the interparticulate spacings in materials from experiments 16 and 17 were substantially smaller than the average droplet size, d_{50} , suggesting entrapment of the SiC_p by a large proportion of the droplet population. The value of the interparticulate spacings shown in Table 17, however, appeared to be of the same order of magnitude as the diameter of the d_{16} droplets. This finding is consistent with observations made in regions of the spray atomized and deposited materials that contained a large proportion of small, pre-solidified droplets with diameters close to d_{16} and is evident from Figure 57 where the SiC_p may be seen decorating prior droplet boundaries. In general, however, numerous experimental observations showed a relatively homogeneous distribution of SiC_p in the Al-Ti matrix (see Figures 54 and 56). On the basis of the present data, it was not possible to determine whether the entrapment of the SiC_p occurred during atomization, or subsequently, during deposition. Further work is continuing in this area.

6.4.2. Secondary Phases and Thermal Stability

The addition of transition elements to α Al under the equilibrium conditions present during ingot solidification commonly results in the formation of coarse, embrittling second phases as a result of their limited liquid and solid solubilities. The presence of intermetallic phases in the matrix leads to a rapid degradation in mechanical properties with thermal exposure, since the large interparticulate spacing associated with these particles is not effective in preventing dislocation motion. In addition, these coarse intermetallic phases contribute to stress concentration during deformation, leading to early crack nucleation and eventual failure. In contrast, when refined and distributed by rapid solidification, intermetallic phases can effectively improve thermal stability as a result of their resistance to coarsening and increased temperatures for decomposition on ageing [176].

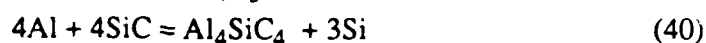
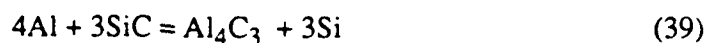
The available experimental evidence shows that the microstructure of the spray atomized and deposited MMCs was characterized by the presence of supersaturated solution of Ti in α Al, with interdispersed Al₃Ti precipitates throughout the matrix. The presence of the Al₃Ti phase is evident in the materials from experiments 15, 16, and 17 (see Figures 56, 57 and 61). One notable exception was the material from experiment 14, in which the

Al_3Ti phase was not detected (see Table 31): X-ray and STEM results showed all of the Ti in solid solution.

The Al_3Ti aluminide phase can be formed by both primary solidification and peritectic transformation [193]. A peritectic phase transformation occurs at 665 °C and 1.15 wt.% Ti¹²: $\text{L} + \tau(\text{Al}_3\text{Ti}) \Rightarrow \text{Al}$. The precise wt. % Ti contained in the first solid to form is reported to be between 1.15-1.3 % [194, 195]. The coarse plate-like morphology of the Al_3Ti phase, as seen in Figure 56, suggests that this particle evolved from a peritectic precipitation reaction in the temperature range of 1000 °C to 665 °C. The flower shape morphology of Al_3Ti phase as sometimes observed throughout the microstructure (Figure 57) is thought to arise presumably as a result of the grouping together of elongated rectangular plates.

Following hot extrusion and thermal annealing (20 hours at 500 °C), the plate-like Al_3Ti precipitates coarsened substantially, and their principal axis became aligned parallel to the extrusion direction. The plate-like phases are readily discernible in the SEM micrograph shown in Figure 58. In addition to coarsening, precipitation of the Al_3Ti phase from the supersaturated aluminum matrix during thermal exposure of the hot extruded reinforced material was evident. Since the lattice parameter of α Al changes only slightly with the addition of Ti, the results from the annealing studies are shown in Figure 64 as the relative intensity of the Al_3Ti peaks, obtained by dividing the height of the $(113)_\gamma$ peak by the height of the $(111)_\alpha$ Al peak. The results shown in this figure concur with the results of thermal stability, because an increase in the relative intensity of the Al_3Ti peak corresponds to the observed increase in hardness levels for the 300-400 °C range (see Figure 60). The results of hardness measurements shown in Figure 60a and 60b suggest that the as-spray atomized and deposited material from experiment 16 remained thermally stable for temperatures of up to 500 °C. In comparison, the cast and cast-and-hot extruded IM Al-6Ti materials suffered a considerable loss of hardness at temperatures as low as 300 °C (see Figure 60a). The microhardness measurements results shown in Figure 60b confirm the previous observation that the as-spray deposited material remains thermally stable up to 500 °C. It is also evident from the results shown in this figure that the hardness of the material increases in the 300-400 °C range. This behavior, which has been reported by other investigators, has been attributed to the precipitation of the Al_3Ti phase [184].

The higher thermal stability of the spray atomized and deposited materials observed in the present study, relative to that noted for the cast ingot material, may be attributed to the faster quench rates, with concomitant microstructural refinement resulting from the spray deposition stage. This suggestion is supported by the sharp reduction in grain size and the absence of primary Al_3Ti phase observed for the as-spray deposited reinforced materials, relative to that of the as-cast Al-Ti ingot. In addition, the relatively high rates of heat extraction during atomization and the short thermal exposure during deposition did not allow the formation of interfacial reactions products at the Al-Ti/SiC_p interface. Experimental support is provided by the SEM, TEM, and X-ray results which failed to reveal the presence of Al_4C_3 phase, normally observed in the Al based MMCs not containing Si additions [167]: the TEM micrograph shown in Figure 59, where the surface of the SiC_p is relatively smooth, suggests little or no interfacial activity. In the Al/SiC system, interfacial phases such as Al_4C_3 and Al_4SiC_4 normally form either as a continuous layer or isolated precipitates [167]. SiC is known to react with molten Al ($T > T_m$) according to the reactions:



Further growth occurs, i.e. the case of the first reaction, by solid state diffusion through the Al_4C_3 layer, and in the case of the second reaction, by the dissolution of the SiC into liquid Al. Significantly the latter reaction is anticipated on the basis of thermodynamics, but the presence of the Al_4SiC_4 has yet to be confirmed experimentally. Although the bonding between SiC and Al_4C_3 is reportedly strong, the Al_4C_3 -SiC interface is generally rough and can lead to regions of stress localization. These results were also supported by those obtained from the X-ray analyses which failed to reveal the presence of Al_4C_3 peaks in the diffractogram (see Figure 63).

The formation of a metastable solid solution of Ti in α Al is unexpected in view of both the low equilibrium solid solubility exhibited by this system and the quench rates present during spray deposition which are considerably lower than those used during gas atomization. In the following section, the various factors affecting excess solid solubility are discussed in light of the present experimental findings.

6.4.3. Excess Solid Solubility

An enthalpy model [38, 71-73, 102], was used in the present study to provide insight into the effects of processing variables on the distribution of droplet sizes, cooling rates and fraction solidified during atomization and co-injection. The mathematical formulation associated with this model and the related assumptions are described in detail elsewhere, and hence will not be reproduced here [38, 72].

Taking into consideration the physical characteristics and processing variables used in the present study (see Table 26 and 32), the aforementioned enthalpy model was used to compute the cooling rate and fraction solid as a function of flight distance for the Al-Ti and Al-Ti-SiC_p experiments. The numerical results are summarized in Table 33. In the following paragraphs, the salient microstructural features observed in the spray atomized and deposited Al-Ti-SiC_p and Al-Ti materials are discussed concurrently with the numerical results. It is important to note, however, that the enthalpy model used in the present study was developed for monolithic materials, and therefore did not incorporate the effects of the SiC_p on the cooling and solidification behavior of the atomized droplets. Hence, the differences in the computed solidification behavior between the reinforced and unreinforced experiments solely reflect the effects of changes in the processing parameters. The possible effects that the SiC_p might have on the thermal and solidification behavior of the atomized Al-Ti droplets are discussed subsequently.

Excess solid solubility is one of the most critical features associated with rapid solidification processing [176, 196]. Various factors influence the extent to which excess solid solubility may be obtained in a particular alloy system. These include the thermodynamic characteristics of the alloy system [82], the cooling rate [188], the velocity of the solidification front [197-199], and the extent of undercooling prior to nucleation of the solid phase [200, 201]. The formation of a supersaturated solid solution is further complicated during spray atomization and deposition processing as a result of the extreme differences in solidification environment prior to, and after impact with a deposition surface. For example, whereas a 80 μm aluminum droplet is exposed to relatively high cooling rates ($0.4 - 1 \times 10^4$ K/sec.), and consequently relatively fast solidification growth velocities (0.2-2.0 m/sec.) [73], the cooling rate after impact is relatively slow (10-20 K/sec.) [75, 106]. In related studies, Ruhr and co-workers [202], estimated the amount of Mn retained in solid solution during spray deposition of an Al-6.5Mn-2.35Li-0.80Zr (wt.%) using X-ray diffractometry techniques. By measuring the

dependence of the (331) Al interplanar spacing on Mn content, it was determined that $2.20\text{-}2.25 \pm 0.10$ Mn remained in solid solution in the α Al matrix after deposition, and an *effective* cooling rate in the range of $5 \times 10^2 - 1 \times 10^3$ K/sec. was suggested.

Table 32. Input Parameters Used in Numerical Model.

Variable	Description	Value	Units
C_{pg}	Specific heat of nitrogen	1070.4	J/kgK
C_{pm}	Specific heat of Al	860	J/kgK
H_f	Heat of fusion of Al	398000	J/kg
k_m	Al thermal conductivity	209	W/mK
ρ_m	Al density	2700	kg/m ³
γ	Ratio of C_p/C_v for gas	1.43	--
σ_m	Melt surface tension	0.840	kg/s ²
ρ_g	Gas density	3.375	kg/m ³
μ_g	Gas viscosity	1.54×10^{-5}	kg/ms
μ_m	Melt viscosity	0.001	kg/ms

In order to provide insight into the present experimental findings while maintaining the problem tractable, the enthalpy model introduced in the results section was used to calculate the fraction solidified and the cooling rate corresponding to a particular droplet diameter; the results are summarized in Table 33. A few comments regarding the cooling rates shown in this table are in order. For cases where the droplet was completely solidified prior to impact with the deposition surface (e.g., $f_s = 1$), the cooling rate shown was averaged over the residence time from the beginning to the completion of solidification. For cases where the droplet was completely liquid prior to impact with the deposition surface (e.g., $f_s = 0$), the cooling rate shown in Table 33 reflects the cooling rate of the material after impact with the deposition surface. This cooling rate has been experimentally determined to be in the $1 \times 10^0 - 1 \times 10^3$ K/sec. range [75, 102, 106], and therefore, a cooling rate of 1×10^1 K/sec. was deemed appropriate for the conditions used

in the present work. Finally, for droplets that were partially solidified during impact with the deposition surface (e.g., $0 < f_s < 1$), the cooling rate shown in this table corresponds to the calculated cooling rate at this flight distance. Once the cooling rate corresponding to each droplet diameter was determined, the wt.% Ti in solid solution was estimated on the basis of a study by Kerr and co-workers [186].

Table 33. Computational Results Showing the Anticipated Retention of Ti in Solid Solution.

Experiment # % Ti	Droplet size (μm)	⁽¹⁾ Fraction solidified (---)	⁽²⁾ Cooling rate (K/sec.)	⁽³⁾ Max. wt retained
1	$d_{16} = 30.0$	1.00	4.73×10^5	$0.87 (1.92)^{(4)}$
	$d_{50} = 60.1$	0.38	9.20×10^3	$0.87 (1.35)^{(4)}$
	$d_{84} = 125.2$	0.00	1.00×10^1	0.30
2	$d_{16} = 14.0$	1.00	1.20×10^5	1.80
	$d_{50} = 28.0$	0.00	1.00×10^1	0.30
	$d_{84} = 61.0$	0.00	1.00×10^1	0.30
3	$d_{16} = 38.0$	1.00	1.67×10^4	1.44
	$d_{50} = 76.0$	0.18	8.68×10^3	0.82
	$d_{84} = 158.0$	0.00	1.00×10^1	0.30
4	$d_{16} = 44.0$	1.00	1.54×10^4	1.42
	$d_{50} = 88.0$	0.00	1.00×10^1	0.30
	$d_{84} = 185.0$	0.00	1.00×10^1	0.30

⁽¹⁾These values correspond to a flight distance equivalent to the position of the substrate.

⁽²⁾The values of the cooling rate are reported as follows: for $f_s = 0$, cooling rate = cooling rate after deposition; $f_s = 1$, cooling rate = average cooling rate experienced by droplet in two phase stage; and when $0 < f_s < 1$, cooling rate = calculated cooling rate corresponding to flight distance.

⁽³⁾The values shown are the maximum anticipated values based on the cooling rate shown in column 4.

⁽⁴⁾In this case the computed values (shown in parentheses) exceeded the actual Ti contents of the alloy.

Following the calculation of the maximum anticipated value of wt.% Ti retained in solution for each droplet size, the wt.% Ti retained in the deposit, wt.% Ti_{deposit}, was estimated using the following equation

$$\text{wt.\% Ti deposit} = 0.16 (\% \text{Ti}_{d_{16}} + \% \text{Ti}_{d_{84}}) + 0.68 (\% \text{Ti}_{d_{50}}) \quad (47)$$

where, $\% \text{Ti}_{d_{16}}$, $\% \text{Ti}_{d_{50}}$ and $\% \text{Ti}_{d_{84}}$, represents the maximum anticipated value of wt. % Ti retained in the d_{16} , d_{50} , and d_{84} droplets, respectively. The value of the coefficients used in Eqn. (47) were selected on the basis of the log-normal distribution of droplets normally associated with atomization processes [37, 102]. The results obtained using Eqn. (47) show that the wt.% Ti retained in solid solution for experiments 14-17 correspond to: 0.78, 0.54, 0.84, and 0.48, respectively. Comparison of these results to those determined experimentally (shown in Table 31) lead to the following observations. First, the microanalysis results appeared to be consistently higher than those determined using X-ray analysis. Although, results for experiment 16 offer one exception, this discrepancy may be explained by the presence of the Al_3Ti phase throughout the matrix, which made accurate microanalysis difficult. Second, there appeared to be a fairly good agreement between the calculated results and those obtained from X-ray analysis, although the calculated values were consistently low (with the exception of experiment 17). This finding is not unexpected if one considers that the results from microanalysis represents the local amount of Ti in solution, whereas the X-ray results represent the global Ti contents in the α Al matrix. The extremely low amount of Ti in solid solution that was calculated for experiments 15 and 17, on the basis of Eqn. (47), may be attributed to the extremely high value of the superheat temperature used in these particular experiments. A high superheat temperature will lead to an increase in the amount of thermal energy that must be dissipated from the atomized droplets during solidification, delaying the onset of solidification. The results of Trapaga and co-workers [203] show that although the initial cooling rate of a fully liquid droplet impacting at the substrate is higher, the arrival of other fully liquid droplets onto this initial layer tends to decrease the overall cooling rate in the deposit. This is further complicated by the presence of presolidified droplets during impact. Work in this area is continuing.

Comparison of the results obtained from experiment 16 to those from experiment 17 provides some insight into the effects associated with the presence of SiC_p . The calculated results and those from X-ray analyses show that the material from experiment 17, containing 12 vol. % SiC_p (experiment 17), retained approximately 50% of the wt.% Ti in solid solution when compared to the material containing only 2 vol. % SiC_p (experiment 16). Some remarks on the possible effects of SiC_p on the interfacial velocity during solidification are pertinent. The presence of SiC_p in front of the interface during solidification increases the viscosity of the liquid and slows down the velocity of

interface. This concept was used by Stefanescu and co-workers [97] in explaining particulate entrapment. Accompanying a reduction in interface velocity will be an increase in the probability that Ti will come out of solution and precipitate in the form of Al_3Ti . Furthermore, the high level of superheat used in experiment 17 will most likely have contributed to the observed low amount of Ti in solid solution, by delaying the onset of solidification until after impact with the deposition surface. Numerical results (Table 33), which show that a large proportion of the droplets were completely liquid at this flight distance, support this hypothesis.

In the above discussion, the excess solid solubility of the spray atomized and co-deposited materials was rationalized on the basis of the cooling rate and the processing conditions used. Other factors, such as local undercooling and interfacial velocity, will affect the formation of an extended solid solution. Nevertheless, our results suggest that the formation of an extended solid solution during spray atomization and deposition processing is closely linked to the solidification environment of the droplets prior to impact.

6.4.4. Elevated Temperature Mechanical Behavior

A summary of the elevated temperature mechanical behavior of the spray atomized, deposited and hot extruded Al-Ti alloys (SD) is shown in Table 30 and Figure 61 and compared to those of equivalent materials prepared by powder metallurgy (PM) and mechanical alloying (MA). The results shown in this table for the Al-4Ti and Al-2.3Ti-SiC_p materials were obtained after a 99 hour anneal, followed by mechanical testing at the designated temperature. The results in Table 30 and Figure 61 shows that the elevated temperature properties of the spray deposited materials compare favorably to those of the powder metallurgical materials, are superior to those of the ingot materials, but are inferior to those of the mechanically alloyed material. The excellent mechanical properties of the mechanically alloyed materials can be attributed to the development of a fine dislocation-precipitate (oxides and carbides) network during alloying that effectively stabilizes the microstructure during deformation [177-180, 182]. The higher thermal stability of the spray atomized and deposited materials, relative to that noted for the cast ingot and extruded material, can be attributed to the faster quench rates, with concomitant microstructural refinement resulting from the spray deposition stage. This observation is supported by the sharp reduction in grain size and the absence of primary

Al_3Ti phase observed for the as-spray deposited reinforced material, relative to that of the as-cast Al-Ti ingot.

Inspection of the σ_{YS} values from Table 30 shows that at 250 °C the MA and SiC_p containing spray deposited materials retained 60% of their room temperature yield strength whereas the unreinforced spray deposited and PM materials retained only 45-50%. The higher thermal stability of the spray deposited material, relative to that obtained with the PM material, can be attributed to the coarser grain size of the former (21.7 μm) relative to that of the latter (1-5 μm). In addition, it is likely that the presence of a dislocation network in the vicinity of the AlSiC_p interface, as previously discussed, will enhance the thermal stability of the spray deposited material. Numerous studies have shown that the dislocation density found in as-quenched, age-hardenable Al alloys is low [204], typically less than $10^5/\text{cm}^2$, the dislocation density in reinforced Al matrices [205] is on the order of $10^{13}/\text{cm}^2$. These dislocations, generated in order to accommodate the thermal mismatch strains associated with the differences in the thermal coefficient of expansion of the matrix and the reinforcement, are located primarily at the reinforcement-matrix interface and decrease with increasing distance from the interface [205]. Finally, inspection of the σ_{YS} values obtained at 350 °C and shown in Table 30 suggests that, except for the mechanically alloyed material ($0.46 \sigma_{YS, RT}$), all of the alloys have lost a substantial fraction of their room temperature yield strength ($0.20\text{-}0.30 \sigma_{YS, RT}$) at this temperature.

The higher room temperature strength of the unreinforced spray deposited material, relative to that of the reinforced spray deposited material can be attributed to the higher concentration of Ti of the former (4 wt.%) relative to that contained in the latter material (2.3 wt.%). The presence of a distribution of nanometer size Al_3Ti particles in the unreinforced material will provide more effective strengthening relative to that which can be obtained with micron size SiC_p in the reinforced material. This relationship is evident from the Orowan equation, where the flow stress for a metal strengthened by a dispersion of secondary phases can be estimated from:

$$\tau = \tau_m + \frac{Gb}{l} \quad (48)$$

where τ_m is the matrix flow stress, G is the modulus of rigidity, b is the Burgers vector, and l is the planar center to center spacing between the dispersoids. Since interparticulate

spacing, λ , is inversely related to the number of particles for a constant volume fraction, a finer dispersoid will provide more effective strengthening.

Significantly, the room temperature flow stress of the spray deposited material was higher than that obtained for the powder metallurgical material, at the expense of elongation. This finding is unexpected in view of the fact that, on the basis of quench rates, the grain size of the powder metallurgical material should be substantially smaller than the grain size resulting from spray atomization and deposition. This behavior, although not clearly understood, is thought to be related to crystallographic induced strengthening resulting from the small diameter extrusions.

Regarding deformation and fracture, analysis of fractured samples from experiments 15 and 16, before and after thermal annealing, revealed the presence of a ductile mode of failure; Figure 62 shows one example from experiment 16. The extent of ductile fracture increased with increasing annealing time, consistent with the results from the elevated temperature tests which showed an increase in elongation at higher temperatures for both the unreinforced and reinforced materials (see Table 30). Regarding the morphology of the dimples it was noted that as the annealing time increased, the edges of the dimples became more irregular in both the unreinforced and reinforced materials, a phenomenon explicable as the precipitation of the Al_3Ti phase in the matrix as a result of thermal exposure.

6.5. Conclusions

1. The results presented in this paper suggest that spray atomization and co-deposition processing may be successfully utilized to manufacture high temperature Al-Ti metal matrix composites.
2. The results of X-ray and microanalysis studies revealed the presence of a supersaturated solid solution of Ti in α Al in the spray atomized and co-deposited material, with Ti concentrations in the 0.8 - 1.1 wt.% range. The formation of an extended solid solution was discussed in light of the cooling rates present during atomization, and subsequently, during deposition. The results from X-ray diffractometry studies showed extensive precipitation and coarsening of the Al_3Ti phase during thermal exposure.

3. The results of hardness studies suggest that the as-spray atomized and deposited materials remained thermally stable for temperatures of up to 500 °C. In comparison, the cast, and cast-and-hot-extruded IM Al-6Ti materials suffered a considerable loss of hardness at temperatures as low as 300 °C.
4. The elevated temperature properties of the spray deposited and extruded materials compared favorably to those of an equivalent alloy made by powder metallurgical materials, were superior to those of the ingot material, but were inferior to those of mechanically alloyed Al-Ti materials. The difference in mechanical behavior was discussed in reference to the microstructural differences noted among the three types of materials.

CHAPTER 7

7.0 Creep Behavior of Discontinuous SiC-Al Composites

7.1. Introduction

Metal matrix composites (MMCs) combine metallic properties (ductility, toughness and environmental resistance) with ceramic properties (high strength and high modulus). Accordingly, MMCs offer several advantages in applications where high strength, high modulus and good conductivities are desirable. Interest in MMCs for structural applications has increased in recent years as a result of (a) the availability of a wide variety of reinforcements, (b) the development of new processing techniques, and (c) the potential of producing superior MMC components for structural applications.

Of the MMCs having reinforcements in a discontinuous form (whiskers and particulates), silicon carbide reinforced aluminum alloys have attracted considerable attention for several reasons. First, SiC fibers, which are derived from rice hulls and which have led to the use of platelet and particulate SiC, are relatively inexpensive and can be produced in large quantities. Second, silicon carbide reinforced aluminum composites can be formed into useful shapes using conventional metal working processes such as forging and extrusion. Third, the composites exhibit isotropic properties with considerably improved strength and modulus compared to unreinforced aluminum alloys; accordingly, these composites are more suitable for general applications where the highly directional properties with continuously reinforced MMCs are not required.

In recent years, the high-temperature creep behavior of discontinuous silicon carbide reinforced aluminum alloys (whisker and particulate) has been the subject of creep investigations [84, 89, 110, 206-208] that aimed at assessing the potential of these composites for use as materials for high temperature applications. As a result of these investigations, several sets of experimental data are now available.

The purpose of this paper is two-fold: (a) to review and discuss the implications of the experimental data of creep investigations on discontinuous SiC-Al composites, and (b) to examine the origin of the high-temperature strengthening in these composites in the light of available suggestions and treatments.

7.2. Analysis and Discussion

7.2.1 Creep Investigations on SiC-Al Composites

Several experimental creep studies on discontinuous silicon carbide aluminum composites were reported (Table 34) and a summary of the results of these studies is given below in chronological order.

Webster [110] conducted compression creep tests on silicon carbide whisker reinforced aluminum composites containing 3 to 5 wt% Li in the temperature range of 505 K - 866 K. The results published by Webster [110] have revealed that lithium addition increases the strengthening effect of SiC_w at room and elevated temperatures; in addition to reducing density, the presence of Li enhances the wetting behavior of the composite. Despite this important finding, the creep data obtained by Webster only covered a very high range of strain rates; $10^{-3} \text{ s}^{-1} \leq \dot{\epsilon} \leq 5 \times 10^{-1} \text{ s}^{-1}$, where $\dot{\epsilon}$ is the compressive creep rate. Also, although the creep results were plotted as stress versus creep rate for various temperatures, no attempt was made to infer the apparent stress exponent or the apparent activation energy for creep.

Nieh [84] studied the creep behavior of SiC whisker and SiC_p reinforced 6061 aluminum composites in the temperature range of 505 K to 644 K. He has reported that while both types of composites exhibit steady-state creep, the whisker reinforced composite is more creep resistant than the particulate composite; this behavior was attributed to the difference in load bearing capabilities and the relative strengths of the two types of composites. Also, the results, as reported by Nieh [84], have indicated that the steady-state creep rate in both materials depends strongly on temperature and the applied stress; the stress exponent is very high ($n \approx 21$) and the activation energy is almost three times as high as the activation energy for self diffusion in aluminum, Q_D .

Nardone and Strife [206] examined the effects of stress and temperature on the creep behavior of SiC whisker reinforced 2124 aluminum (T4). They have reported that the stress exponent changes from a low value of 8.4 at 450 K to a high value of 21 at 561 K and that the measured activation energies are much higher than that for self diffusion in aluminum; the activation energy increases from a value of 277 kJ/mole in the temperature range of 423 K - 477 K to a value of 431 kJ/mole in the temperature range of 547 K - 575 K. These experimental results were interpreted in terms of an effective

Table 34. Summary of Creep Investigations on Discontinuous SiC-Al Composites

Investigators	Reinf.	V _f , %	matrix	T, K	$\dot{\gamma}^{**}$, s ⁻¹	n	Q _a , kJ/mol
Webster (1982)	SiC _w	25*	Al-3%Li	505-866	10 ⁻² -10 ⁰	--	---
Nieh (1984)	SiC _w	20*	6061Al	505-644	10 ⁻⁹ -10 ⁻⁶	21	390
	SiC _p	30*	6061Al	561	10 ⁻⁹ -10 ⁻⁷	--	---
Nardone & Strife (1987)	SiC _w	20	2124Al	450	10 ⁻⁹ -10 ⁻⁷	9	431***
				561	10 ⁻⁹ -10 ⁻⁷	21	227****
Nieh et al. (1988)	SiC _p	20	2124Al	623-723	10 ⁻⁷ -10 ⁻³	9	400
Morimoto et al. (1988)	SiC _w	15	6061Al	573	10 ⁻⁹ -10 ⁻⁶	--	---
Park et al. (1990)	SiC _p	30	6061Al	618-678	3x10 ⁻⁹ -9x10 ⁻²	7-25	270-500

* wt. %

** $\dot{\gamma} = 3\dot{\epsilon}/2$

*** at 90 MPa

**** at 310 MPa

stress, σ_e ($\sigma_e = \sigma - \sigma_0$, where σ is the applied stress and σ_0 is a threshold stress). Nardone and Strife [206] have suggested that three strengthening mechanisms may contribute to the presence of σ_0 . These are: (a) a high rate of composite hardening at lower testing temperature; (b) load transfer from the matrix to SiC whiskers at all temperatures; and (c) the stress necessary to unlock the dislocations from the reinforcement/matrix interface. It is worth mentioning that while Nardone and Strife [206] explained their experimental data in terms of a threshold stress, their data did not show conclusive evidence for the presence of such a threshold stress.

The data of Nardone and Strife [206] were criticized by Nieh et al. [207] who identified the following three problems with the data: (a) Nardone and Strife's claim that steady-state creep was attained; the data of Nieh et al. [207] have shown that steady-state is not well-defined in composites, (b) the measurement of the stress exponents for creep by performing stress change tests; a procedure which is not reliable under the condition of limited creep ductility for composites tested in tension, and (c) the short duration of creep tests at very slow rates.

Nieh et al. [207] studied the creep behavior of 20 vol. percent SiC_p-2124 Al in the temperature range of 623 K- 723 K. In conducting the study, Nieh et al. [207] tested specimens of the composite using a double shear configuration which resulted in strains of the order of 40 percent; these strains are higher than those reported in tension under conditions of constant stress (2-4 percent). The creep data obtained by Nieh et al. [207] have revealed the following: (a) the creep curve of the composite exhibits a very short steady-state stage; a minimum creep rate, rather than steady-state rate, exists, (b) the minimum creep rate depends strongly on both the temperature and the applied stress; the apparent activation energy (400 kJ/mole) is almost three times as high as that for self diffusion in Al (142 kJ/mole) and the stress exponent is about 9.5, (c) the minimum creep rate can be described by a power law of the applied stress according to the equation; $\dot{\gamma} = A\tau^{9.5} \exp\left(-\frac{400,000}{RT}\right)$, (d) the stress exponent is nearly constant over three orders of magnitude of strain rate, and finally (e) the creep strength of the composite is dominated by that of the aluminum matrix.

Morimoto et al. [208] studied the creep behavior of unreinforced 6061 Al and 15 vol. percent SiC_w-6061 Al composite at 573 K. They [208] used an exponential type law ($\dot{\epsilon} = A \exp(\beta\sigma)$) to fit the creep data and to describe the stress dependence of creep rate

for both the matrix alloy and the composite. The results have indicated that the steady-state creep rate of the composite is two orders of magnitude slower than that of the unreinforced matrix. These experimental results on the composite have been explained in terms of a creep model that assumes the occurrence of interfacial debonding with increasing the applied stress.

One important common characteristic of the creep studies conducted by Webster [110], Nieh [84], Nardone and Strife [206], and Nieh et al. [207] on discontinuous reinforced silicon carbide aluminum composites is that the experimental data of these studies describe the creep behavior of the composites over three orders of magnitude of strain rate (or less) [for example, see Figure 65]. Because of this characteristic, it is difficult to establish whether the stress exponent is genuinely constant, as suggested by the above studies, or increases with decreasing the applied stress, as reported for dispersion strengthened (DS) alloys [209, 210]. Very recently, this issue was addressed in an investigation by Park et al. [89] who creep tested a 30 vol. percent silicon carbide particulate reinforced aluminum alloy (SiC_p-6061 Al) over seven orders of magnitude of strain rate ($3 \times 10^{-9}\text{s}^{-1}$ - $9 \times 10^{-2}\text{s}^{-1}$). The creep curves reported by Park et al. [89] (for example, see Figure 66a) are similar to those reported by Nieh et al. [207] in regard to: (a) the short duration of the secondary stage; in most cases, the steady-state stage does not exceed 8% strain, and (b) the large creep strains attained under the condition of double shear testing; SiC-Al crept in tension [84, 206] exhibited small strains of the order of 2-4%. The steady-state creep data of Park et al. [89], which are plotted in Figure 66b as shear strain rate, $\dot{\gamma}$, vs. shear stress, τ , on a logarithmic scale, show that the data are divisible in two regions: high-stress region (region I) and low-stress region (region II). In the high-stress region, the apparent stress exponent, n_a ($n_a = \partial \ln \dot{\gamma} / \partial \ln \tau$), increases very slowly with decreasing the applied stress; as shown in Figure 66c, the experimental data obtained at high stresses can be fitted by a straight line whose slope ($=n_a$) is close to 7.4. The observation that the stress exponent at high stresses (region I) is approximately constant is compatible with those reported by Nieh [84], Nardone and Strife [206], and Nieh et al. [207] (see the above section). In the low-stress region (region II), the apparent stress exponent, n_a , not only is higher than that measured in the high-stress region but also increases rapidly with decreasing stress. This finding is clearly demonstrated in Figure 66d, where the measured stress exponent, n_a , is plotted against the applied shear stress at 648 K. Also, the creep data of Park et al. [89] have indicated that the apparent activation energy for creep in the composite increases with decreasing the applied stress

and that the values of this energy in both regions I and II are much higher than the energy for self-diffusion in Al.

The creep behavior of discontinuous SiC-Al composites, as summarized in the preceding section, is now examined in the light of the predictions of available models and treatments.

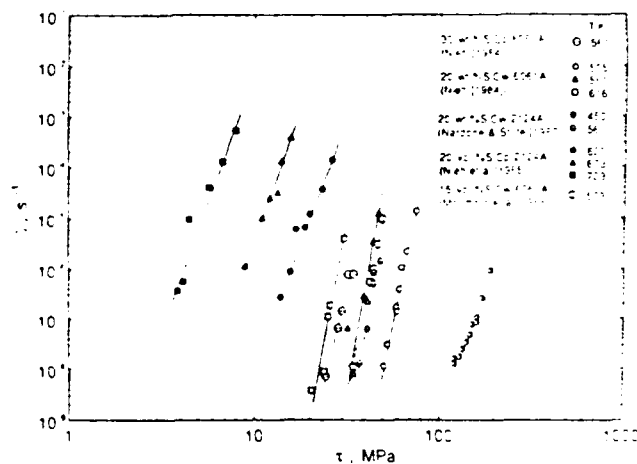


Figure 65 Data of creep investigations on discontinuous SiC-Al alloy composites plotted as shear strain rate, $\dot{\gamma}$, vs. shear stress, τ (logarithmic scale). The tensile data from refs. [84], [206] and [208] were transformed to shear data by using $\tau = \sigma/2$ and $\dot{\gamma} = 3\dot{\epsilon}/2$.

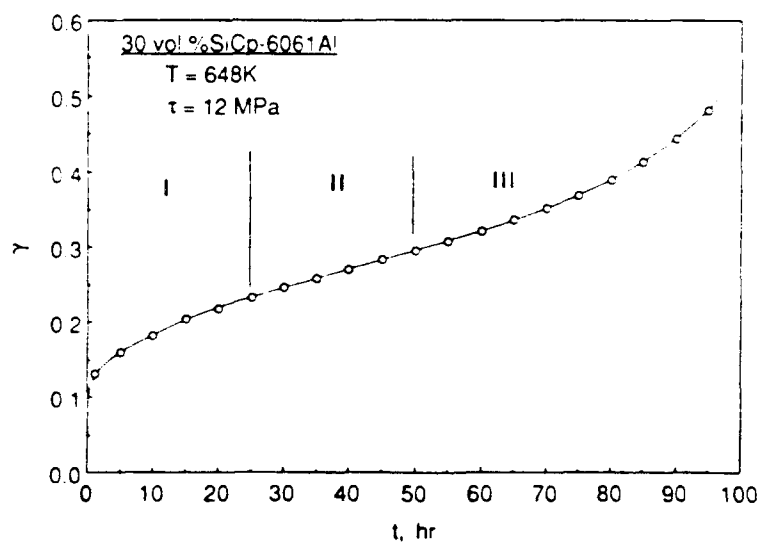


Figure 66 (a) Example of creep curve for 30 vol.% SiC_p-6061Al.

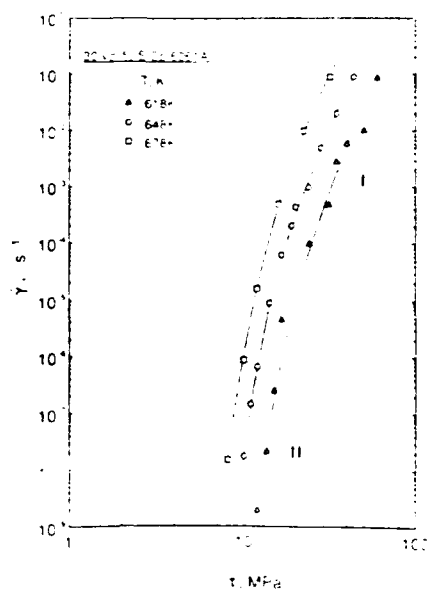


Figure 66 (b) Steady-state creep rate as a function of the applied stress (logarithmic scale) for 30 vol.% SiC_p-6061Al [89]; the experimental data extend over seven orders of magnitude of strain rate.

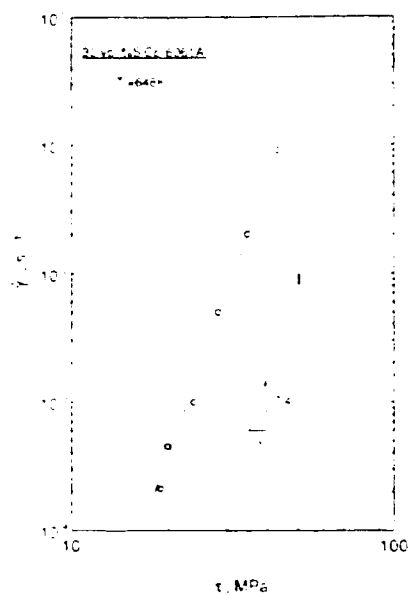


Figure 66 (c) The dependence of steady-state creep rate on the applied stress in the high stress region (region I) for 30 vol.% SiC_p-6061Al at 648K [89]; the apparent stress exponent, n_a , is nearly constant with a value of ~ 7.4 .

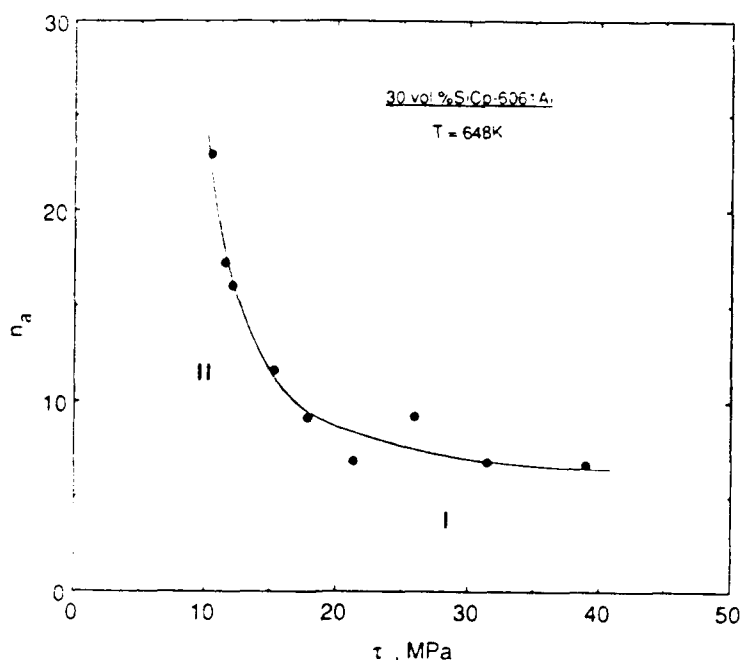


Figure 66 (d) The apparent stress exponent, n_a , as a function of the applied stress, τ , in the 30 vol.% SiCp-6061Al at 648K [89].

7.2.2 The Shear-lag Models

The shear-lag approach [211, 212] was used by Kelly and Street [213] to predict the creep rate of discontinuous composites as a function of the applied stress and some geometric parameters such as the fiber aspect ratio. The basic features of such an approach are: (a) the composite consists of aligned short fibers that are embedded in the creeping matrix, (b) the load is transferred from the matrix to the fiber by shear loading at the fiber/matrix interface, (c) load transfer to the fibers via direct stresses across their ends is negligible, and (d) the matrix creep rate obeys a creep power law ($\dot{\epsilon} = A\sigma^n$). The above shear-lag approach was later modified by other investigators [7, 214, 215] to include the following: (a) the contribution of friction and mean stresses [214], (b) the effect of the transfer of tensile load at the short fiber ends [7], (c) the occurrence of debonding at the interface [215], and (d) the description of the matrix creep behavior by an exponential law ($\dot{\epsilon} = A \exp(\beta\sigma)$) [215].

Although the shear-lag models have provided useful insight into the process of load transfer from the matrix to the fiber and the state of stress within a fiber, some of the

assumptions and predictions of these models are not consistent with the microstructure and creep behavior of discontinuous SiC-Al composites. First, the assumption of aligned short fibers is not representative of the actual case of SiC_w-Al composites where whiskers are usually misoriented. Second, in the shear-lag model proposed by Kelly and Street [213], the stress exponent for the composite in the absence of creep in the fibers[†] is equal to that for the matrix. This characteristic contrasts with available experimental evidence which shows that the stress dependence of creep rate in the composite is much stronger than that in the matrix [84, 207] (see Table 34). Third, the shear-lag analysis performed by Morimoto et al. [208] has shown that under the condition of progressive interfacial debonding with increasing stress, the stress exponent for the composite is higher than that for the matrix. While the results of the analysis of Morimoto et al. [208] seem to provide a possible explanation for the higher stress exponents noted in discontinuous SiC-Al composites, the concept of interfacial debonding, on which the analysis is based, is in conflict with two experimental observations: (a) a preliminary scanning electron microscopy study [208] conducted on a crept SiC_w-Al composite that was unloaded at room temperature revealed no evidence for the occurrence of debonding^{††}, and (b) the creep results of Park et al. [89] on a SiC-Al composite have indicated much stronger stress dependence of the creep rate at low normalized stresses, where debonding, according to the analysis of Morimoto et al. [208], is not expected to occur. Also, the data of Park et al. [89] have shown that the stress exponent measured at 648 K decreases from a value of about 25 at 10 MPa to a value of about 7.4 at 40 MPa. If debonding occurs at 10 MPa, leading to a high stress exponent of 25, it is expected that due to the increasing significance of debonding at higher stresses, the stress exponent would increase with increasing the applied stress from 10 to 40 MPa. This expectation contrasts with the actual behavior [89] which exhibits the opposite trend.

7.2.3 Finite Element Continuum Treatment

Very recently, Dragone and Nix [216] studied the creep behavior of discontinuous metal matrix composites by a continuum mechanics treatment utilizing finite element techniques. The analysis of the treatment was performed under the following conditions:

† Al Under the experimental conditions (temperatures and stresses) used in testing discontinuous SiC-composites, the creep of SiC reinforcement would not be significant.

†† It was suggested [208] that debonding may have been closed upon unloading. However, in the absence of conclusive experimental evidence, the validity of this suggestion cannot be established.

(a) the reinforcement phase of the composite was idealized as a regular, aligned and periodic array of short fibers or plates, and (b) during deformation, the matrix obeyed a creep power law, while the reinforcement phase remained elastic. The numerical results of the above treatment have revealed three main findings. First, large triaxial stresses develop in the matrix near the center of the reinforcement phase, and the presence of these stresses leads to reducing creep rates in the composite. Second, reinforcement phase geometry and arrangement (volume fraction, aspect ratio, separation) have a strong influence on determining the creep rate. Third, the predicted creep law^{†††} is in agreement with the measured creep rates for a silver-40% tungsten composite [217], but not with the measured creep law for a silicon carbide-aluminum composite [84]. Dragone and Nix [216] proposed several explanations for this discrepancy between the behavior of the Ag-40% W composite and the SiC-Al composite including: (a) the operation in the SiC-Al composite of other deformation mechanisms that were not considered in the continuum approach, (b) the presence of a critical reinforcement diameter or dimension below which the continuum mechanics approach is not applicable; however, as pointed out by Dragone and Nix [216], the fine 5 μm diameter of SiC whiskers in the composite tested by Nieh [84] is much larger than the estimate of the critical value, and (c) the accumulation of damage (the formation of voids or the occurrence of debonding) in the SiC-Al composite at the interface and in the matrix; according to Dragone and Nix [216], the accumulation of damage in the matrix would accelerate the creep rate and would introduce a different stress exponent into the creep law [216]. Also, the results of Dragone and Nix [216] have indicated that large stresses develop at the interface, a finding which raises the possibility that interfacial debonding may take place. However, as discussed in section 2.2, preliminary experimental evidence reported elsewhere [208] does not provide strong support for this possibility. Additional work is therefore needed to clarify the issue of interfacial debonding in SiC-Al composites.

7.2.4 Deformation Models Based on Dislocation Motion

Consideration of the results of the experimental investigations on discontinuous SiC-Al composites indicates that the creep behavior of these composites is similar to that of DS alloys [209, 210, 218, 219] in regard to: (a) the high values of the stress exponent, (b) the high values of the activation energy for creep, and (c) the increase in the stress exponent

^{†††} The analysis of Dragone and Nix have shown that the stress exponent for creep in the composite is equal to that for creep in the unreinforced matrix.

with decreasing the applied stress. In view of these similarities, it is interesting to examine whether dislocation processes proposed [209, 220-229] to account for the creep of DS alloys may also be applicable to the description of the creep of discontinuous SiC-Al composites. Before attempting such an examination, it is appropriate to briefly review the characteristics of deformation processes for DS alloys.

It is well-documented that for metals and solid-solution alloys, the dependence of steady-state rate, $\dot{\gamma}_s$, on the applied stress, τ , at intermediate stresses can be represented as a power law of the applied stress according to [230, 231]

$$\dot{\gamma}_s = B (\tau/G)^n \exp\left(-\frac{Q_c}{RT}\right) \quad (1)$$

where B is constant (sensitive to microstructure), n is the stress exponent, G is the shear modulus, Q_c is the activation energy, R is the gas constant, and T is the absolute temperature. For pure metals, such as aluminum, and solid-solution alloys of class II (metal class), such as aluminum-5% zinc [232], $n \approx 5$ whereas for solid-solution alloys of class I (alloy class), such as aluminum-copper alloys [233] and aluminum-magnesium alloys [234, 235], n can be 3 or 5 depending on experimental conditions and materials parameters [236, 237]. The creep behavior of metals and alloys of class II is generally attributed to some form of dislocation climb process [230, 231, 236-238] whereas that of alloys of class I is generally attributed to the presence of a viscous drag process operating on the dislocations during glide [230, 231, 236, 237, 239].

The introduction of incoherent, non-shearable second phase particles into metallic materials leads to improving the creep resistance of these materials. Compared to metals and solid-solution alloys, the creep behavior of DS alloys is unusual in two ways [209, 210, 218, 219]. First, the stress dependence of the creep rate, as described by the value of the stress exponent, is anomalously high and variable; n ranges from about 10 to 75. Second, the temperature dependence of the creep rate, which is measured by creep activation energy, is often much larger than that for self diffusion. Most investigators have attributed the high stress dependence of creep rate to the presence of a threshold stress, τ_0 ; the observed deformation is not driven by the applied stress, τ , but rather by an effective stress, $\tau_e (\tau_e = \tau - \tau_0)$. In this case, the rate controlling equation may be represented by

$$\dot{\gamma}_s = A \left(\frac{\tau - \tau_0}{G} \right)^n \exp \left(- \frac{Q_c}{RT} \right) \quad (50)$$

Three theoretical deformation models that explain the origin, and give the magnitude of threshold stresses, were proposed. In these models, the threshold stress is equal to: (a) the stress required to cause dislocation bowing between particles [209, 220, 221] (the Orowan stress), τ_0 , (b) the extra back stress, τ_b , required to create the additional dislocation line length as the dislocation segment climbs over a particle (local climb) [222, 223], and (c) the stress required to detach the dislocation from the particle after climb is completed [227, 228]. The magnitudes of the above threshold stresses along with the characterization of various parameters involved are given in Table 35.

Table 35. Models Proposed for DS Alloys

Model	Magnitude of τ_0	Ref.
Orowan stress ^a	$\tau_0 = 0.84 Gb/(\lambda - \bar{d})$	[7, 19, 20]
Local climb (back stress)	$\tau_b = 0.3 Gb/\lambda$	[21, 22]
Detachment stress ^b	$\tau_d = \tau_n (1 - K^2)^{1/2}$	[26-28]

a. λ is the planar spacing between particles, and \bar{d} is the average particle size.

b. τ_n is a normalizing stress ($\tau_n = Gb/\lambda$) and K is a relaxation parameter that takes on values between 0 (maximum attractive interaction) and 1 (no attractive interaction).

Recent considerations of the above three threshold stress models have led to the following important findings:

(a) The measured threshold stresses for creep in DS alloys are less than the values predicted from the equation of the Orowan stress by a factor ranging from 1.25 to 2.5 [222, 240]. More significantly, it was suggested [229] that the concept of the Orowan stress may not be applicable to the description of deformation of DS alloys at high temperatures and low stresses, since, under these experimental conditions, the moving dislocations can by-pass hard particles by climbing.

(b) Deformation processes based on dislocation climb alone cannot provide a satisfactory explanation for the creep of DS alloys in terms of a threshold stress. First, although models based on "local" climb [222, 223] yield threshold stresses that are in good agreement with those estimated from experimental data on DS alloys, "local" climb,

if it occurred, would result in a sharp dislocation curvature (at the point where the dislocation meets the particle) [224] that can be rapidly relaxed by diffusion, leading to more "general" climb. Second, models based on "general" climb [224-226] predict either an insignificant threshold stress or a threshold stress that is proportional to the applied stress.

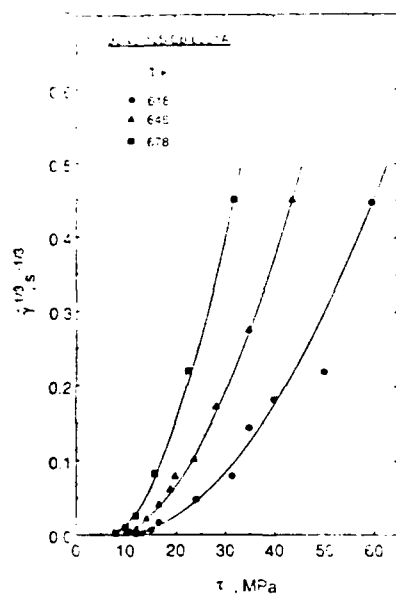
(c) The possibility that an attractive interaction between dislocations and particles exists is supported by both theoretical [241] and experimental studies [242-244]; for example, transmission electron microscopy (TEM) [242-244] studies have revealed that the dislocations remain bound to the particles after climb has been completed. As demonstrated elsewhere [227, 228], such an attractive particle-dislocation interaction in DS alloy leads to a well-defined threshold stress for creep which must be exceeded in order to detach the dislocation from particle after climbing. Most recently, it has been suggested [229] that dislocation detachment from the particle may be thermally activated and that in this case, creep may occur below the athermal "detachment stress". This suggestion, which has been developed quantitatively [229], has resulted in the following rate equation for creep.

$$\dot{\epsilon}/D = \frac{3\lambda\rho}{b} \exp \left(\frac{-Gb^2r \left[(1-K) \left(1 - \frac{\sigma}{\sigma_d} \right) \right]^{3/2}}{kT} \right) \quad (51)$$

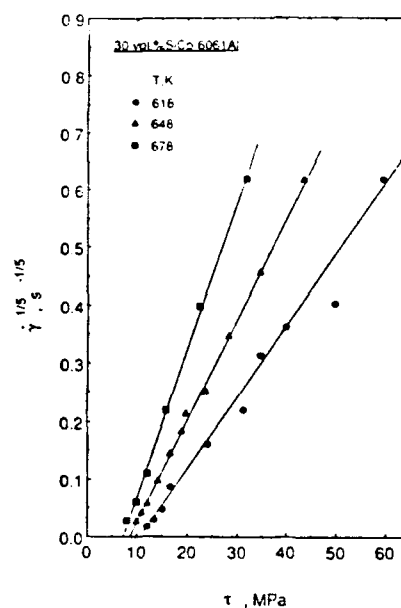
where $\dot{\epsilon}$ is the tensile creep rate, D is the coefficient of self diffusion, λ is the particle spacing, ρ is the mobile dislocation density, b is the Burgers vector, r is the particle radius, K is the relaxation parameter, σ is the tensile creep stress, and σ_d is the tensile detachment stress. The above rate equation, which does not include a "true" threshold stress, was shown to give good agreement with the experimental creep data of some large-grained DS alloys.

The stress exponent and the activation energy for creep in discontinuous SiC-Al composites are now examined in the light of the predictions of the above deformation processes for DS alloys.

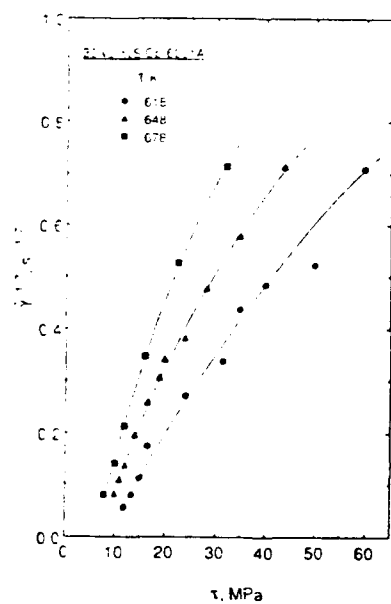
7.2.4.1 The stress exponent for creep. In the present analysis, three basic assumptions are made: (a) the presence of a threshold stress is the cause of the high apparent stress exponent [84, 89, 206-208] and its variation with the applied stress [89] in silicon carbide particulate reinforced aluminum alloys, and accordingly Eqn. 50 describes the creep behavior of these composites, (b) the threshold stress is independent of the



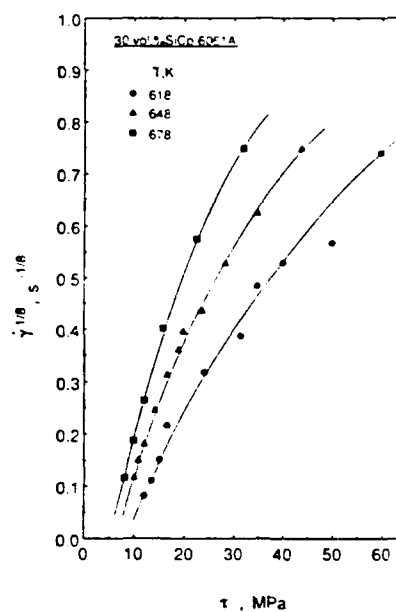
(a)



(b)



(c)



(d)

Figure 67 A plot of $\dot{\gamma}^{1/n}$ against τ for 30 vol.% SiC_p-6061Al [89].

(a) $n = 3$ (b) $n = 5$ (c) $n = 7$ (d) $n = 8$

applied stress, and (c) the true activation energy for creep, Q_c , is independent of the applied stress.

As a first step in the analysis, τ_0 was estimated from the data of Park et al. [89] since these data, unlike those reported by other investigators [84, 110, 206-208], cover a wide range of strain rate (seven orders of magnitude). In estimating τ_0 from the data, two procedures were used. In the first procedure, the experimental data at a single temperature were plotted as $\dot{\gamma}^{1/n}$ against τ on a double linear scale. If the creep of the composite obeys Eqn. 50 and if τ_0 is constant for each test temperature (independent of the applied stress), the data points of the above plot will fit a straight line whose extrapolation to zero strain rate gives the value of τ_0 . Figures 67a, 67b, 67c, and 67d represent the plot of $\dot{\gamma}^{1/n}$ vs. τ for

$n = 3, 5, 7$, and 8 , respectively. These values of the stress exponent, n , were selected to treat four well-documented cases regarding the creep behavior of materials: $n = 3$ for creep controlled by viscous glide processes [230, 231, 236, 239], $n = 5$ for creep controlled by high-temperature dislocation climb (lattice diffusion) [230, 231, 236, 238], $n = 7$ for creep controlled by low-temperature climb (core diffusion) [245], and $n = 8$ for lattice diffusion-controlled creep with a constant structure [246]. Inspection of Figures. 67a, b, c, and d indicates that the stress exponent of 5 yields the best linear fit between $\dot{\gamma}^{1/n}$ and τ ; for $n = 3$, $n = 7$, and $n = 8$, the data of the plot exhibit curvature with increasing the applied stress.

The second procedure for determining τ_0 is based on the finding that when modified power law creep associated with a threshold stress (Eqn. 50) describes the creep behavior of a material, the relation between the apparent stress exponent, n_a , the true stress exponent, n , the applied stress, τ , and the threshold stress, τ_0 , is given by [247]

$$n_a = \frac{n}{1 - \tau_0/\tau} \quad (52)$$

The values of n and τ_0 for each test temperature were estimated from the data of Figure 66b by plotting n_a as a function of τ (see Figure 66d) and by applying Eqn. 52 to such a plot. Table 36 summarizes the results obtained from the above two procedures. An examination of this Table yields the following observations: (a) the values of τ_0 estimated from both procedures are essentially identical, (b) τ_0 is sensitive to temperature; τ_0 increases with decreasing temperature, and (c) the average values of n determined from the second procedure ($n \approx 5$) is consistent with the finding deduced from

the first procedure that the true stress exponent characterizing the creep behavior of the composite is about 5.

Table 36. Estimated Values for τ_0 (MPa)

T, K	Procedure 1*	Procedure 2**
618	10.64	9.85
648	8.56	8.10
678	7.27	7.08

The first procedure used in estimating τ_0 from the data of Park et al. [89] ($\dot{\gamma}^{1/n}$ vs. τ) was applied to the creep data of SiC-Al composites that were reported by Nieh [84], Nieh et al. [207], and Morimoto et al. [208]. In this case, $n = 3$, $n = 5$, $n = 7$, and $n = 8$ were also used, and $\dot{\gamma}^{1/n}$ was plotted against τ ; the tensile data of Nieh [84] and Morimoto et al. [208] were transformed to shear data using $\dot{\gamma} = \frac{3}{2} \dot{\epsilon}$ and $\tau = \frac{\sigma}{2}$. Examination of the data as plotted in this form in Figures 68a, 68b, 68c, and 68d, for $n = 3$, $n = 5$, $n = 7$, and $n = 8$, respectively, reveals the following observation: $n = 5$, $n = 7$, and $n = 8$ are capable of describing these data in terms of a threshold stress; for $n=3$, the data of refs 84 and 208 exhibit curvature. One possible reason for such an observation, if the creep behavior of the composite obeys Eqn. 50 and if the assumptions regarding τ_0 are valid, is that the data of these three investigations extend over only three orders of magnitude of strain rates at high stresses, and accordingly the range of strain rate is too limited to provide an unambiguous answer regarding the appropriate value of the true stress exponent. This explanation is supported by the finding that the high-stress data obtained by Park et al. [89] in region I (extending over three orders of magnitude of strain rate) can be fitted by a straight line on the plot of $\dot{\gamma}^{1/n}$ vs. τ for either $n = 5$, $n = 7$ or $n = 8$. In this context, it is worth mentioning that Mishra and Pandey [248] also analyzed the data of Nieh [84], and Morimoto et al. [208] in terms of a threshold stress assuming $n = 8$. They concluded that the observed linearity between $\dot{\epsilon}^{1/8}$ and σ validated the assumed value of n . However, the present analysis shows that the data can be equally fitted by a straight line when n is assumed to be ~ 5 or 7 .

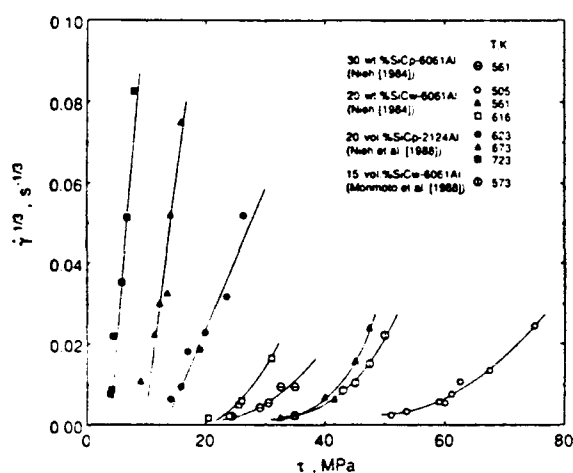
Substructural data regarding subgrain development during the creep of discontinuous SiC-Al composites may provide guiding information that helps establish the value of the true stress exponent associated with the creep of these composites (whether 3, 5, or 8).

As documented elsewhere, viscous glide creep for which $n = 3$ is characterized by the absence of subgrains [235]; climb-controlled creep for which $n \simeq 5$ leads to the formation of subgrains whose average size is inversely proportional to the applied stress [230, 231, 249]; and lattice diffusion-controlled creep with constant structure for which $n \simeq 8$ requires that the subgrain size remain constant over the entire stress range.

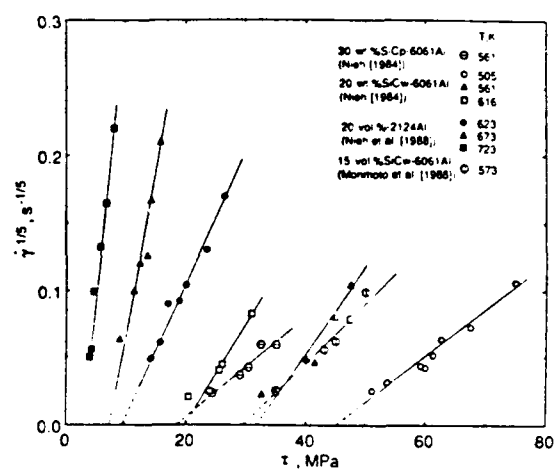
The data of Park et al. [89] are analyzed below in an attempt to explore possible sources of the threshold stress. The selection of the data of Park et al. for such an analysis is justified by several considerations. First, as mentioned previously, the data of Park et al. [89] represent the only set of experimental data on the creep of discontinuous SiC-Al composites that covers an extensive range of strain rates, a characteristic which is important in determining whether the stress exponent is constant or variable. Second, the data of Park et al. [89] were obtained in shear under the condition of large creep strains where steady-state creep can be unambiguously defined. Third, the data were obtained using the procedure of uninterrupted tests (several identical specimens are crept at different stresses). This procedure is more reliable in measuring the stress exponent than that of stress-change test; especially when the duration of the steady-state stage during creep, as reported in discontinuous SiC-Al composites, is short. Finally, the true stress exponent for creep that is inferred from the other creep data on SiC-Al composites [84, 206-208] is not uniquely defined; according to Figures 68a, 68b, 68c, and 68d, n could be 3, 5, 7, or 8.

Table 37 provides a comparison between the values of τ_0 estimated from the creep data reported by Park et al. [89] and those predicted from the three threshold stress models for DS materials. In performing the comparison, the following assumptions, values and approximations have been used [89].

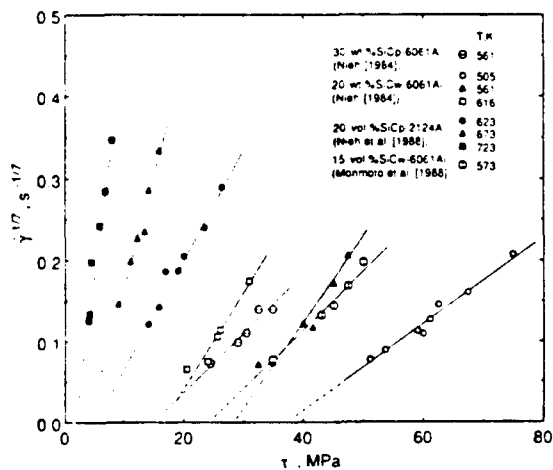
- a. SiC_p serve as barriers to dislocation motion and give rise to the existence of a threshold stress for creep.
- b. The average SiC_p size, $\bar{d} = 3.6 \mu\text{m}$ [89], the SiC_p interparticle spacing, $\lambda = 6.6 \mu\text{m}$ [89], and $b \simeq 2.86 \times 10^{-4} \mu\text{m}$.
- c. The relaxation parameter, $K = 0.85$.



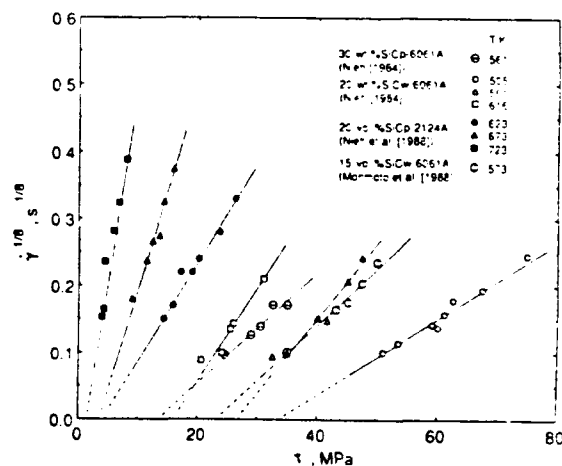
(a)



(b)



(c)



(d)

Figure 68 A plot of $\dot{\gamma}^{1/n}$ against τ for various SiC-Al composites from refs. [84], [207] and [208]. (a) $n = 3$ (b) $n = 5$ (c) $n = 7$ (d) $n = 8$

d. The shear modulus of the matrix 6061 Al is estimated from the equation available for Al; present calculations using the shear moduli of both Al and SiC along with consideration of experimental data [250] on the elastic modulus of SiC-2124 Al show that there is no significant change in the temperature dependence of the shear modulus of the matrix as a result of the presence of SiC_p.

It is clear from the data of Table 37 that for each test temperature, the three values predicted for τ_0 are much smaller than those estimated from experimental data. The discrepancy between prediction and experiment is too large to be attributed to possible errors made in the values of λ , d , G , or K .

The above finding that the SiC_p do not serve as an effective source for τ_0 in discontinuous SiC-Al composites^{††††} at high temperature is consistent with the result of an analysis reported by Park et al. [89], and general statements made by other investigators [84, 207].

In addition, the creep characteristics of the data of Park et al. (high stress exponent and high activation energy) cannot be explained in terms of thermal activation of dislocation detachment from SiC_p [228], since the athermal detachment stress, τ_d , is much lower than the smallest applied stress used in the investigation [89].

Park et al. [89] considered an alternate approach for the source of the threshold stress in SiC_p-6061 Al which was creep tested in their investigation. Such an approach is based on the suggestion that the oxide particles present in the Al matrix, as a result of manufacturing the composite by powder metallurgy, serve as effective barriers to dislocation motion and give rise to a threshold stress for creep. Park et al. [89] have quantitatively examined the validity of this suggestion under the following conditions:

(a) The oxide content, f , is about 0.16 vol. pct. This value was calculated by assuming that the original 6061 Al powder shape is spherical; that the average 6061 Al powder diameter is 15 μm ; that the oxide layer is entirely an Al₂O₃ film; and that the average oxide film thickness is 4 nm.

^{††††} Although present calculations show that the high stress exponents in SiC-Al composites cannot be caused by SiC particulates (by introducing τ_0), experimental data [208] and theoretical analyses [208, 216] indicate that the presence of the particulates reduces the creep rate of the matrix.

Table 37. Comparison between τ_o inferred from the creep data of [89] and those estimated from various threshold models.

T, K	τ_o (MPa)	τ_b (MPa)	τ_d (MPa)	τ_o (MPa)
618	1.61	0.26	0.46	10.64
648	1.57	0.25	0.45	8.56
678	1.53	0.25	0.44	7.27

τ_o = Orowan stress

τ_b = Back stress due to local climb

τ_d = Detachment stress

τ_o = Threshold stress from Park et al.'s data.

(b) The average planar spacing between the oxide particles, λ , is approximately $0.35 \mu\text{m}$. This value of λ was estimated by assuming that oxide particles are in the shape of platelets whose average thickness, t , and length, l , are 4 nm and 50 nm , respectively, and by using the expression [242, 251]: $\lambda = (lt/f)^{1/2}$.

By substituting the above value of λ into the three threshold stress equations, Park et al. [89] have shown that the detachment stress, τ_d , coincides closely with the asymptotic behavior of the creep data on SiC-6061 Al at 648 K and that, for this temperature, the estimated value of τ_d is in good agreement with the value of τ_0 inferred from the data.

The above analysis of Park et al. [89] is extended, here, to include the other two temperatures of their investigation: 618 K and 678 K . The values of τ_d estimated from the expression for the detachment stress along with these inferred from the creep data at 618 K , 648 K , and 678 K are given in Table 38. Examination of the values documented in the Table shows that while the values of τ_d are in general close to the values of τ_0 (inferred from experimental data), the dependence of τ_0 on temperature is stronger than that of τ_d which is attributable to the shear modulus. This difference in temperature dependence between τ_d and τ_0 is illustrated in Figure 69 where τ_d/G and τ_0/G are plotted against T ; because the temperature dependence of τ_d arises from the variation in G with temperature, τ_d/G is independent of temperature (horizontal line).

Table 38. Comparison between Detachment Stresses for oxide particles, τ_d , and Creep Threshold Stresses, τ_0 , Estimated from [89]

T, K	τ_d , MPa	τ_0 , MPa
618	8.65	10.64
648	8.45	8.56
678	8.24	7.08

In order to develop an empirical relationship between τ_0 and T , several trial functions were used. Based on an examination of the plots of these functions, it was concluded that the variation of τ_0 with temperature may be best represented by the following empirical equation:

$$\tau_0/G = B_0 \exp \left(\frac{Q_0}{RT} \right) \quad (53)$$

where R ($=8.31 \text{ mol}^{-1}\text{K}^{-1}$) is the gas constant, B_0 is a constant, and Q_0 is an energy term ($= 19.3 \text{ kJ/mole}$). Figure 70, where the logarithm of τ_0/G is plotted against $1/T$, demonstrates the validity of the above equation.

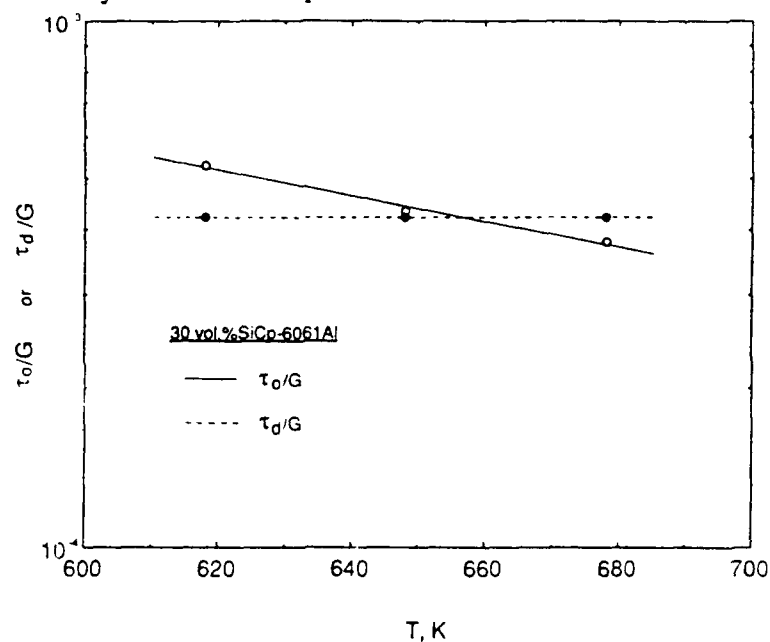


Fig. 69 Comparison between the temperature dependence of the normalized detachment stress (τ_d/G) and the normalized threshold stress (τ_0/G) inferred from the data of 30 vol.% SiCp-6061Al [89].

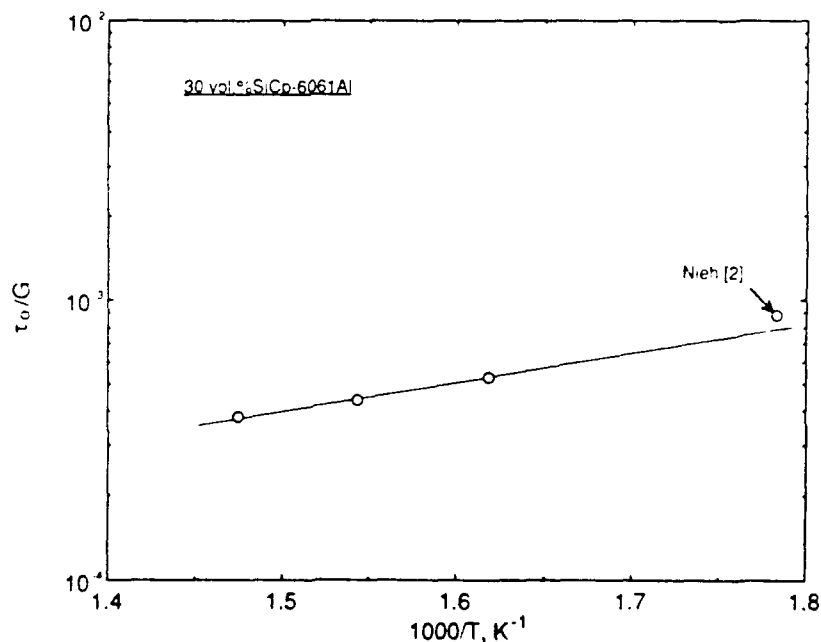


Fig. 70 A plot of the logarithm of the normalized threshold stress (τ_0/G) against $1/T$ for 30 vol.% SiCp-6061Al [89].

Two observations are noted in regard to Eqn. 53. First, the creep data of Nieh [84] on 30wt% SiC_p-6061Al at 561 K, when plotted as $\dot{\gamma}^{1/5}$ vs. τ (Figure 68a), leads to $\tau_0 = 18.6$ MPa. This value of τ_0 , as shown in Figure 6, agrees very well with the position of the line representing Eqn. 53. Second, under the condition that $Q_0 < RT$ and under the condition of using narrow testing temperature range (variation in G with temperature is very small), Eqn. 53 can be expressed as

$$\tau_0 \approx A + \frac{C}{T} \quad (54)$$

Eqn. 54 is identical with that reported by Mishra and Pandey [248] who, as mentioned previously, analyzed the creep data of several SiC-Al composites in terms of a threshold stress, using a true stress exponent of 8 (lattice diffusion-controlled creep with constant structure). Mishra and Pandey [248] stated that the temperature dependence of σ_0 , as described by Eqn. 54 ($\sigma_0 = 2\tau_0$), can be attributed to a change in Young's modulus with temperature. However, this statement is seen to be incorrect since, as demonstrated above, Eqn. 54 was deduced from Eqn. 53 in which the temperature dependence of σ_0 is much stronger than that attributable to the elastic modulus.

7.2.4.2 Activation energy for creep. Activation energy measurements [84, 89, 206, 209] reported for discontinuous SiC-Al composites reveal the following important characteristic: the apparent activation energies, Q_a , for creep in discontinuous SiC-Al composites are high and resemble in trend those reported for DS alloys; $Q_a^\dagger > Q_D$.

It was demonstrated [219] that the high apparent creep activation energies, Q_a , measured in some DS alloys can be corrected to values near those for self diffusion, Q_D , by incorporating the contribution of the temperature dependent elastic modulus. However, present calculations, as shown below, indicate that for SiC-Al composites, the modulus correction is too small to account for the difference between Q_a and Q_D .

[†] Theoretical analyses based on shear-lag models [7, 213-215] and finite element continuum treatment [216] do not explicitly address the issue of the higher activation energies reported for discontinuous composites.

Under the conditions that creep is described by Eqn. 49 and that the stress exponent is constant, the true activation energy, Q_c , for creep is related to the apparent activation energy, Q_a , by the following expression [230, 231]:

$$Q_c = Q_a + \frac{nRT^2}{G} \frac{\partial G}{\partial T} \quad (55)$$

The second term in the right hand side of Eqn. 55 is the modulus correction term and would be largest under the following conditions: (a) high temperatures, (b) high stress exponents, and (c) large values of $\frac{\partial G}{\partial T}$; $\frac{\partial G}{\partial T}$ is always negative and available experimental evidence indicates that in SiC-2124 Al composite, $\frac{\partial G}{\partial T}$ for the composite is essentially similar to that for the matrix alloy [250].

Eqn. 55 was applied to the data of several SiC-Al composites; for the data of Park et al. [89], only the high stress region was considered since in this region the stress exponent can be approximated by a constant value of about 7.4. The results of the application of Eqn. 55 are given in Table 39, in which the modulus corrections were subtracted from the apparent activation energies, Q_a , to obtain the true creep activation energy. It is clear that the calculated true creep activation energies are still higher than that for self diffusion. This finding demonstrates that the difference between Q_a and Q_D in SiC-Al composites cannot be accounted for by the contribution of the temperature dependent elastic modulus.

The present analysis as well as the analysis reported by Mishra and Pandey [248] suggest that if the high stress dependence of creep rate in SiC-Al composites is caused by the existence of a creep threshold stress, such a threshold stress depends strongly on temperature according to Eqn. 53 or 54. Straightforward treatment shows that when Eqn. 53 is combined with Eqn. 50, the relationship between the true creep activation energy, Q_c , and the apparent activation energy, Q_a , can be expressed as

$$Q_c = Q_a + \frac{nRT^2}{G} \frac{\partial G}{\partial T} \left[1 + \frac{1}{\tau/\tau_0 - 1} \right] - \frac{nQ_0}{\tau/\tau_0 - 1} \quad (56)$$

Table 39. Modulus Correction in Discontinuous SiC-Al Composites

Matrix	Reinforcement	Q_a , kJ/mol	n	C.F. kJ/mol.	Q_c , kJ/mol.	ref.
6061 Al	20 wt. % $S_i C_w$	390	20.5	-40	350	[2]
2124 Al	20 vol. % $S_i C_p$	400	9.5	-30	370	[4]
6061 Al	30 vol. % $S_i C_p$	270	7.4	-21	249	[6]*

$$Q_c = Q_a + nRT^2 \left(\frac{1}{G} \right) \left(\frac{\partial G}{\partial T} \right).$$

$$C.F. = nRT^2 \left(\frac{1}{G} \right) \left(\frac{\partial G}{\partial T} \right).$$

* High stress region (region I)

Eqn. 56 was applied to the data of Park et al. [89] using $n = 5$, T (average temperature)= 648K, and Figure 66b which gives Q_a vs. τ . In making the calculations, low values of the applied stress that approach τ_0 were not used since $nQ_a / (\tau/\tau_0 - 1)$ becomes very large as $\tau \rightarrow \tau_0$. The results of the calculation are presented in Table 40 which shows that the values of Q_c are consistently higher than that for self diffusion in Al; the average value of $Q_c \approx 225$ kJ/mole while $Q_D = 142$ kJ/mole. The finding that $Q_c > Q_D$ can also be demonstrated using Eqn. 50 and the plot in Figure 67b ($\dot{\gamma}^{1/5}$ vs. τ). According to Eqn. 50, the slope of the straight line, S , that fits the data at a single temperature in Figure 67b is given by

$$S = \frac{A'}{G} \exp(-Q_c/nRT) \quad (57)$$

Calculating S from three different temperatures (using $n = 5$) yields $Q_c = 208$ kJ/mole, a value which is in agreement with those given in Table 40 and which is higher than Q_D . The reason for the discrepancy between Q_c and Q_D is not known. However, it is worth mentioning that creep activation energies measured in some Al solid-solution alloys^{††} [233, 252, 253] at high stresses, where $n=5$, are higher than that for self diffusion and range from 160-210 kJ/mole: for example, Q_c reported for Al-3% Cu [233] under the above conditions ($\tau > 5$ MPa and $n=5$) is 205 kJ/mole.

Table 40. Creep Activation Energy calculated from Eqn. 56

τ_{app} , MPa	Q_a^* , kJ/mol	Q_c , kJ/mol
12	524	234
14	438	249
16	397	255
18	340	225
20	338	241
22	322	237
24	308	232
26	291	222
28	275	212
30	263	201
32	246	191
Avg.		228

^{††} In these alloys, the stress exponent changes from a value of about 3 at intermediate stress, where $Q_c \approx Q_D$, to a value of 5 at high stresses, where $Q_c > Q_D$.

While the origin of the temperature dependence of the threshold stress in SiC-Al composites, as suggested by the present analysis, is at present not clear, it is interesting to note that Eqn. 53 is similar in form to that reported for the temperature dependence of the threshold stress in superplastic materials [247, 254]. For superplastic materials, it was suggested [247, 254] that impurity atom segregation at boundaries and their interaction with boundary dislocations give rise to a threshold stress which is proportional to $\exp(E/RT)$, where E is the binding energy between an impurity atom and a dislocation. It is quite possible that in Al-SiC composites, impurity atoms play a similar role since experimental evidence documented elsewhere [19] indicates that impurity segregation occurs at the interfaces between the matrix and particles. If these impurities are able to diffuse to the dislocation that is captured at the detachment side of the particle and if binding between impurity atoms and the dislocations is very strong, a threshold stress which would be proportional to $\exp(E/RT)$ is necessary before the dislocation breaks away from the particle (it is assumed that the detachment stress is smaller than the stress required to tear a dislocation from an impurity atmosphere at the interface between the particle and the matrix). While more systematic data which describe the creep behavior of several SiC-Al composites over an extensive range of strain rate are needed to examine the validity of the above possibility, it is worth noting that the value of Q_0 in Eqn. 53 ($19.3 \text{ kJ/mole} = 0.2 \text{ eV}$) is not unreasonable when compared with those estimated for binding energies between impurity atoms and lattice dislocations ($0.1 - 0.3 \text{ eV}$) [255].

7.3. Conclusions

1. The creep behavior of discontinuous SiC-Al composites is similar to that of dispersion strengthened (DS) alloys in regard to: (a) the high values of the stress exponents; the stress exponent, n , in these composites ranges from about 7 to 25, and (b) the high value of the apparent activation energies; the apparent activation energy, Q_a , is much higher than that for self diffusion in Al, Q_D . Also, a very recent experimental study has shown that the creep of a discontinuous SiC-Al composite, like that of some DS alloys, exhibits an increase in the stress exponent with decreasing the applied stress.
2. The creep behavior of discontinuous SiC-Al composites is not entirely consistent with the assumptions and predictions of the shear-lag models and the finite element continuum treatment. However, the results of the models and the treatment have provided new insight into: (a) the process of load transfer from the matrix to the fiber, (b)

the state of stress within a fiber, (c) internal stress distributions in the matrix, (d) the origin of the lower creep rates in discontinuous composites, and (e) the role played by reinforcement phase geometry in affecting the overall deformation rate. Further development and extension of the above models and treatment to address in detail important issues such as void formation and debonding occurrence should lead to enhancing our understanding of high-temperature strengthening in discontinuous composites.

3. The similarity in creep characteristics between discontinuous SiC-Al composites and DS alloys suggests that the creep behavior of the former, like that of the latter, may be explained in terms of a threshold stress for creep. However, by using the various threshold stress models proposed for DS alloys, it is shown that the threshold stresses introduced by SiC reinforcements are much smaller than those estimated from experimental data.

4. Present calculations based on the suggestion that the fine incoherent oxide particles present in Al matrix, as a result of manufacturing SiC-Al composites by powder metallurgy, serve as effective barriers to the dislocation motion result in detachment stresses, τ_d , that closely agree with threshold stresses, τ_0 , estimated from experimental data. Despite this agreement, the temperature dependence of the estimated threshold stresses is much stronger than that of the detachment stresses and is given by

$$\tau_0/G = B_0 \exp \left(\frac{Q_0}{RT} \right)$$

where G is the shear modulus, B_0 is a constant, Q_0 is an activation energy term, R is the gas constant, and T is the absolute temperature.

5. The difference between the apparent activation energies for creep in SiC-Al composites and the activation energy for self diffusion in Al cannot be accounted for by the contribution of the temperature dependent elastic modulus.

6. An expression relating the apparent activation energy for creep, Q_a , to the true activation energy, Q_c , was developed for the situation in which the creep behavior is described by power law creep associated with a threshold stress that is given by the above equation (strong temperature dependence). By using this expression, it is shown that the

high apparent activation energies for creep in a $\text{SiC}_p\text{-Al}$ composite can be reduced to values that are slightly higher than those of creep energies measured in some Al alloys at high stresses.

7. Despite the important contributions of the results of recent studies (experimental investigations and theoretical treatments) on discontinuous SiC-Al composites, additional work (experimental and analytical) is still needed: (a) to examine whether the increase in the stress exponent for creep with decreasing the applied stress, as reported by Park et al. [89], represents a genuine creep characteristic in these composites, (b) to investigate whether the concept of a threshold stress for creep is capable of accounting for the high apparent stress exponent for creep in several discontinuous SiC-Al composites containing different matrices and different reinforcement configurations and shapes, (c) to determine whether interfacial debonding occurs and, if it occurs, to examine its effect on the power law creep, and (d) to study dislocation activities in the composites and to identify the nature and type of particles that may interact with dislocations (whether these particles are SiC reinforcements, oxides, etc...).

II. NOMENCLATURE

$a(d_i)$	acceleration of the droplet of diameter d_i	(m/sec ²)
A	surface area of droplet in contact with a single particulate	(m ²)
A_d	droplet surface area	(m ²)
A_f	area fraction of SiC _p	(m ²)
A_s	SiC _p surface area	(m ²)
b	burger vector	
C	constant	(--)
C_{drag}	drag coefficient for motion of sphere in fluid	(--)
C_L	specific heat of liquid	(J/kg K)
C_p	specific heat of melt	(J/kg K)
C_{PL}	specific heat of the particulates	(J/kg K)
C_{SiC}	specific heat of SiC _p	(J/kg K)
d	interatomic distance	(m)
d_{16}	droplet diameter equal to the upperbound of 16 pct of the droplets	(m)
d_{50}	mass mean droplet diameter	(m)
d_{84}	droplet diameter equal to the upperbound of 84 pct of the droplets	(m)
d_o	diameter of the metal delivery tube	(m)
D	average grain diameter	(m)
$D(f)$	diameter of the fluidization chamber	(m)
D_f	driving force for wetting	(N)
D_{LM}	self diffusion coefficient of the solute computed at the melting temperature	(m ² /sec)
D_p	nominal size of SiC _p	(m)
E	primary electron energy	(Mev)
f	friction factor of the fluidization chamber	(--)
$f(d_i)$	mass fraction of droplets of diameter d_i	(--)
f_l	fraction liquid	(--)
f_s	fraction solid	(--)
F_{impact}	impact force due to impinging droplets	(N)
F_r	repulsive force	(N)
ΔF_{net}	change in free energy	(J)

g	gravitational constant	(m/sec ²)
G	modulus of rigidity	(GPa)
Ga	Galileo's number	(--)
h	heat transfer coefficient between droplets and gas	(W/m ² K)
$H(d_i)$	heat content of a single droplet	(kJ)
H_f	latent heat of fusion	(kJ/kg)
$H_{\text{droplet/Kg}}$	total thermal per unit mass of a single droplet	(kJ)
H_{spray}	total enthalpy of the atomized spray at any specific location	(kJ)
$H_{\text{spray,deposition}}$	enthalpy of the spray at deposition specific location	(KJ)
$H_{\text{spray,SiC}}$	Enthalpy of the spray in the presence of SiC _p	(KJ)
J_{gas}	gas flow rate	(kg/sec)
J_{melt}	metal flow rate	(kg/sec)
k_d	coefficient in powder size correlation	(--)
K	constant	(--)
K_a	thermal conductivity of the atomizing gas	(W/mK)
K_{IC}	plain strain fracture toughness	(MPa.m ^{1/2})
K_L	thermal conductivity of the liquid	(W/mK)
K_m	kinetic growth coefficient	(m/sec K)
K_{PL}	thermal conductivity of the particulate	(W/mK)
K_{SiC}	thermal conductivity of the SiC _p	(W/mK)
l	planar center to center spacing between the dispersoid	(m)
ℓ	length of SiC _p	(m)
L_a	length of interface between droplet and particulate as measured perpendicular to the droplet surface	(m)
L_{SiC}	characteristic length of SiC _p	(m)
$m(d_i)$	mass of a single droplet	(kg)
m_{deposit}	mass of deposit	(kg)
$m_{\text{droplet, i}}$	mass of droplet of diameter d_i	(kg)

m_{droplets}	total mass of droplets	(kg)
m_{metal}	mass of metal	(kg)
m_{SiC}	average mass of SiC_p	(kg)
n	constant	(--)
$n(d_i)$	number of droplets of diameter d_i	(--)
n_s	number of SiC_p in intimate contact with matrix droplet	(--)
n_{SiC}	number of SiC_p	(--)
N	total number of droplets	(--)
N_{Re}	Reynolds number = $2 r_d \rho_g v_g / \mu_g$	(--)
\dot{q}_r	overall rate of conductive heat transfer	(KJ/sec)
$Q_{(\text{SiC}, \text{flight})}$	percentage thermal energy dissipated during flight	(KJ)
$Q_{(d_i)(\text{SiC}, \text{flight})}$	total amount of thermal energy lost by atomized droplets to the SiC_p	(KJ)
$Q_{\text{Total}(\text{SiC}, \text{flight})}$	total amount of thermal energy transferred during flight	(KJ)
Q_{SiC}	thermal energy required to bring SiC_p to the deposit temperature	(KJ)
dQ/dt	radiation loss from the droplet surface	(KJ)
r	radius of the particulate	(m)
r_d	droplet radius	(m)
R	growth rate	(cm/sec)
Re_{Dmf}	Reynold's number for minimum fluidization	(--)
R_b	depth of penetration of electron beam	(μm)
R'	gas constant	(kJ/mol. K)
s	distance travelled	(m)
t	annealing time	(sec)
$t(d_i)$	time taken by a droplet of diameter d_i from injection point to deposition point	(sec)
t_p	thickness of particulate	(m)
T_1	temperature of the surroundings	(K)
T_2	temperature of the droplet	(K)
T	temperature	(K)

T_d	deposit temperature = $\frac{H_{\text{spray, SiC}}}{m_{\text{droplets}} C_p}$	(K)
T_L	liquidus temperature	(K)
T_S	solidus temperature	(K)
T_o	temperature of gas	(K)
ΔT	temperature differential with respect to ambient temperature	(K)
ΔT^*	undercooling	(K)
$u(d_i)$	velocity of droplet at the SiC _p injection point	(m/sec)
U	overall heat transfer coefficient between Al and SiC _p	(J/sec m ² K)
v_d	droplet velocity	(m/sec)
v_g	gas velocity	(m/sec)
V	average operating gas velocity inside the fluidization chamber	(m/sec)
$V(d_i)$	volume of droplet of diameter d_i	(m ³)
V_{cr}	critical velocity for entrapment	(m/sec)
V_f	Volume fraction of particulates	(--)
V_d	droplet volume	(m ³)
V_{ge}	velocity of the gas at nozzle exit	(m/sec)
V_t	terminal velocity of the particulates	(m/sec)
V_{SiC}	velocity of the SiC _p	(m/sec)
w	void fraction	(--)
wt.% Ti _{deposit}	maximum anticipated wt.% Ti in solution	(--)
% Ti _{d₁₆}	maximum anticipated wt.% Ti in solution in a d ₁₆ droplet	(--)
% Ti _{d₅₀}	maximum anticipated wt.% Ti in solution in a d ₅₀ droplet	(--)
% Ti _{d₈₄}	maximum anticipated wt.% Ti in solution in a d ₈₄ droplet	(--)
W	theoretical mass flow rate of the gas	(kg/sec)
W_{ad}	work of adhesion	(J/m ²)
W_{SiC}	theoretical mass flow rate of SiC _p	(kg/sec)
β	constant	(--)

δ	length of an interface step	(m)
γ_{lg}	liquid gas interfacial energy	(J/m ²)
λ	interparticle spacing	(m)
σ_g	standard deviation in powder size distribution (--)	
σ_m	melt surface tension	(kg/sec ²)
σ_{PS}	surface free energy between particulate and solid	(N/m)
σ_{PL}	surface free energy between particulate and liquid	(N/m)
σ_{SL}	surface free energy between solid and liquid	(N/m)
σ_Y	yield strength	(MPa)
$\Delta\sigma_0$	difference in surface tension	(N/m)
ρ	density of the material	(g/cm ³)
$\rho(d_i)$	density of the droplet of diameter d_i	(kg/m ³)
ρ_a	density of absorbing media	(g/cm ³)
ρ_a	density of carrier fluid	(kg/m ³)
ρ_d	droplet density	(kg/m ³)
ρ_g	gas density	(kg/m ³)
ρ_L	liquid density	(kg/m ³)
ρ_m	melt density	(kg/m ³)
ρ_{PL}	density of the particulates	(kg/m ³)
ρ_s	density of solid particulates	(kg/m ³)
η	viscosity of the carrier fluid	(m ² /sec)
η_g	kinematic viscosity of gas	(m ² /sec)
η_m	kinematic viscosity of melt	(m ² /sec)
τ_m	matrix flow stress	(MPa)
μ_g	gas viscosity	(kg/m sec)
μ_m	melt viscosity	(kg/m sec)

III REFERENCES

1. S.G. Fishman: *J. Metals* , 1986, vol. 38, p. 26.
2. Y. Flom and R.J. Arsenault: *J. Metals* , 1986, vol. 38, p. 31.
3. Y. Flom and R.J. Arsenault: *Mat. Sci. Eng.*, 1986, vol. 77, p. 191.
4. A.H.M. Howes: *J. Metals*, 1986, vol. 38, No. (3), p. 28.
5. A. Mortensen, M.N. Gungor, J.A. Cornie and M.C. Flemings: *J. Metals* , 1986, vol. 38, p. 30.
6. A. Mortensen, J.A. Cornie and M.C. Flemings: *J. Metals* , 1988, vol. 40, p. 12.
7. V.C. Nardone and K.W. Prew: *Scr. Metall.*, 1986, vol. 20, p. 43.
8. T.W. Chou, A. Kelly and A. Okura: *Composites*, 1986, vol. 16, p. 187.
9. A.P. Divecha and S.G. Fishman: Mechanical Properties of Silicon Carbide Reinforced Aluminum, in Proc. 3rd Int. Conf. on Composite Materials, 1979, vol. 3, p. 351.
10. A.L. Geiger and M. Jackson: *Adv. Mat. Process*, 1989, vol. 7, p. 23.
11. A.K. Dhingra: *J. Metals*, 1986, vol. 38, p. 17.
12. R.C. Forney: *J. Metals*, 1986, vol. 38, No. 7, p. 18.
13. H.J. Rack: Fabrication of High-Performance Powder Metallurgy Aluminum Matrix Composites, 1988, in press.
14. S.R. Nutt: *American Ceramic Society*, 1984, vol. 67, No. 7, p. 428.
15. A.P. Divecha, S.G. Fishman, and S.D. Karmarkar: *J. Metals* , 1981, vol. 33, p. 12.
16. R.J. Arsenault: *Mat. Sci. Eng.*, 1984, vol. 64, p. 171.
17. C.R. Crowe, R.A. Gray and D.F. Hasson: in Proc. 5th Intl. Conf. in Composite Materials, W. Harrigan, J. Strife and A.K. Dhingra (eds)., The Metallurgical Society of AIME, Warrendale, PA, 1985, 843.
18. S.V. Nair, J.K. Tien. and R.C. Bates: *Int. Met. Rev.*, 1985, vol. 30, p. 275.
19. I.A. Ibrahim, F.A. Mohamed and E.J. Lavernia: *J. Mat. Sci.*, 1991, vol. 26, p. 1137.
20. Duralcan Metal Matrix Composites May-June Data Report Package, Dural Aluminum Composites Corporation, San Diego, CA 92121, 1989.
21. T.W. Clyne, M.G. Bader, G.R. Cappleman, P.A. Hubert: *J. Mat. Sci.*, 1985, vol. 20, p. 85.
22. T.W. Clyne and J.F. Mason: *Metall. Trans. A* , 1987, vol. 18A, p. 1519.
23. J. A. Cornie, A. Mortensen and M. C. Flemings, Proc. 6th Intl. Conf. on Composite Materials, ICCM and ECCM, eds. F.L. Matthews, N.C.R.

- Buskell, J.M. Hodgkinson and J. Morton (London, U.K., Elsevier Applied Science, 1987) p. 2.297.
24. A. Mortensen, J.A. Cornie and M.C. Flemings: *Metall. Trans. A*, 1988, vol. 19A, p. 709.
 25. M.S. Newkirk, A.W. Urguhart, H.R. Zwicker and E.J. Breval: *J. Mat. Res.*, 1986, vol. 1, No. 1, p. 81.
 26. H.L. Marcus, D.L. Bourell, Z. Eliezer, C. Persad and W.F. Weldon: *J. Metals*, 1987, p. 6.
 27. J. Papazian: *Metall. Trans. A*, 1988, vol. 19A, p. 2945.
 28. S. Ochiai and K. Osamura: *Metall. Trans. A*, 1987, vol. 18A, p. 673.
 29. E.F. Fascetta, R.G. Riek, R. Mehrabian and M.C. Flemings: *Trans. AFS*, 1973, vol. 81, p. 81.
 30. R. Mehrabian and M.C. Flemings: *Trans. AFS*, 1972, vol. 80, p. 173.
 31. M. Gupta, F.A. Mohamed and E.J. Lavernia: *Materials and Manufacturing Processes*, 1990, vol. 5, p. 165.
 32. M. Gupta, F.A. Mohamed and E.J. Lavernia: in Proc. Intl. Symp. on Advances in Processing and Characterization of Ceramic Metal Matrix Composites, CIM/ICM, 17, H. Mostaghaci ed., Pergamon press, Aug. 1989, p. 236.
 33. T.C. Willis: *Metals and Materials*, 1988, vol. 4, p. 485.
 34. C.L. Buhrmaster, D.E. Clark and H.O. Smart: *J. Metals*, 1988, vol. 40, p. 44.
 35. A.R.E. Singer: *Annals of the CIRP*, 1983, vol. 32, p. 145.
 36. M. Ruhr, E.J. Lavernia and J.C. Baram: *Metall. Trans. A*, 1990, vol. 21A, p. 1785.
 37. E.J. Lavernia: *Int. J. of Rapid Solidification*, 1989, vol. 5, p. 47.
 38. E. Gutierrez, E.J. Lavernia, G. Trapaga, J. Szekely and N.J. Grant: *Metall. Trans. A*, 1989, vol. 20A, p. 71.
 39. E.S. Balmuth, and R. Schmidt: Aluminum Lithium Alloys, (edited by T.H. Sanders, Jr., and E.A. Starke, Jr.), Metallurgical Society of AIME, 1981, p.69.
 40. E. J. Lavernia, T. S. Srivatsan, and F. A. Mohamed, *J. Mat. Sci.*, 1990, 25, 1137.
 41. R.E. Lewis, D. Webster, and I.G. Palmer: Air Force Materials Laboratory Report Contract F33615-77-C-5186, TR AFML-78-102, 1978.
 42. T.H. Sanders Jr.: Final Report for Naval Air Development Center, NADC Contract No. N62269-76-0271, 1979.
 43. E.A. Starke Jr. and F.S. Lin: *Metall. Trans. A*, 1982, vol. 13A, p. 2259.
 44. D. Webster: *Metall. Trans. A*, 1979, vol. 10A, p. 1913.

45. J.R. Pickens: *J. Mat. Sci.*, 1981, vol. 16, p. 1437.
46. F.R. Billman, J.C. Kuli, Jr., G.J. Hildeman, J.E. Petit, and J.A. Walker: Proceedings of the Third Conference on Rapid Solidification, National Bureau of Standards, Gaithersburg, MD, Dec. 6-8, p. 532, 1982.
47. Y.W. Kim, W.M. Griffith and F.H. Froes: *J. Metals* , 1985, vol. 37, No. 8, p. 27.
48. A. Gysler, R. Crooks and E.A. Starke Jr : Aluminum-Lithium Alloys, edited by T.H. Sanders Jr. and E.A. Starke Jr., (AIME, New York), p. 263, 1981.
49. S. Kang and N.J. Grant: *Mat. Sci. and Eng.*, 1985, vol. 72, p. 155.
50. M. Ahmad: *Metall. Trans. A* , 1987, vol. 18A, p. 681.
51. R.F. Ashton, D.S. Thompson, E.A. Starke and F.S. Lin: Al-Li III, C. Baker, P.J. Gregson, S.J. Harris and C.J. Peel, eds., The Institute of Metals, London, p. 66, 1986.
52. S. Fox, H.M. Flower, and D.S. McDarmaid: Al-Li III, C. Baker, P.J. Gregson, S.J. Harris and C.J. Peel, eds., The Institute of Metals, London, p. 263, 1986.
53. D.J. Field, E.P. Butler and G.M. Scamans: Aluminum -Lithium Alloys, T.H. Sanders and E.A. Starke, eds., AIME, Warrendale, PA, p. 325, 1980.
54. S.J. Donachie and P. S. Gilman: Aluminum-Lithium II, edited by E.A. Starke Jr. and T.H. Sanders, Jr. (AIME, New York), p. 507, 1983.
55. P.S. Gilman, J.W. Books, and J.P. Bridges: The Institute of Metals, London, p. 112, 1986.
56. E.J. Lavernia, T. Ando, and N.J. Grant: Proceedings of ASM's International Conference on Rapidly Solidified Materials, San Diego, CA, 3-5 Feb., P. Lee and R. Carbonara, eds., p. 29, 1986.
57. E.J. Lavernia and N.J. Grant: *J. Mat. Sci.*, 1987, vol. 22, p. 1521.
58. E.J. Lavernia and N.J. Grant: *Mat. Sci. and Eng.*, 1988, vol. 98, p. 381.
59. P.J. Meschter, R.J. Lederich, and J.E. O'Neal: McDonnell Douglas Research Laboratories, St. Louis, MO 63166. E.J. Lavernia and N.J. Grant, Department of Materials Science and Engineering, Massachusetts Institute of Technology, Cambridge, Ma 02139. " Microstructures and Properties of Liquid Dynamic Compacted Al-4Li-1Cu-0.2Zr." TMS Annual Meeting, New Orleans, LA, March 2-6, 1986.
60. P.J. Meschter, R.J. Lederich, and J.E. O'Neal: McDonnell Douglas Research Laboratories, St. Louis, MO 63166. E.J. Lavernia and N.J. Grant, Department of Materials Science and Engineering, Massachusetts Institute of Technology Cambridge, MA 02139. " Microstructures and Mechanical properties of Rapidly

- Processed (RSP) Al-4Li Alloys," International Conference on Aluminum Alloys, Charlottesville, VA, 15-20 June 1986.
61. P.J. Meschter, R.J. Lederich, and J.E. O'Neal: McDonnell Douglas Research Laboratories, St. Louis, MO 63166. E.J. Lavernia and N.J. Grant, Department of Materials Science and Engineering, Massachusetts Institute of Technology, Cambridge, Ma 02139. "Microstructures and Properties of Rapid Solidification Processed Aluminum-High Lithium Alloys," Fourth International Aluminum Lithium Conference, Paris, France, 1987.
 62. W.A. Cassada, G.J. Shiftlet and E.A. Starke Jr.: *Acta Metall.*, 1986, vol. 34, p. 367
 63. E.J. Lavernia and N.J. Grant: *Int. J. of Rapid Solidification*, 1986, vol. 2, No. 2, p. 93.
 64. R.H. Bricknell: *Metall. Trans. A*, 1986, vol. 17A, p. 583.
 65. A.G. Leatham, J.W. Ogilvy, P.F. Chesney and O.H. Metelmann: "The Production of Advanced Materials by means of the Osprey Preform Process", accepted for publication in conference proceedings of the 1988 International Powder Metallurgy Conference, Orlando, Florida June 5-10, 1988.
 66. M. Ruhr, I. Ucock, E. Lavernia and J. Baram, "Metastable Phases and Microstructure of a Rapidly Solidified Al-Li-Mn-Zr Alloy For High Temperature Applications", in *Light Weight Alloys for Aerospace*, E.W. Lee, E.H. Chia and N.J. Kim, editors, The Minerals, Metals and Materials Society, p. 79, 1989.
 67. B. Noble and G.E. Thompson: *Met. Sci. J.*, 1972, vol. 6, p. 167.
 68. J.M. Silcock: *J. Inst. Metals*, 1959-1960, vol. 88, p. 357.
 69. R.J. Rioja and E.A. Ludwiczak: Al-Li-III, Conference Proceedings, The Institute of Metals, London, p. 471, 1986.
 70. N.J. Grant, S. Kang and W. Wang: Aluminum Lithium Alloys, T.H. Sanders Jr., and E.A. Starke Jr., eds., AIME, New York, N.Y., p. 171, 1987.
 71. P. Mathur, D. Apelian and A. Lawley: *Acta Metall.*, 1989, vol. 37, p. 429.
 72. E.J. Lavernia, E. Gutierrez, J. Szekely and N.J. Grant: *Int. J. of Rapid Solidification*, 1991, vol. 4, No. 1/2, p. 89.
 73. C.G. Levi and R. Mehrabian: *Metall. Trans.*, 1982, vol. 13A, p. 221.
 74. O.S. Nichiporenko, and Y.I. Naida: *Sov. Powd. Metall. Met. Ceram.*, 1968, vol. 70, p. 1, vol. 67, No. 7, p. 509 and 1976, vol. 15, No. 9, p. 665.
 75. B.P. Bewlay and B. Cantor: Proceedings of ASM's International Conference on Rapidly Solidified Materials, San Diego, CA, 3-5 Feb., P. Lee and R. Carbonara, eds., p. 15, 1986.

76. E.J. Lavernia: University of California at Irvine, current research, 1989.
77. B.H. Kear, P.R. Holiday and A.R. Cox: *Metall. Trans. A* , 1979, vol. 10A, p. 191.
78. X. Liang and E.J. Lavernia: *Scri. Metall.*, 1991, vol. 25, p. 1199.
79. K. Ogata, E.J. Lavernia, G. Rai, and N.J. Grant: *Int. J. of Rapid Solidification* , 1986, vol. 2, No. 1, p. 21.
80. V.G. McDonnell, E.J. Lavernia and G.S. Samuelson: Synthesis and Analysis in Materials Processing: Advances in Characterization and Diagnosis of Ceramic and Metal Particulate Processing, E.J. Lavernia, H. Henein and I. Anderson, TMS, Warrendale, PA, 1989, p. 29.
81. M. Gupta, F. Mohamed and E. Lavernia: Conference Proceedings of the Al-Li-V International Conference, Williamsburg, VA, March, p. 27, 1989.
82. J.A. Juarez-Islas, H. Jones and W. Kurz: *Mat. Sci. and Eng.*, 1988, vol. 98, p. 201.
83. L. Katgerman and B. Vande Brandt: Conference Proceedings, Aluminum Powder Metallurgy, held during the TMS-AIME fall meeting, Toronto, Canada, p. 65, 1985.
84. T.G. Nieh: *Metall. Trans. A* , 1984, vol. 15A, p. 139.
85. D. L. McDanel: *Metall. Trans. A* , 1985, vol. 16A, p. 1105.
86. H. J. Rack: Proc. 6th Intl. Conf. on Composite Materials, F. L. Matthews, N. C. R. Buskell, J. M. Hodgkinson and J. Morton, editors, London, U.K., Elsevier Applied Science, 1987, p. 2.382.
87. F. Delannay, L. Froyen and A. Deruyttere: *J. Mat. Sci.*, 1987, vol. 22, p. 1.
88. S. G. Fishman: Interfaces in Metal-Ceramic Composites, R. Y. Lin, R. J. Arsenault, G. P. Martins, and S. G. Fishman, editors, The Minerals, Metals, and Materials Society, 1989, p. 3.
89. K.T. Park, E. J. Lavernia and F. A. Mohamed: *Acta Met. et Mat.*, 1990, vol. 38, No. 11, p. 2149.
90. D.J. Lloyd and I. Jin: *Metall. Trans. A* , 1988, vol. 19A, p. 3107.
91. D.R. Uhlmann, B. Chalmers and K.A. Jackson: *J. Appl. Phys.*, 1964, vol. 35 , No. 10, p. 2986.
92. G.F. Bolling and J. Cissé: *J. Crystal Growth*, 1971, vol. 10, p. 56.
93. T. Ertuk, J. A. Cornie and R. G. Dixon: "Interfaces in Metal Matrix Composites", A. K. Dhingra and S. G. Fishman, editors, Conference Proceedings, New Orleans, 1986, TMS-AIME, p. 239.

94. A.M. Zubko, V.G. Lobanov and V.V. Nikonova: *Sov. Phys. Crystallography*, 1973, vol. 18, p. 239.
95. R. Mehrabian, R.G. Riek and M.C. Flemings: *Metall. Trans. A*, 1974, vol. 5A, p. 1899.
96. M.K. Surappa and P.K. Rohatgi: *J. Mater. Sci. Lett*, 1981, vol. 16, No. 2, p. 765.
97. D.M. Stefanescu, B.K. Dhindaw, S.A. Kacar and A. Moitra: *Metall. Trans. A*, 1988, vol. 19A, p. 2847.
98. P.K. Rohatgi, R. Asthana and S. Das: *Int. Met. Rev.*, 1988, vol. 31, No. 3, p. 115.
99. T. Chanda, W.E. Frazier, F.A. Mohamed, and E.J. Lavernia: A Fundamental Study of the Microstructure of Al-Ti-SiC_p Materials using Variable Co-Deposition of Multi-Phase Materials, Conference proceedings Symposium on Metal and Ceramic Matrix Composites: Processing, Modelling & Mechanical Behavior, F.B. Bhagat, A.H. Clauer, P. Kumar, and A. M. Ritter, editors, TMS publication, Anaheim, California, U.S.A, Feb. 19-22, 1990, p. 47.
100. E.J. Lavernia, J. Baram, and E. Gutierrez: "Precipitation and Excess Solid Solubility in Mg-Al-Zr and Mg-Zn-Zr Processed by Spray Atomization and Deposition," accepted for publication, Journal of Materials Science and Engineering, 1990.
101. M. Gupta, F. Mohamed, and E. Lavernia: "Heat Transfer Mechanisms and their Effect on Microstructure during Spray Atomization and Co-Deposition of Metal Matrix Composites," S. Fishman, ed., TMS Fall Meeting, Detroit, U.S.A, Oct. 7-11, 1990.
102. S. Annavarapu, D. Apelian and A. Lawley: *Metall. Trans. A*, 1988, vol. 19A, p. 3077.
103. H.C. Fiedler, T.F. Sawyer, R.W. Koop and A.G. Leatham: *J. Metals*, 1987, vol. 39, No. 8, p. 28.
104. R. Vetter, L.Z. Zhuang, I. Majewska-Glabus and J. Duszczek: A Modified Spray Deposition Model Verified with Ni₃Al-Cr Intermetallic Alloys, *Scripta Metall. et. Mater.*, vol. 24, No. 11, in press, 1990.
105. D.L. Erich: *Int. J. of Powder Met.*, 1987, vol. 23, No. 1, p. 45.
106. P.S. Grant, W.T. Kim, B.P. Bewlay and B. Cantor: *Scripta Metall.*, 1986, vol. 23, p. 1651.
107. A.L. Moran and W.A. Palko: *J. Metals*, 1988, vol. 40, No. 12, p. 12.
108. F. Delannay, L. Froyen and A. Deruyttere: *J. Mater. Sci.*, 1987, vol. 22, p. 1.

109. S.M. Wolf, A.P. Levitt and J. Brown: *Chemical Engineering Progress*, 1966, vol. 62, No. 3, p. 74.
110. D. Webster: *Metall. Trans. A*, 1982, vol. 13A, p. 1511.
111. G.H. Geiger and D. Poirier: *Transport Phenomena in Metallurgy*, Addison-Wesley publishing Co., 1973.
112. T. Mikami, R.G. Cox and S.G. Mason: *Int. J. of Multiphase Flow*, 1975, vol. 2, p. 113.
113. H. Lubanska: *J. Metals*, 1970, vol. 22, p. 45.
114. G. Rai, E. Lavernia, N.J. Grant: *J. Metals*, 1985, vol. 37, No. 8, p. 22.
115. A. H. Shapiro: *The Dynamics and Thermodynamics of Compressible Fluid Flow*, vol. 1, New York, NY, Ronald Press, 1953, p. 85.
116. D. M. Himmelblau and K. B. Bischoff: *Process Analysis and Simulation: Deterministic Systems*, New York, John Wiley and Sons, 1968, p. 43.
117. J. White, I.G. Palmer, I.R. Hughes and S.A. Court: in *Aluminum-Lithium Alloys V*, Vol. 3, T. H. Sanders, Jr. and E. A. Starke, Jr., editors, March 27-31, 1989, Williamsburg, Virginia, p. 1635.
118. K.A. Kojima, R.E. Lewis and M.J. Kaufman: in *Aluminum-Lithium Alloys V*, vol. 1, T.H. Sanders, Jr. and E.A. Starke, Jr., editors, March 27-31, 1989, Williamsburg, Virginia, p. 85.
119. J.C. Baram, M.K. Veistinen, E.J. Lavernia, M. Abinante and N.J. Grant: *J. Mat. Sci.*, 1988, vol. 23, p. 2457.
120. M. Gupta: Ph.D. research, University of California, Irvine (1990).
121. M. Gupta, C. Lane, and E.J. Lavernia: *Scr. Metall. et Materialia*, 1992, in press.
122. M. Gupta, F.A. Mohamed and E.J. Lavernia: *Int. J. of Rapid Solidification*, 1991, vol. 6, p. 247.
123. M. Gupta, F.A. Mohamed, and E.J. Lavernia: *J. Mat. Sci.*, 1991, vol. 26, No. 24, p. 6673.
124. Yue Wu: Ph.D Dissertation research, UCI, Irvine, 1991.
125. R. Willnecker, D.M. Herlach and B. Feuerbacher: *Appl. Phys. Lett.*, 1986, vol. 49, p. 1339.
126. M. Libera: "*Heterogeneous Crystal Nucleation in Atomized Iron-Nickel Powders*", Sc.D. Thesis, Massachusetts Institute of Technology, also presented at the TMS-AIME annual meeting, Jan. 25-28, Phoenix, Arizona, U.S.A, June 1987.
127. M. Gupta, J. Juarez-Islas, W.E. Frazier, F.A. Mohamed and E.J. Lavernia: unpublished research, 1991.

128. E.J. Lavernia, E. Gutierrez, J. Szekely and N.J. Grant: Proceedings of the 1987 Annual Powder Metallurgy Conference and Exhibition, Progress in Powder Metallurgy, vol. 43, May 17-20, 1987, Dallas, Texas, p. 683.
129. E. Gutierrez, E.J. Lavernia, G. Trapaga and J. Szekely: *Int. J. of Rapid Solidification*, 1988, vol. 4, no. 1/2, p. 125.
130. W.E. Ranz, W.R. Marshall: *Chemical Engineering Progress*, 1952, vol. 48, p. 173.
131. R.H. Doremus: *Rates of Phase Transformations*, Orlando, FL, Academic Press, 1985, p. 116.
132. S.R. Coriell, and D. Turnbull: *Acta Metall.*, 1982, vol. 30, p. 2135.
133. J.W. Cahn, W.B. Hillig, and G.W. Sears: *Acta Metall.*, 1964, vol. 12, p. 1421.
134. E. Gutierrez-Miravete and E.J. Lavernia: Conference Proceedings, Physical Chemistry of Powder Metals Production and Processing, edited by W. Murray Small, The Minerals Metals and Materials Society, 1989, p. 175.
135. R.D. Pehlke, A. Jeyarajan and H. Wada: "Summary of Thermal Properties for Casting Alloys and Mold Materials", NSF report, Grant No. DAR78-26171, December 1982.
136. H. Kurten, J. Raasch, and H. Rumpf: *Chemie-Ingenieur-Technik*, 1966, vol. 38, No. 9, p. 941.
137. Frank P. Incropera and David P. DeWitt: *Introduction To Heat Transfer*, John Wiley and Sons, 1985, p. 62.
138. M. Gupta, F.A. Mohamed and E.J. Lavernia: *Metall. Trans.A*, in press 1991.
139. K.T. Park, E.J. Lavernia and F.A. Mohamed: *Acta Metall.Mater.*, 1990, vol. 38, p. 2.
140. Yue Wu and E.J. Lavernia: *J. Metals*, 1991, in press.
141. P.A. Beck, J.C. Kremer, L.J. Demer and M.L. Holzworth: *Trans. Met. Soc. AIME*, 1948, vol. 175, p. 372.
142. P.A. Beck: *J. Appl. Phys.*, 1948, vol. 19, p. 507.
143. P.A. Beck, J. Towers, and W.O. Manley: *Trans. Met. Soc. AIME*, 1951, vol. 175, p. 634.
144. R.L. Fullman: *Metal Interfaces*, American Society for Metals, 1952, p. 179.
145. P. Cotterill, and P.R. Mould: *Recrystallization and Grain Growth in Metals*, Surrey University Press, 1976, p. 275.
146. M. Ueki, M. Kana and I. Okamoto: *J. Mat. Sci. Letters*, 1986, vol. 5, p. 1261.
147. Robert E. Reed Hill: *Physical Metallurgy Principles*, D. Van Nostrand Company, Inc., p. 206.

148. M. Ruhle and A.G. Evans: *Mat. Res. Symp. Proc.*, 1988, vol. 120, p. 293.
149. R.L. Mahar, R. Jakasand C.A. Bruch: '*Behavior Study of Sapphire Wool, Aluminum and Al Alloy Composites*', Tech. Rep. AFML-TR- 68, May. 1968.
150. R.L. Mehan and E. Feingold: *J. Mater.*, 1967, vol. 2, No. 2, p. 239.
151. H.R. Shelty and Twu-Wei Choo: *Metall. Trans. A*, 1985, vol. 16, p. 853.
152. C.G. Levi, G.J. Abaschian and R. Mehrabian: *Metall. Trans. A*, 1978, vol. 9, p. 697.
153. A. Banerjee: MSc Thesis, University of Kerala, India, 1982.
154. M. Ueki, M. Naka and I. Okamoto: *J. Mat. Sci. Letters*, 1986, vol. 5, p. 1261.
155. Doh-Jae Lee, M.D. Vaudin, C.A. Hand werker and U.R. Kattner: *Mat. Res. Symp. Proc.*, 1988, vol. 120, p. 293.
156. S.R. Nutt and R.W. Carpenter: *Mat. Sci. Eng.*, 1985, vol. 75, p. 169.
157. C. Lea and C. Molinari: *J. Mat. Sci.*, 1984, vol. 19, p. 2336.
158. T. Malis and M.C. Chaturvedi: *J. Mat. Sci.*, 1982, vol. 17, p. 1479.
159. Private communication with Tracor-Northern, Middleton, WI 53562.
160. S-Y. Oh, J.A. Cornie and K.C. Russell: *Ceramic Engineering Sci. Proc.*, 1987, vol. 8, No. 7-8, p. 912.
161. J.E. McDonald and J.G. Eberhart: *Trans. TMS-AIME*, 1965, vol. 233, p. 512.
162. V. Laurent, D. Chatain and N. Eustathopoulos: *J. Mat. Sci.*, 1987, vol. 22, p. 244.
163. R. Warren and C.H. Anderson: *Composites*, 1984, vol. 15, p. 101.
164. R.J. Arsenault and C.D. Pande: *Scr. Metall.*, 1984, vol. 18, p. 1131.
165. S. Nourbaksh, H. Margolin and F.L. Liang: *Metall. Trans. A*, 1989, vol. 20, p. 2159.
166. J.M. Yang, W.H. Kao and C.T. Lin: *Metall. Trans. A*, 1989, vol. 20, p. 2459.
167. K. Kannikeswaran and R.Y. Lin: *J. Metals*, (Sept. 87), p. 17.
168. T. Iseki, T. Kameda and T. Maruyama: *J. Mat. Sci.*, 1984, vol. 19, p. 1692.
169. M.J. Couper, M. Nauer, R. Baumann and R.F. Singer: Brown Boveri Laboratory Report, Dec. 1987.
170. D.J. Field, G.M. Scamans, and E.P. Butler: in *Aluminum-Lithium Alloys II*, E.A. Starke, Jr. and T.H. Sanders, Jr., editors, April 12-14, 1983, Monterey, California, p. 657.
171. J.M. Marinkovich, F.A. Mohamed, J.R. Pickens and E.J. Lavernia: *J. Metals*, 1989, vol. 41, No. 9, p. 36.
172. L.S. Darken and R.W. Gurry: *Physical Chemistry of Metals*, McGraw-Hill, New York, 1953.

173. I.M. Lifshitz and V.V. Slyzov: *J. Phys. and Chem. of Solids*, 1961, vol. 19, pp. 35-50.
174. R. Irmann: *Techn. Rundschau*, 1949, vol. 41, pp. 19-27.
175. A.V. Zeerleder: *Z. Metalkunde*, 1950, vol. 41, pp. 228-239.
176. H. Jones: *Aluminium*, 1978, vol. 54, pp. 274-287.
177. D.J. Skinner, R.L. Bye, D. Raybould and A.M. Brown: *Scri. Metall.*, 1986, vol. 20, pp. 867-872.
178. D.J. Skinner: *Dispersion Strengthened Aluminum Alloys*, Y.W. Kim, W.M. Griffith, eds., The Metallurgical Society, Warrendale, PA, 1988, pp. 181-197.
179. Y.W. Kim: *Dispersion Strengthened Aluminum Alloys*, Y.W. Kim, W.M. Griffith, eds., The Metallurgical Society, Warrendale, PA, 1988, pp. 157-180.
180. P.S. Gilman and W.D. Nix: *Metall. Trans. A*, 1981, vol. 12A, pp. 813-824.
181. I.G. Palmer, M.P. Thomas, and G.J. Marshall: *Dispersion Strengthened Aluminum Alloys*, Y.W. Kim, W.M. Griffith, eds., The Metallurgical Society, Warrendale, PA, 1988, pp. 217-241.
182. P.K. Mirchandani and R.C. Benn: *Experimental High Modulus Elevated Temperature Al-Ti Based Alloys by Mechanical Alloying*, SAMPE, Covina, CA (1988).
183. W.E. Frazier and M.J. Koczak: *Elevated Temperature Aluminum-Titanium alloy by Powder Metallurgy Process*, United States Patent, No. 4,834,942, May 30, 1989.
184. W.E. Frazier and M.J. Koczak: *High Strength Powder Metallurgy Aluminum Alloys II*, G.H. Hildeman, M.J. Koczak, eds., The Metallurgical Society, Warrendale, PA, 1985, pp. 353-366.
185. M.E. Fine: *Dispersion Strengthened Aluminum Alloys*, Y.W. Kim, W.M. Griffith, eds., The Metallurgical Society, Warrendale, PA, 1988, pp. 103-121.
186. H.W. Kerr, J. Cisse and G.F. Bolling: *Acta Metall.*, 1974, vol. 22, pp. 677-686.
187. T. Chanda, W.E. Frazier, F.A. Mohamed and E.J. Lavernia: *A Fundamental Study of the Thermal Stability of Spray Atomized and Deposited Al-Ti Materials*, Fall Meeting, Detroit, MI, The Metallurgical Society, Warrendale, PA, 1990.
188. A. Tonejc and A. Bonefacic: *Scri. Metall.*, 1969, vol. 3, pp. 145-148.
189. M. Gupta, F.A. Mohamed, and E.J. Lavernia: *Mater. Sci. Eng.*, 1991, in press.
190. V.G. McDonnell, E.J. Lavernia and G.S. Samuelson: *Synthesis and Analysis in Materials Processing: Advances in Characterization and Diagnosis of Ceramic and Metal Particulate Processing*, E.J. Lavernia, H. Henein and I. Anderson, eds., The Metallurgical Society, Warrendale, PA, 1989, pp. 13-37.

191. E.J. Lavernia: *SAMPE Quarterly*, 1991, vol. 22 (2), pp. 2-12.
192. I.A. Ibrahim, F.A. Mohamed and E.J. Lavernia: *Advanced Aluminum and Magnesium Alloys*, T. Khan, G. Effenberg, eds., ASM International, Amsterdam, 1989, pp. 745-754.
193. Hultgren: *Selected Values of the Thermodynamic Properties of Binary Alloys*, ASM, Metals Park, OH, 1973.
194. D.H. St John and L.M. Hogan: *J. Mater. Sci.*, 1980, vol. 15, pp. 2369-2375.
195. L.F. Mondolfo: in *Aluminum Alloys: Structure and Engineering Materials*, NY, John Wiley, 1976, p. 14.
196. W. Hoffman: *Aluminium*, 1938, vol. 20, p. 865.
197. W. Kurz, B. Giovanola and R. Trivedi: *Acta Metall.*, 1986, vol. 34, pp. 823-830.
198. J.A. Juarez-Islas and H. Jones: *Acta Metall.*, 1987, vol. 35, pp. 499-507.
199. M.J. Aziz: in *An Atomistic Model of Solute Trapping*, Proceedings of the third Conference on Rapid Solidification Processing, edited by R. Mehrabian, held at National Bureau of standards, Dec. 6-8, 1982, Gaithersburg, Maryland, USA, pp. 113-117.
200. C. Mccullough, J. J. Valencia, C.G. Levi and R. Mehrabian: *Mater. Sci. Eng.*, 1990, vol. 124, pp. 83-101.
201. J.J. Valencia, C. Mccullough, C.G. Levi and R. Mehrabian: *Acta Metall.*, 1989, vol. 37, pp. 2517-2530.
202. M. Ruhr, E.J. Lavernia, and J. Baram: *Metall. Trans. A*, 1990, vol. 21A, pp. 1785-1789.
203. E. Gutierrez, G. Trapaga, and J. Szekely: *Casting of Near Net Shape Products*, Y. Sahai, J.E. Battles, R.S. Carbonara, and C.E. Mobley, eds., held at the Fall Extractive and Process Metallurgy Meeting, Honolulu, Hawaii, 1988, pp. 133-151.
204. J.E. Hatch, *Aluminum: Properties and Metallurgy*, ASM, Metals Park, OH, 1984.
205. M. Vogelsang, R.J. Arsenault, and R.M. Fisher: *Metall. Trans. A*, 1986, vol. 17A, pp. 379-389.
206. V.C. Nardone and J.R. Strife: *Metall. Trans. A*, 1987, vol. 18, p. 109.
207. T.G. Nieh, K. Xia and T.G. Langdon: *J. Eng. Mater. Tech.*, 1988, vol. 110, p. 77.
208. T. Morimoto, T. Yamaoko, H. Lilholt and M. Taya: *J. Eng. Mater. Tech.*, 1988, vol. 110, p. 70.
209. W.C. Oliver and W.D. Nix: *Acta Metall.*, 1982, vol. 30, p. 1335.
210. R.W. Lund and W.D. Nix: *Acta Metall.*, 1976, vol. 24, p. 469.

211. S.T. Mileiko: *J. Mat. Sci.*, 1970, vol. 5, p. 254.
212. D. Mclean: *J. Mat. Sci.*, 1972, vol. 7, p. 98.
213. A. Kelly and K.N. Street: *Proc. R. Soc. London*, 1972, vol. 328A, p. 267.
214. H. Liholt: *Comp. Sci. Tech.*, 1985, vol. 22, p. 277.
215. M. Taya and H. Litholt: in S.S. Wang and Y. Rajapakse (eds), modeling of the Second and Third Stage Creep Rates of an aligned Short Fiber Metal Matrix Composites, Proc. of the ASME Applied Mechanics Division Conference, ASME, vol. 822, 1986.
216. T.L. Dragone and W.D. Nix: *Acta Metall.*, 1990, vol. 38, p. 1941.
217. A. Kelly and W.R. Tyson: *J. Mech. Phys. Solids*, 1966, vol. 14, p. 177.
218. B.A. Wilcox and A.H. Clauer: *Trans. Am. Inst. Min. Eng.*, 1966, vol. 236, p. 570.
219. R.W. Lund and W.D. Nix: *Metall. Trans. A*, 1975, vol. 6, p. 1329.
220. E. Orowan: in M. Cohen (ed), Dislocations in Metals, *Am. Inst. Min. Eng.*, New York (1954), p. 131.
221. U.F. Kocks: *Philos. Mag.*, 1966, vol. 13, p. 541.
222. R.S.W. Shewfelt and L.M. Brown: *Philos. Mag.*, 1977, vol. 35, p. 945.
223. E. Arzt and M.F. Ashby: *Scripta Metall.*, 1982, vol. 16, p. 1285.
224. R. Lagneborg: *Scripta Metall.*, 1973, vol. 7, p. 605.
225. W. Blum and B. Reppich: in B. Wilshire and R.W. Evans, Creep Behavior of Crystalline Solids, Pineridge Press, Swansea, U.K. (1985) p. 83.
226. J.H. Hausselt and W.D. Nix: *Acta Metall.*, 1977, vol. 25, p. 1491.
227. E. Arzt and D.S. Wilkinson: *Acta Metall.*, 1986, vol. 34, p. 1893.
228. E. Arzt and J. Rösler: *Acta Metall.*, 1988, vol. 36, p. 1053.
229. J. Rösler and E. Arzt: *Acta Metall.*, 1990, vol. 38, p. 671.
230. J.E. Bird, A.K. Mukherjee and J.E. Dorn: in D.G. Brandon and A. Rosen (eds), Quantitative Relation Between Properties and Microstructures, Israel University Press, Jersualem, 1969, p. 255.
231. O.D. Sherby and P.M. Burke: *Prog. Mater. Sci.*, 1968, vol. 13, p. 325.
232. A. Goel, T.J. Ginter and F.A. Mohamed: *Metall Trans. A.*, 1983, vol. 14, p. 2309.
233. P. Chaudhury and F.A. Mohamed: *Metall. Trans. A*, 1987, vol. 18, p. 2105.
234. K.L. Murty, F.A. Mohamed and J.E. Dorn: *Acta Metall.*, 1972, vol. 20, p. 1009.
235. M.S. Soliman and F.A. Mohamed: *Mater. Sci. Eng.*, 1982, vol. 55, p. 111.
236. F.A. Mohamed and T.G. Langdon: *Acta Metall.*, 1974, vol. 22, p. 779.
237. F.A. Mohamed: *Mater. Sci. Eng.*, 1983, vol. 61, p. 149.

- 238. J. Weertman: *J. Appl. Phys.*, 1957, vol. 28, p. 1185.
- 239. J. Weertman: *J. Appl. Phys.*, 1957, vol. 28, p. 362.
- 240. G.M. Pharr and W.D. Nix: *Scripta Metall.*, 1976, vol. 10, p. 1007.
- 241. D.J. Srolovitz, R.A. Petkovic-Luton and M.J. Luton: *Acta Metall.*, 1983, vol. 31, p. 2151.
- 242. V.C. Nardone and J.K. Tien: *Scripta Metall.*, 1983, vol. 17, p. 467.
- 243. J.H. Schröder and E. Arzt: *Scripta Metall.*, 1985, vol. 19, p. 1129.
- 244. R.S. Herrik, J.R. Weertman, R. Petkovic-Luton and M.J. Luton: *Scripta Metall.*, 1983, vol. 22, p. 1879.
- 245. S.L. Robinson and O.D. Sherby: *Acta Metall.*, 1969, vol. 17, p. 109.
- 246. O.D. Sherby, R.H. Klundt and A.K. Miller: *Metall. Trans. A*, 1977, vol. 8, p. 843.
- 247. P. Chaudhury and F.A. Mohamed: *Acta Metall.*, 1988, vol. 36, p. 1099.
- 248. R.S. Mishra and A.B. Pandey: *Metall. Trans. A*, 1990, vol. 21, p. 2089.
- 249. M.S. Soliman, T.J. Ginter and F.A. Mohamed: *Philos. Mag.*, 1983, vol. 48, p. 63.
- 250. K.K. Chawla: in B. Illschner and N.J. Grant (eds), *Composite Materials, Materials Research and Engineering*, Springer-Verlag, New York Inc., 1987, p. 121.
- 251. P.M. Kelly: *Inst. Metals Rev.*, 1973, vol. 18, p. 31.
- 252. M. Soliman and F.A. Mohamed: *Metall. Trans. A*, 1984, vol. 15, p. 1893.
- 253. P. Chaudhury and F.A. Mohamed: *Mater. Sci. Eng.*, 1988, vol. 101, p. 13.
- 254. F.A. Mohamed: *J. Mat. Sci.*, 1983, vol. 18, p. 582.
- 255. J. Friedel: *Dislocations*, Pergamon, Oxford, 1964, Chapter 16.

IV. LIST OF PUBLICATIONS

A. Journal Papers

1. E.J. Lavernia, "The Evolution of the Microstructure During Spray Atomization and Deposition," *Israel Journal of Technology*, Vol. 24, pp. 79-86, 1988.
2. E.J. Lavernia, T. Srivatsan and F. Mohamed, "Strength, Deformation, Fracture Behavior and Ductility of Aluminum-Lithium Alloys: A Review," *Journal of Materials Science*, Vol. 25, pp. 1137-1158, 1990.
3. E.J. Lavernia, "The Evolution of the Microstructure During Spray Atomization and Deposition," *International Journal of Rapid Solidification*, Vol. 5, pp. 47-85, 1989.
4. J. Marinkovich, F.A. Mohamed, J.R. Pickens and E.J. Lavernia, "The Spray Atomization and Deposition of Weldalite 049," *Journal of Metals*, Vol. 41, No. 9, pp. 36-41, September 1989.
5. K.T. Park, E.J. Lavernia and F.A. Mohamed, "Creep Behavior and Substructure in an Al-Li Alloy," *Acta Metallurgica et Materialia*, Vol. 38, No. 10, pp. 1837-1848, 1990.
6. M. Ruhr, E.J. Lavernia and J. Baram, "Extended Al (Mn) Solution in a Rapidly Solidified Al-Li-Mn-Zr Alloy," *Metallurgical Transactions*, Vol. 21A, pp. 1785-1789, June 1990.
7. M. Gupta, F.A. Mohamed and E.J. Lavernia, "Solidification Behavior of Al-Li-SiC MMCs Processed Using Variable Co-Deposition of Multi-Phase Materials," *Journal of Materials and Manufacturing Processes*, Vol. 5, No. 2, pp. 165-196, 1990.
8. I. Ibrahim, F.A. Mohamed and E.J. Lavernia, "Particulate Reinforced Metal Matrix Composites: A Review," *Journal of Materials Science*, Vol. 26, pp. 1137-1156, 1991.
9. T.S. Srivatsan, E.J. Lavernia, and F.A. Mohamed, "The Influence of Oxides on Powder-Metallurgy Aluminum-Lithium-Copper Alloys," *International Journal of Powder Metallurgy*, Vol. 26, No. 4, pp. 321-334, 1990.
10. T.S. Srivatsan and E.J. Lavernia, "The Presence and Consequences of Precipitate Free Zones in an Aluminum-Copper-Lithium Alloy," *Journal of Materials Science*, Vol. 26, pp. 940-950, 1991.
11. K.T. Park, E.J. Lavernia and F.A. Mohamed, "High Temperature Creep of SiC Particulate Reinforced Aluminum," *Acta Metallurgica et Materialia*, Vol. 38, No. 11, pp. 2149-2159, 1990.
12. T.S. Srivatsan, M. Gupta, F. Mohamed and E.J. Lavernia, "The Influence of Spray Atomization and Deposition Processing on the Microstructure of an Aluminum-Copper-Lithium Alloy," *Aluminum an International Journal*, Vol. 1165, No. 6, pp. 127-144, 1991.

13. E.J. Lavernia, J.A. Ayers and T.S. Srivatsan, "Rapid Solidification Processing with Specific Application to Aluminum Alloys," accepted for publication, *International Materials Reviews*, 1991.
14. M. Gupta, F. A. Mohamed and E.J. Lavernia, "Wetting and Interfacial Reactions in Al-Li-SiC_p MMCs Processed by Spray Atomization and Deposition," *Journal of Materials Science*, Vol. 26, pp. 6673-6684, 1991.
15. E.J. Lavernia, E. Gutierrez and J. Baram, "Precipitation and Excess Solid Solubility in Mg-Al-Zr and Mg-Zn-Zr Processed by Spray Atomization and Deposition," *Journal of Materials Science and Engineering*, Vol. A132, pp. 119-133, 1991.
16. M. Gupta, F. A. Mohamed and E.J. Lavernia, "The Effects of Solidification Phenomena on the Distribution of Ceramic Reinforcements during Spray Atomization and Co-Deposition," *International Journal of Rapid Solidification*, Vol. 6, pp. 247-284, 1991.
17. T.S. Srivatsan, I. Ibrahim, F.A. Mohamed and E.J. Lavernia, "Processing Techniques for Particulate Reinforced Metal Matrix Composites," *Journal of Materials Science*, vol. 26, pp. 5965-5978, 1991.
18. E.J. Lavernia, "Synthesis of Particulate Reinforced Metal Matrix Composites using Spray Atomization and Co-Deposition," *SAMPE Quarterly*, January, pp. 2-12, 1991.
19. Y. Wu and E.J. Lavernia, "Microstructure, Aging Response and Mechanical Behavior of 6061 SiC_p MMCs Processed by Spray Atomization and Co-Deposition," *Journal of Metals*, vol. 43, no. 8, pp. 16-23, August 1991.
20. F. Mohamed, K.T. Park, and E.J. Lavernia, "Creep Behavior of Discontinuous SiC-Al Composites," *Materials Science and Engineering A*, in press, 1992.
21. M. Gupta, F.A. Mohamed, and E.J. Lavernia, "Heat Transfer Mechanisms and their Effect on Microstructure during Spray Atomization and Co-Deposition of Metal Matrix Composites," *Materials Science and Engineering A*, vo. A144, pp. 99-110, 1991.
22. M. Gupta, F.A. Mohamed, and E.J. Lavernia, "The Effect of Ceramic Reinforcements During Spray Atomization and Co-Deposition of Metal Matrix Composites: Part I: Heat Transfer," *Metallurgical Transactions A*, in press, 1992.
23. M. Gupta, F.A. Mohamed, and E.J. Lavernia, "The Effect of Ceramic Reinforcements During Spray Atomization and Co-Deposition of Metal Matrix Composites: Part II: Solid State Cooling Effects," *Metallurgical Transactions A*, in press, 1992.
24. M. Gupta, J. Juarez-Islas, W.E. Frazier, F.A. Mohamed, and E.J. Lavernia, "Microstructure, Excess Solid Solubility and Elevated Temperature Behavior of Spray Atomized and Co-Deposited Al-Ti-SiC," *Metallurgical Transactions B*, in press, 1992.
25. M. Gupta, C. Lane and E.J. Lavernia, "Microstructure and Properties of Spray Atomized and Deposited Al-7Si/SiC_p Metal Matrix Composites," *Scripta Metallurgica et Materialia*, in press, 1992.

26. M. Gupta, F. A. Mohamed and E.J. Lavernia, "Solidification Characteristics of Atomized Al-Ti Powders," *Scripta Metallurgica et Materialia*, in press, 1992.

B. Papers in Conference Proceedings

1. E.Y. Ting and E.J. Lavernia, "Superplastic Behavior in a Spray Deposited Experimental 7075 Al Alloy," *Light Weight Alloys for Aerospace Applications*, edited by E.W. Lee, E.H. Chia and N.J. Kim, The Minerals, Metals & Materials Society, Warrendale, PA, pp. 409-418, 1989.
2. V.G. McDonnell, E.J. Lavernia and G.S. Samuelson, "Simultaneous Measurement of Particle Size and Velocity Using Phase Doppler Interferometry," in *Synthesis and Analysis in Materials Processing: Advances in Characterization and Diagnostics of Ceramic and Metal Particulate Processing*, eds., E.J. Lavernia, H. Henein and I. Anderson, TMS, pp. 30-55, 1989.
3. M. Gupta, F. Mohamed and E. Lavernia "Spray Atomization and Deposition of an Al-Cu-Li-Zr Alloy," *Proceedings of the Fifth International Aluminum-Lithium Conference*, Williamsburg, Va, March 27-31, pp. 75-84, 1989.
4. K.T. Park, E. Lavernia and F. Mohamed, "Creep Behavior of an Aluminum-Lithium Alloy," *Proceedings of the Fifth International Aluminum-Lithium Conference*, Williamsburg, Va, March 27-31, pp. 1155-1162, 1989.
5. M. Gupta, F.A. Mohamed and E.J. Lavernia. "Processing of Al-Li-SiC_p Materials Using Variable Co-Deposition of Multi-Phase Materials," *Proceedings of International Symposium on Advances in Processing and Characterization of Ceramic and Metal Matrix Composites*, Ed., H. Mostaghaci, The Canadian Institute of Mining and Metallurgy, pp. 236-253, 1989.
6. M. Gupta, J. Marinkovich, F. Mohamed and E.J. Lavernia, "Processing of Two Al-Li-X-Zr (X=Cu, Mg and Ge)," *Advances in Powder Metallurgy*, Volume 1-3, Metal Powder Industries Federation, Princeton, N.J., pp. 139-160, 1989.
7. M. Gupta, I. Ibrahim, F. Mohamed, and E. Lavernia, "Wetting and Interfacial Reactions in Al-Li-SiC_p MMCs Using Spray Atomization and Deposition," accepted for publication in *Proceedings of Symposium on Fundamental Relationships between Microstructure & Mechanical Properties of Metal Matrix Composites*, The Metallurgical Society Fall meeting, October 1-5, Indianapolis, Indiana, pp. 1-19, 1989.
8. T. Chanda, W.E. Frazier, F. Mohamed, and E. Lavernia, "A Fundamental Study of the Microstructure of Al-Ti-SiC_p Materials Using Variable Co-Deposition of Multi-Phase Materials," *Metal and Ceramic Matrix Composites: Processing, Modeling and Mechanical Behavior*, R.B. Bhagat, A.H. Clauer, P. Kumar and A.M. Ritter, eds., TMS, pp. 47-66, 1990.
9. M. Gupta, F. Mohamed, and E. Lavernia, "The Effects of Solidification Phenomena on the Distribution of Ceramic Reinforcements During Spray Atomization and Deposition," *Metal and Ceramic Matrix Composites: Processing, Modeling and Mechanical Behavior*, R.B. Bhagat, A.H. Clauer,

P. Kumar and A.M. Ritter, eds., TMS, pp. 91-106, 1990.

10. I.A. Ibrahim, F. Mohamed, and E. Lavernia, "Spray Atomization and Deposition Processing of 6061 Al/SiC_p Metal Matrix Composites," accepted for publication, conference proceedings, *International Conference on Advanced Aluminum and Magnesium Alloys*, ASM International, 20-22 June, Amsterdam, pp. 745-754, 1990.
11. M. Gupta, F.A. Mohamed, and E.J. Lavernia, "Microstructure and Mechanical Properties of Al-Cu Based Metal Matrix Composites Using Spray Atomization and Co-Deposition," to be published in conference proceedings, 1992 TMS meeting, San Diego, CA, The Metallurgical Society, Warrendale, PA.

C. *Book Chapters:*

- C1. E.J. Lavernia, J.A. Ayers, T.S. Srivatsan, chapter in book entitled "Rapid Solidification of Structural Materials," to be published by Technomic Publishing Co., in press 1991. (a modified version of this paper will appear as a comprehensive paper in the *International Materials Reviews*).

D *Invited Papers:*

1. E.J. Lavernia, "Spray Deposition Processing of Aluminum Lithium Alloys," in conference proceedings of the *Fourth Israel International Materials Engineering Conference-I.M.E.C. IV*, Beer-Sheva, Israel, 7-8, pp. 79-86, December 1988.
2. E.J. Lavernia, "Spray Atomization and Deposition Processing of Particulate Reinforced Metal Matrix Composites," in conference proceedings, *International conference, Fifty Years of Evolution in India*, Calcutta, India, 8-9 April, 1990.
3. E.J. Lavernia, "Manufacturing of Particulate Reinforced MMCs using Spray Processes," conference proceedings, *Symposium on Metal Matrix Composites*, organized by the Society of Manufacturing Engineers, Nov. 14, 1990, Anaheim, California.
4. F.H. Froes, C. Suryanarayana, and E.J. Lavernia, "Synthesis of Light Metals for Aerospace Applications," conference proceedings, *Science and Engineering of Light Metals*, edited by K. Hirano, H. Oikawa and K. Ikeda, Sendai, Japan, October 13-16, (1991), The Japan Institute of Light Metals, pp. 43-50.
5. F.H. Froes, W.E. Quist, E.J. Lavernia, and C. Suryanarayana, "Advanced Aerospace Metals, Requirements, and Characteristics - An Overview," conference proceedings, *Second ASM Paris Conference: Synthesis, Processing and Modelling of Materials*, 11-13 September 1991, Paris, France.

E. *Invited Lectures and Seminars:*

1. "Advanced Processing of Materials," seminar on High Density Powder Metallurgy, Materials Processes and Applications, Metal Powder Industries Federation, March 17-19, 1989.

2. "Solidification Behavior of Al-Li -SiCp Materials using Co-Deposition of Multi - Phase Materials," lecture presented at the symposium on: "Metal Spray Deposition - Theory, Applications and Manufacturing Technology," David Taylor Research Center, Annapolis, Maryland, March 16, 1990.
3. "Composite Manufacturing Research," lecture presented at the Western Metal & Tool Exposition & Conference, WESTEC '90, Los Angeles, CA, March 28, 1990.
4. "Interfacial Behavior during Processing of Metal Matrix Composites," lecture presented at the International Conference on Fifty Years of Evolution of Metallurgy, Calcutta, India, April 9, 1990; also presented at the Indian Institute of Science, Bangalore, April 7, 1990.
5. "Solidification Mechanisms during Spray Atomization and Co-Deposition," lecture presented at the Department of Applied Mechanics and Engineering Science of the University of California, San Diego, February 4, 1991.
6. "The Effects of Processing Conditions on the Distribution of Ceramic Reinforcements during Spray Atomization and Co-Deposition," lecture presented at the Department of Materials Science and Engineering, Case Western Reserve University, Cleveland, Ohio, January 31, 1991.
7. "Non-Equilibrium Processing of Advanced Structural Materials," lecture presented at the 27th National Heat Transfer Conference & Exposition, Minneapolis, MN, July 28-31, 1991.
8. "Reactive Spray Processing of Metal Matrix Composites," lecture presented at the Aluminum Company of America Technical Center, Pittsburgh, PA, October 25, 1991.

V LIST OF PARTICIPATING SCIENTIFIC PERSONNEL

1. Dr. E.J. Lavernia: Principal Investigator, UCI, Irvine, CA.
2. Dr. F.A. Mohamed: Co-Principal Investigator, UCI, Irvine, CA.
3. Mr. I. Sauer: Laboratory Technician, UCI, Irvine, CA.
4. Ms. Jean Marinkovich: M.Sc. Degree, awarded September 1990.
5. Mr. Manoj Gupta: Ph.D. candidate (completion date: Winter 1992).
6. Mr. K.T. Park: Ph.D. candidate (completion date: Winter 1992).
7. Mr. Souping Yan: M.Sc. candidate (completion date: Spring 1992).
8. Mr. Peter Lengsfeld: M.Sc. candidate (completion date: Spring 1992).
9. Mr. Chris San Marchi: Undergraduate student, laboratory assistant.